Non-Linear Optical Properties and Time-Resolved Spectroscopic Studies of Functional Materials for Optoelectronic, Quantum Sensing and Catalysis Applications

by

Olusayo Joseph Ogunyemi

A dissertation submitted in partial fulfillment
of the requirements for the degree of
Doctor of Philosophy
(Macromolecular Science and Engineering)
in the University of Michigan
2026

Doctoral Committee:

Professor Theodore G. Goodson III, Chair
Professor Ageeth Bol
Professor Chima Maduka
Professor Jinsang Kim

Olusayo Joseph Ogunyemi

olusayo@umich.edu

ORCID iD: 0009-0004-1118-5634

© Olusayo Joseph Ogunyemi 2026

DEDICATION

My thesis is dedicated to my beautiful wife Blessing Nonye Ogunyemi, my parents (Godwin Ajihinrere Ogunyemi and Roseline Taiwo Ogunyemi), and my younger sister Foluke Raji.

ACKNOWLEDGEMENT

There is a long list of people who have played a huge role in the success of my Ph.D. journey. You are all in my heart and I sincerely appreciate you all.

First, I give all thanks to Jehovah God for his guidance, protection and provision. He is my strength and confidence and has been my helper. I want to acknowledge wholeheartedly my beloved wife whose unwavering love, patience and encouragement carried me through every challenge of this journey. Your support and belief in me gave me strength to believe in myself and soar above every challenge. From the bottom of my heart, I am indebted and grateful to my parents who have been my rock, my support and my backbone. They laid the foundation for my education and development of moral character with their sacrifices, wisdom and support. Everything I accomplish stands on the values you instilled in me.

To my sister (Foluke Raji) and her family for their kindness, prayers and constant reassurance. Your words of encouragement have been a strong and powerful anchor. To my advisor, Professor Theodore Goodson III whose guidance, insight and mentorship shaped not only this thesis but my growth as a researcher; thank you for your commitment, time and belief in my potential.

I also want to acknowledge the Agunbiade family; you have been the shoulder that carried me throughout my undergraduate program. The Odofin's family as my second parent for your prayers and moral character instilled in me while growing up until now. To my friends from Wayne

State University who became family, thank you for the support. I also want to appreciate members of the Goodson group who have become family for their unwavering support during graduate school.

Table Of Contents

Dedication……...ii
Acknowledgement ……iii

List of Figures ……...x
List of Tables……xvi

Abstract……xix

Chapter One: Introduction to Organic Optoelectronic and Functional Materials..... 1
1.1 Background..... 1
1.1.1 Mechanisms and Fundamental Processes of Organic Solar Cell..... 2
1.1.2. Molecular Design and Evolution of OSC Materials..... 5
1.1.3. Organic Materials for Quantum Information Science 7
1.1.4. Organic Materials for Quantum Sensing Application 9
1.1.5. Singlet Exciton Fission..... 10
1.1.6. Singlet Exciton Fission: A Pathway to Entangled Spin Manifolds for Quantum Information Science Application..... 12
1.1.7. Importance of Electronic Coherence in Accessing Quintet State..... 14
1.2. Organic Field-Effect Transistors (OFETs)..... 15
1.2.1. Semiconductor-Dielectric Interface for Governing Charge Transport 16
1.2.2. Charge Transport Mechanisms in OFETs..... 17
1.2.3. Molecular Design Principles for High-Performance OFET Materials..... 19
1.2.4. OFETs as a Platform for Sensing, Logic, and Integrated Photonics 21
1.3. Organic Light-Emitting Diodes (OLEDs)..... 21
1.3.1. Thermally Activated Delayed Fluorescence (TADF): A Pathway to 100% Internal Quantum Efficiency 23
1.3.2. Design Principles and Mechanisms for TADF 24
1.3.3. Mechanism of TADF 27
1.4. Nonlinear and Quantum-Optical Spectroscopic Techniques as Molecular Probes..... 29
1.4.1. Classical Two-Photon Absorption 30

1.4.2. Quantum Entanglement and Its Emerging Role in Light-Matter Interactions 34
1.4.2.1. Entangled Two-Photon Absorption (ETPA): Quantum-Mechanical Perspective and Molecular Insights 36
1.5. Photoinduced Electron Transfer, Single Electron Transfer, and Back Electron Transfer in Photocatalytic Systems 41
1.5.1. Photoinduced Electron Transfer (PET): Excited-State Reactivity and Energy Dynamics 42
1.6. Overview of Dissertation Chapters 46
Chapter Two: Methodology and Instrumentation 72
2.1. Overview of Experimental Method and Techniques 72
2.2. Steady State Absorption 73
2.3. Classical Two-Photon Absorption 79
2.4. Entangled Two-Photon Absorption 82
2.5. Transient Absorption Spectroscopy 84
2.5.1. Nanosecond Transient Absorption Instrumentation and Technique 89
2.5.2. Femtosecond Transient Absorption Instrumentation and Technique 91
2.5.3. Time Correlated Single Photon Counting Instrumentation 93
2.5.4. Fluorescence up-conversion Instrumentation 95
2.6. Near-field scanning optical microscopy (NSOM) Principle and Technique 96
Chapter Three: From Structure to Function: Nonlinear Optical Properties and Excited-State Dynamics of Ladder-Type π-Conjugated Benzo [k] tetraphene Oligomers…….. …..105
3.1. Author Contribution Statement 105
3.2. Abstract 106
3.3. Introduction 106
3.4. Methods 110
3.4.1. Steady State Measurement 110
3.4.2. Fluorescence Quantum Yield 110
3.4.3. Classical Two Photon Absorption 110
3.4.4. Entangled Two Photon Absorption 111
3.4.5. Time Correlated Single Photon Counting 112
3.4.6. Nanosecond Transient Absorption Spectroscopy 112

3.5. Results and Discussion 113
3.5.1. Steady State Optical Properties 113
3.5.1. Electronic Structures calculations 116
3.5.2. Classical Two Photon Absorption....118
3.5.3. Entangled Two Photon Absorption (ETPA).... 121
3.5.4. Time Correlated Single Photon Counting.... 124
3.6. Nanosecond Transient Absorption Spectroscopy.... 126
3.7. Conclusion 133
Chapter Four: Understanding the Correlation of the Quantum Dephasing Time and Entangled Photon Interaction in Crystalline Tetracene Derivatives…….. …..161
4.1. Author Contribution Statement.... 161
4.2. Abstract.... 162
4.3. Introduction.... 163
4.4. Experimental Section.... 166
4.4.1. Sample Preparation.... 166
4.4.2. Absorption and Steady State Emission.... 167
4.4.3. Entangled Two Photon Absorption Measurements (ETPA) 167
4.4.4. Two Photon Absorption (TPA) 168
4.4.5. Time-Resolved Near-Field Scanning Optical Microscopy (NSOM) 168
4.4.6. Fluorescence Quantum Yields 168
4.4.7. Theoretical Calculations 169
4.5. Result 169
4.5.1. Absorption and Emission Spectroscopy of Tetracene Systems.... 169
4.5.2. Time Resolved Electron Paramagnetic Resonance (TREPR) 170
4.5.3. Electronic Structure Calculations of Tetracene Systems 171
4.5.4. Classical Two-Photon Absorption of Tetracene Systems 172
4.5.5. Entangled Two-Photon Absorption (ETPA) 174
4.5.6. Coherence Time measured with Femtosecond Near-Field Optical Microscope 175
4.6. Discussion.... 180
4.7. Conclusion 182

Chapter Five: Linear and Nonlinear Optical Properties of All-*cis* and All-*trans* Poly(*p*-phenylene vinylene) ……192

5.1. Author Contribution Statement 192
5.2. Abstract 193
5.3. Introduction 194
5.4. Experimental Section 198
5.4.1. Synthesis of Monomers and Polymers 198
5.4.2. Entangled Two-Photon Absorption 198
5.5. Results and Discussion 199
5.5.1. Design and synthesis of PPVs for this study 199
5.5.2. Steady-state absorption and emission: 201
5.5.3. Classical two-photon absorption 203
5.5.4. Time-resolved fluorescence up-conversion 206
5.5.5. Femtosecond Transient Absorption 208
5.5.6. Entangled-two photon absorption. 212
5.6. Conclusion 216

Chapter Six*:* Enhancing Reverse Intersystem Crossing Through Higher-Lying Triplet States in Engineered Indacenodithieno[3,2-b]thiophene (IDTT)-Based Molecular Systems…….. …..265

6.1. Author Contribution Statement 265
6.2. Abstract 266
6.2.3. Introduction 267
6.4. Methods and Materials 270
6.4.1. Absorption and Emission 270
6.4.2. Fluorescence Quantum Yield 270
6.4.3. Classical Two Photon Absorption 270
6.4.4. Entangled Two Photon Absorption 271
6.4.5. Nanosecond Transient Absorption Spectroscopy 272
6.4.6. Femtosecond Transient Absorption Spectroscopy 273
6.4.7. TD-DFT Calculations 274

6.5. Result 274
6.5.1. Synthesis 274
6.5.2. Absorption and Emission 275
6.5.3. Electronic Structure Calculations 277
6.5.4. Two-Photon Absorption 278
6.5.5. Entangled Two-Photon Absorption Spectroscopy 281
6.5.6. Femtosecond transient absorption spectroscopy 283
6.5.7. Nanosecond transient absorption spectroscopy 284
6.6. Discussion 287
6.7. Conclusion 298
Chapter Seven: Photocatalytic Alkene Hydrofunctionalization Utilizing Acridine-Lewis Acid Complexes 326
7.1. Author Contribution Statement 326
7.2. Abstract 327
7.3. Introduction 327
7.4. Results and Discussion 329
7.5. Conclusion 344
Chapter Eight: Summary of the Dissertation and Possible Future Direction 351
8.1. Summary of the Dissertation 351
8.2. Future Direction 355

List of Figures

Figure 1.1: Fundamental processes driven by light-matter interaction……....1

Figure 1.2: Processes in Organic Semiconductor Materials……3

Figure 1.3: Structure of molecules utilized in PM6:Y6-based ternary OSCs…….6

Figure 1.4: Diagram for Singlet Exciton Fission (SEF) process for accessing quintet states……13

Figure 1.5: Schematic diagram of OFET……16

Figure 1.6: Generation of optical emission from organic material……22

Figure 1.7: Processes in TADF molecules (a) Photoluminescence (b) Electroluminescence…....24

Figure 1.8: Examples of D-A TADF-type explored molecules……..25

Figure 1.9: Molecular design of MR-TADF……...27

Figure 1.10: Classical two photon absorption process……31

Figure 1.11: Entangled two photon absorption process…….37

Figure 1.12: Generation of entangled photons via SPDC……..38

Figure 1.13: Mechanism of photo redox catalyst……43

Figure 1.14: Acridine-based photocatalyst for reductive dehalogenation……..45

Figure 2.1: Schematic diagram of UV-Vis Spectrometer……75

Figure 2.2: Fundamental Processes Involved in Fluorescence (Emission)……75

Figure 2.3: Horiba Scientific_PTI Quantamaster Series……77

Figure 2.4: TPEF experimental set-up……80

Figure 2.5: Schematic Diagram of the ETPA set-up……83

Figure 2.6: Pump-probe spectroscopy process……...85

Figure 2.7: Signals obtained in the TA……88

Figure 2.8: Diagram of the ns-TA instrumentation…….90

Figure 2.9: Schematic diagram of the fs-TA setup…….92

Figure 2.10: Schematic diagram of the TCSPC set-up……..94

Figure 2.11: Schematic diagram for the TCSPS instrument…….95

Figure 2.12: Schematic diagram of the NSOM instrumentation……..101

Figure 3.1: Structures of the series of BTp oligomers…….109

Figure 3.2: (A) Normalized steady state absorption spectra in chloroform. Excitation wavelength was 400 nm in all cases (B) Normalized steady state emission spectra in chloroform. Excitation wavelength was at their absorption maxima: 310 nm, 340 nm, 353……114

Figure 3.3: Molecular orbital of the BTp 5, BTp 7, BTp 9 and BTp 11……..117

Figure 3.4: (A) Two photon fluorescence of the BTps oligomers (B) Classical Two-Photon Absorption of the BTp ladder oligomers. All measurements were done in chloroform……118

Figure 3.5: (A) Comparison of the TPA cross-section of the BTp with their conjugation length (B) Plot of the ratio of δ to the number of π-electrons (δ/Ne); and the oscillator strength against the number of conjugated electrons……119

Figure 3.6: Rate of the Entangled Two-Photon absorption versus the input photon flux. Chloroform was used as solvent…….....122

Figure 3.7: Time resolved measurement of the emission lifetime of the BTp oligomers in chloroform……125

Figure 3.8: ns-TA spectra of the BTp: (a) BTp 5, (b) BTp 7, (c) BTp 9, (d) BTp 11 in chloroform

.....126

Figure 3.9: Kinetic spectra of the BTp: (a) BTp 5, (b) BTp 7, (c) BTp 9, (d) BTp 11 in chloroform……129

Figure S3.1: Schematic diagram of the nanosecond transient absorption setup ……149
Figure S3.2: Kinetic of the ground state bleaching……..154
Figure S3.3: Kinetic of the ESA 1…….. 151
Figure S3.4: Kinetic of the purged ESA 2……...152
Figure S3.5: Molecular orbital of BTp 5…….153

Figure S3.6: Molecular orbital of BTp 7…….153

Figure S3.7: Molecular orbital of BTp 9…….154

Figure S3.8: Molecular orbital of BTp 11……154

Figure 4.1. The structures of the tetracene, TIPS-tetracene and TCHS-tetracene…….....165

Figure 4.2. (A) Absorption and (B) steady-state emission spectra of tetracene, TIPS-tetracene and TCHS-tetracene……170
Figure 4.3. Molecular orbitals of the tetracene, TIPS-tetracene and TCHS-tetracene……..172

Figure 4.4 (A) Two-photon intensity dependence spectra; and (B) Two-photon excited fluorescence spectra for tetracene, TIPS-tetracene, and TCHS-tetracene……173
Figure 4.5. Rate of the ETPA absorption of the tetracene, TIPS-tetracene and TCHS-tetracene……...175
Figure 4.6. (A) NSOM images of tetracene obtained from the two-photon Fluorescence profile on a 500 × 500 nm area and (C) NSOM images of TIPS-tetracene obtained from the two-photon Fluorescence profile on a 500 × 500 nm area. (B) Corresponding AFM profile of the tetracene.
and (D) Corresponding AFM profile of the TIPS-tetracene……176
Figure 4.7. NSOM Images of TCHS-tetracene obtained from the two-photon NSOM, (A) Fluorescence profile on a 500 × 500 nm area, (B) Corresponding AFM profile on the same area……...177

Figure 4.8. (A) NSOM photoluminescence modulation as a function of the interpulse delay for autocorrelation function (blue curve), inset represents the photoluminescence oscillation for TCHS-tetracene in the range of (166 – 180) fs. (B) Normalized photoluminescence modulation amplitude of the Tetracene (green star), TIPS-tetracene (purple triangle), and TCHS-tetracene (red spheres) as a function of the interpulse delay time. Dashed lines indicate the best fitting result to the single decay exponential function. Grey squares (blue dotted line) show the autocorrelation function. (C) Normalized photoluminescence modulation amplitude of the TCHS-tetracene, (D) Photoluminescence oscillations for TCHS-tetracene……..179

Figure 5.1. Schematic energy diagram of a two-photon absorption process happens from ground state (GS) through virtual state (VS) to two-photon excited state (ES). The olefin geometry of all-trans PPV and all-cis PPV investigated here is also shown…….197

Figure 5.2. Synthesis of diblock copolymers containing either an all-*cis* or an all-*trans* PPV segment: Sequential stereoretentive ROMP of monomers 1 and 2 using catalyst Ru-St delivered poly-*cis*-1-*b*-*cis*-2. Subsequent PPV-selective photoisomerization afforded poly-*cis*-1-*b*-*trans*-2……201

Figure 5.3. Normalized steady state absorption (C = 25.0 and 12.5 μg/mL, respectively) and emission (C = 4.2 and 1.6 ng/mL, respectively) spectra of poly-*cis*-1-*b*-*cis*-2 and poly-*cis*-1-*b*-*trans*-2 in chloroform. Excitations for poly-*cis*-1-*b*-*cis*-2 and poly-*cis*-1-*b*-*trans*-2 were 389 and 442 nm, respectively……202

Figure 5.4. (A) Excitation power dependent classical TPA fluorescence (at 520 nm) and (B) two-photon excited fluorescence spectra of the investigated compounds. The excitation wavelength was 800 nm. ……205

Figure 5.5. Fluorescence decay traces of poly-*cis*-1-*b*-*cis*-2 and poly-*cis*-1-*b*-*trans*-2 at the emissive wavelength of 517 nm after excitation at 400 nm. Inset are the emissive decay traces in 10 ps time window……207

Figure 5.6. Femtosecond transient absorption spectra (*fs*TAS) for poly-*cis*-1-*b*-*cis*-2 (A) and poly-*cis*-1-*b*-*trans*-2 (B) corroborated with steady state absorption and emission spectra. Lower panel shows time traces of poly-*cis*-1-*b*-*cis*-2 and poly-*cis*-1-*b*-*trans*-2 in 1.6 ns and 20 ps (inset) time windows. The excitation wavelength for both compounds was 400 nm. ……..209

Figure 5.7. Entangled two-photon absorption as a function of input (i.e., excitation power) for poly-*cis*-**1**-*b*-*cis*-**2** and poly-*cis*-**1**-*b*-*trans*-**2** in chloroform solution……215

Figure 5.8. Frontier molecular HOMO−1 through LUMO+1 orbitals of *trans*- (left panel) and *cis*-PPV (right panel) calculated at the CAM-B3LYP-D3/6-311+G(d,p)-SMD($CHCl_3$) level of theory……...216

Figure S5.1. ^{1}H NMR (400 MHz, $CDCl_3$) spectrum of poly-*cis*-1-*b*-*cis*-2…….236

Figure S5.2. ^{13}C NMR (125 MHz, $CDCl_3$) spectrum of poly-*cis*-1-*b*-*cis*-2……236

Figure S5.3: ^{1}H NMR (400 MHz, $CDCl_3$) spectrum of poly-*cis*-1-*b*-*trans*-2…….237

Figure S5.4: ^{13}C NMR (125 MHz, $CDCl_3$) Spectrum of poly-*cis*-1-*b*-*trans*-2……238

Figure S5.5. Size exclusion chromatography trace of poly-*cis*-1-*b*-*cis*-2……239

Figure S5.6. Integrated emission intensity vs. absorbance for poly-*cis*-1-*b*-*cis*-2 and Coumarin 153 standard……240

Figure S5.7. Integrated emission intensity vs. absorbance for poly-*cis*-1-*b*-*trans*-2 and Fluorescein standard……241

Figure S5.8. Femtosecond transient absorption spectra for poly-*cis*-1-*b*-*cis*-2 and poly-*cis*-1-*b*-*trans*-2 (B) at different delay time in chloroform……241

Figure S5.9. Boltzmann weighted UV-Vis spectra of (a) *trans*- and (b) *cis*-PPV calculated at the CAM-B3LYP/6-311+G(d,p) level of theory in chloroform (SMD)……249

Figure S5.10. Boltzmann weighted UV-Vis spectra of (a) *trans*- and (b) *cis*-PPVcalculated at the B3LYP/6-311+G(d,p) level of theory inchloroform (SMD)……250

Figure S5.11. Boltzmann weighted UV-Vis spectra of (a) *trans*- and (b) *cis*-PPV calculated at the M06-2X/6-311+G(d,p) level of theory in chloroform (SMD)…….250

Figure S5.12. Single point calculations for the HOMO and HOMO-1 orbitals for the *trans*- (left panel) and *cis*-PPV (right panel) calculated at the CAM-B3LYP-D3/6-311G(d,p)-SMD($CHCl_3$) level of theory……..252

Figure S5.13. Single point calculations for the HOMO and HOMO-1 orbitals for the *trans*-PPV fragments calculated at the CAM-B3LYP-D3/6-311G(d,p)-SMD($CHCl_3$) level of theory …..254

Figure S5.14. Single point calculations for the HOMO and HOMO-1 orbitals for the *cis*-PPV fragments calculated at the CAM-B3LYP-D3/6-311G(d,p)-SMD ($CHCl_3$) level of theory….255

Figure S5.15. Comparison of the HOMO and HOMO-1 orbitals for the *trans/cis*-PPV fragments calculated at the CAM-B3LYP-D3/6-311G(d,p)-SMD ($CHCl_3$) level of theory…….256

Figure 6.1 (A) Absorption spectra of M1, D1 and T1 (B) Emission spectra of M1, D1 and T1 in chloroform……276

Figure 6.2: Molecular orbital of the M1, D1 and T1…….278

Figure 6.3: Plot of the classical 800 nm excitation TPA of M1, D1 and T1……278

Figure 6.4. Plot of the classical 880 nm excitation TPA of M1, and 1040 nm excitation TPA of D1 and T1……..280

Figure 6.5: ETPA rate of M1, D1 and T1 in chloroform…….282

Figure 6.6. fsTA spectra at different time delays for (a) monomer and (b) trimer. The excitation wavelength was set to 400 nm. The absorption spectra are shown in black solid lines. Decay-associated spectra, DAS, and their corresponding time constants, τ for (c) monomer and (d) trimer…….. 283

Figure 6.7: Nanosecond transient absorption spectra of M1, D1 and T1 in chloroform……..285

Figure 6.8: Transient absorption decay kinetic of the chromophores in chloroform: M1 probed at 600 nm (a) unpurged, (d) purged; D1 probed at 670 nm (b) unpurged (e) purged ; and T1 probed at 680 nm (c) unpurged and (f) purged……286

Figure 6.9. Excited-to-excited state transition matrices of Monomer Dimer and Trimer for the first 6 excited states. Each element in the matrix corresponds to the oscillator strength of the electronic transition……..288

Figure 6.10: NTO for the triplet excited state of T1……291

Figure 6.11: Excited state energies as obtained from the TD-DFT calculations of M1, D1 and T1…….294

Figure S6.1: NMR spectrum of M1-Br in CD_2Cl_2 ……..319

Figure S6.2: NMR spectrum of D1 in $CDCl_3$ …….320

Figure S6.3: NMR spectrum of T1 in $CDCl_3$ ……320

Figure S6.4: Kinetic of the GSB for the M1, D1 and T1 ……321

Figure S6.5: NTO of the excited state of the M1 ……..322

Figure S6.6: NTO of the excited state of the D1 ……322

Figure S6.7: NTO of the excited state of the T1 …….323

Figure 7.1. (A) General, photocatalytic *anti*-Markovnikov alkene hydrofunctionalization with mechanism (B) Proposed transformations using in situ LA-Acr PC……329

Figure 7.2. Hydroamination Scope of Styrenyl Alkenes……..334

Figure7.3. Hydrofunctionalization of alkenes with varied nucleophiles…….336

Figure 7.4. Lewis acid modularity screens for representative alkenes…….339

Figure 7.5. (a) Kinetic of the ESA growth time of the (i) Sc PC with anethole (ii) Al PC with anethole and (iii) Fukuzumi PC with anethole……343

List of Tables

Table 3.1: Steady state absorption and emission of the BTP oligomers in chloroform……116

Table 3.2: TPA and ETPA cross-section of the BTp oligomer…….120

Table 3.3: Table Showing the Emission Lifetime of the BTP Oligomers in chloroform. The excitation wavelength for all samples was 400 nm……..125

Table 3.4: Excited state lifetime of the BTp oligomers……133

Table S3.1: Electronic calculation of the BTp 5……..155

Table S3.2: Electronic calculation of the BTp 7…….156

Table S3.3: Electronic calculation of the BTp 9……..158

Table S3.4: Electronic calculation of the BTp 11……159

Table 4.1. Table showing the TPA cross-section of the tetracene, TIPS-tetracene and TCHS-tetracene……...173

Table 4.2: Table showing the ETPA cross-section of the tetracene, TIPS-tetracene and TCHS-tetracene……...174

Table 5.1. Steady-state Absorption and Emission Properties of poly-*cis*-1-*b*-*cis*-2 and poly-*cis*-1-*b*-*trans*-2 in chloroform……...203

Table 4.2. Summary of Classical TPA Cross-sections of the Copolymers in Chloroform……..205

Table 5.3. Summary of the Fluorescence Up-conversion with both Copolymers……..207

Table 5.4. Transient Absorption Data for poly-*cis*-1-*b*-*cis*-2 and poly-*cis*-1-*b*-*trans*-2……..210

Table 5.5. ETPA Cross-sections for poly-*cis*-1-*b*-*cis*-2 and poly-*cis*-1-*b*-*trans*-2 in chloroform……...215

Table S5.1. Molecular weight and dispersity values for poly-*cis*-**1**-*b*-*cis*-2……238

Table S5.2. Energetic data for the top 20 conformations of *trans*-PPV calculated at the CAM-B3LYP-D3/6-311+G(d,p) level of theory in chloroform (SMD)…….243

Table S5.3. Energetic data for the top 20 conformations of *trans*-PPV calculated at the B3LYP-D3/6-311+G(d,p) level of theory in chloroform (SMD)……..244

Table S5.4. Energetic data for the top 20 conformations of *trans*-PPV calculated at the M06-2X-D3/6-311+G(d,p) level of theory in chloroform (SMD)……245

Table S5.5. Energetic data for the top 20 conformations of *cis*-PPV calculated at the CAM-B3LYP-D3/6-311+G(d,p) level of theory in chloroform (SMD) ……246

Table S5.6. Energetic data for the top 20 conformations of *cis*-PPV calculated at the B3LYP-D3/6-311+G(d,p) level of theory in chloroform (SMD)……..247

Table S5.7. Energetic data for the top 20 conformations of *cis*-PPV calculated at the M06-2X-D3/6-311+G(d,p) level of theory in chloroform (SMD) ……248

Table S5.8. Fragment orbital composition analysis for the HOMO/HOMO-1 orbitals for the *trans*-PPV(1), *trans*-PPV(2), *trans*-PPV(3), and *trans*-PPV(4) fragments indicated in Figure S12 calculated at the CAM-B3LYP-D3/6-311G(d,p)-SMD($CHCl_3$) level of theory……252

Table S5.9. Fragment orbital composition analysis for the HOMO/HOMO-1 orbitals for the *cis*-PPV(1), *cis*-PPV(2), *cis*-PPV(3), and *cis*-PPV(4) fragments indicated in Figure S12 calculated at the CAM-B3LYP-D3/6-311G(d,p)-SMD($CHCl_3$) level of theory……..253

Table S5.10. Change in energy for the HOMO/HOMO-1 orbitals from the *trans*- to *cis*-PPV fragments calculated at the CAM-B3LYP-D3/6-311G(d,p)-SMD($CHCl_3$) level of theory…….257

Table 6.1: Steady state properties of the M1, D1 and T1…….277

Table 6.2. Classical TPA cross-sections at 800 nm excitation and at resonance (maxima one photon absorption spectra) for M1, D1, T1……..281

Table 6.3: Entangled TPA cross-section for the investigated compounds in chloroform……....282

Table 6.4: Decay lifetimes and K_{rISC} of the chromophores ……..287

Table 6.5: Spin orbit coupling and transition states involved for M1, DI and T1……293

Table S6.1: Electronic calculation of the coupling between the singlet and triplet states……...324

Table S6.2: Electronic calculation of the energy of the singlet and triplet states ……...325

Table 7.1. Photocatalytic Alkene Hydroamination Catalyst Optimization……..332

Table 7.2. Summary of photophysical data comparing catalysts……..341

Table 7.3: Kinetic of the PC's with anethole, where τ_{Growth} = growth time at 600 nm, K_{growth} = rate of growth, τ_{ESA} = ESA lifetime at 600 nm and K_{ESA} = rate of decay of the ESA……343

ABSTRACT

The rapid advancement of optoelectronic and quantum technologies has created a critical need for molecular systems that can precisely control electronic, optical, and spin-dependent processes. Organic molecules are particularly well suited to meet this challenge because their structure can be chemically tuned, synthesized with high flexibility, and produced at low cost. Their molecular architecture can be deliberately designed to influence key photophysical processes including charge transfer, exciton formation, excited-state relaxation, and spin coherence directly at the molecular level. These processes govern the performance of organic light-emitting diodes (OLEDs) and organic field-effect transistors (OFETs), and are also central to emerging quantum technologies such as quantum computing and quantum sensing.

Despite extensive research, detailed molecular-level understanding of how molecular structure influences fundamental processes that dictate device efficiency remain incomplete. Many organic materials exhibit complex and competing relaxation channels, including ultrafast charge transfer, intersystem crossing, and nonradiative decay, which governs device efficiency. In the emerging field of quantum information science, organic molecules are increasingly explored as candidates for molecular qubits and quantum transducers, where the preservation and control of electronic coherence and spin states are essential.

A central challenge lies in understanding how molecular structure governs coherence lifetimes, spin mixing, and the generation of quantum correlations through light-matter

interactions. Overcoming these challenges requires the development of new molecular systems with well-defined electronic and spin properties, as well as experimental techniques capable of directly resolving ultrafast dynamics and nonclassical photonic interactions at the molecular scale. This thesis addresses these gaps through the design and investigation of emerging conjugated and fused-ring organic molecules including ladder-type oligomers, and molecular systems engineered to access long-lived excited and spin states. These materials are designed to provide precise control over electronic coupling, charge-transfer character, and triplet-state, enabling direct investigation of the mechanisms that govern exciton dynamics, spin-dependent relaxation, and electronic coherence.

A central component of this research is the combined use of advanced spectroscopic techniques and electronic structure calculations to probe molecular processes. Transient absorption and fluorescence lifetime spectroscopy are used to resolve charge separation, energy transfer, and excited-state relaxation dynamics. Entangled two-photon spectroscopy is employed to investigate non-classical light-matter interactions and quantum correlations in molecular systems. These measurements are complemented by electronic structure calculations that provide insight into excited-state character, electronic coupling, and spin-vibronic interactions, enabling a consistent interpretation of experimental observations. The results of this thesis provide new insight into how molecular design governs charge, exciton, and spin dynamics in organic materials, with direct implications for both optoelectronic devices and quantum technologies. The findings identify molecular design strategies for improving OLED and OFET performance while simultaneously enabling long-lived excited and spin states relevant to molecular qubits, quantum sensing, photonic quantum transduction and quantum computing.

Finally, this thesis explores modular organic photocatalysts, demonstrating that coordination with metal centers can tune excited-state redox potentials and control the formation of reactive intermediates, enhancing catalyst efficiency across a range of chemical transformations. These studies, combined with the investigation of optoelectronic and quantum-functional molecules, establish general principles for the rational design of multifunctional organic materials capable of advancing organic electronics, quantum photonic devices, and photoredox catalysis.

Chapter One

Introduction to Organic Optoelectronic and Functional Materials

1.1 Background

Light-matter interactions plays a fundamental role in nearly every modern technological advancement in energy harvesting, optical communication, sensing, and catalysis.[1–4] The ability to tailor how a material absorbs, emits, or transforms light determines its suitability for technologies ranging from organic light-emitting diodes (OLEDs) and solar cells to single-photon quantum sensors and photocatalytic systems for activating reaction processes (**Figure 1.1**). In each of these cases, the molecular structure and electronic properties of materials dictate the flow of charge following photoexcitation, linking photophysics directly to functionality.[5,6] Thus, the fundamental study of light-matter interactions extends beyond physics or chemistry, it is a central question of materials science, where understanding how structure controls excited-state processes enabling the rational design of next-generation functional materials.

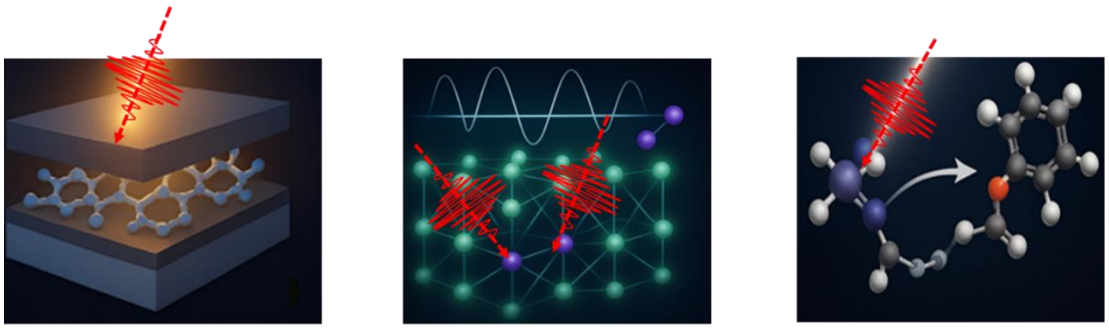


Figure 1.1: Fundamental processes driven by light-matter interaction

1.1.1 Mechanisms and Fundamental Processes of Organic Solar Cell

Organic solar cells (OSCs) are a class of photovoltaic devices that utilize organic semiconductors as light-absorbing and charge-transporting materials. The growing interest in OSCs arises from their tunable optoelectronic properties, solution processability, mechanical flexibility, and potential for low-cost, large-area fabrication.[7–9] Unlike conventional inorganic solar cells materials which directly generate free electrons and holes upon photon absorption, organic semiconductors exhibit strongly bound excitons due to their low dielectric constants. The bounded nature of these excitons necessitates pathways for exciton migration, dissociation, and charge transport to achieve efficient photovoltaic conversion.[9,10] Understanding these mechanisms is critical for the rational design of materials and device architectures that maximize power conversion efficiency (PCE).

Upon illumination, photons with energy equal to or greater than the band gap of the material are absorbed, promoting electrons from the highest occupied molecular orbital (HOMO) to the lowest unoccupied molecular orbital (LUMO). This process creates a singlet exciton, a bound electron-hole pair held together by Coulombic attraction. The binding energy of such excitons in organic materials typically ranges from 0.3 to 1 eV, substantially higher than in inorganic semiconductors. Consequently, excitons cannot spontaneously separate into free carriers and must reach a donor-acceptor interface to undergo dissociation.

The donor-acceptor interface is the critical site where exciton dissociation occurs. The donor, typically a p-type organic semiconductor, and the acceptor, typically an n-type material are chosen such that their energy levels are offset in a manner that facilitates electron transfer from the donor to the acceptor while retaining the hole in the donor. Specifically, the LUMO of the acceptor must be lower in energy than the LUMO of the donor to provide the driving force for electron

transfer, while the HOMO of the donor remains higher than that of the acceptor to stabilize the hole (**Figure 1.2**). The exciton reaches this interface via diffusion, which is limited by the exciton diffusion length, usually between 10 and 20 nanometers. If the exciton fails to reach the interface within its lifetime, it recombines either radiatively or non-radiatively, leading to energy loss.

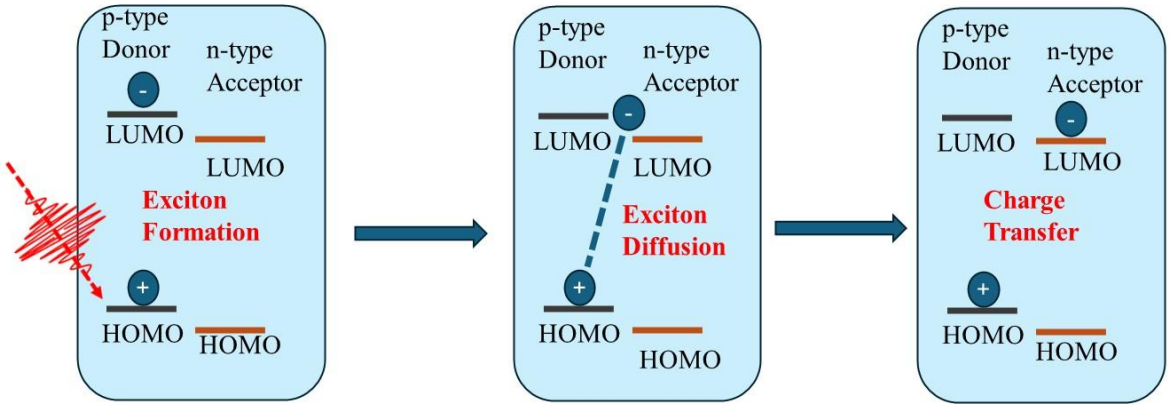


Figure 1.2: Processes in Organic Semiconductor Materials

At the interface, the electron is transferred to the acceptor LUMO, while the hole remains on the donor HOMO, creating a charge-transfer (CT) state. The CT state represents an intermediate between the exciton and fully separated charges. The separation efficiency of this CT state is determined by multiple factors: the energetic offset between donor and acceptor orbitals, the electronic coupling at the interface, and the local morphology, which affects the probability of excitons reaching the interface. This coupling depends on the molecular orientation, π-π stacking, and orbital overlap at the interface. Stronger coupling facilitates rapid electron transfer and minimizes the likelihood of exciton recombination before dissociation[11,12]. Conversely, weak coupling or disordered interfaces can trap excitons or slow their separation, reducing overall CT efficiency.

Once the charges are separated, they must migrate through the respective donor and acceptor domains toward the electrodes. The mobility of electrons and holes is a critical parameter at this stage, as it influences how effectively charges can be collected before recombination occurs. Electron and hole mobilities in organic semiconductors are typically lower than in crystalline inorganic materials, often ranging from 10^{-4} to 1 $cm^2/V \cdot s$. Therefore, the molecular ordering, and crystallinity, are crucial in facilitating continuous pathways for charge transport. Trap states can act as recombination centers, reducing the overall current generated by the device. The morphology of the active layer plays a central role in balancing exciton dissociation and charge transport. Bulk heterojunction architectures, where donor and acceptor materials form nanoscale interpenetrating networks, are widely employed to maximize the interfacial area for exciton dissociation while maintaining continuous pathways for carrier transport.[13] The domain size within the blend is typically optimized to match the exciton diffusion length, ensuring that most excitons can reach an interface before recombining.[14,15] Simultaneously, domain purity and continuity are critical for efficient charge collection, as electrons and holes must travel long enough distances to reach their respective electrodes.

From an energetic perspective, each material possesses valence and conduction bands corresponding to HOMO and LUMO levels. The energy level between the donor and acceptor defines both the driving force for exciton dissociation and the open-circuit voltage (V_{OC}) of the device. The CT state energy at the interface establishes the upper limit of the V_{OC}, whereas the short-circuit current density (J_{SC}) depends on the absorption properties of the active materials, the efficiency of exciton dissociation, and the transport and collection of free carriers.[11,16,17] Together with the fill factor (FF), which reflects resistive losses and recombination within the device, these parameters determine the PCE, expressed as:

$$\text{PCE} = \frac{J_{SC} \times V_{OC} \times FF}{P_{in}} \qquad \text{(Equation 1.1)}$$

where P_{in} is the incident light power. High PCE requires optimal performance at each stage of the photophysical and electronic processes, from photon absorption to charge extraction. Experimental characterization of OSCs relies heavily on current-voltage (J-V) measurements, typically performed under simulated solar illumination using the AM1.5G spectrum. These measurements provide quantitative insight into J_{SC}, V_{OC}, and FF, enabling the assessment of device efficiency. By comparing these parameters across devices with different materials or morphologies, one can infer the effectiveness of exciton diffusion, charge separation, and carrier transport, thereby guiding material design and device engineering.

1.1.2. Molecular Design and Evolution of OSC Materials

Early OSC architectures were dominated by polymer-fullerene bulk heterojunctions (BHJs), where conjugated polymers served as electron donors and fullerene derivatives such as [6,6]-phenyl-C_{61}-butyric acid methyl ester (PCBM) acted as electron acceptors.[13] The P3HT:PCBM blend was a broadly explored system, offering a robust and reproducible platform for studying charge separation and transport in organic semiconductors. Despite its simplicity, the P3HT:PCBM system exhibited inherent limitations, including narrow optical absorption, poor energy-level tunability, and restricted morphological control, resulting in modest power conversion efficiencies (PCEs) of approximately 4%. These limitations highlighted the need for a deeper molecular understanding and a more diversified chemical design space to unlock the full potential of organic photovoltaics.[18,19]

An equally significant trend is the movement toward small-molecule donors and polymerized small molecules, which combine the well-defined electronic structure of molecular semiconductors with the film-forming and morphological control of polymers (**Figure 1.3**). Small molecules allow precise molecular weight and purity control, yielding reproducible device performance. At the same time, introducing minimal polymerization or non-covalent supramolecular interactions can help overcome the brittleness and crystallization tendencies of purely molecular systems, providing a tunable route to achieve both processability and performance.

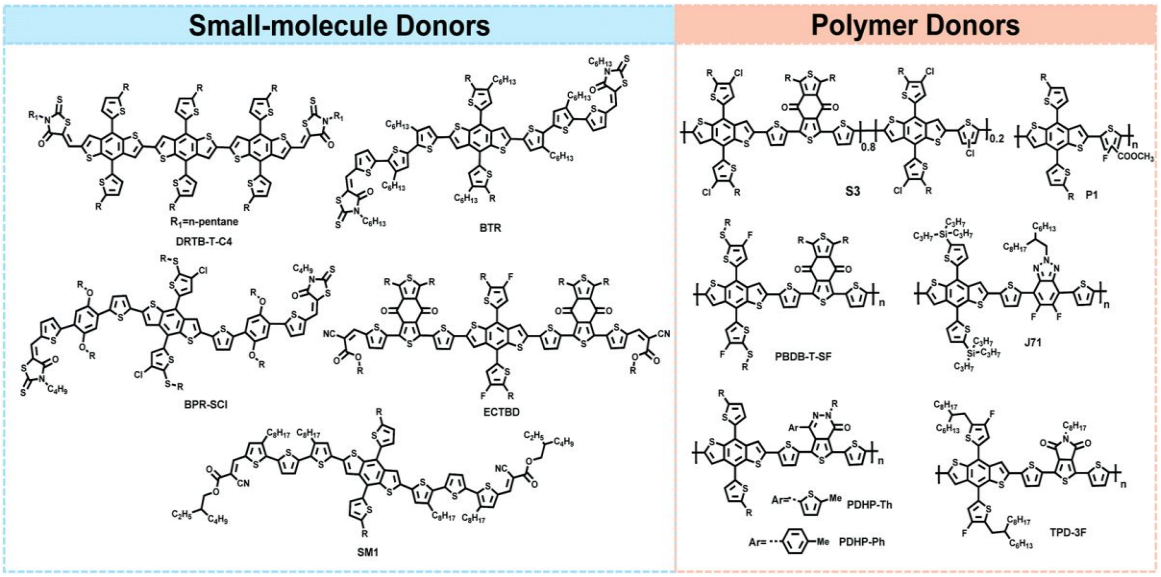


Figure 1.3: Structure of molecules utilized in PM6:Y6-based ternary OSCs.[20]

The design strategies for high-efficiency OSCs also increasingly consider energy-loss minimization; a critical factor for improving Voc and overall PCE. Non-radiative voltage losses arise primarily from energetic disorder and charge recombination via low-lying CT states. Materials that exhibit narrow energetic distributions and shallow energetic traps can mitigate these losses. By enhancing molecular rigidity, suppressing vibronic coupling, and achieving better dielectric screening, researchers have achieved record-low energy losses (as low as 0.5 eV) in

state-of-the-art systems such as PM6:Y6.[20] These advances have been guided by both empirical and theoretical insights, demonstrating how photophysical coherence and molecular order are intimately linked to macroscopic device performance.

Another frontier in molecular design involves the control of exciton dynamics and electronic delocalization through molecular packing and aggregation. Recent studies suggest that delocalized interfacial CT states spanning several donor and acceptor units can reduce Coulombic binding and enhance charge separation efficiency.[21,22] This concept resonates with the broader idea of coherence-assisted charge separation, where vibrational and electronic coherence sustain the correlated motion of electron and hole across the interface before decoherence sets in. Such mechanisms mirror those proposed for photosynthetic complexes and quantum-coherent systems, revealing a deep conceptual bridge between molecular photophysics and natural light-harvesting processes. The progress in OSC materials is thus a direct consequence of synthetic innovation guided by photophysical understanding. From fullerene-based blends to designer non-fullerene architectures, each generation of materials has expanded the boundaries of what is possible through molecular control. The contemporary research scope emphasizes not only energy-level engineering and morphology but also quantum-level design, where the interplay of coherence, delocalization, and non-adiabatic coupling becomes a tunable design variable. This convergence of synthetic chemistry, quantum dynamics, and materials engineering defines the next phase of OSC research, where understanding and manipulating excited-state processes at the molecular level are central to achieving higher efficiency, stability, and scalability.

1.1.3. Organic Materials for Quantum Information Science

Quantum information science (QIS) relies fundamentally on the ability to create, manipulate, and preserve quantum states. The realization of practical quantum technologies

ranging from quantum computing to secure quantum communication requires qubits with long coherence times, high fidelity, and scalability. Traditionally, solid-state inorganic systems have dominated the field such as nitrogen-vacancy (NV) centers in diamond, silicon carbide defects, and quantum dots. These inorganic platforms offer several advantages: NV centers, for instance, exhibit room-temperature operation, long spin coherence times, and well-understood optical transitions that allow for high-fidelity initialization and readout of quantum states. Similarly, semiconductor quantum dots provide tunable energy levels and integration potential with existing photonic technologies.

Despite their remarkable properties, inorganic materials face several intrinsic limitations. The fabrication of high-purity, defect-free crystals can be technically demanding and expensive, limiting scalability. Moreover, precise control over individual defect centers or quantum dots requires sophisticated lithography or implantation techniques, which can introduce additional defects or strain. In some systems, achieving uniformity across multiple qubits remains a persistent challenge, complicating the implementation of large-scale quantum architectures. These constraints motivate the exploration of alternative qubit platforms that can combine quantum functionality with molecular tunability and chemical versatility.

Organic materials offer an intriguing complementary approach. Molecular qubits, individual molecules designed to exhibit specific spin or optical properties present opportunities for bottom-up design, chemical modification, and solution-based processing. Organic systems can be synthesized with precise control over their chemical structure, enabling systematic tuning of electronic properties, spin interactions. For example, conjugated organic radicals, organic triplet excitons, and optically active chromophores have all emerged as candidates for molecular

qubits.[23,24] Such systems promise modularity, potential for integration into hybrid devices, and scalability via self-assembly or thin-film fabrication techniques.

Nevertheless, several challenges remain for organic qubits. In general, organic materials exhibit shorter dephasing times compared to their inorganic counterparts. The coupling of electronic states to molecular vibrations and environmental phonons accelerates decoherence, limiting the timescales over which quantum information can be reliably stored or manipulated. Additionally, achieving high purity and chemical stability is critical; even trace impurities or photoinduced degradation can drastically reduce coherence times.

The emerging field of organic quantum materials thus occupies a promising niche. While currently limited in terms of coherence time relative to well-established inorganic qubits, organic systems offer unmatched tunability, modularity, and integration potential. Continued advances in synthetic chemistry, materials processing, and coherent spectroscopic techniques are rapidly expanding the development of molecular qubits. Exploring organic chromophores, radical-bearing molecules will lead in significant advancement in developing strategies for stabilizing quantum states and extending dephasing times, moving closer to viable, scalable organic quantum devices.

1.1.4. Organic Materials for Quantum Sensing Application

Another significant area of quantum information science is quantum sensing, which utilizes quantum correlations and coherence to detect weak signals with sensitivities beyond classical limits. Of particular relevance is the development of quantum sensing strategies for biological and biomedical applications, where measurements must be performed with minimal perturbation to fragile molecular and cellular systems. In this context, recent advances in quantum optics have

opened a new research direction in which nonclassical states of light especially entangled photons are employed as probes of complex molecular environments.

Unlike classical laser illumination, quantum light exhibits strong correlations in time and energy that fundamentally modify light-matter interactions. As a result, the response of molecular materials, particularly organic chromophores and fluorophores to quantum light can differ markedly from their response under classical excitation. Multiple experimental studies have demonstrated that entangled photons can efficiently excite organic fluorophores through entangled two-photon absorption at photon fluxes orders of magnitude lower than those required for classical two-photon processes.[25,26] This behavior has been exploited in quantum-light enhanced imaging of breast cancer cells, where biologically relevant fluorescence contrast was achieved at ultralow excitation powers, significantly reducing photobleaching and phototoxic effects.[25] This has driven increasing interest in understanding and engineering the interaction between organic materials and quantum light, positioning this research area at the intersection of quantum optics, molecular spectroscopy, and biomedical sensing. As a result, quantum-light enabled biosensing using organic materials is emerging as a rapidly advancing and highly impactful direction within quantum information science.

1.1.5. Singlet Exciton Fission

Singlet exciton fission (SEF) is a spin-allowed, multi-exciton generation process in which a high-energy singlet exciton splits into two lower-energy triplet excitons.[27–29] This process effectively increases the number of excitons available for charge generation, presenting a pathway to enhance the photocurrent and overcome the traditional efficiency limits imposed by single-junction organic solar cells. SEF is particularly relevant in organic photovoltaics (OPVs), where thermalization of high-energy excitons leads to energy loss. By converting one singlet exciton into

two triplet excitons, SEF reduces such losses, potentially allowing efficiencies to exceed the Shockley-Queisser limit.[30,31]

Mechanistically, SEF requires precise energetic and structural conditions. The singlet energy must be at least twice that of the triplet energy ($E(S_1) \geq 2\ E(T_1)$) to allow the formation of a correlated triplet pair. Additionally, the spatial arrangement of chromophores must enable efficient electronic coupling between neighboring molecules, facilitating rapid exciton splitting while suppressing competing deactivation pathways. Once formed, the spin-correlated triplet pair can separate into two independent triplet excitons, which diffuse to donor-acceptor interfaces for subsequent charge transfer.[27,32,33]

There are two principal pathways for SEF. In the direct mechanism, the singlet exciton interacts with an adjacent chromophore to generate a correlated double-triplet state. This $^1(T_1T_1)$ state is initially spin-singlet in character and can subsequently undergo spin dephasing to yield two free triplets. In the mediated mechanism, SEF occurs via intermediate states such as higher-lying charge transfer or excimer states, which facilitate coupling between the singlet and double-triplet states. Charge transfer states can accelerate intramolecular singlet fission by providing virtual or real intermediate energy levels that enhance the splitting process, while excimer states may either assist or hinder SEF depending on their relative energies and electronic character. SEF can be intermolecular or intramolecular. Intermolecular SEF occurs between neighboring molecules, making the process highly dependent on molecular packing, π-π stacking, and intermolecular orientation. Achieving reproducible and well-ordered packing is challenging but critical for efficient triplet formation. Intramolecular SEF, on the other hand, takes place within a single molecule that contains multiple coupled chromophoric units.[8,34–36] This approach offers

advantages in solution processability and tunability of both electronic and structural properties, allowing for controlled interfaces and improved process reproducibility.

The efficiency of SEF is influenced not only by molecular design but also by environmental and material factors. Solvent polarity, dielectric constant, and local intermolecular interactions can stabilize or destabilize charge transfer states that mediate singlet fission. For instance, low-dielectric environments can favor SEF by minimizing the stabilization of intermediate CT states, enabling coherent super exchange between the singlet and double-triplet states. Conversely, high-dielectric environments may trap the exciton in a stabilized CT state, reducing SEF efficiency. Additionally, vibrational motions and symmetry-breaking modes can mediate coherent SEF, allowing partial mixing of the singlet and triplet-pair states and facilitating ultrafast fission.[36,37]

Chromophore design plays a pivotal role in SEF. Acene dimers, tetracene derivatives, and perylene diimides have been extensively studied for their tunable packing, triplet energies, and electronic coupling. Structural flexibility, linker position, and conjugation length influence the formation of the correlated triplet pair and the subsequent diffusion of triplets to interfaces. Excimer formation also modulates SEF: low-lying excimer states may act as precursors that facilitate triplet formation or, in some cases, act as traps that inhibit fission, depending on the energetic alignment and coupling with the singlet and triplet states.

1.1.6. Singlet Exciton Fission: A Pathway to Entangled Spin Manifolds for Quantum Information Science Application

Singlet exciton fission (SEF) provides a unique and highly controllable mechanism for generating entangled spin states in purely organic systems, bridging the fields of organic photophysics and quantum information science (QIS).[38,39] In SEF, the absorption of a single photon produces a singlet exciton (S_1), which can subsequently split into a correlated pair of triplet

excitons ($T_1 + T_1$). Critically, the process conserves the total spin angular momentum, producing a spin-correlated $^1(TT)$ state with overall singlet character. The triplet pair may further access higher spin manifolds, including the triplet $^3(TT)$ and quintet $^5(TT)$ states, corresponding to total spin quantum numbers S = 1 and S = 2, respectively. Among these, the quintet state is of particular interest because it embodies a system of four coupled electron spins, coherently entangled and magnetically addressable (**Figure 1.4**).

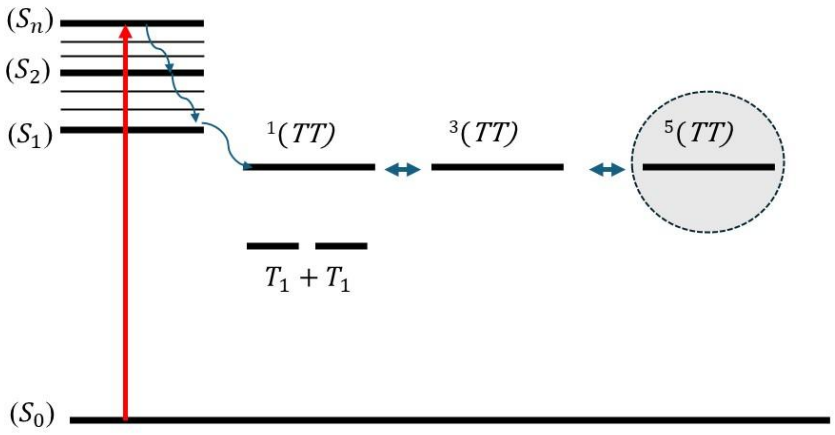


Figure 1.4: Diagram for Singlet Exciton Fission (SEF) process for accessing quintet states

The formation of the quintet $^5(TT)$ state through SEF is a deterministic, photon-driven pathway to entangled spin manifolds. Unlike conventional single-spin systems, SEF produces a multi-spin configuration in which the spins are initialized coherently via the photophysical dynamics of singlet fission.[39,40] The $^5(TT)$ state is optically "dark," meaning it does not undergo strong radiative decay, yet it retains magnetic activity. Its coherent evolution can be probed through time-resolved techniques such as transient absorption spectroscopy, time-resolved electron paramagnetic resonance (EPR), and magnetic field-dependent photoluminescence. Lifetimes for these quintet states can extend from hundreds of nanoseconds to tens of microseconds, providing a temporal window suitable for coherent spin manipulation.

1.1.7. Importance of Electronic Coherence in Accessing Quintet State

The coherence of the S_1 state is central to the physics of singlet fission and, by extension, to the realization of coherently entangled spin states for quantum applications. Its electronic phase memory, defined by the coherence time (T_2), determines whether the fission event proceeds through a coherent superposition or a stochastic population transfer. When the S_1 state maintains phase coherence on a timescale comparable to or longer than the coupling period ($\hbar/J$) between the chromophores, the system can evolve through a coherence in which the singlet and multiexciton wavefunctions remain quantum-mechanically mixed.[41,42]

When coherence in the S_1 state manifold is rapidly lost due to vibronic dephasing, solvent fluctuations, or conformational disorder, this delicate superposition collapses into an incoherent mixture. As a result, the coupling between S_1 and $^1(TT)$ weakens, diminishing the probability of populating the quintet $^5(TT)$ subspace. Conversely, molecular systems that maintain long-lived S_1coherence typically through structural rigidity, delocalized electronic coupling, or suppressed vibrational decoherence facilitate the ballistic transfer of coherence into the triplet-pair manifold. This coherent of the S_1 state forms the basis for generating quantum-entangled triplet pairs with measurable spin correlations and oscillatory magnetic responses. The ability to preserve S_1 coherence directly determines the purity and entanglement of the generated spin state. Consequently, the photophysical control of S_1 dynamics through molecular symmetry, exciton delocalization, and vibrational coherence serves as a molecular lever for defining quantum coherence at the material level.

The research presented in this thesis builds upon this foundation by developing and probing new fused-ring organic materials as chemically tunable molecular platforms for QIS. By utilizing

nonlinear optical and time-resolved spectroscopic probes, including entangled two-photon absorption (ETPA) and Near-Field Scanning Optical Microscope (NSOM), this work explores how structural and electronic modulation influences the formation and coherence of the $^5(TT)$ states. The goal is to elucidate how molecular rigidity, conjugation length, and orbital symmetry determine the rates of singlet fission, triplet-pair coupling, and decoherence. These insights advance a design framework for optically addressable, room-temperature molecular qubits, where photon-driven processes are used to initialize and manipulate spin-entangled manifolds for quantum sensing, communication, and networked information transfer.

1.2. Organic Field-Effect Transistors (OFETs)

Organic field-effect transistors (OFETs) have emerged as a central platform in organic electronics, enabling lightweight, flexible, and low-cost devices with applications in sensing, display backplanes, neuromorphic circuits, and integrated optoelectronic systems.[43] Their operation relies on the ability of π-conjugated molecules to transport charge along ordered domains near an interfacial dielectric, where the device forms a two-dimensional accumulation layer analogous in function, though distinct in mechanism, to conventional inorganic FETs. Unlike traditional semiconductors where charge transport is governed by rigid band structures, organic semiconductors exhibit localized electronic states, strong electron-phonon coupling, and transport pathways that depend sensitively on molecular packing. These fundamental differences give OFETs a set of unique physical principles, which in turn guide their material design, device architecture, and operational behavior.[44–46]

At the core of an OFET is a semiconducting organic layer sandwiched between source, drain, and gate electrodes, separated from the channel region by a dielectric layer. When a voltage

is applied to the gate, an accumulation layer of charge carriers forms at the semiconductor-dielectric interface (**Figure 1.5**). The density, mobility, and spatial coherence of these accumulated carriers determine the transistor's output characteristics.[47,48] Charge is transported primarily through π-π intermolecular overlap, meaning that molecular planarity, crystallinity, and packing motifs directly influence device mobility. The interplay between molecular structure and interfacial energetics therefore defines OFET performance more strongly than in nearly any other class of organic electronic device.

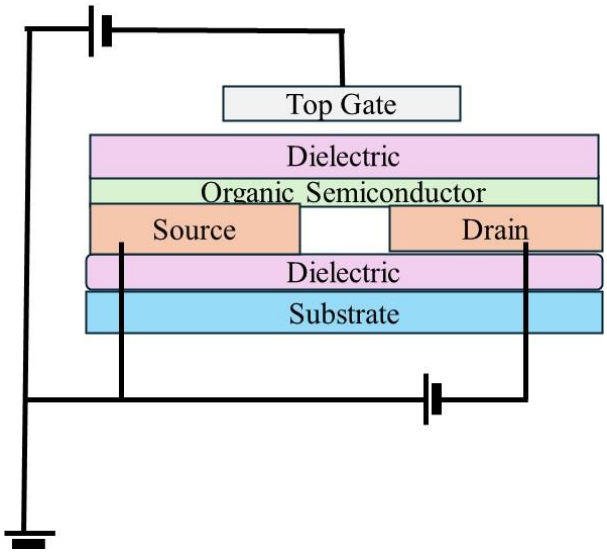


Figure 1.5: Schematic diagram of OFET

1.2.1. Semiconductor-Dielectric Interface for Governing Charge Transport

Unlike bulk transport in inorganic semiconductors, carriers in OFETs traverse a narrow interfacial channel only a few molecular layers thick.[49] This region is highly sensitive to energetic disorder, electrostatic traps, polar surface groups, and lattice fluctuations. Even small variations in molecular orientation or dielectric surface chemistry can alter charge distribution and mobility. For p-type semiconductors such as pentacene, rubrene, diketopyrrolopyrrole (DPP) derivatives, and ladder-type fused aromatics, the gate-induced accumulation of holes occurs when the highest

occupied molecular orbital (HOMO) is sufficiently close to the Fermi level of the electrode. For n-type materials such as perylene diimides (PDIs), naphthalene diimides (NDIs), and fluorinated fused rings, electron accumulation is favored when the lowest unoccupied molecular orbital (LUMO) aligns with the injecting contact.[50–53]

The semiconductor-dielectric interface is therefore a principal determinant of OFET performance. High-κ dielectrics can induce increased charge density but also introduce dipolar disorder and stronger carrier trapping.[54,55] Hydrophobic polymeric dielectrics, such PMMA, suppress trap density by reducing surface hydroxyl groups, thereby improving mobility and threshold voltage stability. Surface treatment strategies including self-assembled monolayers (SAMs), fluorinated interlayers, or dielectric surface passivation can modulate the interfacial dipole and molecular orientation, improving band-edge alignment and enhancing mobility.[56–61]

1.2.2. Charge Transport Mechanisms in OFETs

Charge transport in OFETs occurs through a combination of hopping, transient localization, and band-like mechanisms depending on temperature, packing order, and the intrinsic electronic structure of the organic layer. In amorphous polymers or disordered small molecules, carriers hop between localized sites with thermally activated kinetics. In contrast, highly crystalline organic semiconductors can exhibit “band-like” transport with mobility that increases as temperature decreases due to reduced phonon scattering. Rubrene single-crystal OFETs serve as a canonical example, showing hole mobilities exceeding 20-40 $cm^2/V \cdot s$.[62,63]

The duality of hopping and delocalized transport is a defining feature of OFETs. In many polycrystalline thin films, carriers experience transient localization caused by dynamic molecular motions. Here, the electronic wavefunction is momentarily trapped but can regain coherence when

thermal fluctuations restore π-stacking. This produces a mobility regime that shows weak temperature dependence and is highly sensitive to molecular rigidity. Increasing planarity, extending conjugation, and suppressing torsional degrees of freedom enhance packing stability and reduce dynamic disorder, enabling higher mobility.

Energetic disorder also plays a critical role. Broad distributions of site energies arising from chemical heterogeneity, interfacial traps, or electrostatic dipoles produce potential fluctuations that impede carrier motion. Reducing this disorder through molecular design (e.g., rigid fused backbones, minimal side-chain sterics), purification, and controlled thin-film growth directly enhances field-effect mobility. Key performance metrics for OFETs include field-effect mobility, threshold voltage, on/off current ratio, subthreshold swing, and operational stability. Threshold voltage is influenced by traps at the semiconductor–dielectric interface and by fixed charges in the dielectric layer. Reducing trap densities shifts the threshold voltage toward more ideal values, allowing low-voltage operation. The on/off ratio often exceeding 10^5 in well-designed devices depends on the ability to achieve high accumulation currents in the on-state while suppressing leakage currents in the off-state.[64,65]

Long-term device stability remains one of the primary challenges for OFET technologies. Exposure to moisture and oxygen can introduce trap states, shift threshold voltage, or lead to irreversible degradation of the semiconductor. Encapsulation, hydrophobic dielectrics, and chemically stable π-systems mitigate environmental sensitivity. Additionally, the stability of the accumulated charge layer during continuous bias operation affects device lifetime. Polaron formation, interfacial dipoles, and local heating can induce degradation or morphological rearrangement, especially in polymers with soft backbones. Rigid fused-ring systems typically

offer enhanced stability due to reduced conformational freedom and superior resistance to photooxidation.

1.2.3. Molecular Design Principles for High-Performance OFET Materials

Achieving high charge-carrier mobility in organic field-effect transistors requires a molecular structure that promotes efficient intermolecular charge transport while maintaining the stability and processability needed for device fabrication. Organic semiconductors differ fundamentally from conventional inorganic materials because their charge transport is governed by van der Waals interactions, dynamic disorder, and thermally activated hopping between localized sites. The design of high-mobility organic semiconductors relies on tailoring backbone planarity, intermolecular packing, frontier orbital energies, and overall rigidity. Fused aromatic systems such as pentacene, anthradithiophenes, and fused diketopyrrolopyrroles achieve strong π-π coupling by minimizing torsional disorder.[66–70]

Side-chain substitution provides another method for tuning intermolecular interactions and film morphology. Branched alkyl chains enhance solubility for solution processing but can hinder backbone packing if positioned incorrectly. Linear side chains, in contrast, promote crystalline domains and reduce lamellar spacing, often resulting in higher mobility. The position and symmetry of substituents determine whether thin films adopt edge-on, face-on, or mixed orientations relative to the substrate. Since OFET conduction occurs predominantly in the first few molecular layers adjacent to the dielectric interface, controlling this orientation is crucial. For example, edge-on orientation in many p-type semiconducting polymers aligns the π-stacking direction within the charge transport plane, significantly increasing mobility.

For n-type OFETs, molecular design must address an additional challenge: ensuring the stability of the reduced state against oxygen and moisture. Electron transport materials require a sufficiently low-lying LUMO (typically below –4.0 eV) to prevent spontaneous electron trapping by ambient species. Strategies to stabilize the LUMO include incorporating electron-withdrawing substituents such as fluorine, cyano groups, imide functionalities, and heteroatoms with strong inductive effects.[71–73] Well-designed n-type systems such as naphthalene diimides (NDIs) and perylene diimides (PDIs) now consistently achieve mobilities in the 5–10 $cm^2/V \cdot s$ range, a level once exclusive to the best p-type materials. Their success demonstrates the effectiveness of combining rigid aromatic cores with strong electron-withdrawing units to create stable electron-transport structures.[74–77]

Recent developments have also highlighted the importance of suppressing dynamic disorder, an intrinsic limitation of soft organic materials. Dynamic fluctuations in molecular positions and torsional angle variations lead to temporal changes in electronic coupling, which can localize carriers and limit band-like transport. Ladder-type molecules with fused backbones, rigid polymers with minimized torsional freedom, and crystals with strong noncovalent locking interactions (e.g., S···S, N···H, and halogen bonding) help reduce these fluctuations.[44,78–80] These structural motifs create transport pathways with reduced energetic variance, supporting higher mobility even at room temperature.

Together, these molecular design principles form the foundation for developing high-performance OFET materials. By integrating rigid conjugated backbones, optimized side-chain architectures, stable frontier orbital energies, low-disorder interfaces, and controlled doping strategies, organic semiconductors have achieved mobilities approaching or exceeding those of

amorphous silicon. Continued progress in molecular engineering, interface design, and thin-film processing promises further improvements, enabling OFETs to play a central role in flexible electronics, low-cost sensing platforms, wearable devices, and emerging quantum-relevant organic materials.

1.2.4. OFETs as a Platform for Sensing, Logic, and Integrated Photonics

Beyond their role as simple switching elements, OFETs serve as sensitive probes of chemical, mechanical, and biological environments. Because charge transport in organic semiconductors is strongly influenced by molecular interactions at the surface, OFETs can act as highly responsive sensing platforms where adsorption of analytes modulates threshold voltage or channel conductivity. Flexible OFET arrays have been incorporated into wearable sensors, neuromorphic circuits, and optically active systems such as phototransistors and excitonic logic elements.[81–83]

Of particular interest is the integration of OFETs with excitonic materials and optical processes such as singlet fission, thermally activated delayed fluorescence, and exciton-polaron interactions. These hybrid systems enable phototransistors with enhanced responsivity, optically gated transistors, and device architectures that couple electronic transport with optical coherence or spin-correlated exciton states. The chemical tunability of organic semiconductors provides a foundation for future convergence between OFET platforms and quantum-enabled photonic circuitry, where controlled spin or excitonic states may be interfaced with transistor-level logic.

1.3. Organic Light-Emitting Diodes (OLEDs)

Organic light-emitting diodes (OLEDs) represent one of the most explored applications of π-conjugated organic semiconductors, where light emission arises from the radiative

recombination of electrically generated excitons.[84,85] The advent of OLEDs has revolutionized display and lighting technologies by offering mechanically flexible, lightweight, and energy-efficient devices capable of high color purity and wide viewing angles. The central physical principle behind OLED operation lies in the ability of organic molecules to convert electrical excitation into optical emission with high quantum efficiency, a process intrinsically governed by the electronic configuration of the molecule and the spin statistics of exciton formation.[86,87]

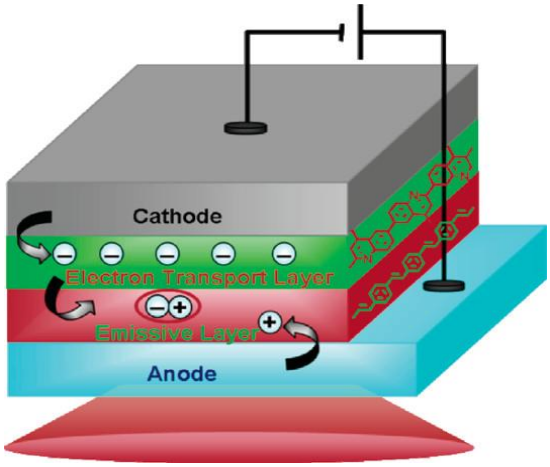


Figure 1.6: Generation of optical emission from organic material[88]

When an electric current passes through an OLED, electrons and holes are injected into the lowest unoccupied (LUMO) and highest occupied (HOMO) molecular orbitals, respectively (**Figure 1.6**) .[88] Their recombination in the emissive layer forms excitons bound electron-hole pairs distributed statistically as 25% singlet (S_1) and 75% triplet (T_1) states, following spin multiplicity rules. In early-generation fluorescent OLEDs, only singlet excitons contributed to emission through prompt fluorescence, limiting the internal quantum efficiency (IQE) to a theoretical maximum of 25%. The non-radiative loss of triplet excitons represented a major barrier to achieving high-efficiency devices. Overcoming this limitation has driven decades of research into mechanisms that harvest triplet excitons and convert them into radiative states.

1.3.1. Thermally Activated Delayed Fluorescence (TADF): A Pathway to 100% Internal Quantum Efficiency

Thermally Activated Delayed Fluorescence (TADF) has emerged as one of the mechanisms for achieving 100% IQE in purely organic emitters. The core concept of TADF is based on reverse intersystem crossing (RISC), wherein non-emissive triplet excitons (T_1) are thermally upconverted to the emissive singlet manifold (S_1). The RISC process is activated by thermal energy that overcomes the small singlet-triplet energy gap (ΔE_{ST}), typically in the range of 0.05-0.2 eV. This energy gap is determined by the exchange interaction between the highest occupied and lowest unoccupied molecular orbitals, essentially the overlap between the hole and electron wavefunctions. Minimizing this overlap reduces ΔE_{ST} and promotes efficient RISC.[89–91] Organic emitters that exhibit TADF typically display two distinct emissive pathways, often categorized as prompt fluorescence and delayed fluorescence (**Figure 1.7)**. Immediately following photoexcitation, a population of singlet excitons relaxes radiatively from the first excited singlet state (S_1) back to the ground state (S_0), producing emission on the nanosecond timescale, this constitutes the prompt fluorescence channel.

In contrast, the delayed fluorescence pathway arises when a fraction of these photoexcited singlets undergo intersystem crossing (ISC) into the triplet manifold, generating long-lived (T_1) excitons. For TADF-active molecules, thermal energy can promote these triplet excitons back to the S_1 state through RISC process, provided that the singlet-triplet energy gap (ΔE_{ST}), is sufficiently small. Because this route requires an additional spin-forbidden transition followed by repopulation of S_1, the resulting emission occurs with microsecond-scale lifetimes, substantially longer than prompt fluorescence.

Thus, whereas prompt fluorescence reflects direct radiative decay of initially populated singlet excitons, delayed fluorescence represents a thermally enabled recycling of triplet excitons back into the emissive singlet manifold. This mechanistic interplay between ISC, RISC, and radiative decay is fundamental to the operational efficiency of TADF materials, enabling near-unity internal quantum efficiency by harvesting both singlet and triplet exciton reservoirs.

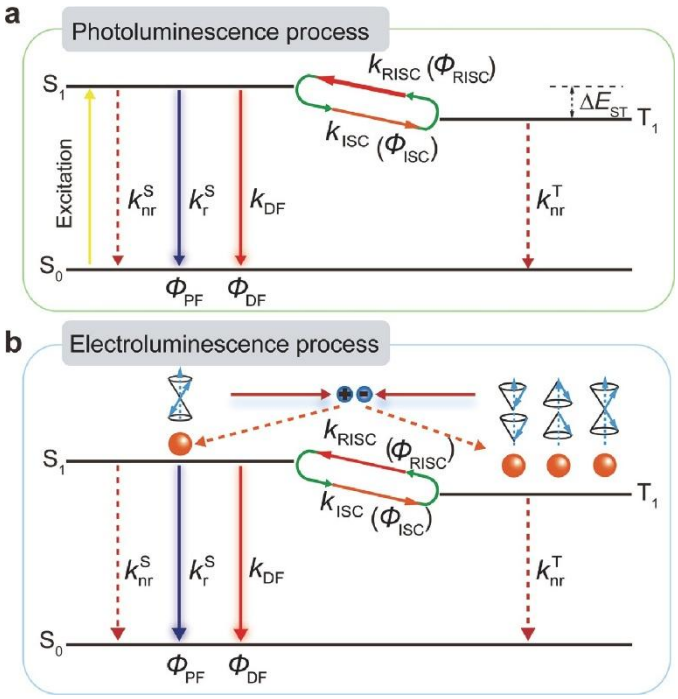


Figure 1.7: Processes in TADF molecules (a) Photoluminescence (b) Electroluminescence[92]

1.3.2. Design Principles and Mechanisms for TADF

A central principle in the development of thermally activated delayed fluorescence (TADF) materials is the precise control of electron distribution within donor-acceptor (D-A) molecular architectures. Early generations of TADF emitters relied heavily on this strategy: electron-rich donor units were covalently linked to electron-deficient acceptor fragments through a π-conjugated backbone, with the dihedral angle between these fragments adjusted to govern orbital communication (**Figure 1.8**). This structural configuration deliberately localizes the HOMO on the donor and the LUMO on the acceptor, thereby reducing their spatial overlap and minimizing

the singlet-triplet energy gap (ΔE_{ST}).[93–95] However, while D-A TADF materials effectively lower ΔE_{ST}, excessive spatial separation between HOMO and LUMO can also suppress the radiative rate constant k_r due to diminished orbital overlap, leading to slow fluorescence and efficiency roll-off at high brightness.

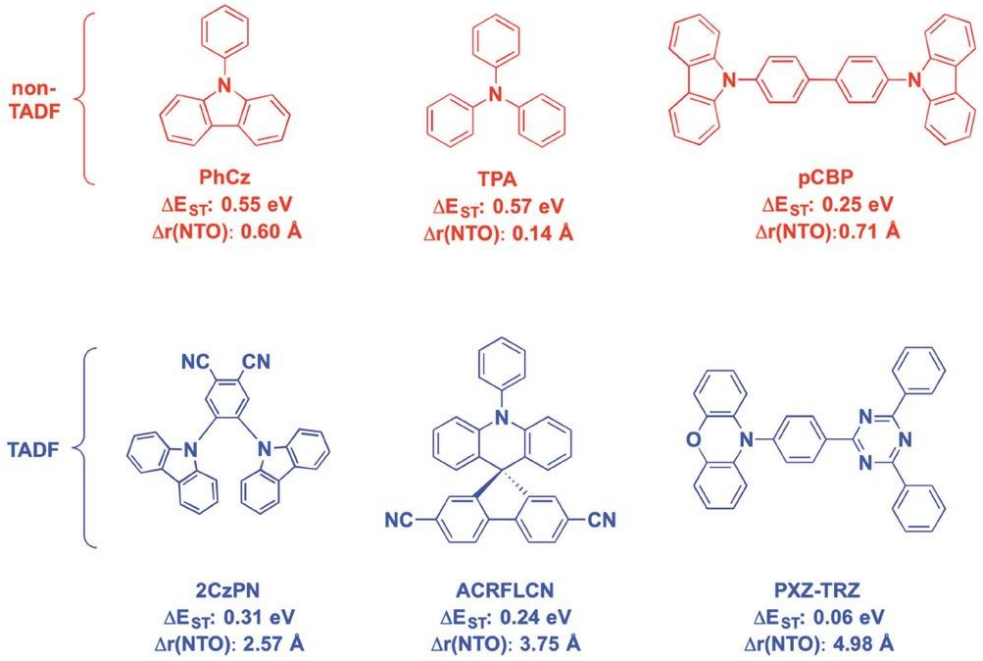


Figure 1.8: Examples of D-A TADF-type explored molecules.[95]

Conversely, structures that preserve a modest degree of HOMO-LUMO overlap maintain a stronger transition dipole, enabling faster radiative decay and better operational stability. These insights underscore that TADF efficiency depends not only on minimizing ΔE_{ST}, but on carefully tuning the degree of electron-hole separation to optimize the interplay between RISC rate, radiative rates, and excited-state dynamics.

Recent molecular design strategies have therefore moved beyond simple D-A twisting to incorporate subtler structural controls. Strengthening or extending the donor moiety can localize

electron density at the molecular periphery, while judicious acceptor substitution can fine-tune the LUMO energy without excessively weakening orbital overlap. Other approaches use conformational locking or structural interlocking to impose higher torsional barriers between donor and acceptor units. Such rigidified architectures preserve charge-transfer character while stabilizing a more defined excited-state geometry. This improved structural rigidity reduces nonradiative losses and often sharpens the emission profile, particularly in blue emitters where color purity is sensitive to vibrational broadening. These design strategies demonstrate that the most effective TADF materials emerge not from maximizing charge-transfer separation, but from precisely balancing charge-transfer character with controlled orbital delocalization and backbone rigidity.

MR-TADF materials represent a new paradigm in organic emissive design. Unlike D-A molecules that rely on spatial separation of charge, MR-TADF emitters such as those containing boron-nitrogen (B-N) doped frameworks achieve small ΔE_{ST} through local resonance effects between electron-donating and withdrawing atoms embedded within a rigid conjugated backbone (**Figure 1.9**).[96] This localized excited-state character preserves high oscillator strength and narrow emission bandwidths, producing pure color emission with high radiative efficiency.[97–100] The rigid planar framework of MR-TADF materials also suppresses non-radiative decay and reduces molecular reorganization energy, yielding enhanced stability and operational lifetime. Moreover, the confinement of frontier orbitals on specific atomic sites enables highly localized spin-orbit coupling (SOC) modulation, facilitating efficient RISC despite the absence of heavy atoms. Consequently, MR-TADF materials bridge the gap between purely organic and phosphorescent systems, achieving narrowband, high-color-purity emission without metal centers.

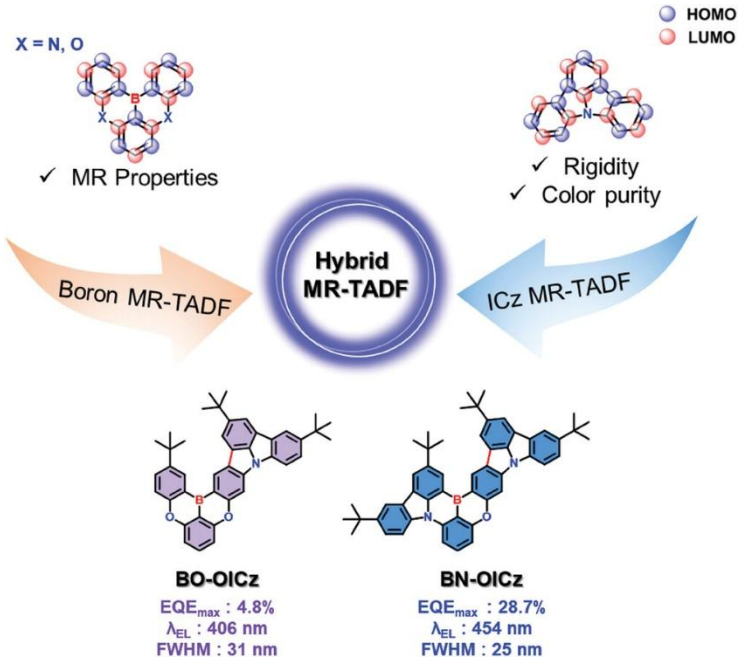


Figure 1.9: Molecular design of MR-TADF[96]

1.3.3. Mechanism of TADF

The rate of RISC is governed by both the magnitude of ΔE_{ST} and the spin-orbit coupling (SOC) between the singlet and triplet states. These two parameters jointly determine how efficiently a triplet exciton can be thermally promoted and electronically converted into its emissive singlet counterpart. In the formalism of Fermi's Golden Rule, the RISC rate is expressed as:

$$k_{\mathrm{RISC}} = \frac{2\pi}{\hbar}\rho_{\mathrm{FC}} \mid \langle S_1 \mid \hat{H}_{\mathrm{SO}} \mid T_1 \rangle \mid^2 \qquad \text{(Equation 1.2)}$$

where ρ_{FC} is the Franck-Condon weighted density of vibrational states and $\langle S_1 \mid \hat{H}_{\mathrm{SO}} \mid T_1 \rangle$ is the SOC matrix element that mixes the two electronic wavefunctions. A small ΔE_{ST} ensures that thermally accessible vibrational levels can bridge the energetic separation between S_1 and T_1, while SOC dictates the probability that a spin-forbidden transition can actually occur once the nuclear

framework reaches the appropriate configuration. In purely organic molecules, the intrinsic SOC is weak; however, it can be effectively amplified when the singlet and triplet states differ in orbital character, in accordance with El-Sayed selection rules. This is typical in TADF materials, for which the emissive S_1 state adopts a charge-transfer (CT) configuration while the corresponding T_1 state maintains a greater proportion of locally excited (LE) character. The CT nature of S_1 minimizes ΔE_{ST} by reducing the exchange integral, whereas the LE admixture in T_1 enhances SOC by providing the requisite change in orbital symmetry.

Recent studies have demonstrated that higher-lying triplet states (T_n) with local-excitation (LE) character can serve as intermediates that enhance the effective coupling between $S_1$and T_1.[101] This spin-vibronic coupling mechanism allows efficient RISC by mixing CT and LE character through molecular vibrations, effectively bridging the otherwise forbidden transition. The recognition that multiple triplet states participate in RISC has fundamentally reshaped the understanding of TADF.[102,103] The spin-vibronic coupling model posits that vibronic interactions particularly out-of-plane modes that modulate donor-acceptor torsion facilitate interconversion between $S_1(CT)$, $T_1(CT)$, and $T_n(LE)$ states. When the energy spacing between $T_1(CT)$ and $T_n(LE)$ is small, these modes can induce transient state mixing, amplifying SOC and promoting efficient RISC even when direct S_1-T_1 coupling is weak. This coupling mechanism provides a physical explanation for why TADF can occur efficiently in rigid, organic frameworks without heavy atoms.

Despite the remarkable success of TADF emitters in achieving near-unity internal efficiency, several fundamental questions remain. Among them is the microscopic mechanism of RISC, including the extent to which vibronic coherence and nonadiabatic coupling determine

delayed fluorescence yield. Moreover, while spin-vibronic coupling explains many experimental observations, other processes such as triplet-triplet annihilation, thermally assisted upconversion, or exciplex formation can also contribute to delayed emission. Therefore, a deeper spectroscopic and theoretical exploration of these intertwined processes is essential for advancing OLED efficiency, stability, and color precision. In this thesis, nonlinear and time-resolved spectroscopies are used as molecular probes to elucidate these mechanisms, revealing the pathways that govern charge transfer, spin conversion, and coherent coupling in organic emitters.

1.4. Nonlinear and Quantum-Optical Spectroscopic Techniques as Molecular Probes

In the nonlinear regime, the optical response of a material becomes dependent on higher powers of the incident electric field, giving rise to phenomena such as two-photon absorption (TPA), second-harmonic generation (SHG), and sum-frequency generation (SFG).[104] These effects serve as sensitive probes of molecular symmetry, polarizability, and electronic delocalization. In functional π-conjugated materials such as fused-ring organic semiconductors and donor-acceptor frameworks, nonlinear processes directly reflect the extent of intramolecular charge transfer and orbital hybridization. The magnitude and spectral shape of nonlinear responses thus encode valuable information about electronic coupling, transition dipole orientation, and optical anisotropy.[105,106] Moreover, emerging quantum-correlated nonlinear techniques, such as entangled two-photon absorption (ETPA), extend these insights to the quantum limit of light-matter interactions, enabling the interrogation of molecular transitions with sub-classical precision and minimal photodamage.[107–109] Such capabilities are particularly relevant for probing delicate materials intended for optoelectronic and quantum sensing applications.

1.4.1. Classical Two-Photon Absorption

Two-photon absorption (TPA) is a third-order nonlinear optical (NLO) process in which a molecule simultaneously absorbs two photons of lower energy to reach an excited electronic state whose total energy corresponds to the sum of both photons.[110,111] Conceptually, this process represents one of the most fundamental manifestations of nonlinear light-matter interaction, providing deep insights into molecular electronic structure, delocalization, and charge-transfer dynamics. Unlike the familiar one-photon absorption (OPA), which depends linearly on light intensity, TPA depends quadratically on the photon flux and therefore becomes significant only under high-intensity excitation conditions such as those achieved with pulsed lasers.

To understand the TPA process, it is instructive to begin from the macroscopic viewpoint of polarization. When a molecule is subjected to an oscillating electric field $E(t)$from an incident light wave, its electronic cloud becomes distorted, inducing a dipole moment $P(t)$. The molecular polarization can be expressed as a power series expansion in the electric field:

$$P_i(t) = \mu_i + \alpha_{ij}E_j + \beta_{ijk}E_jE_k + \gamma_{ijkl}E_jE_kE_l + \cdots \qquad \text{(Equation 1.3)}$$

Here, $\mu_i$is the permanent dipole moment, while α, β, and γrepresent the linear, second-order, and third-order polarizability tensors, respectively. The first term describes the static dipole; the second corresponds to linear optical effects (e.g., OPA and refractive index); the third and higher-order terms account for nonlinear optical responses such as second-harmonic generation, sum-frequency generation, and two-photon absorption.[112,113]

In centrosymmetric molecules, the second-order term β vanishes due to symmetry, making the third-order term **(γ)** the dominant contributor to nonlinear optical phenomena. This term describes the electronic response that scales with the cube of the electric field and underlies third-

order processes including TPA, third-harmonic generation (THG), and four-wave mixing (FWM). Therefore, the TPA process becomes a sensitive probe of the third-order susceptibility $\chi^{(3)}$of the material, providing direct information about the electronic delocalization and the efficiency of virtual-state coupling.[113,114]

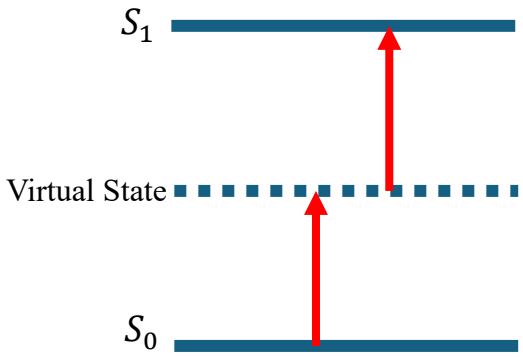


Figure 1.10: Classical two photon absorption process

In TPA, the simultaneous absorption of two photons involves a virtual intermediate state rather than a real, energetically accessible level (**Figure 1.10**). The transition proceeds via second-order perturbation, where the system transiently occupies a non-resonant virtual level for an extremely short period (on the order of 10^{-15} s). The probability for such a transition depends on the availability of intermediate states that can couple the ground and excited states through dipole-allowed transitions.

The TPA rate, R, can be expressed as:

$$R = \delta I^2 \qquad \text{(Equation 1.4)}$$

where I is the photon intensity and $\delta$is the TPA cross-section, often expressed in Göppert–Mayer (GM) units, with $1\,\text{GM} = 10^{-50}\,\text{cm}^4 \cdot \text{s} \cdot \text{photon}^{-1}$. The quadratic dependence on intensity

distinguishes TPA from OPA, and experimentally it requires the focused, ultrafast pulses of femtosecond lasers to achieve the required instantaneous photon flux.[110,115]

The probability of a TPA event is characterized by the two-photon absorption cross-section, δ_r, which determines how efficiently a molecule can absorb two photons of frequencies $\omega_1$and ω_2. This cross-section is defined in terms of the molecular two-photon strength $\langle S_r^2 \rangle$and the line shape function $g_r(\omega_0, \Gamma)$, which describes the energetic distribution of accessible states:

$$\delta_r = \pi^2 \omega_1 \omega_2 \langle S_r^2 \rangle g_r(\omega_0, \Gamma) \qquad \text{(Equation 1.4)}$$

In this expression, $\omega_1$and ω_2 correspond to the frequencies of the two absorbed photons, while ω_0 denotes the transition frequency between the ground and excited states. The line shape function $g_r(\omega_0, \Gamma)$depends on the excited-state damping factor, Γ, which accounts for dephasing due to vibrational coupling, solvent interactions, and homogeneous broadening.[107,116]

The molecular contribution, $\langle S_r^2 \rangle$, represents the rotationally averaged two-photon strength and depends critically on the transition dipole moments and the energy detuning of the intermediate states:

$$S_{if}^{r,ab} = \sum_j \left[\frac{D_{ab}^{(j)}}{\Delta_1^{(j)} - ik_j/2} + \frac{D_{ba}^{(j)}}{\Delta_2^{(j)} - ik_j/2}\right] \qquad \text{(Equation 1.5)}$$

Here, $D_{ab}^{(j)}$ denotes the transition dipole product between states $a \to j$and $j \to b$; k_j represents the linewidth of the intermediate state j, encompassing dephasing contributions from vibronic and solvent effects. The terms $\Delta_1^{(j)} = \epsilon_j - \epsilon_i - \omega_1$ and $\Delta_2^{(j)} = \epsilon_j - \epsilon_i - \omega_2$ describe detuning energies between the photon frequencies and the intermediate energy levels.

From a molecular design standpoint, the magnitude of the two-photon absorption cross-section, δ_r, is inherently tied to the degree of electronic delocalization and the coupling between molecular dipoles across the ground, intermediate, and excited states. The process involves the simultaneous absorption of two photons, each interacting with the molecular electronic system in a correlated manner. This correlation effectively probes how the electronic density is redistributed within the molecular framework during excitation, revealing the nature and extent of charge transfer (CT).[117–119]

In conjugated organic systems, TPA thus acts as a molecular probe for charge-transfer phenomena.[119–121] The probability of two-photon excitation depends on the transition dipole moment matrix elements, $\langle \psi_i \mid \mu \mid \psi_j \rangle$, which quantify the extent of electronic coupling between states. Molecules that exhibit strong CT character where the excitation involves significant electron displacement from donor-like to acceptor-like regions tend to display enhanced TPA cross-sections. This enhancement arises because charge separation increases the change in the permanent dipole moment ($\Delta\mu$) and modulates the polarizability of the molecular system.[122–124] Consequently, the induced second-order polarization becomes more sensitive to the applied optical field, amplifying the nonlinear optical response. In fully π-conjugated organic molecules, the delocalized π-electron network itself supports subtle, symmetry-dependent charge transfer within the molecular core. The magnitude and directionality of the transition dipole between ground and excited states are governed by molecular symmetry and orbital overlap, meaning that variations in backbone, planarity, and conjugation length can lead to measurable shifts in TPA intensity and polarization anisotropy. These shifts reflect underlying changes in electronic coherence and localization, which can be quantitatively analyzed through polarization-dependent TPA

spectroscopy. The dipole correlation function connecting the ground, intermediate, and excited states effectively encodes information about the charge displacement pathway during photoexcitation. The coupling strength between these states depends on both the transition dipole coupling and the permanent dipole reorientation, which together determine whether the photoexcited charge density remains localized or evolves toward a delocalized CT state. Thus, TPA does not merely measure the presence of electronic transitions; it directly probes the symmetry breaking, changes in dipole moments, and dynamic electron correlation that reveals charge-transfer processes in organic semiconductors and quantum materials.

Furthermore, TPA spectroscopy allows selective interrogation of even-parity (gerade) excited states that are inaccessible via one-photon absorption due to parity restrictions.[125,126] Many of these states are characterized by strong CT or mixed π-π* character, providing a unique window into hidden electronic couplings that dictate photophysical outcomes. The resulting insights are invaluable for guiding the rational design of materials where controlled CT interactions govern device efficiency, whether in organic light-emitting diodes (OLEDs), organic solar cells (OSCs), or molecular qubits for quantum sensing.

1.4.2. Quantum Entanglement and Its Emerging Role in Light-Matter Interactions

Quantum entanglement introduces correlations between photons that far exceed what is possible with classical light, enabling new regimes of control and measurement in light-matter interactions. In contrast to classical light, where the properties of photons are statistically independent, entangled photons exhibit strong temporal, spectral, and polarization correlations that fundamentally dictate how electronic states are accessed and how information is extracted from materials.[127,128] These nonclassical features allow quantum light to interact with molecules in ways that reveal deeper electronic structure, facilitate selective excitation pathways, and enhance

sensitivity. A key advantage of entangled-photon excitation is its ability to exploit quantum interference between distinct optical pathways. As a result, entangled light can access electronic levels and virtual states that are weakly allowed or completely inaccessible under classical light excitation. This capability opens new spectroscopic tools and enables molecular investigation beyond classical regime. Importantly, entangled photon pairs can be engineered to have tunable joint spectral properties, allowing for precise control over the total excitation energy independent of individual photon energies. This unique properties of quantum light offers a powerful tool for selectively probing congested excited-state, especially in complex organic, biological, or condensed-phase environments.

One of the most transformative implications of using entangled photons is the possibility of transferring entanglement from the light field into the material system itself. This process of field-matter entanglement can induce new quantum-coherent material states not observed under classical excitation. Such states provide valuable insight into electron delocalization, vibronic coherence, and quantum transport mechanisms.[129,130] Furthermore, because entangled photons can couple into virtual states with remarkable selectivity, they can activate molecular properties that remain dormant using classical light.

Another critical advantage arises from the noise characteristics of entangled light. Due to the strong correlations between photon pairs, measurements performed with entangled photons can exhibit substantially reduced noise compared to classical light. In many cases, the signal-to-noise ratio can be enhanced without increasing the photon flux, making entangled-photon spectroscopy particularly useful for studying fragile materials and photosensitive molecules. This low-flux advantage is especially relevant for quantum sensing applications, where the ability to

obtain high-quality measurements under limited photon exposure is essential. Entangled-light excitation thus offers an experimental regime where sensitivity, selectivity, and resolution can be simultaneously improved beyond classical limits.

Collectively, these capabilities make quantum entanglement a powerful new frontier for spectroscopy and materials research. The ability to shape excitation pathways, access normally hidden electronic states, induce new material responses, and reduce measurement noise positions entangled-photon methods as transformative tools for probing next-generation quantum materials. As organic materials, molecular qubits, and quantum-sensing architectures continue to evolve, the integration of entangled light provides a pathway for probing photophysical mechanisms with unprecedented depth. From creating new avenues for molecular-state control, to enabling high-sensitivity detection of weak interactions, entanglement-driven spectroscopy is poised to play a foundational role in the design and understanding of advanced quantum materials. Through the unique capability to merge quantum optical correlations with molecular electronic structure, entangled light introduces a fundamentally new dimension to the study of light-matter interactions one that stands to reshape how we characterize, manipulate, and ultimately engineer materials for quantum science and emerging photonic technologies.

1.4.2.1. Entangled Two-Photon Absorption (ETPA): Quantum-Mechanical Perspective and Molecular Insights

Entangled Two-Photon Absorption (ETPA) spectroscopy exploits the nonclassical correlations between pairs of photons to probe molecular electronic transitions with enhanced sensitivity.[131] Unlike classical two-photon absorption (TPA), which relies on the simultaneous absorption of two independent photons from a high-intensity light source, ETPA uses entangled photon pairs whose quantum states are strongly correlated in energy, time, momentum, and

polarization (**Figure 1.11**).[109,132,133] Furthermore, unlike classical two-photon absorption (TPA), which requires extremely high photon flux to achieve sufficient probability of coincident photon arrival, ETPA takes advantage of the temporal and spectral correlations between paired photons to drive molecular transitions with dramatically lower light intensities. These correlations allow molecular excitation to occur at photon fluxes many orders of magnitude lower than classical TPA, enabling the interrogation of fragile molecular systems without photodamage while simultaneously revealing subtle details of electronic coherence and charge-transfer dynamics that are inaccessible to conventional techniques.[133–135]

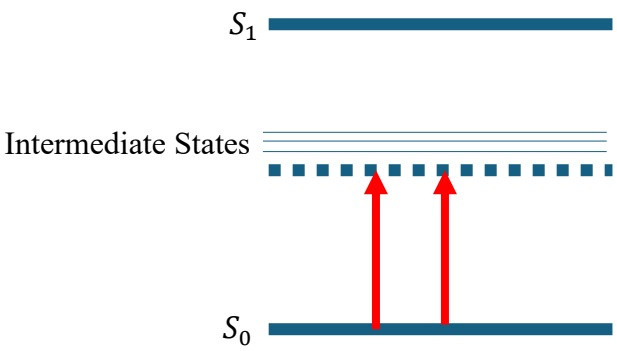


Figure 1.11: Entangled two photon absorption process

The physical basis of ETPA in the generation of entangled photon pairs through spontaneous parametric down-conversion (SPDC), a second-order nonlinear optical process that occurs in non-centrosymmetric crystals such as beta-barium borate (BBO), potassium dihydrogen phosphate (KDP), or lithium niobate ($LiNbO_3$). In SPDC, a pump photon of energy $\hbar\omega_p$ from a laser beam interacts with the nonlinear medium and spontaneously splits into two lower-energy photons, conventionally referred to as the signal and idler photons, with energies $\hbar\omega_s$ and $\hbar\omega_i$, respectively.[4,107,133,135] Energy and momentum conservation govern the process through the phase-matching conditions:

$$\omega_p = \omega_s + \omega_i, \vec{k}_p = \vec{k}_s + \vec{k}_i \qquad \text{(Equation 1.6)}$$

These relationships ensure that while the individual photon energies may vary within the limits of the pump bandwidth and crystal dispersion, their sum frequency remains fixed, an intrinsic feature that binds them in an energy-time entangled state. Because of this correlation, measurements on one photon immediately determine the frequency or arrival time of its partner, regardless of the distance between them, a hallmark of quantum entanglement.[4,109,128]

Two principal geometries are typically used in SPDC: Type-I and Type-II phase matching. In Type-I, both photons have the same polarization but propagate in different spatial directions, whereas in Type-II, the signal and idler photons are orthogonally polarized (**Figure 1.12**). By adjusting the crystal orientation, temperature, or pump wavelength, the degree of spectral and temporal entanglement can be finely tuned.

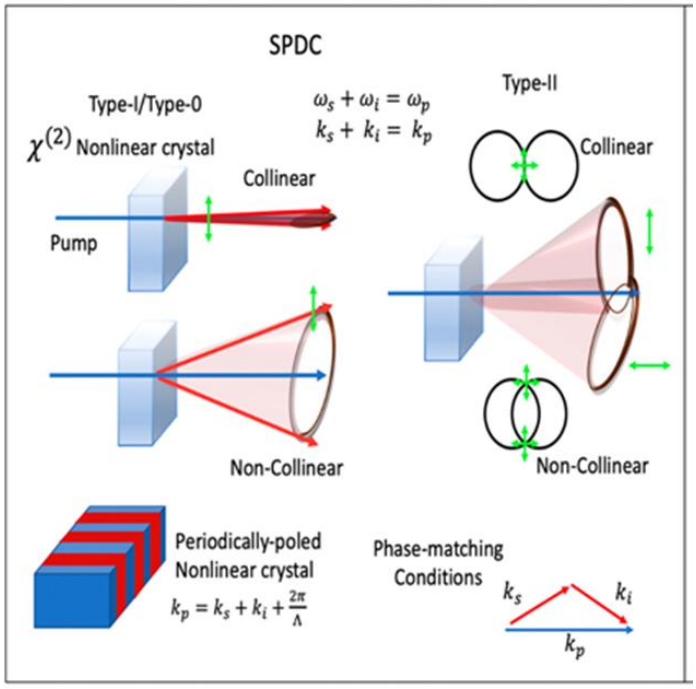


Figure 1.12: Generation of entangled photons via SPDC.[135]

Within the framework of quantum optics, the ETPA process can be rigorously described by the transition amplitude of a molecule interacting with an entangled twin-photon field. The corresponding ETPA cross-section (σ_e) represents the effective molecular area for absorption of a correlated photon pair and is defined as:

$$\sigma_e = \frac{\pi^4}{A_e T_e} \omega_1 \omega_2 \langle S_e^2 \rangle g_e(\omega_f) \qquad \text{(Equation 1.7)}$$

Here, A_e denotes the entanglement area, reflecting the spatial correlation region over which the two photons remain phase-coherent, while T_e represents the entanglement time, i.e., the temporal correlation window between the photon pair. $\omega_1$and ω_2 correspond to the angular frequencies of the signal and idler photons, respectively, and $\langle S_e^2 \rangle$ is the rotationally averaged entangled two-photon transition strength. This term incorporates the transition dipole matrix elements and the detuning energies of the intermediate virtual states involved in the two-photon transition.[116,136]

The line-shape function, $g_e(\omega_f)$, captures how the entangled-photon energy distribution overlaps with the molecular absorption resonance. It has been expressed as:

$$g_e(\omega_f) = \frac{1}{\pi \tau_f} \frac{\Gamma^2}{[2\omega - (\varepsilon_f - \varepsilon_g)/\hbar]^2 + \Gamma^2} \qquad \text{(Equation 1.8)}$$

where Γ is the damping (or dephasing) constant of the excited state, and $\tau_f$is the radiative lifetime of the two-photon excited state.

These relations emphasize that, while both classical and entangled TPA line-shapes depend on photon frequency and damping, the ETPA lineshape incorporates an additional dependence on the radiative lifetime (τ_f) and scales with Γ^2 rather than Γ. As a result, the spectral broadening and lifetime interplay differ markedly from classical TPA: in ETPA, the effective linewidth is governed

more strongly by the intrinsic excited-state dynamics than by the damping term alone. Consequently, the ETPA cross-section is particularly sensitive to the molecular environment, making it a more informative parameter for probing excited-state lifetimes and dephasing processes.[107,131,133,137,138]

From a molecular standpoint, ETPA acts as a quantum interferometric probe of electronic delocalization, dipole reorientation, and charge redistribution. When a molecule absorbs an entangled photon pair, the two correlated photons jointly interact with the electronic cloud, inducing polarization fluctuations that reflect the coherent coupling between ground, intermediate, and excited states. The transition probability depends on the two-time dipole–dipole correlation function, $\langle \mu(t_1)\mu(t_2) \rangle$, which links the temporal structure of the biphoton field to the evolution of the molecular dipole moment. Consequently, variations in the magnitude and direction of the molecular dipole, arising from charge-transfer or conjugation effects, modulate the ETPA signal intensity.

In conjugated organic systems, especially those featuring donor–acceptor architectures or extended π-conjugation, excitation often involves partial charge transfer between molecular fragments. The absorption of entangled photon pairs effectively probes these charge-transfer transitions by detecting the coherent redistribution of electronic density within the biphoton correlation time. Because entangled photons "arrive together" within this temporal window, they can sense electronic motion that occurs on sub-femtosecond scales timescales comparable to intramolecular charge-transfer processes and vibronic relaxation.

The change in dipole moment during excitation plays a central role in determining the coupling strength between the molecule and the biphoton field. Systems with large $\Delta\mu$ indicative

of strong polarizable charge-transfer states display enhanced ETPA cross-sections. This makes ETPA uniquely sensitive to electronic asymmetry and long-range delocalization, providing a direct molecular fingerprint of charge-transfer strength. Furthermore, because the entangled photon pair interacts coherently with multiple transition moments, ETPA measurements can reveal intermediate-state coherence lifetimes and vibronic coupling strengths that govern relaxation pathways in complex molecular systems.

1.5. Photoinduced Electron Transfer, Single Electron Transfer, and Back Electron Transfer in Photocatalytic Systems

Photocatalysis occupies a central position at the intersection of light-matter interactions, excited-state reactivity, and organic functional materials; three pillars that define the scientific direction of this dissertation. When a photocatalyst absorbs light, it enters an electronically excited state with a redistribution of charge density that significantly alters its redox potential. This excited state acts as a transient chemical species capable of initiating electron transfer reactions with surrounding molecules or substrates.[139,140] Photoredox catalysis has transformed modern synthetic organic chemistry by enabling challenging oxidative and reductive transformations under mild conditions using visible light. The ability to generate open-shell species from simple hydrocarbon substrates has made it possible to forge C-C and C-heteroatom bonds with remarkable selectivity, often circumventing multistep sequences associated with classical redox chemistry. Central to these advances is the concept that a photocatalyst, upon absorbing a photon, reorganizes its electron density and redox potentials, thereby creating a transient reactive state capable of performing single-electron processes with high precision. This excited state opens pathways for the activation of inert C-H bonds, the oxidation of electron-rich alkenes, and the diversification of simple feedstock molecules into synthetically valuable building blocks. The ensuing sequence of

photoinduced electron transfer (PET), single electron transfer (SET), and back electron transfer (BET) events defines the efficiency and selectivity of a photochemical process. Understanding these processes at a mechanistic level particularly how molecular structure modulates them is essential for the rational design of next-generation photocatalytic systems for energy conversion, photoredox catalysis, and quantum photochemistry.

1.5.1. Photoinduced Electron Transfer (PET): Excited-State Reactivity and Energy Dynamics

A unifying feature of photoredox methods whether hydrofunctionalization, C-H amination, etherification, or cation-radical cycloadditions is the formation of a short-lived charge-transfer state through photoinduced electron transfer (PET). Upon photon absorption, a photocatalyst is promoted from its ground electronic state to an excited singlet or triplet state, where the redistribution of electron density lowers or raises its reduction and oxidation potentials relative to the ground state.[139] This altered redox potential allows the excited photocatalyst (PC^*) to either donate or accept an electron to or from a substrate (S), producing charge-separated intermediates:

$$PC^* + S \rightarrow PC^{\cdot -} + S^{\cdot +}$$

The thermodynamics of PET depend on the relative driving force ($\Delta G°$), which can be estimated through the Rehm-Weller equation, combining the excited-state redox potentials of the catalyst and substrate. The rate of PET, however, is determined by both the electronic coupling between donor and acceptor and the reorganization energy associated with solvent and intramolecular relaxation. Within the Marcus theory framework, efficient PET occurs when the driving force approximately matches the reorganization energy; a regime known as the activationless region.

Single electron transfer (SET) refers specifically to the net one-electron exchange between a photocatalyst and its substrate or co-catalyst. Whereas PET describes the general class of light-

driven charge transfer processes, SET represents the elementary step in which a single electron is formally transferred to yield radical intermediates. In photoredox catalysis, this step underpins both oxidative and reductive quenching cycles (**Figure 1.13**):[141]

$$\text{Oxidative quenching: } PC^{*} + S \rightarrow PC^{-} + S^{+}$$

$$\text{Reductive quenching: } PC^{*} + S \rightarrow PC^{+} + S^{-}$$

The distinction between oxidative and reductive pathways depends on the relative positioning of the excited-state redox potentials of the photocatalyst with respect to the substrate frontier orbitals. Electron-rich substrates promote oxidative quenching, while electron-poor substrates favor reductive cycles. In both cases, the resulting radical ions serve as key reactive intermediates that engage in subsequent bond-forming or bond-breaking transformations.

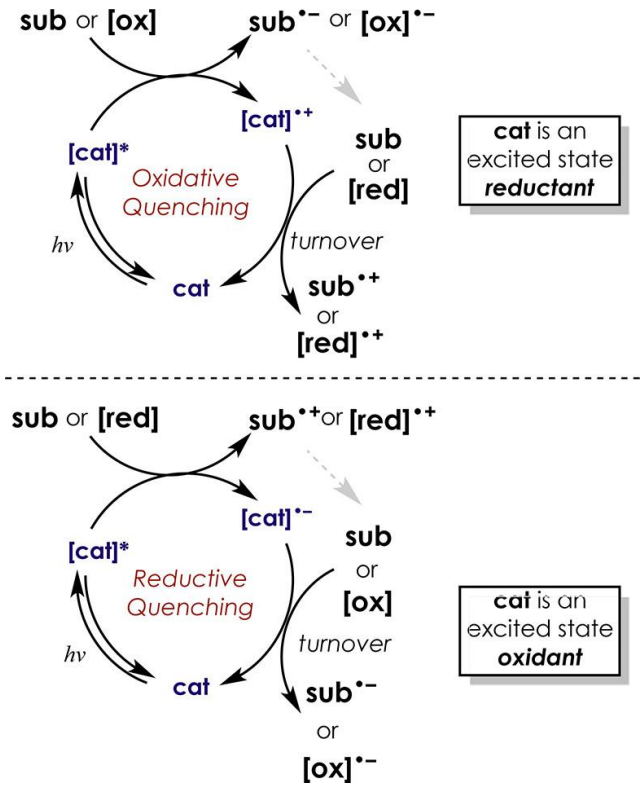


Figure 1.13: Mechanism of photo redox catalyst[141]

The oxidative radical cation formed in this step constitutes the reactive intermediate responsible for subsequent C-N, C-O, or C-C bond formation. The success of SET in these catalytic cycles relies on achieving a delicate balance between thermodynamic driving force and kinetic accessibility. If the excited-state oxidizing power is too weak, the substrate is not activated; if it is too strong, uncontrolled BET or degradation pathways can dominate. Thus, photoredox catalysis relies on tuning the redox properties of the photocatalyst to align with the electronic demands of the substrate class.

Once a charge-separated state is formed via PET or SET, the subsequent back electron transfer (BET) process becomes an unavoidable competing pathway. BET corresponds to the recombination of the photogenerated radical ion pair, returning the system to its ground state or a low-lying excited state without productive chemical transformation:

$$PC^{\cdot-} + S^{\cdot+} \rightarrow PC + S$$

The rate of BET governs the lifetime of the charge-separated state and, consequently, the quantum efficiency of the photochemical reaction. Fast BET leads to rapid recombination, quenching the reaction before further chemistry can occur, whereas slower BET allows sufficient time for catalytic turnover, diffusion, or secondary bond formation.

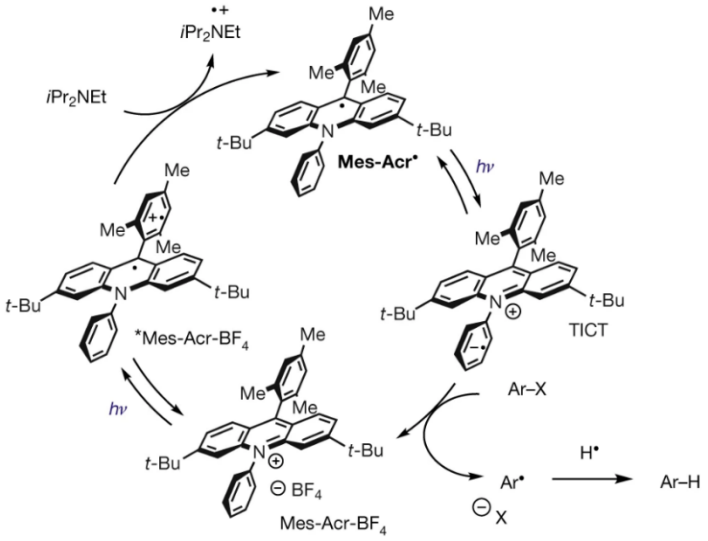


Figure 1.14: Acridine-based photocatalyst for reductive dehalogenation.[142]

Because PET, SET, and BET are all fundamentally tied to the electronic structure of the photocatalyst, molecular design plays an significant role in dictating reaction outcome. In recent years, organic cationic photocatalysts, particularly acridinium-based systems have emerged as powerful platforms for oxidative photocatalysis due to their ability to reach excited-state potentials exceeding +2.5 V vs SCE (**Figure 1.14**).[142] Modulation of the acridinium core through heteroatom incorporation, or substitution pattern directly tunes excited-state lifetimes and redox potentials. Even more remarkable is the discovery that coordination of Lewis acids to acridine derivatives generates in situ photocatalysts with dramatically altered electronic structure. Subtle changes in coordination geometry can shift the excited-state reduction potential by hundreds of millivolts, thereby unlocking reactivity toward substrates that are beyond the oxidative reach of preassembled acridinium salts. This modularity provides access to electronically diverse catalyst systems without laborious synthesis and offers fine control over PET thermodynamics.

The interplay between photocatalyst structure and reaction kinetics becomes particularly important when targeting transformations of electronically complex substrates such as multisubstituted alkenes, unactivated aromatics, and heterocycles. Electron-rich alkenes, for example, are excellent candidates for oxidative SET but may undergo ultrafast BET unless the photocatalyst structure is optimized to stabilize the charge-separated state. A major emphasis of this thesis is therefore to understand how molecular structure controls the relative rates of PET, SET, and BET in photocatalytic systems used for the functionalization of alkenes and C-H bonds. By integrating time-resolved spectroscopic technique with synthetic reactivity, this work seeks to uncover how specific structural modifications to organic photocatalysts alter excited-state redox properties, govern radical cation lifetimes, and ultimately dictate reactivity trends across different substrate classes.

1.6. Overview of Dissertation Chapters

This dissertation provides a comprehensive investigation into the fundamental relationships between molecular structure and the photophysical processes that govern the performance of organic semiconductors, emerging quantum materials, and photocatalytic systems. By integrating nonlinear optical spectroscopy, time-resolved techniques, and electronic-structure calculations, this work systematically elucidates how variations in conjugation length, conformational rigidity, and electronic coupling dictate key excited-state properties, including charge-transport efficiency, exciton generation and decay pathways, and multistep electron-transfer dynamics in new classes of organic material. Through experimental and electronic calculations approach, this dissertation providing insights essential for the rational development of next-generation optoelectronic, quantum-photonic, and catalytic materials.

Chapter 3 focuses on elucidating the intrinsic photophysical properties of rigid ladder-type π-conjugated oligomers, a class of materials increasingly relevant for advanced optoelectronic and quantum technologies. Unlike many prior studies that rely on heavily substituted systems, this chapter examines a systematically extended series of unsubstituted Benzo[k]tetraphene (BTp) oligomers to isolate the fundamental effects of backbone rigidity and conjugation length. Through a combination of time-resolved spectroscopy and nonlinear optical measurements, the chapter demonstrates that increasing the conjugation length enhances electronic delocalization and promotes more efficient intersystem crossing, thereby facilitating triplet-state formation. However, classical and entangled two-photon absorption experiments reveal that this enhancement is not indefinite. The nonlinear optical response reaches a clear saturation point once the effective conjugation length surpasses a critical threshold. Excited-state lifetimes exhibit an analogous plateau, indicating that further structural extension no longer significantly alters the underlying excited-state properties. Together, these results establish the intrinsic limit of electronic tunability in unsubstituted BTp systems and provide a foundational background for the rational design of ladder-type materials with optimized excited-state and nonlinear optical properties.

Chapter four investigates how substituted tetracene derivatives interact with classical and quantum light, and how these interactions relate to the electronic coherence, properties required for photon-to-spin quantum transduction. Using complementary measurements of classical two-photon absorption (TPA), entangled two-photon absorption (ETPA), and near-field scanning optical techniques, I examined how molecular structure modulates both nonlinear optical response and the enhancement of coherent excitonic states. Across all measurements, TCHS-tetracene and TIPS-tetracene exhibit significantly higher TPA and ETPA cross-sections than unsubstituted tetracene. The increased ETPA response suggests a higher probability of entangled-photon

absorption, consistent with recent predictions that stronger radiative lifetimes and longer coherence durations enhance entangled-photon absorption rates. To connect these optical signatures to coherent excited-state behavior, electronic coherence lifetimes were determined using NSOM. TCHS-tetracene displays the longest coherence time in the series, substantially exceeding those measured for tetracene and TIPS-tetracene. This extended coherence originates from the bulky tricyclohexylsilyl groups, which sterically isolate the tetracene cores and suppress strong intermolecular packing. The resulting reduction in environmental decoherence preserves S_1-state coherence long enough to support the coherent formation and evolution of entangled triplet-pair states reported previously for TCHS-tetracene, including the long-lived ^{5}(TT) quintet that forms the basis of multiqubit architectures. From my experiment, I revealed that: molecules that minimize intermolecular coupling show higher classical and entangled two-photon absorption cross-sections and significantly longer excited-state coherence lifetimes. These properties directly enhance the probability of coherent entanglement transfer, from entangled photons to entangled triplet pairs and point to TCHS-tetracene as a leading molecular platform for demonstrating photon-to-spin quantum transduction.

Additionally, in chapter five, I investigated the nonlinear optical properties of cis- and trans-poly(p-phenylene vinylene) (PPV) to understand how molecular conformation influences charge-transfer behavior and optical functionality. I demonstrate that the extended and more planar conformation of trans-PPV significantly enhances its charge-transfer (CT) character, a property that is particularly advantageous for OLED and related optoelectronic applications. In contrast, cis-PPV exhibits a higher sensitivity to quantum-entangled photons, making it a promising candidate for quantum sensing and low-photon-flux detection. These observations are supported by electronic structure calculations, which reveal clear differences in energy-level alignment and

CT propensity between the two conformers. Complementary time-resolved upconversion and femtosecond transient absorption (fs-TA) measurements confirm the accelerated CT dynamics in trans-PPV compared to its cis counterpart. Collectively, these findings highlight how conformational control in PPV derivatives can be leveraged to tailor materials for both advanced optoelectronic devices and emerging quantum photonic technologies.

Parallel to these studies, Chapter six of this thesis also examines the mechanisms that govern reverse intersystem crossing (RISC) and thermally activated delayed fluorescence (TADF) in ladder-type indacenodithieno[3,2-b]thiophene (IDTT) molecular systems. By investigating a series of IDTT derivatives with increasingly extended fused cores, I show how systematic extension of the IDTT units influences spin-vibronic coupling, enhances electronic coupling, and modulates the singlet-triplet energy gaps that control RISC efficiency. As the fused backbone becomes larger and more electronically coupled, the molecules exhibit more effective population transfer from triplet to singlet states, leading to significantly enhanced delayed fluorescence. These observations are supported by nanosecond transient absorption (ns-TA) measurements, which reveal accelerated triplet depopulation, and by electronic structure calculations showing increased mixing between the excited singlet state and higher-lying triplet states. Together, these results establish the IDTT as a versatile design molecular system for the development of TADF materials, providing a molecular strategy to optimize electronic coupling contributions, tunable singlet-triplet energy gap, and achieve efficient delayed fluorescence in advanced organic light-emitting systems.

The final part of this thesis explores the chemical dynamics of electron transfer in photocatalytic systems, with a focus on understanding how molecular and metal-centered properties influence radical formation and reaction efficiency. In this work, I investigate Sc- and

Al-based acridine catalysts and their interactions with the substrate anethole. Using nanosecond transient absorption (ns-TA) spectroscopy, I show that the Al-based acridine generates the radical cation species more rapidly than the Sc-based catalyst, consistent with experimental observations where Al catalysis leads to higher reaction yields. These results highlight the influence of metal–substrate coordination strength and electron-transfer kinetics on catalytic efficiency and provide molecular-level insight into the rational design of more effective photocatalysts. Overall, this study demonstrates how tuning metal coordination environments can control electron-transfer pathways and optimize photocatalytic performance.

References

(1) Fundamentals of Light–Matter Interaction. In *Modern Luminescence from Fundamental Concepts to Materials and Applications*; Woodhead Publishing, 2023; pp 185–218. https://doi.org/10.1016/B978-0-323-89954-3.00009-0.

(2) Andrews, D. L. Energy Harvesting: A Review of the Interplay between Structure and Mechanism. *J. Nanophotonics* **2008**, *2* (1), 022502. https://doi.org/10.1117/1.2976172.

(3) Mohamadpour, F.; Mohammad Amani, A. Photocatalytic Systems: Reactions, Mechanism, and Applications. *RSC Adv.* **2024**, *14* (29), 20609–20645. https://doi.org/10.1039/D4RA03259D.

(4) Szoke, S.; Liu, H.; Hickam, B. P.; He, M.; Cushing, S. K. Entangled Light–Matter Interactions and Spectroscopy. *J. Mater. Chem. C* **2020**, *8* (31), 10732–10741. https://doi.org/10.1039/D0TC02300K.

(5) Mai, S.; González, L. Molecular Photochemistry: Recent Developments in Theory. *Angew. Chem. Int. Ed.* **2020**, *59* (39), 16832–16846. https://doi.org/10.1002/anie.201916381.

(6) Astruc, D.; Boisselier, E.; Ornelas, C. Dendrimers Designed for Functions: From Physical, Photophysical, and Supramolecular Properties to Applications in Sensing, Catalysis, Molecular Electronics, Photonics, and Nanomedicine. *Chem. Rev.* **2010**, *110* (4), 1857–1959. https://doi.org/10.1021/cr900327d.

(7) Menke, S. M.; Ran, N. A.; Bazan, G. C.; Friend, R. H. Understanding Energy Loss in Organic Solar Cells: Toward a New Efficiency Regime. *Joule* **2018**, *2* (1), 25–35. https://doi.org/10.1016/j.joule.2017.09.020.

(8) Hedley, G. J.; Ruseckas, A.; Samuel, I. D. W. Light Harvesting for Organic Photovoltaics. *Chem. Rev.* **2017**, *117* (2), 796–837. https://doi.org/10.1021/acs.chemrev.6b00215.

(9) Brédas, J.-L.; Norton, J. E.; Cornil, J.; Coropceanu, V. Molecular Understanding of Organic Solar Cells: The Challenges. *Acc. Chem. Res.* **2009**, *42* (11), 1691–1699. https://doi.org/10.1021/ar900099h.

(10) Chamberlain, G. A. Organic Solar Cells: A Review. *Sol. Cells* **1983**, *8* (1), 47–83. https://doi.org/10.1016/0379-6787(83)90039-X.

(11) Dimitrov, S. D.; Durrant, J. R. Materials Design Considerations for Charge Generation in Organic Solar Cells. *Chem. Mater.* **2014**, *26* (1), 616–630. https://doi.org/10.1021/cm402403z.

(12) Jailaubekov, A. E.; Willard, A. P.; Tritsch, J. R.; Chan, W.-L.; Sai, N.; Gearba, R.; Kaake, L. G.; Williams, K. J.; Leung, K.; Rossky, P. J.; Zhu, X.-Y. Hot Charge-Transfer Excitons Set the Time Limit for Charge Separation at Donor/Acceptor Interfaces in Organic Photovoltaics. *Nat. Mater.* **2013**, *12* (1), 66–73. https://doi.org/10.1038/nmat3500.

(13) Vandewal, K.; Tvingstedt, K.; Gadisa, A.; Inganäs, O.; Manca, J. V. Relating the Open-Circuit Voltage to Interface Molecular Properties of Donor:Acceptor Bulk Heterojunction Solar Cells. *Phys. Rev. B* **2010**, *81* (12), 125204. https://doi.org/10.1103/PhysRevB.81.125204.

(14) Li, P.; Lu, Z.-H. Interface Engineering in Organic Electronics: Energy-Level Alignment and Charge Transport. *Small Sci.* **2021**, *1* (1), 2000015. https://doi.org/10.1002/smsc.202000015.

(15) Burke, T. M.; Sweetnam, S.; Vandewal, K.; McGehee, M. D. Beyond Langevin Recombination: How Equilibrium Between Free Carriers and Charge Transfer States Determines the Open-Circuit Voltage of Organic Solar Cells. *Adv. Energy Mater.* **2015**, *5* (11), 1500123. https://doi.org/10.1002/aenm.201500123.

(16) Vandewal, K.; Tvingstedt, K.; Gadisa, A.; Inganäs, O.; Manca, J. V. On the Origin of the Open-Circuit Voltage of Polymer–Fullerene Solar Cells. *Nat. Mater.* **2009**, *8* (11), 904–909. https://doi.org/10.1038/nmat2548.

(17) Fu, Y.; Lee, T. H.; Chin, Y.-C.; Pacalaj, R. A.; Labanti, C.; Park, S. Y.; Dong, Y.; Cho, H. W.; Kim, J. Y.; Minami, D.; Durrant, J. R.; Kim, J.-S. Molecular Orientation-Dependent Energetic Shifts in Solution-Processed Non-Fullerene Acceptors and Their Impact on Organic Photovoltaic Performance. *Nat. Commun.* **2023**, *14* (1), 1870. https://doi.org/10.1038/s41467-023-37234-0.

(18) Beaupré, S.; Boudreault, P.-L. T.; Leclerc, M. Solar-Energy Production and Energy-Efficient Lighting: Photovoltaic Devices and White-Light-Emitting Diodes Using Poly(2,7-Fluorene), Poly(2,7-Carbazole), and Poly(2,7-Dibenzosilole) Derivatives. *Adv. Mater.* **2010**, *22* (8), E6–E27. https://doi.org/10.1002/adma.200903484.

(19) Sharma, V.; Arora, E. K.; Jaison, M.; Vashist, T.; Jagtap, S.; Adhikari, A.; Kumar, P.; Dash, J. K.; Patel, R. Tuning the Work Function and Properties of the Conducting Polymer PEDOT:PSS for Enhancing Optoelectronic Device Performance of Solar Cells and Organic Light Emitting Diodes. *Polym.-Plast. Technol. Mater.* **2025**, *64* (7), 1019–1045. https://doi.org/10.1080/25740881.2024.2449006.

(20) Guo, Q.; Guo, Q.; Geng, Y.; Tang, A.; Zhang, M.; Du, M.; Sun, X.; Zhou, E. Recent Advances in PM6: Y6-Based Organic Solar Cells. *Mater. Chem. Front.* **2021**, *5* (8), 3257–3280.

(21) Carlotti, B.; Cai, Z.; Kim, H.; Sharapov, V.; Madu, I. K.; Zhao, D.; Chen, W.; Zimmerman, P. M.; Yu, L.; Goodson, T. I. Charge Transfer and Aggregation Effects on the Performance of Planar vs Twisted Nonfullerene Acceptor Isomers for Organic Solar Cells. *Chem. Mater.* **2018**, *30* (13), 4263–4276. https://doi.org/10.1021/acs.chemmater.8b01047.

(22) Sim, M.; Shin, J.; Shim, C.; Kim, M.; Jo, S. B.; Kim, J.-H.; Cho, K. Dependence of Exciton Diffusion Length on Crystalline Order in Conjugated Polymers. *J. Phys. Chem. C* **2014**, *118* (2), 760–766. https://doi.org/10.1021/jp409776s.

(23) Jacobberger, R. M.; Qiu, Y.; Williams, M. L.; Krzyaniak, M. D.; Wasielewski, M. R. Using Molecular Design to Enhance the Coherence Time of Quintet Multiexcitons Generated by Singlet Fission in Single Crystals. *J. Am. Chem. Soc.* **2022**, *144* (5), 2276–2283. https://doi.org/10.1021/jacs.1c12414.

(24) Villabona-Monsalve, J. P.; Tcyrulnikov, N. A.; Lorenzo, E. R.; LaBine, N.; Burdick, R.; Krzyaniak, M. D.; Young, R. M.; Wasielewski, M. R.; Goodson, T. I. Two-Photon Absorption in Electron Donor–Acceptor Dyads and Triads Using Classical and Entangled Photons: Potential Systems for Photon-to-Spin Quantum Transduction. *J. Phys. Chem. C* **2022**, *126* (14), 6334–6343. https://doi.org/10.1021/acs.jpcc.2c00830.

(25) Varnavski, O.; Gunthardt, C.; Rehman, A.; Luker, G. D.; Goodson, T. Quantum Light-Enhanced Two-Photon Imaging of Breast Cancer Cells. *J. Phys. Chem. Lett.* **2022**, *13* (12), 2772–2781. https://doi.org/10.1021/acs.jpclett.2c00695.

(26) Varnavski, O.; Johnson, P.; Liu, T.; Pal, D.; Mashour, G. A.; Goodson, T. Imaging Brain Tissue with Quantum Light at Low Power. *J. Phys. Chem. B* **2024**, *128* (47), 11516–11524. https://doi.org/10.1021/acs.jpcb.4c03225.

(27) Hudson, R. J.; Stuart, A. N.; Huang, D. M.; Kee, T. W. What Next for Singlet Fission in Photovoltaics? The Fate of Triplet and Triplet-Pair Excitons. *J. Phys. Chem. C* **2022**, *126* (12), 5369–5377. https://doi.org/10.1021/acs.jpcc.2c00273.

(28) Baldacchino, A. J.; Collins, M. I.; Nielsen, M. P.; Schmidt, T. W.; McCamey, D. R.; Tayebjee, M. J. Y. Singlet Fission Photovoltaics: Progress and Promising Pathways. *Chem. Phys. Rev.* **2022**, *3* (2), 021304. https://doi.org/10.1063/5.0080250.

(29) Ito, S.; Nagami, T.; Nakano, M. Molecular Design for Efficient Singlet Fission. *J. Photochem. Photobiol. C Photochem. Rev.* **2018**, *34*, 85–120. https://doi.org/10.1016/j.jphotochemrev.2018.01.002.

(30) Smith, M. B.; Michl, J. Singlet Fission. *Chem. Rev.* **2010**, *110* (11), 6891–6936. https://doi.org/10.1021/cr1002613.

(31) Smith, M. B.; Michl, J. Recent Advances in Singlet Fission. *Annu. Rev. Phys. Chem.* **2013**, *64* (Volume 64, 2013), 361–386. https://doi.org/10.1146/annurev-physchem-040412-110130.

(32) Casanova, D. Theoretical Modeling of Singlet Fission. *Chem. Rev.* **2018**, *118* (15), 7164–7207. https://doi.org/10.1021/acs.chemrev.7b00601.

(33) Weiss, L. R.; Bayliss, S. L.; Kraffert, F.; Thorley, K. J.; Anthony, J. E.; Bittl, R.; Friend, R. H.; Rao, A.; Greenham, N. C.; Behrends, J. Strongly Exchange-Coupled Triplet Pairs in an Organic Semiconductor. *Nat. Phys.* **2017**, *13* (2), 176–181. https://doi.org/10.1038/nphys3908.

(34) Weiss, L. R.; Bayliss, S. L.; Kraffert, F.; Thorley, K. J.; Anthony, J. E.; Bittl, R.; Friend, R. H.; Rao, A.; Greenham, N. C.; Behrends, J. Strongly Exchange-Coupled Triplet Pairs in an Organic Semiconductor. *Nat. Phys.* **2017**, *13* (2), 176–181. https://doi.org/10.1038/nphys3908.

(35) Pace, N. A.; Rugg, B. K.; Chang, C. H.; Reid, O. G.; Thorley, K. J.; Parkin, S.; Anthony, J. E.; Johnson, J. C. Conversion between Triplet Pair States Is Controlled by Molecular

Coupling in Pentadithiophene Thin Films. *Chem. Sci.* **2020**, *11* (27), 7226–7238. https://doi.org/10.1039/D0SC02497J.

(36) Monahan, N.; Zhu, X.-Y. Charge Transfer–Mediated Singlet Fission. *Annu. Rev. Phys. Chem.* **2015**, *66* (Volume 66, 2015), 601–618. https://doi.org/10.1146/annurev-physchem-040214-121235.

(37) He, G.; Busby, E.; Appavoo, K.; Wu, Q.; Xia, J.; Campos, L. M.; Sfeir, M. Y. Charge Transfer States Impact the Triplet Pair Dynamics of Singlet Fission Polymers. *J. Chem. Phys.* **2020**, *153* (24), 244902. https://doi.org/10.1063/5.0029858.

(38) Bayliss, S. L.; Weiss, L. R.; Kraffert, F.; Granger, D. B.; Anthony, J. E.; Behrends, J.; Bittl, R. Probing the Wave Function and Dynamics of the Quintet Multiexciton State with Coherent Control in a Singlet Fission Material. *Phys. Rev. X* **2020**, *10* (2), 021070. https://doi.org/10.1103/PhysRevX.10.021070.

(39) Tayebjee, M. J. Y.; Sanders, S. N.; Kumarasamy, E.; Campos, L. M.; Sfeir, M. Y.; McCamey, D. R. Quintet Multiexciton Dynamics in Singlet Fission. *Nat. Phys.* **2017**, *13* (2), 182–188. https://doi.org/10.1038/nphys3909.

(40) Jacobberger, R. M.; Qiu, Y.; Williams, M. L.; Krzyaniak, M. D.; Wasielewski, M. R. Using Molecular Design to Enhance the Coherence Time of Quintet Multiexcitons Generated by Singlet Fission in Single Crystals. *J. Am. Chem. Soc.* **2022**, *144* (5), 2276–2283. https://doi.org/10.1021/jacs.1c12414.

(41) Ricci, F.; Marougail, V.; Varnavski, O.; Wu, Y.; Padgaonkar, S.; Irgen-Gioro, S.; Weiss, E. A.; Goodson, T. I. Enhanced Exciton Quantum Coherence in Single CsPbBr3 Perovskite Quantum Dots Using Femtosecond Two-Photon Near-Field Scanning Optical Microscopy. *ACS Nano* **2021**, *15* (8), 12955–12965. https://doi.org/10.1021/acsnano.1c01615.

(42) Landig, A. J.; Koski, J. V.; Scarlino, P.; Mendes, U. C.; Blais, A.; Reichl, C.; Wegscheider, W.; Wallraff, A.; Ensslin, K.; Ihn, T. Coherent Spin–Photon Coupling Using a Resonant Exchange Qubit. *Nature* **2018**, *560* (7717), 179–184. https://doi.org/10.1038/s41586-018-0365-y.

(43) Peltier, J.-D.; Heinrich, B.; Donnio, B.; Rault-Berthelot, J.; Jacques, E.; Poriel, C. Electron-Deficient Dihydroindaceno-Dithiophene Regioisomers for n-Type Organic Field-Effect Transistors. *ACS Appl. Mater. Interfaces* **2017**, *9* (9), 8219–8232. https://doi.org/10.1021/acsami.6b16333.

(44) Wang, C.; Nishida, J.; Bryce, M. R.; Yamashita, Y. Synthesis, Characterization, and OFET and OLED Properties of π-Extended Ladder-Type Heteroacenes Based on Indolodibenzothiophene. *Bull. Chem. Soc. Jpn.* **2012**, *85* (1), 136–143. https://doi.org/10.1246/bcsj.20110255.

(45) Hüttner, S.; Sommer, M.; Thelakkat, M. N-Type Organic Field Effect Transistors from Perylene Bisimide Block Copolymers and Homopolymers. *Appl. Phys. Lett.* **2008**, *92* (9), 093302. https://doi.org/10.1063/1.2885712.

(46) Wu, J.-S.; Cheng, Y.-J.; Lin, T.-Y.; Chang, C.-Y.; Shih, P.-I.; Hsu, C.-S. Dithienocarbazole-Based Ladder-Type Heptacyclic Arenes with Silicon, Carbon, and Nitrogen Bridges: Synthesis, Molecular Properties, Field-Effect Transistors, and Photovoltaic Applications. *Adv. Funct. Mater.* **2012**, *22* (8), 1711–1722. https://doi.org/10.1002/adfm.201102906.

(47) Thuau, D.; Begley, K.; Dilmurat, R.; Ablat, A.; Wantz, G.; Ayela, C.; Abbas, M.; Thuau, D.; Begley, K.; Dilmurat, R.; Ablat, A.; Wantz, G.; Ayela, C.; Abbas, M. Exploring the Critical Thickness of Organic Semiconductor Layer for Enhanced Piezoresistive Sensitivity in Field-Effect Transistor Sensors. *Materials* **2020**, *13* (7). https://doi.org/10.3390/ma13071583.

(48) Guo, Y.; Yu, G.; Liu, Y. Functional Organic Field-Effect Transistors. *Adv. Mater.* **2010**, *22* (40), 4427–4447. https://doi.org/10.1002/adma.201000740.

(49) Braga, D.; Horowitz, G. High-Performance Organic Field-Effect Transistors. *Adv. Mater.* **2009**, *21* (14–15), 1473–1486. https://doi.org/10.1002/adma.200802733.

(50) Broggi, A.; Tomasi, I.; Bianchi, L.; Marrocchi, A.; Vaccaro, L. Small Molecular Aryl Acetylenes: Chemically Tailoring High-Efficiency Organic Semiconductors for Solar Cells and Field-Effect Transistors. *ChemPlusChem* **2014**, *79* (4), 486–507. https://doi.org/10.1002/cplu.201400001.

(51) Herwig, P. T.; Müllen, K. A Soluble Pentacene Precursor: Synthesis, Solid-State Conversion into Pentacene and Application in a Field-Effect Transistor. *Adv. Mater.* **1999**, *11* (6), 480–483. https://doi.org/10.1002/(SICI)1521-4095(199904)11:6%253C480::AID-ADMA480%253E3.0.CO;2-U.

(52) Tilley, A. J.; Guo, C.; Miltenburg, M. B.; Schon, T. B.; Yan, H.; Li, Y.; Seferos, D. S. Thionation Enhances the Electron Mobility of Perylene Diimide for High Performance N-Channel Organic Field Effect Transistors. *Adv. Funct. Mater.* **2015**, *25* (22), 3321–3329. https://doi.org/10.1002/adfm.201500837.

(53) Cheon, H. J.; An, T. K.; Kim, Y.-H. Diketopyrrolopyrrole (DPP)-Based Polymers and Their Organic Field-Effect Transistor Applications: A Review. *Macromol. Res.* **2022**, *30* (2), 71–84. https://doi.org/10.1007/s13233-022-0015-y.

(54) Xu, Y.; Liu, T.; Liu, K.; Zhao, Y.; Liu, L.; Li, P.; Nie, A.; Liu, L.; Yu, J.; Feng, X.; Zhuge, F.; Li, H.; Wang, X.; Zhai, T. Scalable Integration of Hybrid High-κ Dielectric Materials on Two-Dimensional Semiconductors. *Nat. Mater.* **2023**, *22* (9), 1078–1084. https://doi.org/10.1038/s41563-023-01626-w.

(55) Yu, H.; Chen, Y.; Wei, H.; Gong, J.; Xu, W. High-k Polymeric Gate Insulators for Organic Field-Effect Transistors. *Nanotechnology* **2019**, *30* (20), 202002. https://doi.org/10.1088/1361-6528/ab00a4.

(56) Wang, Y.; Huang, X.; Li, T.; Li, L.; Guo, X.; Jiang, P. Polymer-Based Gate Dielectrics for Organic Field-Effect Transistors. *Chem. Mater.* **2019**, *31* (7), 2212–2240. https://doi.org/10.1021/acs.chemmater.8b03904.

(57) Naderi, P.; Grau, G. Hydrophobic Gate Dielectric Materials for Thin-Film Transistors: Advances, Challenges, and Applications. *ACS Appl. Electron. Mater.* **2025**, *7* (14), 6243–6264. https://doi.org/10.1021/acsaelm.5c00729.

(58) Baeg, K.-J.; Noh, Y.-Y.; Ghim, J.; Lim, B.; Kim, D.-Y. Polarity Effects of Polymer Gate Electrets on Non-Volatile Organic Field-Effect Transistor Memory. *Adv. Funct. Mater.* **2008**, *18* (22), 3678–3685. https://doi.org/10.1002/adfm.200800378.

(59) *Self-assembled monolayer organic field-effect transistors | Nature*. https://www.nature.com/articles/35099520 (accessed 2025-11-28).

(60) Gámez-Valenzuela, S.; Comí, M.; Rodríguez González, S.; Ruiz Delgado, M. C.; Al-Hashimi, M.; Ortiz, R. P. The Fluorination Effect: The Importance of Backbone Planarity in Achieving High Performance Ambipolar Field Effect Transistors. *J. Mater. Chem. C* **2023**, *11* (24), 8027–8036. https://doi.org/10.1039/D2TC05073K.

(61) Yang, S. Y.; Shin, K.; Park, C. E. The Effect of Gate-Dielectric Surface Energy on Pentacene Morphology and Organic Field-Effect Transistor Characteristics. *Adv. Funct. Mater.* **2005**, *15* (11), 1806–1814. https://doi.org/10.1002/adfm.200400486.

(62) McGarry, K. A.; Xie, W.; Sutton, C.; Risko, C.; Wu, Y.; Young, V. G. Jr.; Brédas, J.-L.; Frisbie, C. D.; Douglas, C. J. Rubrene-Based Single-Crystal Organic Semiconductors: Synthesis,

Electronic Structure, and Charge-Transport Properties. *Chem. Mater.* **2013**, *25* (11), 2254–2263. https://doi.org/10.1021/cm400736s.

(63) Xie, W.; Prabhumirashi, P. L.; Nakayama, Y.; McGarry, K. A.; Geier, M. L.; Uragami, Y.; Mase, K.; Douglas, C. J.; Ishii, H.; Hersam, M. C.; Frisbie, C. D. Utilizing Carbon Nanotube Electrodes to Improve Charge Injection and Transport in Bis(Trifluoromethyl)-Dimethyl-Rubrene Ambipolar Single Crystal Transistors. *ACS Nano* **2013**, *7* (11), 10245–10256. https://doi.org/10.1021/nn4045694.

(64) Dheepika, R.; Mohamed Imran, P.; Bhuvanesh, N. S. P.; Nagarajan, S. Solution-Processable Unsymmetrical Triarylamines: Towards High Mobility and ON/OFF Ratio in Bottom-Gated OFETs. *Chem. – Eur. J.* **2019**, *25* (66), 15155–15163. https://doi.org/10.1002/chem.201903450.

(65) Devibala, P.; Balambiga, B.; Mohamed Imran, P.; Bhuvanesh, N. S. P.; Nagarajan, S. Butterfly-Like Triarylamines with High Hole Mobility and On/Off Ratio in Bottom-Gated OFETs. *Chem. – Eur. J.* **2021**, *27* (62), 15375–15381. https://doi.org/10.1002/chem.202102568.

(66) Sakamoto, Y.; Suzuki, T.; Kobayashi, M.; Gao, Y.; Fukai, Y.; Inoue, Y.; Sato, F.; Tokito, S. Perfluoropentacene: High-Performance P−n Junctions and Complementary Circuits with Pentacene. *J. Am. Chem. Soc.* **2004**, *126* (26), 8138–8140. https://doi.org/10.1021/ja0476258.

(67) Hauschild, M.; Chen, L.; Etschel, S. H.; Ferguson, M. J.; Hampel, F.; Halik, M.; Tykwinski, R. R. Anthracene−Pentacene Dyads: Synthesis and OFET Characterization. *ChemPlusChem* **2020**, *85* (5), 921–926. https://doi.org/10.1002/cplu.202000233.

(68) Okamoto, T.; Senatore, M. L.; Ling, M.-M.; Mallik, A. B.; Tang, M. L.; Bao, Z. Synthesis, Characterization, and Field-Effect Transistor Performance of Pentacene Derivatives. *Adv. Mater.* **2007**, *19* (20), 3381–3384. https://doi.org/10.1002/adma.200700298.

(69) Fregoso, G.; Rupasinghe, G. S.; Shahi, M.; Thorley, K.; Parkin, S.; Paterson, A. F.; Anthony, J. Functionalized Anthrathienothiophenes: Synthesis, Properties, and Integration into OFETs. *J. Mater. Chem. C* **2022**, *10* (39), 14439–14443. https://doi.org/10.1039/D2TC02977D.

(70) Liu, Q.; Bottle, S. E.; Sonar, P. Developments of Diketopyrrolopyrrole-Dye-Based Organic Semiconductors for a Wide Range of Applications in Electronics. *Adv. Mater.* **2020**, *32* (4), 1903882. https://doi.org/10.1002/adma.201903882.

(71) Kim, H. S.; Huseynova, G.; Noh, Y.-Y.; Hwang, D.-H. Modulation of Majority Charge Carrier from Hole to Electron by Incorporation of Cyano Groups in Diketopyrrolopyrrole-Based Polymers. *Macromolecules* **2017**, *50* (19), 7550–7558. https://doi.org/10.1021/acs.macromol.7b01524.

(72) Zhou, Y.; Zhang, W.; Yu, G. Recent Structural Evolution of Lactam- and Imide-Functionalized Polymers Applied in Organic Field-Effect Transistors and Organic Solar Cells. *Chem. Sci.* **2021**, *12* (20), 6844–6878. https://doi.org/10.1039/D1SC01711J.

(73) Balambiga, B.; Devibala, P.; Imran, P. M.; Nagarajan, S. Tunable Charge Transport Using Heterocycles-Flanked Alkoxyphenanthrenes for High-Performing OFETs. *ACS Omega* **2024**, *9* (41), 42091–42102. https://doi.org/10.1021/acsomega.4c01166.

(74) Guo, X.; Kim, F. S.; Seger, M. J.; Jenekhe, S. A.; Watson, M. D. Naphthalene Diimide-Based Polymer Semiconductors: Synthesis, Structure–Property Correlations, and n-Channel and Ambipolar Field-Effect Transistors. *Chem. Mater.* **2012**, *24* (8), 1434–1442. https://doi.org/10.1021/cm2034273.

(75) Durban, M. M.; Kazarinoff, P. D.; Luscombe, C. K. Synthesis and Characterization of Thiophene-Containing Naphthalene Diimide n-Type Copolymers for OFET Applications. *Macromolecules* **2010**, *43* (15), 6348–6352. https://doi.org/10.1021/ma100997g.

(76) Cheng, P.; Zhao, X.; Zhan, X. Perylene Diimide-Based Oligomers and Polymers for Organic Optoelectronics. *Acc. Mater. Res.* **2022**, *3* (3), 309–318. https://doi.org/10.1021/accountsmr.1c00191.

(77) Cao, J.; Li, Y.; Wu, T.; Yang, S. Synthesis, Characterization and OFET Performance of A–D–A Semiconducting Small Molecules Functionalized with Perylene Diimide Groups. *J. Mater. Chem. C* **2025**, *13* (22), 11427–11437. https://doi.org/10.1039/D5TC00610D.

(78) Teo, Y. C.; Lai, H. W. H.; Xia, Y. Synthesis of Ladder Polymers: Developments, Challenges, and Opportunities. *Chem. – Eur. J.* **2017**, *23* (57), 14101–14112. https://doi.org/10.1002/chem.201702219.

(79) Lee, J. Recent Progress in Synthesis of Conjugated Ladder Polymers. *Asian J. Org. Chem.* **2023**, *12* (5), e202300104. https://doi.org/10.1002/ajoc.202300104.

(80) Yang, J. S.-J.; Fang, L. Conjugated Ladder Polymers: Advances from Syntheses to Applications. *Chem* **2024**, *0* (0). https://doi.org/10.1016/j.chempr.2024.04.002.

(81) Prosa, M.; Benvenuti, E.; Kallweit, D.; Pellacani, P.; Toerker, M.; Bolognesi, M.; Lopez-Sanchez, L.; Ragona, V.; Marabelli, F.; Toffanin, S. Organic Light-Emitting Transistors in a Smart-Integrated System for Plasmonic-Based Sensing. *Adv. Funct. Mater.* **2021**, *31* (50), 2104927. https://doi.org/10.1002/adfm.202104927.

(82) Zhang, Q.; Jin, T.; Ye, X.; Geng, D.; Chen, W.; Hu, W. Organic Field Effect Transistor-Based Photonic Synapses: Materials, Devices, and Applications. *Adv. Funct. Mater.* **2021**, *31* (49), 2106151. https://doi.org/10.1002/adfm.202106151.

(83) Di, C.; Zhang, F.; Zhu, D. Multi-Functional Integration of Organic Field-Effect Transistors (OFETs): Advances and Perspectives. *Adv. Mater.* **2013**, *25* (3), 313–330. https://doi.org/10.1002/adma.201201502.

(84) Geffroy, B.; le Roy, P.; Prat, C. Organic Light-Emitting Diode (OLED) Technology: Materials, Devices and Display Technologies. *Polym. Int.* **2006**, *55* (6), 572–582. https://doi.org/10.1002/pi.1974.

(85) Bauri, J.; Choudhary, R. B.; Mandal, G. Recent Advances in Efficient Emissive Materials-Based OLED Applications: A Review. *J. Mater. Sci.* **2021**, *56* (34), 18837–18866. https://doi.org/10.1007/s10853-021-06503-y.

(86) Guo, J.; Zhao, Z.; Tang, B. Z. Purely Organic Materials with Aggregation-Induced Delayed Fluorescence for Efficient Nondoped OLEDs. *Adv. Opt. Mater.* **2018**, *6* (15), 1800264. https://doi.org/10.1002/adom.201800264.

(87) Salehi, A.; Fu, X.; Shin, D.-H.; So, F. Recent Advances in OLED Optical Design. *Adv. Funct. Mater.* **2019**, *29* (15), 1808803. https://doi.org/10.1002/adfm.201808803.

(88) Kulkarni, A. P.; Tonzola, C. J.; Babel, A.; Jenekhe, S. A. Electron Transport Materials for Organic Light-Emitting Diodes. *Chem. Mater.* **2004**, *16* (23), 4556–4573. https://doi.org/10.1021/cm0494731.

(89) Chen, X.-K.; Kim, D.; Brédas, J.-L. Thermally Activated Delayed Fluorescence (TADF) Path toward Efficient Electroluminescence in Purely Organic Materials: Molecular Level Insight. *Acc. Chem. Res.* **2018**, *51* (9), 2215–2224. https://doi.org/10.1021/acs.accounts.8b00174.

(90) Dos Santos, J. M.; Hall, D.; Basumatary, B.; Bryden, M.; Chen, D.; Choudhary, P.; Comerford, T.; Crovini, E.; Danos, A.; De, J.; Diesing, S.; Fatahi, M.; Griffin, M.; Gupta, A. K.; Hafeez, H.; Hämmerling, L.; Hanover, E.; Haug, J.; Heil, T.; Karthik, D.; Kumar, S.; Lee,

O.; Li, H.; Lucas, F.; Mackenzie, C. F. R.; Mariko, A.; Matulaitis, T.; Millward, F.; Olivier, Y.; Qi, Q.; Samuel, I. D. W.; Sharma, N.; Si, C.; Spierling, L.; Sudhakar, P.; Sun, D.; Tankelevičiūtė, E.; Duarte Tonet, M.; Wang, J.; Wang, T.; Wu, S.; Xu, Y.; Zhang, L.; Zysman-Colman, E. The Golden Age of Thermally Activated Delayed Fluorescence Materials: Design and Exploitation. *Chem. Rev.* **2024**, *124* (24), 13736–14110. https://doi.org/10.1021/acs.chemrev.3c00755.

(91) Zhao, Z.; Yan, S.; Ren, Z. Regulating the Nature of Triplet Excited States of Thermally Activated Delayed Fluorescence Emitters. *Acc. Chem. Res.* **2023**, *56* (14), 1942–1952. https://doi.org/10.1021/acs.accounts.3c00175.

(92) Tao, Y.; Yuan, K.; Chen, T.; Xu, P.; Li, H.; Chen, R.; Zheng, C.; Zhang, L.; Huang, W. Thermally Activated Delayed Fluorescence Materials Towards the Breakthrough of Organoelectronics. *Adv. Mater.* **2014**, *26* (47), 7931–7958. https://doi.org/10.1002/adma.201402532.

(93) Kim, K.-H.; Kim, J.-J. Origin and Control of Orientation of Phosphorescent and TADF Dyes for High-Efficiency OLEDs. *Adv. Mater.* **2018**, *30* (42), 1705600. https://doi.org/10.1002/adma.201705600.

(94) Aydemir, M.; Xu, S.; Chen, C.; Bryce, M. R.; Chi, Z.; Monkman, A. P. Photophysics of an Asymmetric Donor–Acceptor–Donor′ TADF Molecule and Reinterpretation of Aggregation-Induced TADF Emission in These Materials. *J. Phys. Chem. C* **2017**, *121* (33), 17764–17772. https://doi.org/10.1021/acs.jpcc.7b06299.

(95) Mageswari, G. V.; Chitose, Y.; Tsuchiya, Y.; Lin, J.-H.; Adachi, C. Rational Molecular Design for Balanced Locally Excited and Charge- Transfer Nature for Two-Photon Absorption

Phenomenon and Highly Efficient TADF-Based OLEDs. *Angew. Chem.* **2025**, *137* (8), e202420417. https://doi.org/10.1002/ange.202420417.

(96) Moon, J.; Han, S.; Lee, J. Y. Hybrid Multi-Resonance Thermally Activated Delayed Fluorescent Emitters with High Efficiency and High Color Purity. *Adv. Opt. Mater.* **2025**, *13* (3), 2402214. https://doi.org/10.1002/adom.202402214.

(97) Wu, S.; Zhang, L.; Wang, J.; Kumar Gupta, A.; Samuel, I. D. W.; Zysman-Colman, E. Merging Boron and Carbonyl Based MR-TADF Emitter Designs to Achieve High Performance Pure Blue OLEDs. *Angew. Chem.* **2023**, *135* (28), e202305182. https://doi.org/10.1002/ange.202305182.

(98) Cheon, H.-J.; Woo, S.-J.; Baek, S.-H.; Lee, J.-H.; Kim, Y.-H. Dense Local Triplet States and Steric Shielding of a Multi-Resonance TADF Emitter Enable High-Performance Deep-Blue OLEDs. *Adv. Mater.* **2022**, *34* (50), 2207416. https://doi.org/10.1002/adma.202207416.

(99) Wu, X.; Ni, S.; Wang, C.-H.; Zhu, W.; Chou, P.-T. Comprehensive Review on the Structural Diversity and Versatility of Multi-Resonance Fluorescence Emitters: Advance, Challenges, and Prospects toward OLEDs. *Chem. Rev.* **2025**, *125* (14), 6685–6752. https://doi.org/10.1021/acs.chemrev.5c00021.

(100) Madayanad Suresh, S.; Hall, D.; Beljonne, D.; Olivier, Y.; Zysman-Colman, E. Multiresonant Thermally Activated Delayed Fluorescence Emitters Based on Heteroatom-Doped Nanographenes: Recent Advances and Prospects for Organic Light-Emitting Diodes. *Adv. Funct. Mater.* **2020**, *30* (33), 1908677. https://doi.org/10.1002/adfm.201908677.

(101) Lin, S.; Pei, Z.; Zhang, B.; Ma, H.; Liang, W. Vibronic Coupling Effect on the Vibrationally Resolved Electronic Spectra and Intersystem Crossing Rates of a TADF Emitter: 7-PhQAD. *J. Phys. Chem. A* **2022**, *126* (2), 239–248. https://doi.org/10.1021/acs.jpca.1c08456.

(102) Franca, L. G.; Long, Y.; Li, C.; Danos, A.; Monkman, A. The Critical Role of Nπ* States in the Photophysics and Thermally Activated Delayed Fluorescence of Spiro Acridine-Anthracenone. *J. Phys. Chem. Lett.* **2021**, *12* (5), 1490–1500. https://doi.org/10.1021/acs.jpclett.0c03314.

(103) Huang, R.; Avó, J.; Northey, T.; Chaning-Pearce, E.; Santos, P. L. dos; Ward, J. S.; Data, P.; Etherington, M. K.; Fox, M. A.; Penfold, T. J.; Berberan-Santos, M. N.; Lima, J. C.; Bryce, M. R.; Dias, F. B. The Contributions of Molecular Vibrations and Higher Triplet Levels to the Intersystem Crossing Mechanism in Metal-Free Organic Emitters. *J. Mater. Chem. C* **2017**, *5* (25), 6269–6280. https://doi.org/10.1039/C7TC01958K.

(104) Senge, M. O.; Fazekas, M.; Notaras, E. G. A.; Blau, W. J.; Zawadzka, M.; Locos, O. B.; Ni Mhuircheartaigh, E. M. Nonlinear Optical Properties of Porphyrins. *Adv. Mater.* **2007**, *19* (19), 2737–2774. https://doi.org/10.1002/adma.200601850.

(105) Delaire, J. A.; Nakatani, K. Linear and Nonlinear Optical Properties of Photochromic Molecules and Materials. *Chem. Rev.* **2000**, *100* (5), 1817–1846. https://doi.org/10.1021/cr980078m.

(106) Bella, S. D. Second-Order Nonlinear Optical Properties of Transition Metal Complexes. *Chem. Soc. Rev.* **2001**, *30* (6), 355–366. https://doi.org/10.1039/B100820J.

(107) Varnavski, O.; Giri, S. K.; Chiang, T.-M.; Zeman, C. J.; Schatz, G. C.; Goodson, T. Colors of Entangled Two-Photon Absorption. *Proc. Natl. Acad. Sci.* **2023**, *120* (35), e2307719120. https://doi.org/10.1073/pnas.2307719120.

(108) Guzman, A. R.; Harpham, M. R.; Süzer, Ö.; Haley, M. M.; Goodson, T. G. I. Spatial Control of Entangled Two-Photon Absorption with Organic Chromophores. *J. Am. Chem. Soc.* **2010**, *132* (23), 7840–7841. https://doi.org/10.1021/ja1016816.

(109) Tabakaev, D.; Montagnese, M.; Haack, G.; Bonacina, L.; Wolf, J.-P.; Zbinden, H.; Thew, R. T. Energy-Time-Entangled Two-Photon Molecular Absorption. *Phys. Rev. A* **2021**, *103* (3), 033701. https://doi.org/10.1103/PhysRevA.103.033701.

(110) Rumi, M.; Perry, J. W. Two-Photon Absorption: An Overview of Measurements and Principles. *Adv. Opt. Photonics* **2010**, *2* (4), 451–518. https://doi.org/10.1364/AOP.2.000451.

(111) Pawlicki, M.; Collins, H. A.; Denning, R. G.; Anderson, H. L. Two-Photon Absorption and the Design of Two-Photon Dyes. *Angew. Chem. Int. Ed.* **2009**, *48* (18), 3244–3266. https://doi.org/10.1002/anie.200805257.

(112) Marder, S. R.; Gorman, C. B.; Tiemann, B. G.; Perry, J. W.; Bourhill, G.; Mansour, K. Relation Between Bond-Length Alternation and Second Electronic Hyperpolarizability of Conjugated Organic Molecules. *Science* **1993**, *261* (5118), 186–189. https://doi.org/10.1126/science.261.5118.186.

(113) Geskin, V. M.; Lambert, C.; Brédas, J.-L. Origin of High Second- and Third-Order Nonlinear Optical Response in Ammonio/Borato Diphenylpolyene Zwitterions: The Remarkable Role of Polarized Aromatic Groups. *J. Am. Chem. Soc.* **2003**, *125* (50), 15651–15658. https://doi.org/10.1021/ja035862p.

(114) Meyers, F.; Marder, S. R.; Pierce, B. M.; Bredas, J. L. Electric Field Modulated Nonlinear Optical Properties of Donor-Acceptor Polyenes: Sum-Over-States Investigation of the Relationship between Molecular Polarizabilities (.Alpha., .Beta., and .Gamma.) and Bond Length Alternation. *J. Am. Chem. Soc.* **1994**, *116* (23), 10703–10714. https://doi.org/10.1021/ja00102a040.

(115) Reinhardt, B. A.; Brott, L. L.; Clarson, S. J.; Dillard, A. G.; Bhatt, J. C.; Kannan, R.; Yuan, L.; He, G. S.; Prasad, P. N. Highly Active Two-Photon Dyes: Design, Synthesis, and

Characterization toward Application. *Chem. Mater.* **1998**, *10* (7), 1863–1874. https://doi.org/10.1021/cm980036e.

(116) Rani, C.; Goodson, T. I. Enhanced Exciton Coherence Time and Correlation with Probability of Absorption of Classical and Entangled Light in Quantum-Confined Systems. *J. Phys. Chem. C* **2024**. https://doi.org/10.1021/acs.jpcc.4c01747.

(117) Kang, G.; Nasiri Avanaki, K.; Mosquera, M. A.; Burdick, R. K.; Villabona-Monsalve, J. P.; Goodson, T. I.; Schatz, G. C. Efficient Modeling of Organic Chromophores for Entangled Two-Photon Absorption. *J. Am. Chem. Soc.* **2020**, *142* (23), 10446–10458. https://doi.org/10.1021/jacs.0c02808.

(118) Moura, G. L. C.; Simas, A. M. Two-Photon Absorption Cross-Sections from Electronic Structure Methods: Mesoionic Compounds. *Chem. Mater.* **2008**, *20* (12), 4142–4155. https://doi.org/10.1021/cm070369o.

(119) Wang, W.; Mao, Y.; Yang, Z.; Chen, M. Theoretical Study on Photoinduced Charge Transfer in One-Photon and Two-Photon Absorption of Branching Oligofluorenes. *Spectrochim. Acta. A. Mol. Biomol. Spectrosc.* **2024**, *309*, 123826. https://doi.org/10.1016/j.saa.2023.123826.

(120) He, G. S.; Xu, G. C.; Prasad, P. N.; Reinhardt, B. A.; Bhatt, J. C.; Dillard, A. G. Two-Photon Absorption and Optical-Limiting Properties of Novel Organic Compounds. *Opt. Lett.* **1995**, *20* (5), 435–437. https://doi.org/10.1364/OL.20.000435.

(121) Cai, Z.; Vázquez, R. J.; Zhao, D.; Li, L.; Lo, W.; Zhang, N.; Wu, Q.; Keller, B.; Eshun, A.; Abeyasinghe, N.; Banaszak-Holl, H.; Goodson, T. I.; Yu, L. Two Photon Absorption Study of Low-Bandgap, Fully Conjugated Perylene Diimide-Thienoacene-Perylene Diimide Ladder-

Type Molecules. *Chem. Mater.* **2017**, *29* (16), 6726–6732. https://doi.org/10.1021/acs.chemmater.7b01512.

(122) Pawlicki, M.; Collins, H. A.; Denning, R. G.; Anderson, H. L. Two-Photon Absorption and the Design of Two-Photon Dyes. *Angew. Chem. Int. Ed.* **2009**, *48* (18), 3244–3266. https://doi.org/10.1002/anie.200805257.

(123) Villabona-Monsalve, J. P.; Varnavski, O.; Palfey, B. A.; Goodson, T. I. Two-Photon Excitation of Flavins and Flavoproteins with Classical and Quantum Light. *J. Am. Chem. Soc.* **2018**, *140* (44), 14562–14566. https://doi.org/10.1021/jacs.8b08515.

(124) Villabona-Monsalve, J. P.; Tcyrulnikov, N. A.; Lorenzo, E. R.; LaBine, N.; Burdick, R.; Krzyaniak, M. D.; Young, R. M.; Wasielewski, M. R.; Goodson, T. Two-Photon Absorption in Electron Donor–Acceptor Dyads and Triads Using Classical and Entangled Photons: Potential Systems for Photon-to-Spin Quantum Transduction. *J. Phys. Chem. C* **2022**, *126* (14), 6334–6343. https://doi.org/10.1021/acs.jpcc.2c00830.

(125) Abe, S. Two-Photon Probe of Forbidden Exciton States in Symmetric Aggregates of Asymmetric Molecules. *Chem. Phys.* **2001**, *264* (3), 355–363. https://doi.org/10.1016/S0301-0104(01)00258-0.

(126) Gallavardin, T.; Armagnat, C.; Maury, O.; L. Baldeck, P.; Lindgren, M.; Monnereau, C.; Andraud, C. An Improved Singlet Oxygen Sensitizer with Two- Photon Absorption and Emission in the Biological Transparency Window as a Result of Ground State Symmetry-Breaking. *Chem. Commun.* **2012**, *48* (11), 1689–1691. https://doi.org/10.1039/C2CC15904J.

(127) Li, H.; Piryatinski, A.; Srimath Kandada, A. R.; Silva, C.; Bittner, E. R. Photon Entanglement Entropy as a Probe of Many-Body Correlations and Fluctuations. *J. Chem. Phys.* **2019**, *150* (18), 184106. https://doi.org/10.1063/1.5083613.

(128) Roslyak, O.; Marx, C. A.; Mukamel, S. Nonlinear Spectroscopy with Entangled Photons: Manipulating Quantum Pathways of Matter. *Phys. Rev. A* **2009**, *79* (3), 033832. https://doi.org/10.1103/PhysRevA.79.033832.

(129) Zhong, C.; Han, X.; Jiang, L. Quantum Transduction with Microwave and Optical Entanglement. arXiv February 9, 2022. https://doi.org/10.48550/arXiv.2202.04601.

(130) Lauk, N.; Sinclair, N.; Barzanjeh, S.; Covey, J. P.; Saffman, M.; Spiropulu, M.; Simon, C. Perspectives on Quantum Transduction. *Quantum Sci. Technol.* **2020**, *5* (2), 020501. https://doi.org/10.1088/2058-9565/ab788a.

(131) Schlawin, F.; Dorfman, K. E.; Mukamel, S. Entangled Two-Photon Absorption Spectroscopy. *Acc. Chem. Res.* **2018**, *51* (9), 2207–2214. https://doi.org/10.1021/acs.accounts.8b00173.

(132) Villabona-Monsalve, J. P.; Burdick, R. K.; Goodson, T. I. Measurements of Entangled Two-Photon Absorption in Organic Molecules with CW-Pumped Type-I Spontaneous Parametric Down-Conversion. *J. Phys. Chem. C* **2020**, *124* (44), 24526–24532. https://doi.org/10.1021/acs.jpcc.0c08678.

(133) Burdick, R. K.; Varnavski, O.; Molina, A.; Upton, L.; Zimmerman, P.; Goodson, T. I. Predicting and Controlling Entangled Two-Photon Absorption in Diatomic Molecules. *J. Phys. Chem. A* **2018**, *122* (41), 8198–8212. https://doi.org/10.1021/acs.jpca.8b07466.

(134) Raymer, M. G.; Landes, T.; Marcus, A. H. Entangled Two-Photon Absorption by Atoms and Molecules: A Quantum Optics Tutorial. *J. Chem. Phys.* **2021**, *155* (8), 081501. https://doi.org/10.1063/5.0049338.

(135) Eshun, A.; Varnavski, O.; Villabona-Monsalve, J. P.; Burdick, R. K.; Goodson, T. I. Entangled Photon Spectroscopy. *Acc. Chem. Res.* **2022**, *55* (7), 991–1003. https://doi.org/10.1021/acs.accounts.1c00687.

(136) Sandoval, J. S.; Haley, M. M.; Goodson, T. I. Nonlinear Optical Properties of Bis(Dehydrobenzoannuleno)Benzenes: An Experimental and Computational Approach. *J. Phys. Chem. A* **2025**, *129* (5), 1240–1251. https://doi.org/10.1021/acs.jpca.4c06285.

(137) Tabakaev, D.; Djorović, A.; La Volpe, L.; Gaulier, G.; Ghosh, S.; Bonacina, L.; Wolf, J.-P.; Zbinden, H.; Thew, R. T. Spatial Properties of Entangled Two-Photon Absorption. *Phys. Rev. Lett.* **2022**, *129* (18), 183601. https://doi.org/10.1103/PhysRevLett.129.183601.

(138) Burdick, R. K.; Schatz, G. C.; Goodson, T. Enhancing Entangled Two-Photon Absorption for Picosecond Quantum Spectroscopy. *J. Am. Chem. Soc.* **2021**, *143* (41), 16930–16934. https://doi.org/10.1021/jacs.1c09728.

(139) Lee, Y.-M.; Nam, W.; Fukuzumi, S. Redox Catalysis via Photoinduced Electron Transfer. *Chem. Sci.* **2023**, *14* (16), 4205–4218. https://doi.org/10.1039/D2SC07101K.

(140) Dadashi-Silab, S.; Doran, S.; Yagci, Y. Photoinduced Electron Transfer Reactions for Macromolecular Syntheses. *Chem. Rev.* **2016**, *116* (17), 10212–10275. https://doi.org/10.1021/acs.chemrev.5b00586.

(141) Romero, N. A.; Nicewicz, D. A. Organic Photoredox Catalysis. *Chem. Rev.* **2016**, *116* (17), 10075–10166. https://doi.org/10.1021/acs.chemrev.6b00057.

(142) MacKenzie, I. A.; Wang, L.; Onuska, N. P. R.; Williams, O. F.; Begam, K.; Moran, A. M.; Dunietz, B. D.; Nicewicz, D. A. Discovery and Characterization of an Acridine Radical Photoreductant. *Nature* **2020**, *580* (7801), 76–80. https://doi.org/10.1038/s41586-020-2131-1.

Chapter Two

Methodology and Instrumentation

2.1. Overview of Experimental Method and Techniques

Because the materials investigated in this dissertation span ladder-type oligomers, molecular chromophores, and photocatalytic systems, each exhibiting distinct absorption cross-sections, excited-state lifetimes, and nonlinear responses, the experimental methods were carefully selected and calibrated to yield quantitative, reproducible insight across diverse systems. Steady-state absorption and emission measurements provide the baseline optical signatures required to determine appropriate excitation wavelengths, assess sample purity, and identify reference standards for fluorescence quantum yield and lifetime analysis. For all solution-phase studies, samples were freshly prepared, optically matched, and checked for photostability by comparing pre- and post-measurement absorption spectra. When triplet-state dynamics or electron-transfer intermediates were of interest, measurements were performed under both ambient and oxygen-free conditions, with oxygen exclusion achieved by extended nitrogen purging.

Time-resolved fluorescence methods, including ultrafast up-conversion and time-correlated single-photon counting (TCSPC) were used to quantify radiative and nonradiative decay pathways, resolve prompt versus delayed fluorescence contributions, and extract kinetic signatures associated with intersystem crossing, reverse intersystem crossing, and charge recombination. Nanosecond transient absorption spectroscopy provided complementary access to long-lived triplet populations, radical ions, excimer states, and charge-separated intermediates, enabling mechanistic assignment of processes inaccessible through fluorescence alone.

Nonlinear optical methods played a central role in this dissertation. Classical two-photon absorption (TPA) measurements were employed to quantify multi-photon cross-sections, evaluate charge-transfer character, and probe electronic delocalization in conjugated ladder systems. Entangled two-photon absorption (ETPA), leveraging photon pairs generated through spontaneous parametric down-conversion, provided a uniquely sensitive probe of excited-state symmetry, coherence, and transition pathways under ultralow photon flux offering mechanistic information inaccessible to classical excitation. Finally, near-field optical techniques enabled nanoscale mapping of coherent excitations and local electronic structure, directly linking spectroscopic observables to structural inhomogeneity and molecular packing.

Collectively, these experimental tools allow the probing of excited-state dynamics with high temporal, spectral, and spatial precision. The methods described in this chapter establish the context within which the subsequent mechanistic studies of optoelectronic, quantum, and photocatalytic systems were conducted, forming the empirical foundation of the dissertation.

2.2. Steady State Absorption

Steady-state absorption spectroscopy is the most fundamental optical measurement used to establish how a material interacts with incident electromagnetic radiation. When a broadband light source passes through a sample, specific wavelengths are attenuated according to the energies required to promote electrons from the ground electronic state to higher-lying excited states. The recorded absorption spectrum therefore represents the differential transmission of light as a function of wavelength and provides a direct measure of the allowed electronic transitions of the system.

The quantitative relationship between the incident light intensity and the transmitted intensity is described by the Beer-Lambert law, which formalizes absorption in terms of an exponential loss of radiant power as light propagates through an absorbing medium. In its logarithmic form, the absorbance A is given by

$$A = -\log T = \log\left(\frac{I_0}{I}\right) = \varepsilon c\, l \qquad \text{(Equation 2.1)}$$

where $T = I/I_0$ is the transmittance, I_0 is the intensity of the incident beam, I is the intensity after passage through the sample, c is the concentration of the absorbing species, l is the optical path length, and ε is the molar absorption coefficient. The quantity ε carries the physical meaning of how strongly the material absorbs light at a particular wavelength and is determined by both electronic structure and transition probability. Under conditions where scattering and reflection are negligible or properly corrected by baseline measurements, the Beer-Lambert relation provides a linear dependence between absorbance and concentration, enabling quantitative comparisons across samples and solvents. The resulting absorption spectrum is plotted with wavelength (or photon energy) on the x-axis and absorbance (A) on the y-axis, where absorbance quantifies the logarithmic loss of intensity relative to the incident beam.

All steady state absorption experiments in this thesis was done using a Cary 60 UV-Visible spectrometer equipped spectrally stable light source such as the xenon directed through a 1 cm quartz cuvette containing the sample solution (**Figure 2.1**). A reference measurement of the neat solvent is first collected to remove contributions from cell windows and solvent absorption. The sample spectrum is then acquired by recording the transmitted intensity across the instrument's detection range, typically 190 -1100 nm, yielding the wavelength-dependent absorbance. Care is taken to ensure that absorbance remains within the linear response range of the detector and that

samples do not undergo photodegradation; this is verified by re-measuring the spectrum after irradiation and preparing fresh solutions when necessary.

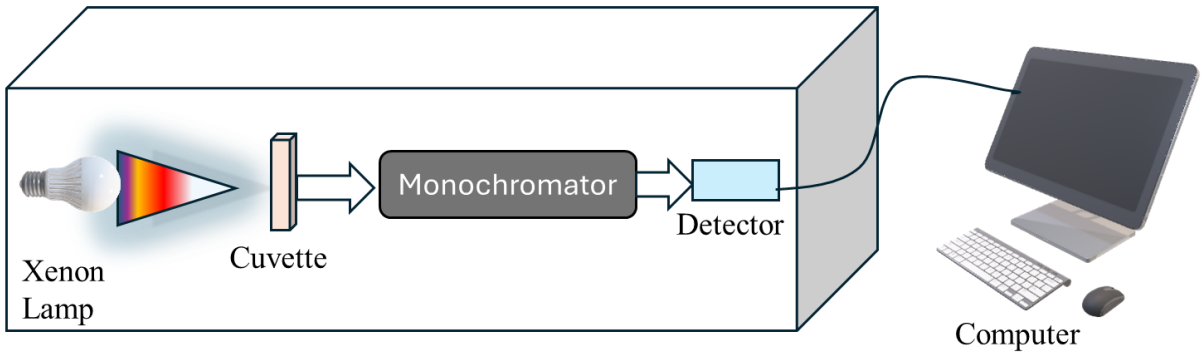


Figure 2.1: Schematic diagram of UV-Vis Spectrometer

Steady-state emission spectroscopy provides a quantitative description of the light a molecule emits after being promoted to an electronically excited state. Whereas steady-state absorption characterizes how a material interacts with incident photons, steady-state emission captures the radiative relaxation pathway specifically the photons emitted as the excited electronic population returns to the ground state.

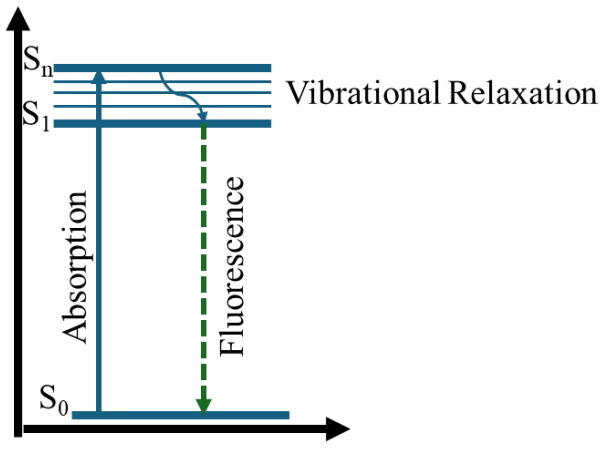


Figure 2.2: Fundamental Processes Involved in Fluorescence (Emission)

In a typical experiment, the sample is excited at a fixed wavelength selected from its absorption spectrum. Once excited, the molecule rapidly undergoes vibrational relaxation and internal conversion, ultimately populating the lowest excited singlet state, S_1. Radiative relaxation from S_1 to the ground state, S_0, produces fluorescence, which is collected as a function of emission wavelength (**Figure 2.2**). The resulting plot of the steady-state emission spectrum is displayed with emission intensity on the y-axis and emission wavelength (or photon energy) on the x-axis.

A defining feature of steady-state emission is the Stokes shift, the energy difference between the maxima of the absorption and emission spectra. Because vibrational relaxation precedes fluorescence, emission typically occurs at lower energy (longer wavelength) than absorption. The Stokes shift can be expressed as:

$$\Delta\lambda = \lambda_{\text{em,max}} - \lambda_{\text{abs,max}} \qquad \text{(Equation 2.2)}$$

where $\lambda_{\text{em, max}}$ is the wavelength of maximum fluorescence intensity and $\lambda_{\text{abs,max}}$ is the wavelength of peak absorption. The magnitude of the Stokes shift provides insight into the degree of structural relaxation and solvation dynamics in the excited state, and helps distinguish intrinsic molecular emission from scattered excitation light.

Steady-state emission measurements are performed using a Horiba Scientific_PTI Quantamaster Series fluorimeter equipped with an excitation source, an excitation monochromator, sample chamber, emission monochromator, and detector (**Figure 2.3**). The sample is typically held in a 1 cm quartz cuvette mounted at 90° relative to the excitation beam. This geometry minimizes collection of the transmitted excitation light and maximizes the detection of fluorescence emitted isotropically from the sample. The emission monochromator then isolates

specific wavelengths of the emitted light, which are recorded by a photomultiplier tube or photodiode array before being transmitted to the instrument's acquisition software.

Accurate fluorescence measurements require careful optical preparation. Samples are prepared at sufficiently low concentration to maintain absorbance values (optical density) below approximately 0.1 at the excitation wavelength, preventing self-absorption, re-absorption, and inner-filter effects that distort spectrum shape and intensity. The instrument's background signal arising from solvent scattering or cuvette fluorescence is measured separately and subtracted from the sample spectrum to ensure that only true molecular emission is captured.

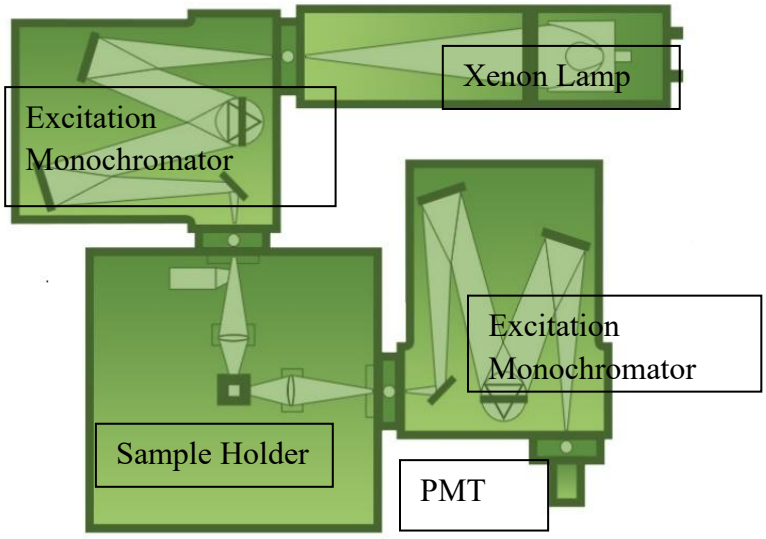


Figure 2.3: Horiba Scientific_PTI Quantamaster Series

The fluorescence quantum yield (Φ) represents the fraction of absorbed photons that are re-emitted as fluorescence, and thus serves as a fundamental descriptor of radiative efficiency. Because absolute quantum yield measurements require integrating spheres and calibrated detectors, a more practical and widely adopted approach for solution-phase studies is the comparative or relative method. In this method, the emission response of an unknown sample is

evaluated against a reference compound whose quantum yield has been rigorously established in the literature.

The comparative method relies on selecting a standard whose absorption and emission profiles overlap those of the sample, ensuring similar excitation conditions and detector response. Common reference emitters include coumarin and rhodamine derivatives due to their well-characterized photophysical behavior and high photostability. Both sample and standard are prepared at low absorbance values (typically <0.1 at the excitation wavelength) to avoid inner-filter effects and ensure linearity between absorbed photons and emitted intensity. For each solution, a series of dilutions is prepared and the integrated fluorescence intensity is plotted against the corresponding absorbance at the excitation wavelength. The slope of this linear fit reflects the fluorescence output per absorbed photon under the given optical conditions. The quantum yield of the unknown sample, Φ_s, is then determined using the relation:

$$\Phi_s = \Phi_{\text{std}}\left(\frac{\text{Grad}_s}{\text{Grad}_{\text{std}}}\right)\left(\frac{\eta_s^2}{\eta_{\text{std}}^2}\right) \qquad \text{(Equation 2.3)}$$

where: Φ_s is the sample quantum yield, Φ_{std} is the known quantum yield of the standard; Grad_s is the slope obtained from plotting the fluorescence area versus the optical density of the sample's absorption; Grad_{std} is the slope obtained from plotting the fluorescence area versus the optical density of the standard's absorption; η_s^2 is the refractive index of the solvent used for the sample; η_{std}^2 is the refractive index of the solvent used for the standard; the refractive index correction accounts for differences in how each solvent influences the emission collection efficiency based on its optical density. When identical solvents are used for both sample and standard, this term simplifies to unity.[1]

2.3. Classical Two-Photon Absorption

The efficiency with which a molecular system undergoes two-photon absorption is quantified by its two-photon absorption cross-section, δ_r, which measures the probability of simultaneous absorption of two photons within an optical field. The δ_r is measured experimentally using the two-photon excited fluorescence (TPEF) technique.[2–4]

Fluorescence generated from two-photon absorption is collected orthogonally to the excitation beam to avoid scattered fundamental light and directed to a photomultiplier tube (PMT). Because two-photon absorption depends on the square of the photon flux, the detected fluorescence intensity grows quadratically with excitation power, allowing σ to be obtained by comparison with a reference chromophore of known cross-section.

The detected fluorescence signal $F(t)$under two-photon excitation can be expressed as:

$$F(t) = \frac{1}{2}\,\phi\,\sigma\,[c]\,\eta\,\frac{g_p}{\pi\nu\lambda\tau f}\,\langle P(t)\rangle^2 \qquad \text{(Equation 2.4)}$$

Where:

ϕ is the fluorescence quantum yield of the material; σ is the two−photon absorption cross−section of the sample; $[c]$ is the concentration; η is the refractive index of the solvent; g_p is the shape factor of the pulsed laser, which is 0.66 for a Gaussian shape; ν is the frequency of the laser; λ is the excitation wavelength; τ is the pulsed duration; f is the collection efficiency and $P(t)$ is the input power intensity;

Because the instrument-dependent parameters $(g_p, \nu, \lambda, \tau, f)$are constant for a given experiment, Eq. (2.4) can be rearranged in logarithmic form:

$$\log F(t) = 2\log\langle P(t)\rangle + \log\left(\frac{1}{2}\phi\sigma[c]\eta\frac{g_p}{\pi\nu\lambda\tau_f}\right) \qquad \text{(Equation 2.5)}$$

This relation predicts a slope of two when plotting $\log F(t)$ versus $\log P(t)$ for both sample and standard, confirming the quadratic power dependence characteristic of two-photon absorption.

If we denote the constant term for the sample and standard as b_{sample} and b_{std}, respectively, then:

$$\log F(t)_{\text{sample}} - b_{\text{sample}} = \log F(t)_{\text{std}} - b_{\text{std}} \qquad \text{(Equation 2.6)}$$

$$\log F(t)_{\text{sample}} - \log F(t)_{\text{std}} = b_{\text{sample}} - b_{\text{std}} \qquad \text{(Equation 2.7)}$$

Through comparison with a reference molecule of known σ, the sample's cross-section is determined using:

$$\delta_{sample} = 10^{(b_{\text{sample}} - b_{\text{std}})}\,\sigma_{\text{std}}\,\frac{\phi_{\text{std}}\,[c]_{\text{std}}\,\eta_{\text{std}}}{\phi_{\text{sample}}\,[c]_{\text{sample}}\,\eta_{\text{sample}}} \qquad \text{(Equation 2.8)}$$

This comparative approach eliminates the need to determine instrument constants explicitly and yields reliable two-photon cross-sections provided that sample and standard are measured under identical optical and geometric conditions.

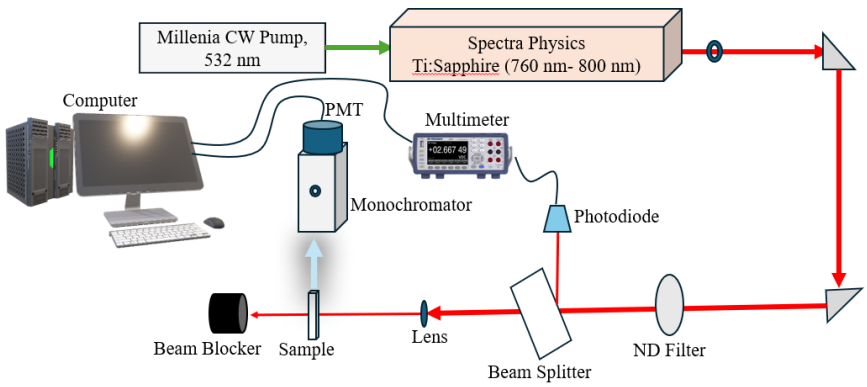


Figure 2.4: TPEF experimental set-up

The two-photon excited fluorescence measurements in this work were performed using a femtosecond Ti:Sapphire laser system capable of delivering high-intensity, ultrashort pulses required to drive nonlinear optical processes. As shown in the schematic (**Figure 2.4**), a continuous-wave Millenia 532 nm pump laser optically pumped a Spectra Physics Ti:Sapphire oscillator, producing tunable near-infrared output spanning approximately 760–800 nm. The oscillator generated pulses on the order of ∼100 fs at an 80 MHz repetition rate, providing the photon flux necessary to achieve simultaneous two-photon absorption within the focal volume of the sample.

The laser beam was directed through a series of dielectric mirrors to define the beam path and ensure optical isolation. A neutral density filter was positioned in the beam line to finely regulate the incident photon flux, allowing systematic control of excitation power during. A small fraction of the beam was diverted onto a photodiode connected to a digital multimeter. This photodiode served as a continuous monitor of incident laser power, enabling accurate correlation of fluorescence intensity with excitation flux.

The main portion of the beam was focused into a 1 cm path-length quartz cuvette containing the sample solution. Two-photon absorption at the focal region generates fluorescence that propagates isotropically; to collect only the emission and avoid contamination from the excitation beam, the detection optics were positioned orthogonally (90° geometry) relative to the excitation axis. Fluorescence was directed into a monochromator (Oriel Cornerstone) that spectrally dispersed the emission prior to detection by a Hamamatsu photomultiplier tube (PMT). The PMT output was routed to a photon-counting unit interfaced with a computer, enabling time-integrated acquisition of fluorescence counts over a controlled integration period.

During measurement, the excitation power was systematically varied using the neutral density filter, and corresponding fluorescence intensities were recorded. A log-log plot of fluorescence counts versus excitation power was used to confirm the quadratic dependence characteristic of two-photon excitation. By comparing the power-dependent response of the sample to that of a well-established reference chromophore (e.g., coumarin 307 or rhodamine B), the two-photon absorption cross-section was extracted via the standard comparative method.

2.4. Entangled Two-Photon Absorption

Entangled two-photon absorption (ETPA) measurements in this dissertation is measured as a function of linear dependence between the entangled-photon absorption rate and the incident biphoton flux; an optical signature that distinguishes ETPA from classical two-photon absorption. At low photon flux, the total two-photon absorption rate can be expressed as

$$R_{\mathrm{TPA}} = \sigma_E \Phi + \delta_{\mathrm{r}} \Phi^2 \quad \text{(Equation 2.9)}$$

where σ_E is the ETPA cross-section, δ_{r} is the classical (random) two-photon cross-section, and $\Phi$is the incident photon flux. By working exclusively in the low-flux regime, the linear term dominates, allowing the ETPA response to be measured in a manner analogous to weak single-photon attenuation. The transmitted flux through a solution of concentration $[C]$ and optical path length L is therefore described by

$$I_{\mathrm{out}} = I_{\mathrm{in}} \exp\left(-\sigma_E N_A [C] L\right) \quad \text{(Equation 2.10)}$$

where N_A is Avogadro's number. For small absorption, the exponential expression may be linearized, giving the absorption rate

$$A = I_{\mathrm{in}} - I_{\mathrm{out}} = I_{\mathrm{in}} \left(\sigma_E N_A [C] L\right) \quad \text{(Equation 2.11)}$$

The ratio A/I_{in} appears as the slope of a linear fit when the absorbed photon rate is plotted against the incident flux, enabling extraction of the molecular ETPA cross-section:

$$\sigma_E = \frac{A/I_{\text{in}}}{N_A[C]L} \quad \text{(Equation 2.12)}$$

This transmission-based methodology was adopted because it provides a direct quantitative measure of ETPA at photon levels well below the threshold for any classical nonlinear optical response.[5,6]

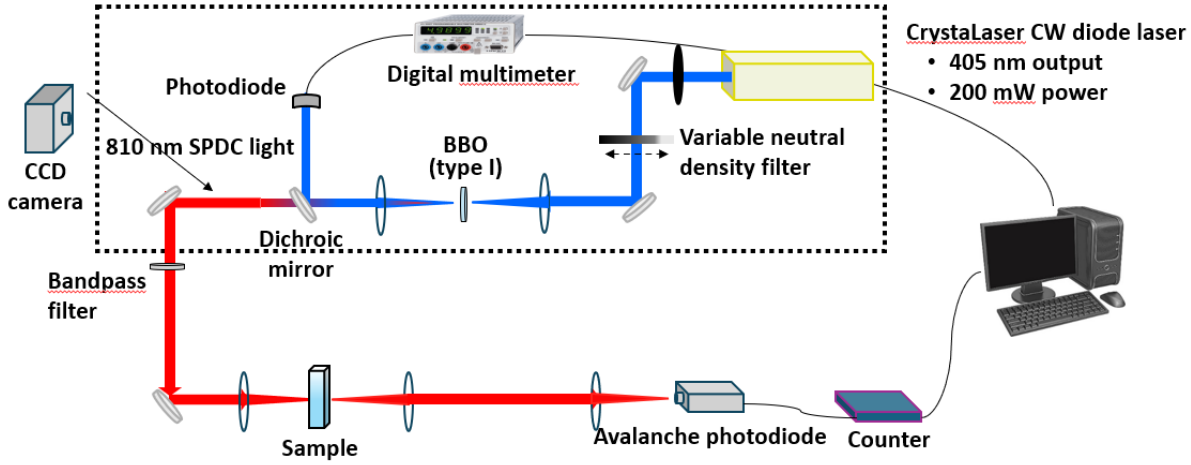


Figure 2.5: Schematic Diagram of the ETPA set-up

The ETPA measurements were done using a 405 nm continuous-wave (cw) beam from a CrystaLaser Inc. CL-2000 laser as the pump source for spontaneous parametric down-conversion (SPDC). The 405 nm beam was directed onto a type-I β-barium borate (BBO) crystal, where SPDC generated frequency-correlated photon pairs at degenerate wavelengths centered near 800 nm. The charge-coupled device (CCD) camera was used to confirm the generation of the entangled photons (**Figure 2.5**). The entangled photon pair were collimated and directed through a 1 mm × 1 mm quartz cuvette held in a fixed mount. Because ETPA occurs at low photon fluxes, even small deviations in alignment can produce apparent changes in transmission that mimic weak absorption.

For this reason, the cuvette holder, collimating optics, and detector were all re-aligned at the beginning of this project to re-establish a stable transmission pathway that had not been fully implemented at the start of the work. After the sample, the transmitted entangled photons were refocused onto a silicon avalanche photodiode (APD) operated in single-photon counting mode. The detector's quantum efficiency at 800 nm is approximately 60%, while its efficiency at 400 nm is roughly 7%, a beneficial property because it suppresses any residual pump leakage that might otherwise introduce false absorption signals. The intrinsic dark count rate of the detector is ~300 counts/s, setting the baseline for distinguishing true absorption from background fluctuations. Since the APD active area is only ~175 μm in diameter, precise focusing was required; the detector was mounted on an Ultralign XYZ translation stage so that the transmitted beam could be centered and optimized while monitoring the photon count rate in real time.

2.5. Transient Absorption Spectroscopy

Transient absorption (TA) spectroscopy is a pump-probe, time-resolved technique used to monitor how molecules evolve after photoexcitation. A TA measurement produces two primary data sets: spectral profiles and kinetic traces. The spectra reveal the energies of the transient electronic states that become populated following excitation, while the kinetic traces report how these states evolve or decay over time. Together, these data provide a detailed picture of excited-state dynamics.

Jablonski diagram traditionally illustrates radiative pathways such as fluorescence and phosphorescence. TA extends this concept by simultaneously capturing both radiative and nonradiative processes, enabling direct observation of mechanisms such as internal conversion, intersystem crossing, fluorescence, phosphorescence, charge separation, and other photophysical

pathways. Because TA measurements can track dynamics from the femtosecond (10^{-15} s) regime through the microsecond (10^{-6} s) regime, the technique yields a comprehensive excited-state energy pathway, mapping not only the energies of transient states but also their associated lifetimes.

In a transient absorption experiment, the sample is first driven into an excited electronic state by one optical pulse, and a second pulse is subsequently used to interrogate the population of those excited states. Because the method relies on two temporally separated beams, it is classified as a pump-probe spectroscopy technique. The pump beam often referred to as the excitation pulse provides the energy required to promote molecules from the ground electronic state (S_0) into higher-lying singlet states. Its wavelength is selected on the basis of the molecule's steady-state absorption spectrum, which reveals the allowed electronic transitions between S_0 and the various excited singlet manifolds (S_n). For instance, the absorption maximum typically corresponds to the $S_0 \rightarrow S_1$ transition, and choosing a pump wavelength resonant with this feature ensures efficient population of S_1. More generally, the pump energy is tuned to the specific transition relevant to the excited-state process under investigation (**Figure 2.6).**

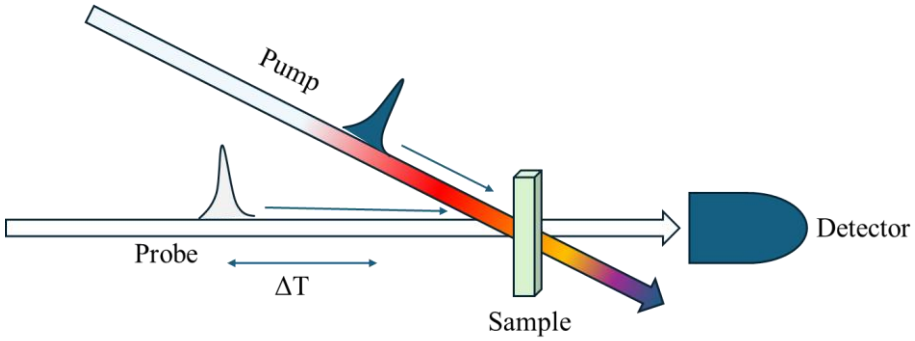


Figure 2.6: Pump-probe spectroscopy process

The second pulse, known as the probe beam, monitors the evolution of these excited states after the pump interaction. The probe consists of a broadband continuum spanning the ultraviolet, visible, or near-infrared regions typically ranging from approximately 350 to 2000 nm. This broadband light, commonly referred to as a white-light continuum, can be generated in different ways depending on the temporal regime of the experiment. In femtosecond TA setups, the continuum is usually produced by focusing intense ultrafast pulses into a sapphire or CaF_2 plate. In contrast, nanosecond TA systems generally employ a xenon lamp to provide a broad spectral background extending from the UV to the near-IR. The role of the probe beam is to record how the absorption characteristics of the molecule change after excitation, thereby revealing which electronic states are populated and how those populations evolve across time.

In a transient absorption experiment, the excitation pulse is periodically interrupted while the probe continuum remains continuous. This modulation producing alternating intervals in which the pump is either incident on the sample ("pump-on") or blocked ("pump-off"). This controlled alternation is essential because it enables the probe beam to record how the sample absorbs light both in the presence and absence of photoexcitation. By comparing these two conditions, the experiment isolates the spectral changes that arise exclusively from the excited-state population created by the pump.

The fundamental observable extracted from this comparison is the differential absorbance, ΔA, which is defined by:

$$\Delta A = -\log\left(\frac{\text{Intensity}_{\text{pump-On}}}{\text{Intensity}_{\text{pump-Off}}}\right) \qquad \text{(Equation 2.13)}$$

Here, $\text{Intensity}_{\text{pump-On}}$ represents the probe intensity recorded when both the pump and probe simultaneously interact with the sample, whereas $\text{Intensity}_{\text{pump-Off}}$ corresponds to the probe-only condition when the pump beam is blocked. As in standard Beer-Lambert analysis, taking the negative logarithm of the ratio of these two measured intensities yields the transient absorbance signal.

Depending on the instrument and analysis protocol, this same information may alternatively be expressed as the fractional change in transmission, ΔT/T, which is mathematically equivalent but differs in sign convention. Both ΔA and ΔT/T are dimensionless quantities and are commonly used to represent TA data.

From these differential signals, three characteristic photophysical signatures emerge in TA measurements: Ground-state bleach (GSB), stimulated emission (SE), an excited-state absorption (ESA).

The GSB shows as a negative signal ($\Delta A < 0$) in the TA spectrum. It arises from a depletion of molecules in the ground state (S_0) due to their promotion to excited states by the pump pulse. This reduction in the S_0 population leads to a decrease in the sample's absorption at wavelengths corresponding to its steady-state absorption spectrum. Consequently, the spectral profile of the GSB band typically mirrors the linear absorption spectrum of the molecule, marking the regions where ground-state absorption has been diminished (**Figure 2.7**).

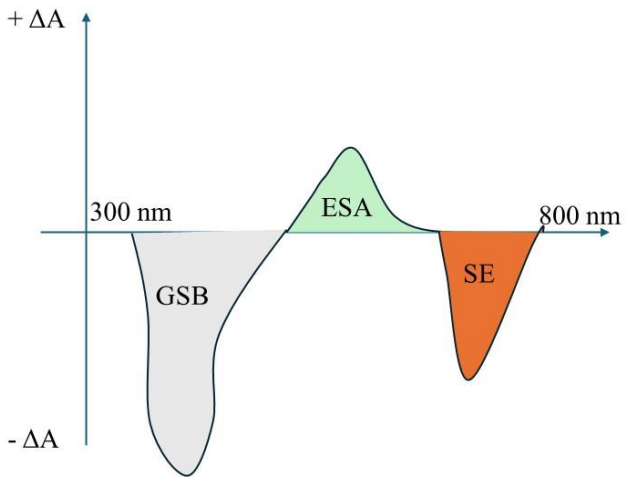


Figure 2.7: Signals obtained in the TA

In contrast, ESA appears as a positive signal (ΔA > 0). This feature results from molecules that are already in an excited state (e.g., S_1) absorbing a second photon from the broadband probe pulse to reach a higher-lying excited state (S_n). The ESA signal therefore provides a direct spectral signature of these higher-energy states. It is important to note that ESA can originate from various excited-state species, including higher singlets (S_n) or, at longer time delays, triplet states (T_n) following intersystem crossing. The SE is also a negative signal (ΔA < 0), but it has a different physical origin than the GSB. SE occurs when the probe beam stimulates molecules in the first excited singlet state (S_1) to undergo a radiative transition back to the ground state (S_0). This process coherently amplifies the probe light, resulting in increased transmission at the corresponding wavelengths. The spectrum of the SE signal often aligns with the molecule's steady-state fluorescence spectrum. These spectral features collectively describe how the populations of the ground and excited electronic states evolve following photoexcitation and form the basis for interpreting excited-state dynamics in both femtosecond and nanosecond TA experiments.

2.5.1. Nanosecond Transient Absorption Instrumentation and Technique

Nanosecond transient absorption spectroscopy (ns-TAS) is a pump-probe technique designed to monitor the evolution of electronically excited states on timescales from nanoseconds to microseconds. The method enables access to both emissive and non-emissive species and is widely used to characterize long-lived singlet, triplet, charge-separated, or radical intermediates. The experimental setup used in this work consists of three principal components: a pulsed Nd:YAG laser system, an optical parametric oscillator (OPO) for wavelength tunability, and a transient absorption spectrometer configured for probe generation, spectral selection, and time-resolved detection.

The pump source is a Spectra Physics Quanta-Ray Lab Series 170 Nd:YAG laser, which operates by optically exciting Nd:YAG rods using dual xenon flash lamps. The lasing medium produces the 1064 nm fundamental, which is subsequently shaped into short, high-energy pulses through Q-switching (**Figure 2.8**). The Q-switch assembly contains a polarizer, a quarter-wave plate, and a Pockels cell. Under no applied voltage, the Pockels cell allows the cavity to maintain high losses due to repeated polarization rotation within the quarter-wave plate-polarizer sequence. When triggered by a high-voltage pulse from the Marx-bank circuit, the Pockels cell rapidly changes birefringence, suppresses the polarization rotation, and briefly permits constructive resonator buildup. This process releases an intense, nanosecond-scale pulse with peak powers in the tens of megawatts.

The pulsed 1064 nm beam is then routed through the harmonic generation stage. Potassium dideuterium phosphate (KD*P) crystals convert the fundamental to its second harmonic (532 nm) via second-harmonic generation (SHG), and additional nonlinear mixing with residual 1064 nm produces the third harmonic (355 nm). This 355 nm output is used as the pump for the optical

parametric oscillator (OPO). Inside the OPO, a β-barium borate (BBO) crystal mediates parametric down-conversion driven by the 355 nm pump, allowing access to a broad tunable range of excitation wavelengths appropriate for varying molecular absorption characteristics.

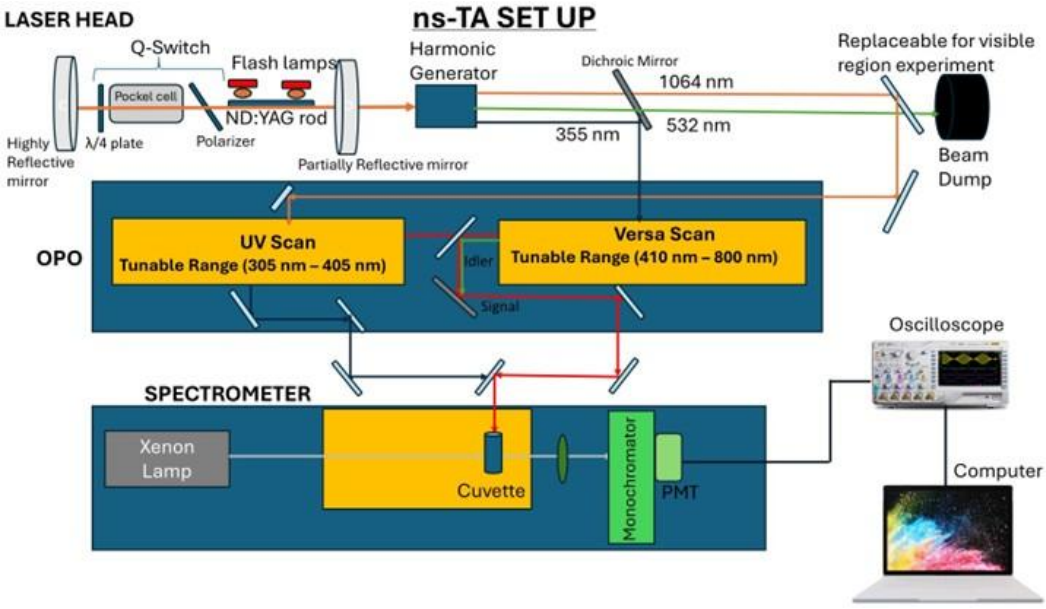


Figure 2.8: Diagram of the ns-TA instrumentation

Transient absorption detection is performed using an Edinburgh Instruments spectrometer, which includes a pulsed or continuous probe source, a sample compartment, a monochromator, and a photomultiplier-based detection module. During a measurement, the pump pulse excites the sample, and a time-delayed probe beam interrogates the resulting population of transient species. Probe light transmitted through the sample is spectrally dispersed by the monochromator and monitored by fast photodetectors, enabling measurement of the differential absorbance (ΔA) as a function of time and wavelength. By varying the pump–probe delay, the full kinetic evolution of excited states can be reconstructed. The system is equipped with electronic timing controls that synchronize pump pulses with probe sampling windows, allowing nanosecond temporal resolution across the full spectral window supported by the detection optics.

2.5.2. Femtosecond Transient Absorption Instrumentation and Technique

The femtosecond transient absorption (fs-TA) measurements were conducted using a dedicated ultrafast spectrometer system. The core of the setup consisted of a Spectra-Physics amplified Ti:Sapphire laser system integrated with an Ultrafast Systems Helios transient absorption spectrometer. The fs-TA setup consist of Tsunami Ti:Sapphire oscillator, which was pumped by a Millennia Pro continuous-wave laser at 532 nm. The oscillator generated a train of ~80 fs pulses at a center wavelength of 790 nm with an 80 MHz repetition rate (**Figure 2.9**). This femtosecond seed pulse was then introduced into a Spitfire Amplifier, which was pumped by a separate Q-switched Empower laser at 527 nm. The amplification process converted the high-repetition, low-energy oscillator output into a robust 1 kHz train of pulses, yielding an amplified 790 nm beam with a pulse width of approximately 110 fs and an average power of 1 W.

The amplified 790 nm beam was passed through a beamsplitter to create the separate pump and probe pathways. The majority of the beam (~95%) was directed into a Spectra-Physics Optical Parametric Amplifier (OPA-800C). Within the OPA, the fundamental 790 nm light was converted to the desired excitation wavelength. For the studies presented here, a pump wavelength of 600 nm was typically generated. To ensure that the measurements were conducted within the linear excitation regime and to minimize multiphoton processes or sample damage, the pump beam power was attenuated using a neutral density filter to an energy of approximately 1.0 μJ/pulse at the sample position. For experiments requiring UV excitation, the signal beam from the OPA was further frequency-doubled in a series of barium borate (BBO) crystals inside the OPA cavity.

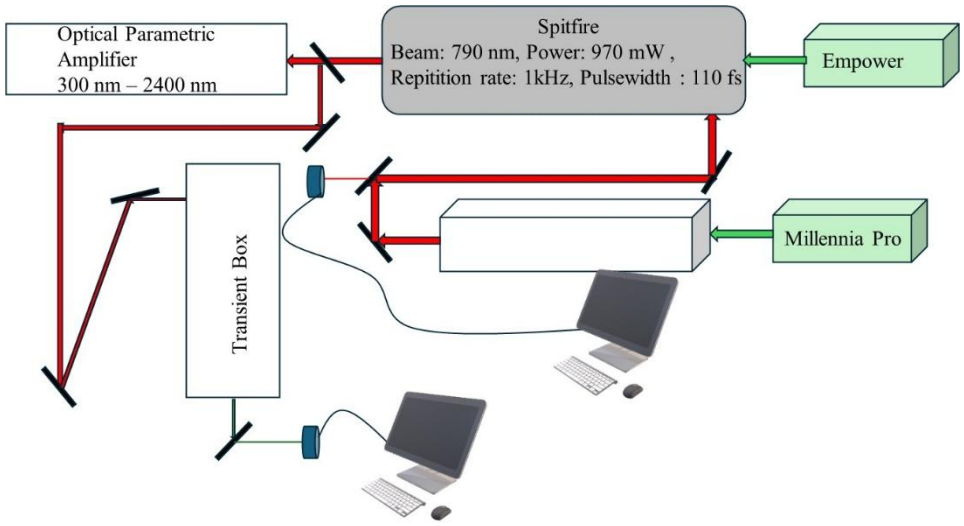


Figure 2.9: Schematic diagram of the fs-TA setup

The remaining small portion (~5%) of the amplified 790 nm beam was used to generate the broadband probe pulse. This beam was routed through a computer-controlled motorized delay stage, which precisely controlled the temporal delay between the pump and probe pulses. The delayed beam was then focused onto a nonlinear medium to generate a white light continuum. For probing the visible spectral region (450–800 nm), a static 3 mm sapphire plate was used. For UV probe measurements (350–750 nm), the beam was focused onto a rotating rectangular calcium fluoride (CaF_2) window to distribute the heat load and prevent optical damage.

The pump and probe beams were focused and spatially overlapped within the sample. The pump beam was modulated at 500 Hz by a mechanical optical chopper, creating the alternating "pump-on" and "pump-off" condition required for the differential measurement. After passing through the sample, the probe light was collected and focused into a fiber-optic cable coupled to a CCD spectrometer. The Helios software (Ultrafast Systems) was used for automated data

acquisition, recording the change in absorption (ΔA) as a function of probe wavelength and pump-probe delay time.

2.5.3. Time Correlated Single Photon Counting Instrumentation

Time-Correlated Single Photon Counting (TCSPC) was employed to characterize the time-resolved photoluminescence of materials exhibiting decay lifetimes on the nanosecond to microsecond timescale, a temporal range beyond the reach of the fluorescence up-conversion technique.

The TCSPC apparatus, depicted in **Figure 2.10**, utilized a Spectra-Physics Millenia continuous-wave Nd:YVO4 laser operating at 532 nm (4 W output) to pump a Ti:Sapphire oscillator (Kapteyn Murnane Laboratories). The oscillator produced a tunable output, which was fixed at 800 nm for all experiments presented in this dissertation, with a pulse duration of 30 fs and a repetition rate of 90 MHz. This fundamental 800 nm beam was then frequency-doubled using a beta-barium borate (BBO) nonlinear crystal to generate the excitation source at 400 nm. The resulting pulsed beam was focused onto the sample, contained in a 1.0 cm path length cuvette, using an 11.5 cm focal length lens.

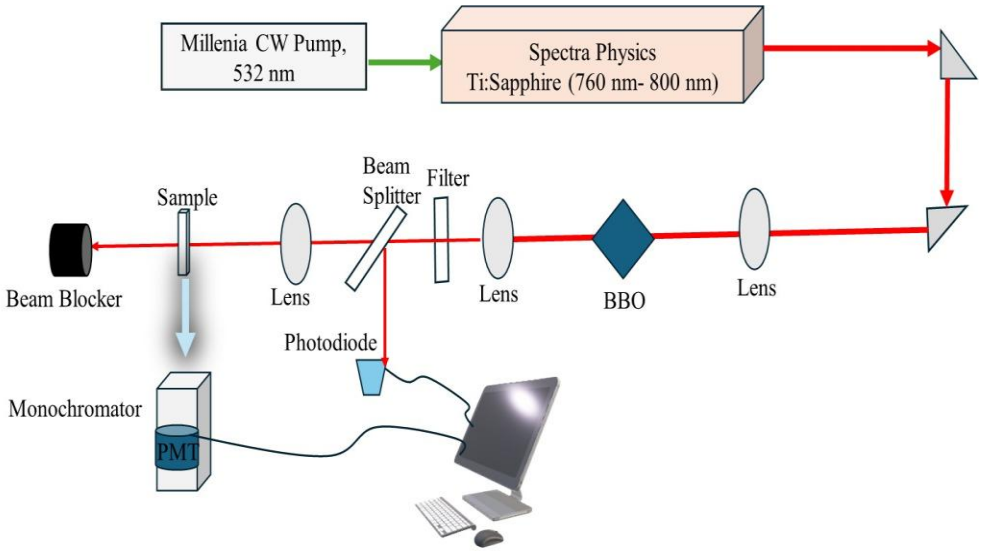


Figure 2.10: Schematic diagram of the TCSPC set-up

The time-resolved emission was collected at a 90-degree angle relative to the excitation path to minimize scattered light and electrical interference. A monochromator was positioned before the detector to select the specific emission wavelength and block ambient photons. Signal detection was achieved using a photomultiplier tube (PMT). The TCSPC technique operates by building a histogram of photon arrival times relative to the excitation laser pulse; this was managed by a TimeHarp200 interface card and the accompanying PicoQuant software.

The instrument response function (IRF), critical for defining the temporal resolution of the system, was characterized using Rayleigh scattering and was determined to have a full width at half maximum (FWHM) of 330 ps. The resulting fluorescence decay histograms were analyzed by fitting the data to appropriate exponential models to extract the characteristic lifetimes of the emissive states.

2.5.4. Fluorescence up-conversion Instrumentation

Fluorescence up-conversion (FUC) is an ultrafast spectroscopic technique employed to measure the radiative decay and emissive dynamic processes of molecular systems, with a typical temporal resolution ranging from hundreds of femtoseconds to several picoseconds.

The FUC apparatus used in this work is illustrated in **Figure 2.11**. The system integrates a Spectra-Physics Millenia laser, which is a continuous-wave (CW) source utilizing a neodymium-doped yttrium vanadate (Nd:YVO_4) gain medium to produce 4.21 W of power at 532 nm. This 532 nm beam serves as the pump for a Spectra-Physics Tsunami Ti:Sapphire oscillator. Through mode-locking, the Tsunami generates ultrafast pulses with a duration of approximately 80 fs, a repetition rate of 82 MHz, and an average power between 680 and 720 mW. For all experiments described in this dissertation, the oscillator was tuned to a central wavelength of 800 nm.

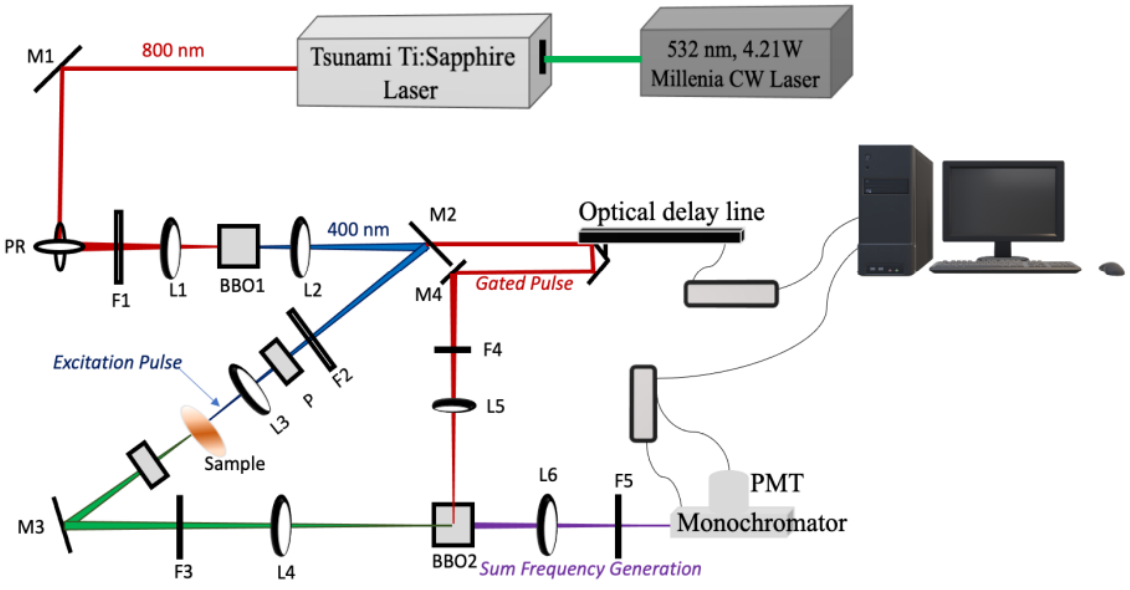


Figure 2.11: Schematic diagram for the TCSPS instrument

The fundamental 800 nm beam is split into two primary paths. One portion is frequency-doubled in a beta-barium borate (BBO) crystal to produce the excitation beam at 400 nm, which is separated from the fundamental using a dichroic mirror. This 400 nm pump beam is directed towards the sample, which is housed in a rotating 1 mm path length cuvette to mitigate photodegradation. The polarization of the excitation beam is controlled using a Berek compensator to ensure parallel polarization for all measurements.

The second portion of the fundamental 800 nm beam, termed the "gate" pulse, is routed through a computer-controlled delay line with a step resolution of 6.25 fs. The photoluminescence emitted from the sample is collected and focused onto a second BBO crystal. Within this crystal, the time-delayed gate pulse and the sample fluorescence undergo sum-frequency generation (SFG). This nonlinear process effectively converts the fluorescence to a shorter wavelength (in the 300-400 nm range), but only for the fraction of the fluorescence that temporally overlaps with the gate pulse. By scanning the delay of the gate pulse and measuring the intensity of the up-converted signal, the fluorescence decay profile is directly mapped in time. The resulting sum-frequency beam is collimated, focused into a monochromator for spectral selection, and finally detected by a photomultiplier tube (PMT, Hamamatsu R152P). The intensity of this signal as a function of the gate delay provides the time-resolved fluorescence decay.

2.6. Near-field scanning optical microscopy (NSOM) Principle and Technique

Near-field scanning optical microscopy (NSOM) is a powerful imaging technique that overcomes the diffraction limit by collecting or delivering light through a nanoscale probe positioned within the near-field region of a sample.[7,8] By accessing these evanescent optical fields, NSOM provides spatial resolution far below conventional optical microscopy, enabling direct

visualization of nanoscale structural and photophysical heterogeneity. This high spatial resolution is particularly important for studying electronic coherence, a quantum phenomenon in which excited electronic states maintain a well-defined phase relationship. Electronic coherence, once considered an abstract quantum-mechanical construct, has become directly measurable owing to the development of ultrafast pulsed laser systems. The use of femtosecond pulses enables the preparation of an excited-state wave packet, a coherent superposition of molecular eigenstates whose dynamical evolution reflects the fundamental optical response of a material. When a system is excited with an ultrashort pulse of temporal width τ, the electric field can be described as

$$\vec{E}(t) = \vec{E}_0 \exp\ (-\frac{t^2}{\alpha\tau^2}) \cos(\omega t) \qquad \text{(Equation 2.14)}$$

This initial coherence decays over time due to interactions between the excited system and its local environment. Fluctuations in solvent configuration, vibrational motions, and inter- or intramolecular couplings all induce phase scrambling of the electronic oscillations, giving rise to a characteristic dephasing time. The total homogeneous dephasing rate combines the contributions from population relaxation (T_1) and pure dephasing (T_2^*), expressed as

$$\frac{1}{T_2} = \frac{1}{2T_1} + \frac{1}{T_2^*} \qquad \text{(Equation 2.15)}$$

Measuring this dephasing time provides direct information on the strength of electronic interactions, environmental coupling, and the extent to which coherent quantum behavior survives in a material.

The detection of electronic coherence relies on interference phenomena: coherence persists only as long as phase relationships between quantum states are maintained. Once phase memory is lost, interference patterns vanish, and the system behaves as an ensemble of independent

classical oscillators. In condensed-phase environments, these processes occur extremely rapidly typically on femtosecond to picosecond timescales making ultrafast spectroscopic methods essential for their observation. A two-pulse sequence is generally required: the first pulse prepares the coherent superposition, and the second pulse monitors how the phase evolves after a controlled time delay. By scanning the interpulse delay, one maps the evolution of the system's polarization and extracts the coherence time from the decay of the resulting interference fringes.[8–10]

In our laboratory, these coherence measurements are performed not only in solution but also with nanoscale spatial resolution using time-resolved NSOM. The time-resolved NSOM instrument integrates a phase-locked pair of femtosecond pulses with a near-field probe, enabling simultaneous ultrafast temporal resolution and sub-diffraction spatial resolution. In this experiment, the first pulse prepares a coherent wave packet in the excited-state manifold, while the delayed second pulse interacts with this evolving polarization. Depending on the relative phase between the wave packet and the second pulse, the local polarization amplitudes experience constructive or destructive interference. Monitoring the emitted photoluminescence as a function of the interpulse delay produces an interferogram whose fringe contrast directly reflects the electronic coherence lifetime.[7]

For a pair of phase-locked pulses separated by delay τ, the electric field at the sample is

$$E(t) = A(t)e^{-i\omega_L t} + A(t-\tau)e^{-i\omega_L(t-\tau)} \qquad \text{(Equation 2.16)}$$

where $A(t)$is the slowly varying pulse envelope; demonstrating that the excited-state population is modulated by the interpulse delay τ. Three regimes arise as τ is scanned:

(1) Laser interference region, where τ is comparable to the pulse width and the response is dominated by optical pulse-pulse interference; (2) Coherent polarization interference region, in which molecular coherence governs the signal; and (3) No-interference region, where coherence has decayed and only population dynamics remain.

The ability to resolve these ultrafast processes at the nanoscale is made possible through the NSOM approach. Traditional optical microscopes are diffraction-limited, with their spatial resolution defined by

$$d = \frac{\lambda}{2\,NA} \qquad \text{(Equation 2.17)}$$

where λ is the wavelength and NA is the numerical aperture. Near-field microscopy circumvents this limitation by using a subwavelength aperture positioned within a distance much smaller than λ from the sample surface, accessing the non-propagating (evanescent) optical field. This near-field component contains high spatial-frequency information that would be lost through far-field propagation.

Our time-resolved NSOM system employs a non-metalized tapered single-mode fiber as a local excitation source. The phase-locked pulse pair is coupled into the fiber, and the tip apex delivers the excitation field directly into the near-field region of the sample. Because the evanescent field decays exponentially with distance, maintaining precise probe–sample separation typically tens of nanometers is essential. The instrument uses a shear-force feedback mechanism based on a quartz tuning fork to regulate this distance. The fiber is attached to one prong of the tuning fork, which is driven at its resonance frequency. As the probe approaches the sample, shear

forces dampen its oscillation amplitude; the feedback loop keeps the amplitude at a constant setpoint, thereby stabilizing the probe height with nanometer precision.[7,9]

A high-aperture objective positioned beneath the sample collects the emitted photoluminescence generated by the two-pulse excitation sequence. The signal is directed onto a photomultiplier tube for detection. Because the measurement is performed in the near-field, the technique simultaneously provides topographic information (via the tuning-fork feedback) and optical information (via the ultrafast PL response). This dual data stream makes it possible to map electronic coherence with spatial resolution far below the diffraction limit, down to the scale of single nanoparticles or molecular aggregates.

In summary, time-resolved NSOM combines phase-locked femtosecond spectroscopy with near-field optical probing to measure electronic coherence lifetimes with both ultrafast temporal precision and nanometer spatial resolution. By tracking the decay of interference between phase-locked pulses, the method provides a direct measure of electronic dephasing, offering insight into environmental interactions, excitonic coupling, and intrinsic electronic structure at the nanoscale. This powerful combination of techniques enables visualization of coherent phenomena that are otherwise obscured in ensemble-averaged measurements, thereby advancing our understanding of quantum behavior in complex optoelectronic materials.

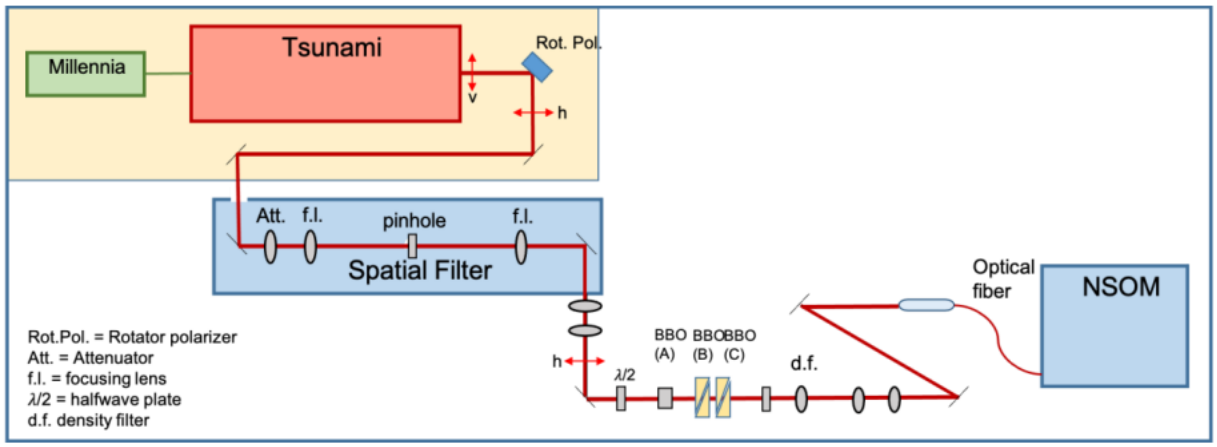


Figure 2.12: Schematic diagram of the NSOM instrumentation.[7,8]

The core excitation source was a Ti:Sapphire femtosecond laser (Spectra-Physics Mai Tai) producing 124 fs pulses at a wavelength of 800 nm with a repetition rate of 80 MHz. A critical component of the setup was an interferometric block designed to generate and control a pair of time-delayed pulses from the initial single pulse. This was achieved by directing the beam through a half-wave plate, followed by two mutually orthogonal birefringent beta-barium borate (BBO) crystals. The specific orientation of the crystals' optical axes imparted different group velocities to orthogonally polarized components of the input pulse, effectively splitting it into two distinct pulses. The temporal separation, or inter-pulse delay (τ), between these pulses was precisely controlled by translating a wedged delay block of variable thickness. A high-precision linear translation stage provided a delay resolution of 0.2 fs, enabling scans from 0 to 1 ps. Subsequent optical elements, including an angular dispersion compensator and a polarizer, were used to recombine the pulses spatially and ensure correct polarization before injection into the NSOM probe.

The prepared pulse pair was coupled into a non-metalized NSOM fiber probe using a 10x objective lens (N.A. = 0.25). The fiber probe featured a sharp tip with an aperture of approximately

30 nm, enabling localized excitation and guaranteeing spatial resolution below the diffraction limit. The probe-to-sample distance was maintained at a constant nanometer-scale separation using a shear-force feedback mechanism. For imaging, a 5 μm x 5 μm area was raster-scanned with a resolution of 100 x 100 pixels. Thin-film samples for NSOM analysis were prepared by spin-coating a 4 μL volume of a 1 nM sample solution onto plasma-cleaned glass coverslips at 1400 rpm. The films were subsequently dried in a vacuum oven prior to measurement. Photoluminescence from the sample was collected in transmission mode through a far-field inverted objective lens situated beneath the sample. To isolate the sample emission from the intense excitation laser light, a notch filter was placed in the detection path. The filtered signal was then detected by a photomultiplier tube (PMT). For optimal light coupling into the fiber probe, a cleanly cleaved fiber end face was essential, observable under a microscope as a distinct central feature.

REFERENCES

(1) Williams, A. T. R.; Winfield, S. A.; Miller, J. N. Relative Fluorescence Quantum Yields Using a Computer-Controlled Luminescence Spectrometer. *The Analyst* **1983**, *108* (1290), 1067. https://doi.org/10.1039/an9830801067.

(2) Villabona-Monsalve, J. P.; Tcyrulnikov, N. A.; Lorenzo, E. R.; LaBine, N.; Burdick, R.; Krzyaniak, M. D.; Young, R. M.; Wasielewski, M. R.; Goodson, T. I. Two-Photon Absorption in Electron Donor–Acceptor Dyads and Triads Using Classical and Entangled Photons: Potential Systems for Photon-to-Spin Quantum Transduction. *J. Phys. Chem. C* **2022**, *126* (14), 6334–6343. https://doi.org/10.1021/acs.jpcc.2c00830.

(3) Villabona-Monsalve, J. P.; Varnavski, O.; Palfey, B. A.; Goodson, T. I. Two-Photon Excitation of Flavins and Flavoproteins with Classical and Quantum Light. *J. Am. Chem. Soc.* **2018**, *140* (44), 14562–14566. https://doi.org/10.1021/jacs.8b08515.

(4) Cai, Z.; Vázquez, R. J.; Zhao, D.; Li, L.; Lo, W.; Zhang, N.; Wu, Q.; Keller, B.; Eshun, A.; Abeyasinghe, N.; Banaszak-Holl, H.; Goodson, T. I.; Yu, L. Two Photon Absorption Study of Low-Bandgap, Fully Conjugated Perylene Diimide-Thienoacene-Perylene Diimide Ladder-Type Molecules. *Chem. Mater.* **2017**, *29* (16), 6726–6732. https://doi.org/10.1021/acs.chemmater.7b01512.

(5) Villabona-Monsalve, J. P.; Varnavski, O.; Palfey, B. A.; Goodson, T. I. Two-Photon Excitation of Flavins and Flavoproteins with Classical and Quantum Light. *J. Am. Chem. Soc.* **2018**, *140* (44), 14562–14566. https://doi.org/10.1021/jacs.8b08515.

(6) Villabona-Monsalve, J. P.; Burdick, R. K.; Goodson, T. I. Measurements of Entangled Two-Photon Absorption in Organic Molecules with CW-Pumped Type-I Spontaneous Parametric

Down-Conversion. *J. Phys. Chem. C* **2020**, *124* (44), 24526–24532. https://doi.org/10.1021/acs.jpcc.0c08678.

(7) Ricci, F.; Mandal, H.; Wajahath, M.; Burdick, R. K.; Villabona-Monsalve, J. P.; Hussain, S.; Goodson, T. I. Investigations of Coherence in Perovskite Quantum Dots with Classical and Quantum Light. *J. Phys. Chem. C* **2023**, *127* (7), 3579–3593. https://doi.org/10.1021/acs.jpcc.2c08455.

(8) Ricci, F.; Marougail, V.; Varnavski, O.; Wu, Y.; Padgaonkar, S.; Irgen-Gioro, S.; Weiss, E. A.; Goodson, T. I. Enhanced Exciton Quantum Coherence in Single CsPbBr3 Perovskite Quantum Dots Using Femtosecond Two-Photon Near-Field Scanning Optical Microscopy. *ACS Nano* **2021**, *15* (8), 12955–12965. https://doi.org/10.1021/acsnano.1c01615.

(9) Rani, C.; Goodson, T. I. Enhanced Exciton Coherence Time and Correlation with Probability of Absorption of Classical and Entangled Light in Quantum-Confined Systems. *J. Phys. Chem. C* **2024**. https://doi.org/10.1021/acs.jpcc.4c01747.

(10) Ricci, F.; Marougail, V.; Varnavski, O.; Wu, Y.; Padgaonkar, S.; Irgen-Gioro, S.; Weiss, E. A.; Goodson, T. I. Enhanced Exciton Quantum Coherence in Single CsPbBr3 Perovskite Quantum Dots Using Femtosecond Two-Photon Near-Field Scanning Optical Microscopy. *ACS Nano* **2021**, *15* (8), 12955–12965. https://doi.org/10.1021/acsnano.1c01615.

Chapter Three

From Structure to Function: Nonlinear Optical Properties and Excited-State Dynamics of Ladder-Type π-Conjugated Benzo [k] tetraphene Oligomers

3.1. Author Contribution Statement

This chapter describes the result and conclusion of the collaborative work done by Professor Theodore G. Goodson III's group, Department of Chemistry and Macromolecular Science & Engineering, University of Michigan, Ann Arbor and Professor Lei Fang, Department of Chemistry, Texas A&M University. In this work, my contribution was on the experimental part where I worked on the steady state, two-photon absorption (TPA) and entangled two-photon absorption (ETPA), time-correlated single photon counting and the nanosecond transient absorption spectroscopy of these materials. Wajahath, R. assisted with the ETPA experiment and the data analysis, while Norscia II, M., worked on the time-correlated single photon counting experiment and electronic structure calculation. Yang, J. S. J from Professor Lei Fang group synthesized and characterized these materials.

This collaborative research is published in the *Journal of Physical Chemistry C* – full citation: Ogunyemi, O. J., Norscia II, M., Wajahath, R., Yang, J. S. J., Fang, L., & Goodson III, T. (2025). From Structure to Function: Nonlinear Optical Properties and Excited-State Dynamics of Ladder-Type π-Conjugated Benzo [k] tetraphene Oligomers. *The Journal of Physical Chemistry C*, *129*(39), 17862-17874.

3.2. Abstract

Ladder-type oligomers are emerging building blocks for optoelectronic and quantum applications, owing to their rigid, planar backbones that enhances charge transport, exciton delocalization, and structural stability compared to their linear counterparts. However, the fundamental structure-function relationships in unsubstituted ladder systems remain largely unexplored, as most studies focus on chemically modified derivatives. In this work, we investigate the excited-state dynamics and nonlinear optical (NLO) properties of a series of unsubstituted Benzo[k]tetraphene (BTp) ladder-type oligomers with systematically extended conjugation lengths (BTp 5, BTp 7, BTp 9, and BTp 11). Our results reveal that electron delocalization, induced by the extended conjugation, facilitates intersystem crossing (ISC) which enhances efficient formation of the triplet excited states. However, both classical and entangled two-photon absorption measurements show a clear saturation in the NLO response beyond a critical conjugation threshold. This trend is consistent with excited-state lifetimes, which remain largely unchanged with further molecular extension, revealing a critical limit of electronic tunability in the BTp series. These findings provide fundamental insights for optimizing the excited-state dynamics and NLO properties of unsubstituted BTps.

3.3. Introduction

Polycyclic aromatic hydrocarbons (PAH) represent an interesting class of carbon-rich organic compounds featuring multiple fused rings, with extended π-conjugation and rigid coplanar conformation.[1,2] Ladder-type oligomers are unique class of PAH containing uninterrupted sequence of fused aromatic rings connected via sharing of two or more similar adjacent atoms.[3,4] As a result, the π system of ladder molecules are locked in a planar structure, and are completely different from linear conjugated organic molecules that are connected via carbon-carbon bonds.[5,6]

This structural rigidity of ladder-type conjugated molecules suppresses electron-phonon interactions which typically hinder efficient charge transport in conjugated organic molecules.[7,8] The evidence of reduced electron-phonon interaction in organic ladder systems has been demonstrated using single molecule spectroscopy on methyl-substituted ladder-type poly(*p*-phenylene) (MeLPPP).[8,9] This rigid geometry conformation of organic ladder systems enhances the charge transport properties desirable for optoelectronic applications in comparison to linear conjugated counterparts.[10] For example, high charge mobility of 0.1 $cm^2 V^{-1} s^{-1}$ had been previously reported for ladder polymer, poly(benzobisimidazobenzophenanthroline) (BBL) which is 10^5 times higher compared to its non-ladder analog (BBB) with mobility of 10^{-6} $cm^2 V^{-1} s^{-1}$.[11] Hence, ladder-type molecules are being explored for NLO applications. For instance, ladder-type dithienosilolo-carbazole (DTSC) and dithienopyrrolo-carbazole (DTPC) have been utilized to synthesize poly(dithienosilolo-carbazole-alt-benzothiadiazole) and poly(dithienocyclopenta-carbazole-alt-benzothiadiazole) respectively, for application in organic field-effect transistors (OFET).[12] Furthermore, in the context of organic photovoltaics, ladder-type dithienonaphthalene (DTN) has been synthesized as an electron-rich donor unit for constructing donor-acceptor copolymers. A range of electron-deficient acceptor moieties-including benzo[c][1,2,5]thiadiazole (BT), 5,6-bis(hexyloxy)-4,7-di(thiophen-2-yl)benzo[c][1,2,5]thiadiazole (TBT), and 2,5-bis(2-ethylhexyl)-3,6-di(thiophen-2-yl)pyrrolo[3,4-c]pyrrole-1,4(2H,5H)-dione (TDPP) have been paired with DTN to produce high-performance donor-acceptor copolymers for organic solar cell (OSC) applications.[13]

The architectural rigidity and coplanarity of ladder-type conjugated polymers not only enhance their thermal and morphological stability but also have profound effects on their electronic properties.[14] Interestingly, ladder-type conjugated systems exhibit quasi-two-dimensional (Quasi-

2D) charge transport behavior, which contributes to enhanced charge mobility and conductivity.[15] This Quasi-2D behavior arises from their rigid, coplanar and extended π-conjugation backbones. The coplanar geometry and extended conjugation facilitate efficient intramolecular charge delocalization and promote strong intermolecular π-π interactions through close face-to-face stacking in the solid state.[16,17] Furthermore, ladder-type conjugated materials, with their graphene-like architecture, offer defect-free structures and exceptional film-forming properties. Unlike graphene, which has a zero band gap, these oligomers feature tunable band gaps, making them versatile semiconducting materials for a variety of electronic devices.[11,18]

However, while significant efforts have been directed towards donor-acceptor (D-A) modifications on ladder-type molecules to improve charge mobility, a fundamental understanding of intrinsic charge dynamics in unsubstituted ladder systems remains limited. To understand the fundamental relationship between molecular structure and charge transfer properties in extended conjugated ladder systems, we previously reported the synthesis of a series of unsubstituted Benzo[k]tetraphene (BTp) oligomers with systematically increased conjugation lengths (n = 5, 7, 9 and 11) using iterative Suzuki-Miyaura coupling and ring-closing olefin metathesis (**Figure 3.1**).[19] BTps represent a class of fully conjugated ladder oligomers with an armchair graphene nanoribbon-like architecture, structurally analogous to [n]acenes and [n]phenacenes which have garnered interest in a broad range of optoelectronic applications.[19–21] Unlike D-A systems, where substituents groups can obscure intrinsic charge transport behavior, the unsubstituted BTp oligomers were deliberately synthesized to directly investigate how systematic variations in molecular length influence charge mobility, electronic coherence, and excited-state dynamics.

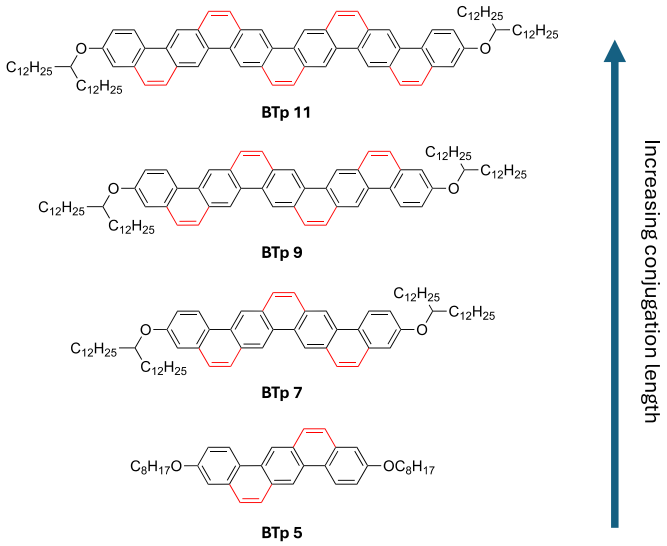


Figure 3.1: Structures of the series of BTp oligomers

In our previous study, we demonstrated that molecular size critically influences solid-state packing in the BTps for which smaller oligomers like BTp-7 crystallizes readily at room temperature due to higher molecular mobility, whereas larger oligomers such as BTp-11 require thermal annealing to overcome kinetic trapping induced by stronger intermolecular interactions to achieve high crystallinity. We further highlighted the critical balance between molecular mobility and intermolecular interaction in obtaining highly ordered films which is a key factor for optimizing device performance. Initial spectroscopic investigations of the BTp series revealed rapid saturation of optical properties with increasing conjugation length, suggesting that further π-extension beyond its critical threshold does not significantly enhance optical properties. However, a deeper understanding of how the saturation of the optical properties correlates with fundamental photophysical processes such as charge transfer and excited-state dynamics in the BTps is required.[19]

In this paper, we demonstrate how tuning molecular length of unsubstituted BTp ladder oligomers governs their charge transfer efficiency, excited-state dynamics, and nonlinear optical

response. By identifying an optimal conjugation length that balances extended π-delocalization, enhanced intramolecular charge transfer and prolonged excited-state lifetimes, we provided insights into their intrinsic structure-function relationships critical toward guiding their design as efficient organic semiconductors materials.

3.4. Methods

3.4.1. Steady State Measurement

The steady state absorption and emission experiment were done in dilute chloroform solution using a 1cm path lengths cuvette for all measurement. For the steady state absorption, the Agilent Cary 60 UV-Vis spectrometer containing a xenon lamp that measures from 190 nm to 1100 nm was used. The BTp spectra were measured from 200nm to 800 nm. The FluoroMax-4 fluorimeter with an entrance and exit slit of 1.0 nm and an integration time of 1.0 s was used to measure the fluorescence emission of the BTp samples.

3.4.2. Fluorescence Quantum Yield

The fluorescence quantum yield (Φ_F) of the BTp oligomers were determined using the Williams comparative methods.[22,23] The solutions were diluted with optical densities ranging from 0.1 to 0.05. 9,10-dichloroanthracene in diluted dichloromethane was used as the standard for comparison. The absorption and emission spectra measurement were done with a 1 cm quartz cuvette using the Agilent Cary 60 UV-Vis spectrometer and the FluoroMax-4 fluorimeter respectively.

3.4.3. Classical Two Photon Absorption

The classical two photon absorption cross-sectional area of the BTp oligomers were determined using the Two-Photon Excited Fluorescence (TPEF) technique.[24] The Ti:Sapphire mode-locked Tsunami laser which is tunable from 700 nm to 900 nm was used giving a 110 fs

pulse output with 80 MHz repetition rate. The power dependence scan was done was done to calibrate the system and obtain a dependence used for the experiment. The TPA fluorescence emission was measured by excitation at 400 nm and the maximum emission wavelength was obtained. A neutral density filter was used to control the input photon flux of the laser. Coumarin 307 was used as a standard for the experiments. The absorbance of the BTp were less than 1.0 to prevent any oversaturation effect during the measurement. The Two-photon power dependence fluorescence intensity plot was used as a function of the Log of the counts per seconds to the Log of the input photon flux in (mW) was used in calculating the TPA cross-sectional area.

3.4.4. Entangled Two Photon Absorption

The entangled two photon absorption of the BTp oligomers setup previously described by Goodson and coworkers was used for the measurement.[25] The entangled photons were generated via a Spontaneous Parametric Down Conversion (SPDC) using a Type I Barium Beta Borate (BBO) crystal with a continuous wave (CW) laser. The pump of 405 nm from the CW laser passes through a motorized adjustable neutral density filter to control the pump power into the BBO crystal thereby generating the entangled photons. The entangled photons are directed towards a band pass filter to remove other wavelength of light other than the entangled photons and is focused toward the 1cm path length quartz cuvette containing the diluted BTp solutions. The entangled photons pass through the cuvettes and enter the avalanche photodiode (APD). Chloroform was used as a solvent for calibration to set the baseline used in measuring the entangled photon transmission rate with about 5.0 x 10^6 input photon flux. The solvent is introduced into the cuvette and the entangled photon transmission was measured by adjusting the motorized neutral density filter to control the input photons to obtained about five measurements to get a good signal-to-

noise ratio. The loss in the entangled photon transmitted is observed in comparison to the chloroform.

3.4.5. Time Correlated Single Photon Counting

The time resolved fluorescence and phosphorescence lifetime of the BTp oligomers were measured using the Time Correlated Single Photon Counting (TCSPC) system. The Kapteyn-Murnane mode-locked TI:Sapphire laser was used which pumps the Beta Barium Borate (BBO) crystal with 800 nm wavelength to generate a 400 nm pump via frequency doubling. The 400 nm light is directed to a 1cm path length cuvette containing the diluted solution and the emission is detected with a monochromator. The photomultiplier tube converts the photons to count and the plot of counts against wavelength is obtained.

3.4.6. Nanosecond Transient Absorption Spectroscopy

The lifetime of the long-lived transient species of the BTp oligomers were investigated using the nanosecond transient absorption technique. The ND: YAG (Neodymium Yttrium Aluminum Garnet) laser was used which is used to pump the tunable GWU Optical Parametric Oscillator (OPO) (**Figure S3.1**). The Xenon flash lamps pump the ND: YAG rods and generate the 1064 beam. The 1064 nm fundamental beam is used to pump the harmonic generator which composes of the KD*P crystal to generate the 532 nm and 355 nm beam which goes into the OPO. The desired excitation pump from the (OPO) was directed to the LP980 Edinburg spectrometer which contains the probe light, the sample holder, and the monochromator for detection. Rubppy was used as a standard for calibrating the spectrometer. For the β-band, the pump wavelength was set at 310 nm, 330 nm, 353 nm and 363 nm for the BTp 5, BTp 7, BTp 9 and BTp 11respectively. The transmitted signal is converted to electric signal by oscilloscope and the change in absorption

is measured by the LP980 software. The graph of the change in absorption versus the wavelength gives the dynamic of the charge species present.

3.5. Results and Discussion

3.5.1. Steady State Optical Properties

The UV-vis absorption spectra of the BTp oligomers exhibit features characteristic of ladder-type polycyclic aromatic hydrocarbons (PAHs), with well-defined bands corresponding to distinct $\pi \rightarrow \pi^*$ electronic transitions.[26] Just like most PAH, the three highly resolved distinctives peaks were assigned as α, β and p-band corresponding to different energies levels.[27] The α-band, typically the lowest-energy feature, arises from a symmetry-forbidden transition and appears with weak intensity. In contrast, the β-band corresponds to a symmetry-allowed transition with strong oscillator strength and represents the fundamental absorption peak in the near-UV region. As seen from **Figure 3.2A**, a red shift in the absorption maxima was observed in the BTps with wavelength of 310 nm, 340 nm, 353 nm and 362 nm for the BTp 5, BTp 7, BTp 9 and BTp 11 indicating a strong dependence of the optical properties on conjugation length. The p-band, although formally dipole-forbidden, gains intensity through vibrational coupling, with oscillator strength borrowed from the adjacent β-band transitions. The p-band corresponds to the direct HOMO → LUMO transitions which reflect the core electronic properties of the BTps.[27] Interestingly, the p-band shows a red-shift with increasing intensity in the extended conjugated BTps. This is due to enhanced orbital overlaps which allow for stronger electronic transitions. The optical band gaps of the BTp series, determined from the onset of the p-band, exhibits a clear narrowing trend with increasing conjugation length (**Table 3.1**). However, the change in optical band gap between BTp-

9 and BTp-11 is minimal, indicating a saturation effect in the electronic properties supported by effective conjugation length (ECL) analysis.[19]

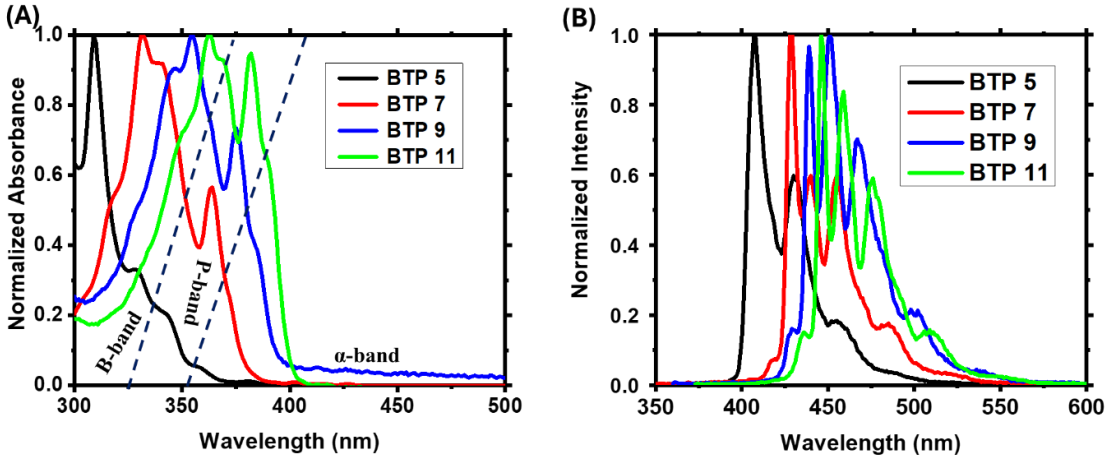


Figure 3.2: (A) Normalized steady state absorption spectra in chloroform. Excitation wavelength was 400 nm in all cases (B) Normalized steady state emission spectra in chloroform. Excitation wavelength was at their absorption maxima: 310 nm, 340 nm, 353

Fluorescence emission spectra shows a similar red shift with increasing conjugation, with emission maxima at 420 nm, 440 nm, 460 nm, and 475 nm for BTp-5, BTp-7, BTp-9, and BTp-11, respectively (**Figure 3.2B**). This trend further reveals the influence of conjugation on the electronic structure of the BTps. However, the emission maxima (λ_{ems}) exhibit minimal change between BTp-7, BTp-9, and BTp-11, indicating that the energy of the lowest excited state stabilizes beyond the critical conjugation length. Our steady state experimental data suggests that further extension of the conjugated backbone does not substantially alters the excited-state energy thereby providing insight into the onset of saturation effect in the optical properties of the unsubstituted BTps oligomers. This saturation effect is evident from the fluorescence quantum yields (Φ) (9.1%–9.9%), which remain relatively constant across the BTp series, despite differences in conjugation

length (Table 1). The Φ of the BTps is in the same range with similar ladder system such as the monomeric perylene diimide (PDI) with reported low Φ of < 1%, which was attributed to be due to slow spin-orbit induced intersystem crossing.[28] Wasielewski and co-workers had previously reported a constant range of Φ (0.18 - 0.20) for Perylene-3,4:9,10-bis(dicarboximide) (PDI) derivatives with increasing PDI units.[28] The saturation of the Φ reflects a structural threshold in the effective conjugation length, beyond which additional extension of the π-system no longer significantly influence radiative efficiency. This behavior is similar to observations in organic ladder polymeric systems, where the excited-state wavefunction is delocalized over multiple repeat units, and increasing the monomer size result in negligible change on the photophysical properties.[29,30] In the BTps, although being discrete oligomers, the excited-state density is already spread across a sufficiently long conjugated segment by BTp 7 to BTp 9, such that further π-extension (as in BTp 11) does not lead to enhanced radiative decay rates or additional suppression of nonradiative pathways. Moreover, the rigid, planarized backbone of the unsubstituted BTps ensures that the electronic structure is saturated once optimal delocalization is achieved. Thus, the near-constant quantum yields across the higher members of the series are a manifestation of a conjugation-dependent saturation effect, where further increases in molecular length do not translate to enhancement in emissive efficiency.

Table 3.1: Steady state absorption and emission of the BTP oligomers in chloroform

Compound	$\lambda_{abs\text{-}exp}$ (nm)	$\lambda_{abs\text{-}cal}$ (nm)	λ_{ems} (nm)	Optical band gap (ev)	Φ (%)	Oscillator Strength
BTp 5	310	294	410	3.07	9.55 ± 1	1.848
BTp 7	330	340	428	2.92	9.91 ± 2	2.023
BTp 9	353	359	439	2.85	9.20 ± 2	2.397
BTp 11	362	379	447	2.80	9.10 ± 2	2.106

Where $\lambda_{abs\text{-}exp}$ = Experimental Absorption Maximum, $\lambda_{abs\text{-}cal}$ = Theoretical Absorption Maximum, λ_{ems} = Emission maximum and Φ = fluorescence quantum yield. * B3LYP/6-311G (d,p) was used for the theoretical calculations. * Oscillator strength values are obtained theoretically.

3.5.1. Electronic Structures calculations

Time-dependent density functional theory (TD-DFT) calculations using the ORCA software package was used to simulate the UV-Vis absorption spectra and determine fundamental parameters governing optical transitions in the BTps. The resonant peak obtained from the calculated absorption maximum was used in determining the oscillator strength of the BTp oligomers (**Table S3.1- S3.4)**. As seen from Table 1, the calculated absorption maximum for the BTp 5, BTp 7, BTp 9 and BTp 11 were 294 nm, 340 nm, 359 nm and 379 nm respectively, which matches with the experimental results where a red shift in the absorption wavelength was observed as the conjugation length increases. We further determined the oscillator strengths associated with these transitions in the BTps ladder system. From BTp 5 to BTp 9, we observed a modest increase in oscillator strength, consistent with enhanced HOMO-LUMO overlap arising from enhanced π-extension and increased electron delocalization across the conjugated backbone. However, in BTp

11, although the molecular framework is more extended, the frontier molecular orbitals begin to show signs of spatial confinement. The HOMO and LUMO become more localized toward the central aromatic rings, reducing their effective overlap across the full π-system (**Figure 3.3**). This orbital localization correlates with the observed leveling off in oscillator strength, suggesting that additional conjugation beyond this length does not significantly enhance the transition probability.[31,32]

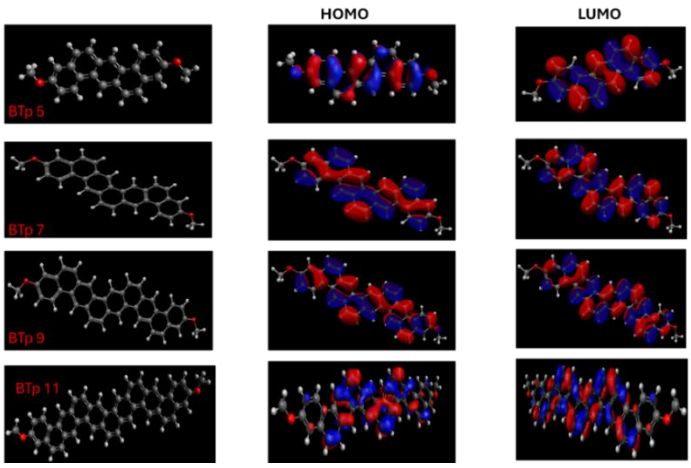


Figure 3.3: Molecular orbital of the BTp 5, BTp 7, BTp 9 and BTp 11

3.5.2. Classical Two Photon Absorption

To investigate the intrinsic NLO response of the unsubstituted BTp ladder-type oligomers under nonlinear excitation, we measured their two-photon absorption (TPA) properties using fluorescence-based spectroscopy.[24,33]

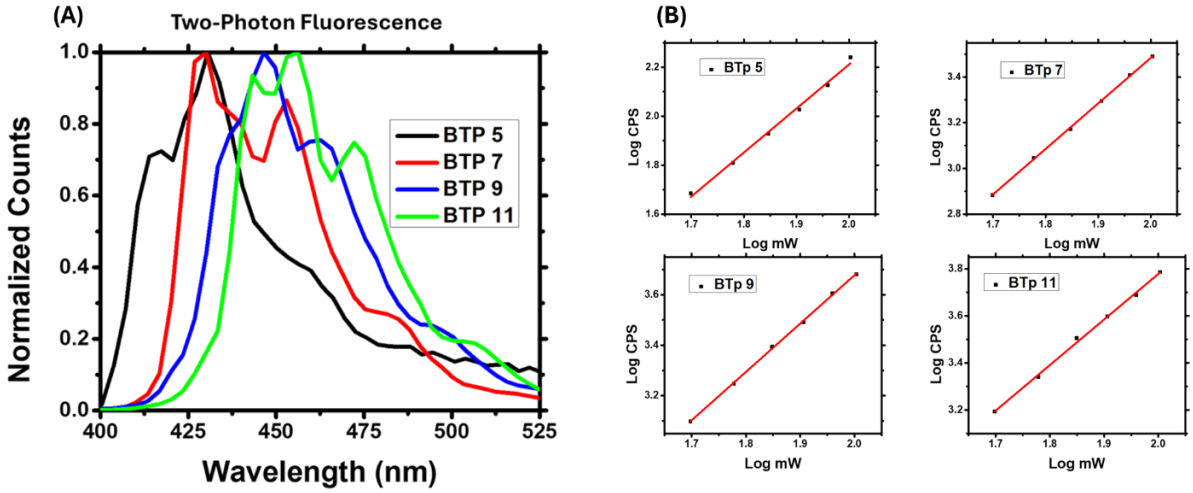


Figure 3.4: (A) Two photon fluorescence of the BTps oligomers (B) Classical Two-Photon Absorption of the BTp ladder oligomers. All measurements were done in chloroform.

The fluorescence emission spectra obtained upon two photon excitation (**Figure 3.4A**) shows a red-shift from BTp 5 to BTp 11, consistent with the trends observed in their steady-state absorption and emission spectra. The fluorescence intensity scales quadratically with excitation intensity (**Figure 3.4B**), confirming the nonlinear two-photon excitation process across the BTp series. The TPA cross-sections (δ) increased progressively from 0.64 GM in BTp 5 to 4.73 GM in BTp 11 (**Table 3.2**), in line with enhanced π-conjugation and transition dipole strength across the series. The plot of the δ to the conjugation length is shown in **Figure 3.5A**. To account for effect of molecular size on the NLO response, we normalized δ by the number of π-electrons (N_e), yielding the δ/N_e ratio. This δ per-electron metric increased linearly from BTp 5 to BTp 7 (**Figure**

3.5B), reflecting efficient charge redistribution, enhanced oscillator strength and coherent orbital coupling with increasing conjugation.[34–38]

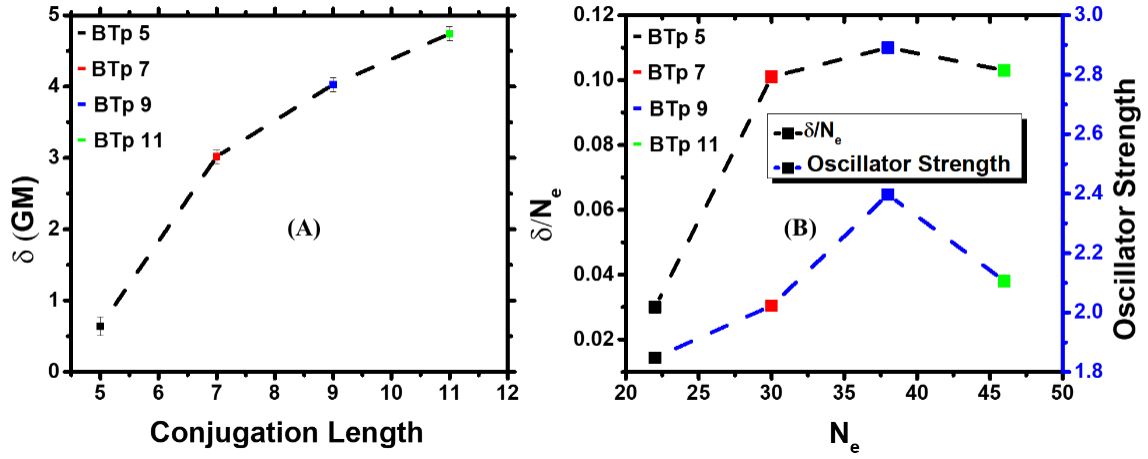


Figure 3.5: (A) Comparison of the TPA cross-section of the BTp with their conjugation length (B) Plot of the ratio of δ to the number of π-electrons (δ/Ne); and the oscillator strength against the number of conjugated electrons

However, the trend plateaued beyond BTp 7, with δ/N_e showing negligible change between BTp 9 and BTp 11 suggesting saturation in nonlinear optical response (**Figure 3.5B**). This observation aligns with prior findings in extended conjugated systems, where δ increases with oligomer length up to a critical threshold, beyond which further extension yields no significantly enhancement on the nonlinear response.[39] Theoretical calculations support this interpretation. As shown in Figure 3, HOMO and LUMO delocalization increases from BTp 5 to BTp 9, but begins to localize in BTp 11, reducing effective orbital overlap and transition dipole density. [40–42] This loss of coherence in the excited-state wavefunction limits the nonlinear susceptibility, leading to the observed plateau in δ/N_e in the longer BTps.

The nonlinear optical response across the BTp series offers direct access to the electronic nature of the p-band, associated with the lowest-energy HOMO → LUMO transition. The δ across the series correlates to the red-shift and increased intensity of the p-band in the steady-state spectra, establishing a clear correlation between nonlinear susceptibility and the underlying frontier orbital properties. While the intensity of the p-band appears to increase as seen in the one photon absorption, the δ/N_e beyond BTp 9 reveals the onset of saturation and sensitivity to nonlinear optical response. Our experimental data demonstrates the importance of tuning the electronic properties of the unsubstituted BTps via donor-acceptor engineering rather than just molecular extension, for optimizing the charge transfer and excited-state dynamics to enhanced nonlinear optical performance beyond the intrinsic conjugated limit.

Table 3.2: TPA and ETPA cross-section of the BTp oligomer

Compound	Conc[a] (M)	δ (GM)	Conc[b] (M)	σ_e(cm^2/molecule)
BTp 5	2.52 x10^{-5}	0.64 ± 0.13	6.15 x10^{-5}	1.24 x10^{-19}
BTp 7	4.00 x10^{-5}	3.02 ± 0.10	5.40 x10^{-5}	1.32 x10^{-19}
BTp 9	8.53 x10^{-5}	4.03 ± 0.10	8.33 x10^{-5}	1.76 x10^{-19}
BTp 11	7.00 x10^{-5}	4.73 ± 0.10	9.37 x10^{-5}	2.07 x10^{-19}

Conc[a] = Concentration used in TPA calculation, δ = TPA cross-section, Conc[b] = Concentration used in ETPA calculation and σ_e = ETPA cross-section. All experiments were done in chloroform. Excitation wavelength for the TPA was 810 nm. For the ETPA (signal and idler wavelengths are 810 respectively)

3.5.3. Entangled Two Photon Absorption (ETPA)

We extended our investigation of the nonlinear optical properties of the BTp ladder-type oligomers into the quantum domain using ETPA spectroscopy. ETPA takes advantage of the unique temporal and energy-time correlations of entangled photon (EP) pairs, [43–47] which allow is sensitive to electronic transitions that are often inaccessible or weakly coupled under classical excitation, providing a deeper understanding into the photophysical properties of the molecular system during the transition.[48–50] The EPs are generated via spontaneous parametric down conversion (SPDC). In SPDC, a high-intensity pump beam with frequency (ω_p) interacts with a second-order (χ^2) nonlinear crystal, producing a pair of lower-energy EPs (signal and idler) that are strongly correlated.[45] Unlike classical TPA which requires high photon fluxes, ETPA can occur efficiently even at low light intensities because the strong quantum correlations between the photons effectively enhance the two-photon interaction probability. This makes ETPA a sensitive probe of a material's ability to preserve and transfer quantum correlations, providing direct insight into potential suitability for quantum information applications.[44,46] The plot of the ETPA rate versus the input photon flux of the BTps is shown in **Figure 3.6**.

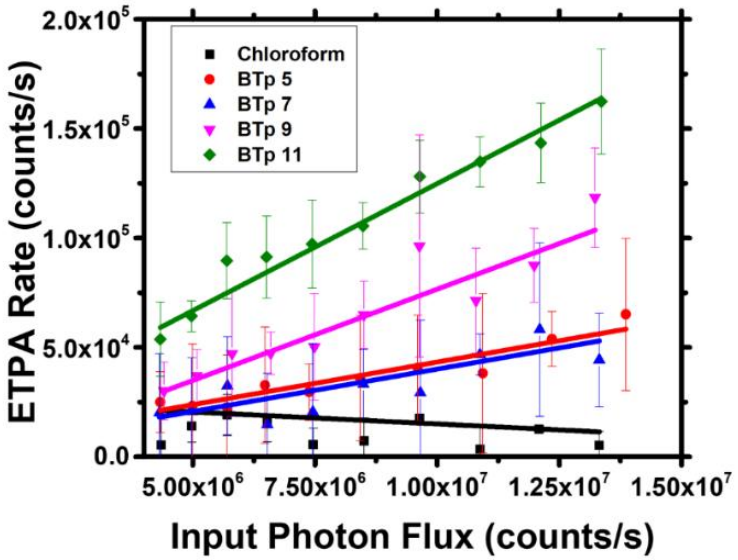


Figure 3.6: Rate of the Entangled Two-Photon absorption versus the input photon flux. Chloroform was used as solvent

The NLO response of the BTp ladder oligomers under entangled photon excitation reveals a clear structure-property relationship governed by molecular conjugation and electronic delocalization. As shown in Table 2, while all BTps interact with entangled photons on the same order of magnitude, we observed a progressive increase in the ETPA cross-section (σ_e) with increasing π-conjugation length. The σ_e of the BTp 5, BTp 7, BTp 9 and BTp 11 are 1.24 x10^{-19} cm^2/molecule, 1.32 x10^{-19} cm^2/molecule, 1.76 x10^{-19} cm^2/molecule and 2.07 x10^{-19} cm^2/molecule respectively. This increase in the σ_e arises from enhanced orbital delocalization and improved HOMO-LUMO overlap across the extended π-backbone of the BTps, which increases the transition dipole moment and facilitate stronger coherent coupling with entangled photon pairs. The σ_e correlate strongly with the oscillator strengths and the degree of spatial electronic delocalization observed in the molecular orbitals of the BTps, demonstrating the role of electronic structure in contributing to quantum effects. Previous studies has demonstrated that the σ_e depends

not only on the magnitude of the transition dipole moment induced by the entangled photons but also on the excited state lifetime and coherence during the absorption process.[44,51] While a modest increase in σ_e is observed across the series, the change becomes less pronounced beyond BTp 7, with little enhancement observed between BTp 9 and BTp 11. This suggests that extension of the π-conjugated backbone beyond BTp 7 contributes minimally to entangled two-photon absorption, indicating a saturation in effective orbital overlap. This leveling effect in the σ_e correlates with the reduction in oscillator strength of BTp 11 and spatial confinement of the electron density as seen from the molecular orbitals, suggesting saturation in effective orbital overlap and transition dipole coupling.[43,44,52]

Our findings is consistent with the previous observation by Kang and co-workers who reported an initial increase in the σ_e of extended oligothiophenes from 1.3 x10^{-19} cm^2/molecule to 7.1 x10^{-19} cm^2/molecule for 6 and 18 thiophene units respectively, but also predicted that further increase in the molecular extension may induce conformational disorder, vibrational coupling, and enhanced intermolecular interactions leading to a possible decoherence in the ETPA process.[51] Such interactions are known to facilitate nonradiative decay and shorten excited-state coherence times.[44,51,53,54] Since ETPA processes are sensitive to both electronic delocalization and excited-state lifetime,[44,53] this suggests that saturation in the electron density and the possible coherence loss due to stronger intermolecular interaction in the longer BTps contributes to the minimal effect on the σ_e despite increasing molecular conjugation, providing a further evidence for the observed saturation. Our findings further show that the BTps demonstrate sensitivity to entangled photons as a function of excited-state coherence and electron delocalization which can be tuned through

molecular conjugation. The tunability of the electronic properties and synthetic versatility of the BTps make them a promising candidate for future developments in quantum sensing applications.

3.5.4. Time Correlated Single Photon Counting

The emissive dynamics of the BTps were investigated using the time-correlated single-photon counting (TCSPC). The fluorescence dynamic of the BTp oligomers is shown in **Figure 3.7**, and the results are summarized in Table 3. Interestingly, as seen from Figure 2 A and Figure 2B, the BTps series display relatively large Stokes shifts (~85 nm), suggesting that the emissive state is not purely locally excited (LE), but likely exhibits mixed LE-CT character arising from internal polarization along the extended π-conjugated backbone. We observed that the fluorescence lifetime increases systematically with conjugation length. In this context, the shorter lifetime observed for BTp 5 reflects a more localized and less stabilized excited state, while the longer lifetimes in BTp 7 and BTp 9 indicate enhanced excited-state delocalization and partial charge redistribution. Such a relaxation pathway supports reduced exciton recombination and promotes longer diffusion lengths, properties that are desirable in optoelectronic applications.[55–57] However, the slight reduction in lifetime observed in BTp 11 points to the onset of excited-state saturation consistent with the decreased oscillator strength and increased orbital localization predicted by TD-DFT calculations.

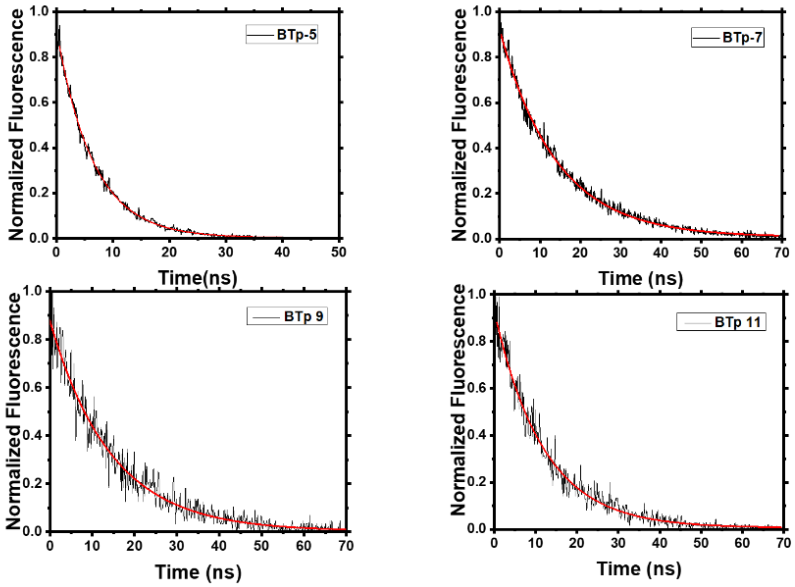


Figure 3.7: Time resolved measurement of the emission lifetime of the BTp oligomers in chloroform.

Table 3.3: Table Showing the Emission Lifetime of the BTP Oligomers in chloroform. The excitation wavelength for all samples was 400 nm

Compound	τ- (ns)	k (s^{-1})
BTP 5	6.97 ± 0.04	1.43 x10^{7}
BTP 7	13.94 ± 0.18	6.59 x10^{6}
BTP 9	14.40 ± 0.23	6.38 x10^{6}
BTP 11	11.90 ± 0.21	7.64 x10^{6}

This is consistent with our earlier observations in both TPA and ETPA measurements, reinforcing the conclusion that BTp 9 defines the upper threshold for effective electronic

delocalization in this series. Beyond this point, additional conjugation does not enhance excited-state coherence or transport-relevant photophysical properties, suggesting a transition from dynamic tunability to electronic saturation.

3.6. Nanosecond Transient Absorption Spectroscopy

Nanosecond transient absorption (ns-TA) spectroscopy was utilized to investigate the excited-state dynamics of the BTp oligomers. The schematic diagram of our ns-TA spectroscopic setup used for the experiment is shown in Figure S1. All the BTPs have strong absorption in the UV-region and were excited at their absorption maxima: 310 nm, 330 nm, 355 nm and 363 nm for the BTp 5, BTp 7, BTp 9 and BTp 11 respectively. The spectra showing the time dynamics at different wavelengths is shown in **Figure 3.8**.

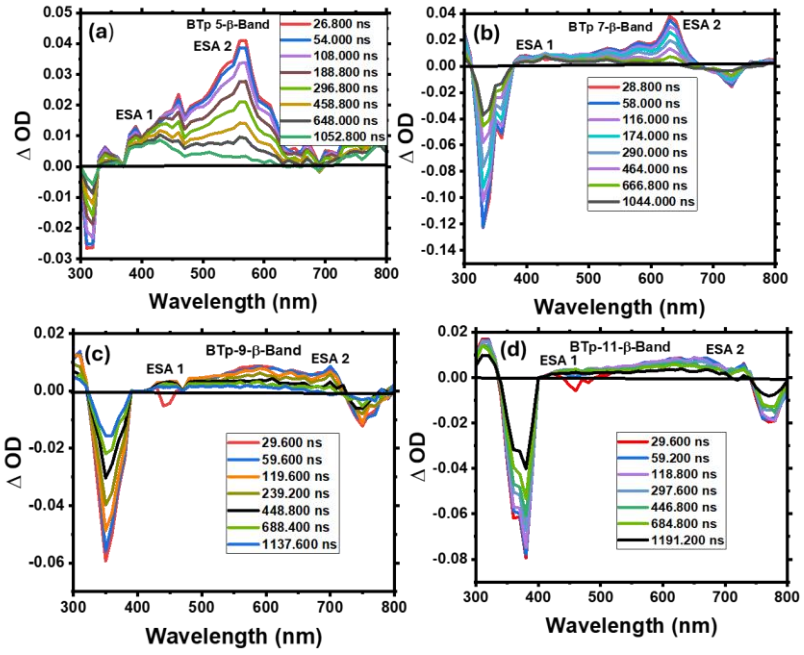


Figure 3.8: ns-TA spectra of the BTp: (a) BTp 5, (b) BTp 7, (c) BTp 9, (d) BTp 11 in chloroform

The ns-TA spectra of the BTps reveal two key features: a negative ground state bleach (GSB) signal, corresponding to their steady-state absorption spectra, and a positive excited state absorption (ESA) signal (**Figure 3.8**). The transient spectra of the BTps display a broad ESA signal, ranging from 400 nm to 610 nm in BTp 5, 400 nm to 680 nm in BTp 7, 400 nm to 700 nm in BTp 9, and 400 nm to 750 nm in BTp 11 (Figure 8). These broad ESA features reflect the extended conjugation and delocalization of electronic states across the π-backbone of the BTps, suggesting a strong coupling between the excited states and the underlying molecular orbitals.[58]

In BTp 5, the intensity of ESA peak is most prominent at 520 nm. As the conjugation length increases in BTp 7, the ESA shifts to longer wavelengths, with the ESA intensity reaching a maximum at 630 nm. In contrast, for the longer oligomers, BTp 9 and BTp 11, the ESA feature becomes progressively broader with reduced intensity. The broadening of the ESA is consistent with findings from previous studies, which have shown similar spectral broadening in extended conjugated systems.[58,59] This broadening is often attributed to multiple low-energy molecular conformations contributing to the excited-state manifold, which is pronounced in longer and more delocalized conjugated systems.[59] A closer examination of the transient spectra of the BTps reveals two distinct ESA bands around 430 nm and above 530 nm (**Figure 3.8**). These features persist throughout the ns-TA temporal window, with similar decay profiles, indicating the presence of multiple conformers that absorbs at slightly different energies but share the same excited-state configuration. This observation aligns with our theoretical calculations, which show contributions from different molecular orbitals. (**Figure S3.5 – S3.8**). Similar features have been reported in oligofluorene systems where vibronic progressions and conformation inhomogeneity leads to multiple ESA bands with similar dynamics.[58,60] These multiple ESA bands in oligofluorenes were attributed to transitions from the lowest singlet excited state (^1B_u) to higher mA_g states with all

exhibiting identical kinetics.[60] Hayes and co-worker proposed that these transitions involve significant contributions from delocalized states in the oligofluorenes, which is consistent with the observed redshift in the ESA band as the conjugation length increases. This suggests that the two ESA features observed in the unsubstituted BTps originate from the same excited state, but with different contributions from mixed molecular orbitals, resulting in absorption at distinct wavelengths.

The GSB of the BTp series was analyzed by fitting the decay profiles with a bi-exponential function, revealing two distinct relaxation pathways: a fast component associated with short-lived excited states and a slower component indicative of a long-lived species (**Figure S3.2).** The decay of the fast component (τ_1) of the GSB for the BTp series closely matches the decay of the fast (τ_1) component of the ESA, indicating the deactivation of the singlet excited state evident from the BTp 5 and BTp 7.[58,61] However, BTp 9 and BTp 11 exhibit a longer GSB decay compared to their ESA decay, suggesting multiple deactivation pathway in the extended oligomers. The extended GSB decay likely points to additional relaxation processes, such as the involvement of higher-lying triplet states or stabilization of charge transfer state in the longer BTps.[58,62]

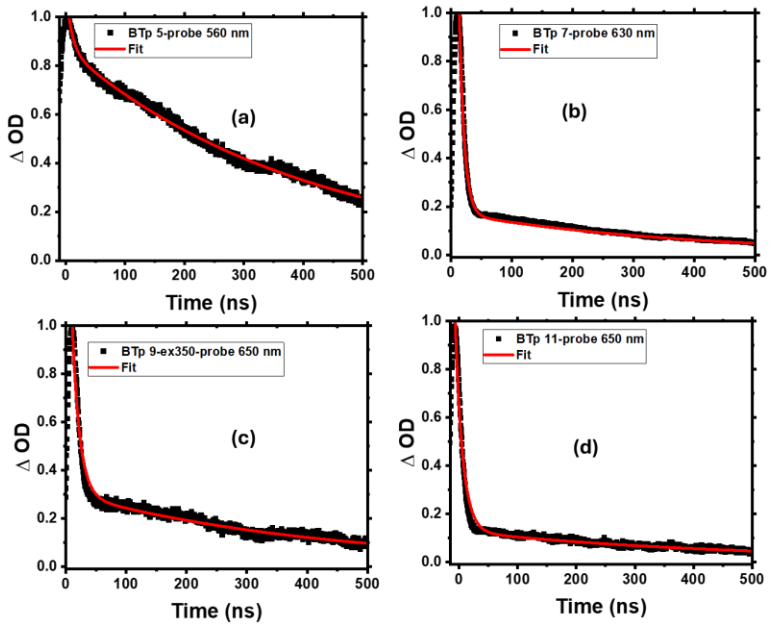


Figure 3.9: Kinetic spectra of the BTp: (a) BTp 5, (b) BTp 7, (c) BTp 9, (d) BTp 11 in chloroform

As discussed earlier regarding the two ESA features, the dynamics of ESA 1 are shown in Figure S3. Meanwhile, we show the dynamic of the ESA 2 from 0 ns to 500 ns in **Figure 3.9**. This kinetic trace monitored at their ESA band exhibited a biexponential decay comprising of a fast component and long-lived component. Notably, the fast component (τ_1) of the ESA decay remains unaffected upon purging with nitrogen, revealing the singlet character of the excited states. The ESA lifetime of the fast component (τ_1) of the BTps corresponds closely to their florescence lifetime independently measured by our TCSPC (**Table 3.3 and Table 3.4**), thus we assigned this component to a convolution of charge recombination process and decay of the singlet excited state.[66,67] This is consistent with the report by Lin Chen and co-workers, on the excited-state dynamics of fused-ring perylenediimide–thienoacene dimers, where the correlation between the fast ESA component and the emission lifetime was attributed to the recovery of the CT state.[58]

However, despite the relatively longer singlet lifetime, the BTps exhibits low fluorescence quantum yield (approximately 0.09) indicating only small fraction of the singlet state decay radiatively. This suggests that the singlet state is depopulated through non-radiative pathway like intersystem crossing (ISC).[65]

The BTps exhibit longer decay of the singlet excited state dynamic in comparison with well-known perylene diimide (PDI) monomer with a singlet excited state lifetime of (~ 3.5 ns) and a fluorescence quantum yield approaching infinity (~ 0.9).[63,66] This indicate that the deactivation of the singlet state in PDI monomer occurs radiatively with negligible ISC which limit efficient triplet population.[65,67] The prolonged S_1 lifetime of the BTp ladder oligomers can be attributed to their rigid planar structure which promotes exciton delocalization and this in effect stabilizes the singlet excited state and the CT promoting efficient intersystem crossing. This facilitates triplet formation in the BTps with significant implications for application in triplet-harvesting where long-lived singlet and triplet state are desired. The effect of conjugation length on excited-state dynamics is evident from the ESA measurements. The BTp 5, the shortest oligomer in the series exhibits a rapid ESA decay ($\tau_1 \sim 9.4$ ns), indicating faster relaxation dynamics likely due to limited exciton delocalization. In contrast, the BTp 7 and BTp 9 oligomers, with increased conjugation lengths, show longer ESA lifetimes ($\tau_1 \sim 11.5$ ns and $\tau_1 \sim 12.1$ ns, respectively), consistent with enhanced exciton delocalization and more stable excited states. This suggests efficient ISC in the extended BTp in comparison to the BTp 5. Molecular orbital calculations further support this trend, revealing increase in electronic delocalization as the conjugation length increases from BTp 5 to BTp 9 (Figure 3). This suggests that the BTp 7 and BTp 9 oligomers exhibit more stable singlet and CT states, which reduces non-radiative decay pathways and promotes efficient triplet

formation. Interestingly, electronic delocalization appears to reach a saturation point beyond BTp 9, which corresponds with the observed leveling off in the ESA lifetimes.

Additionally, a significant increase in the τ_2 ESA lifetime from nanoseconds to microseconds was observed upon nitrogen purging, confirming the presence of triplet states in these systems (**Table 3.4 and Figure S3.4**).[68,69] The extended ESA lifetimes associated with triplet excitons play a crucial role in enhancing charge separation and exciton mobility, both of which are essential for the performance of organic solar cells (OSCs).[70,71] Similar molecular architectures to BTp, such as tetracene and pentacene, have been widely studied for their potential in high-performance OSCs, utilizing efficient triplet state formation via singlet exciton fission to improve photovoltaic efficiency.[72–77] The triplet exciton dynamics in the BTp series suggest that extended conjugation improves the efficiency of triplet state formation, which is a valuable characteristic for OSC materials.

The triplet excited-state dynamics of the BTp oligomers show a clear dependence on conjugation length, offering valuable insights into how extended conjugation influences dynamics of triplet excitons. As seen from Table 4, the triplet excited-state lifetime (τ_2) in BTp 7 and BTp 9 upon purging with nitrogen is approximately three times longer than in BTp 5, highlighting the role of enhanced delocalization in extending the triplet state lifetime. However, beyond BTp 9, no significant increase in triplet lifetime is observed, indicating a saturation of triplet state dynamics. The decay rate of the triplet excited states was determined to be 7.6 $x10^5$ s^{-1}, 2.1 $x10^5$ s^{-1}, 2.2 $x10^5$ s^{-1}, and 2.3 $x10^5$ s^{-1} for the BTp 5, BTp 7, BTp 9 and BTp 11 respectively. As conjugation length increases from BTp 5 to BTp 9, the decay rates decrease, indicating longer-lived triplet excitons. However, the decay rates for BTp 9 and BTp 11 are nearly identical, indicating that the triplet state

dynamics have reached a limit, and further elongation of the conjugation length does not significantly improve the triplet excited state lifetime. Previous studies have shown that the triplet lifetime increases with conjugation length up to an optimal point, after which the system reaches a threshold where further conjugation does not improve the triplet exciton dynamics.[29] We suggested that the extended π-delocalization in the longer BTps reduces the exchange interaction, leading to a narrower singlet-triplet energy gap, thereby promoting more efficient ISC. This spatial delocalization lowers the electronic coupling between the triplet excited state and the ground state by reducing electron-phonon interactions and minimizing vibrational reorganization energies. Consequently, the efficiency of nonradiative decay pathways is significantly suppressed as we increase the conjugation from BTp 5 to the longer BTps. The leveling effect in the rate of decay of the triplet excited state observed in the longer BTp 11 indicates the critical point of electronic delocalization. The result from the ns-TA indicating a saturation in the excited state dynamic of the BTps is consistent with our TPA and emissive dynamic experimental data. These confirm the critical threshold in the conjugation length where further extension of the BTp oligomer no longer enhances the CT properties and NLO response. This correlation suggests that the excited state dynamic and the NLO properties of the BTps are governed by a shared mechanism in which electronic delocalization through conjugation length plays a pivotal role. This correlation suggests that the BTp oligomers optical properties are controlled by a common mechanism for which the extent of electronic delocalization dictated by the conjugation length modulates both the excited-state dynamics and the NLO properties.

Table 3.4: Excited state lifetime of the BTp oligomers

	GSB		ESA 1		ESA 2		ESA 2 Purged		k (s^{-1})
	(τ_1) ns	(τ_2) ns	(τ_1) ns	(τ_2) ns	(τ_1) ns	(τ_2) ns	(τ_1) ns	(τ_2) µs	
BTp 5	6.2	377	7.6	425	9.4	405	9.98	1.3	7.6 x10^5
BTp 7	8.5	391	14.0	412	11.5	420	12.3	4.6	2.1 x10^5
BTp 9	21.7	401	11.2	434	12.1	433	13.9	4.5	2.2 x10^5
BTp 11	18.8	411	10.1	456	12.6	450	11.5	4.3	2.3 x10^5

k = decay rate of the ESA 2 (τ_2). Kinetics experiments were done in oxygenated and deoxygenated (purged) chloroform. The BTp 5, BTp 7, BTp 9 and BTp 11 were excited at 310 nm, 330 nm, 355 nm and 363 nm respectively.

3.7. Conclusion

This study reveals how the structural design of rigid ladder-type BTp oligomers fundamentally influences their excited-state dynamics and NLO properties. By systematically extending the conjugation length, we show that enhanced electron delocalization within the molecular framework leads to significant changes in the excited-state relaxation processes, driving faster ISC and efficient formation of triplet excited state. We attributed the longer triplet excited state dynamics to be due to the rigid conformation of the extended BTps which reduces the electron-phonon interaction and lowers the electronic coupling between the triplet excited state and the ground state. As conjugation length increases, the triplet excited-state lifetimes also increase, highlighting the role of extended conjugation in stabilizing triplet states. The impact of this delocalization is seen in both the excited-state lifetimes and the NLO response, which initially increases with conjugation length but eventually saturates beyond BTp 9. This saturation point

marks a critical limit in the tunability of these chromophores, where further elongation of the conjugation chain no longer leads to significant improvements in their NLO properties. These findings provide essential insights into the limits of tunability for the BTp oligomers, paving the way for the rational design with controlled NLO properties, essential for advanced organic optoelectronics and photonics applications.

References

(1) Yang, J. S.-J.; Fang, L. Conjugated Ladder Polymers: Advances from Syntheses to Applications. *Chem* **2024**, *10* (6), 1668–1724. https://doi.org/10.1016/j.chempr.2024.04.002.

(2) Lee, J.; Kalin, A. J.; Yuan, T.; Al-Hashimi, M.; Fang, L. Fully Conjugated Ladder Polymers. *Chem. Sci.* **2017**, *8* (4), 2503–2521. https://doi.org/10.1039/C7SC00154A.

(3) Metanomski, W. V.; Bareiss, R. E.; Kahovec, J.; Loening, K. L.; Shi, L.; Shibaev, V. P. Nomenclature of Regular Double-Strand (Ladder and Spiro) Organic Polymers (IUPAC Recommendations 1993). *Pure Appl. Chem.* **1993**, *65* (7), 1561–1580. https://doi.org/10.1351/pac199365071561.

(4) Chong, K. C.; Tam, T. L. D.; Tao, R.; Chin, K. L. O.; Chua, M. H.; Xu, J. Conjugated Ladder Polymers: Unique Organic π-Conjugated Materials for Optoelectronics, Transistors, and Energy Harvesting and Storage. *Energy Mater. Adv.* **2025**, *6*, 0134. https://doi.org/10.34133/energymatadv.0134.

(5) Teo, Y. C.; Lai, H. W. H.; Xia, Y. Synthesis of Ladder Polymers: Developments, Challenges, and Opportunities. *Chem. – Eur. J.* **2017**, *23* (57), 14101–14112. https://doi.org/10.1002/chem.201702219.

(6) Xia, C.; Advincula, R. C. Ladder-Type Oligo(p-Phenylene)s Tethered to a Poly(Alkylene) Main Chain: The Orthogonal Approach to Functional Light-Emitting Polymers. *Macromolecules* **2001**, *34* (20), 6922–6928. https://doi.org/10.1021/ma0100192.

(7) Baderschneider, S.; Scherf, U.; Köhler, J.; Hildner, R. Influence of the Conjugation Length on the Optical Spectra of Single Ladder-Type (p-Phenylene) Dimers and Polymers. *J. Phys. Chem. A* **2016**, *120* (2), 233–240. https://doi.org/10.1021/acs.jpca.5b10879.

(8) Hildner, R.; Winterling, L.; Lemmer, U.; Scherf, U.; Köhler, J. Single-Molecule Spectroscopy on a Ladder-Type Conjugated Polymer: Electron–Phonon Coupling and Spectral Diffusion. *ChemPhysChem* **2009**, *10* (14), 2524–2534. https://doi.org/10.1002/cphc.200900445.

(9) Hildner, R.; Lemmer, U.; Scherf, U.; van Heel, M.; Köhler, J. Revealing the Electron–Phonon Coupling in a Conjugated Polymer by Single-Molecule Spectroscopy. *Adv. Mater.* **2007**, *19* (15), 1978–1982. https://doi.org/10.1002/adma.200602718.

(10) Kim, F. S.; Park, C. H.; Na, Y.; Jenekhe, S. A. Effects of Ladder Structure on the Electronic Properties and Field-Effect Transistor Performance of Poly(Benzobisimidazobenzophenanthroline). *Org. Electron.* **2019**, *69*, 301–307. https://doi.org/10.1016/j.orgel.2019.03.049.

(11) Babel, A.; Jenekhe, S. A. High Electron Mobility in Ladder Polymer Field-Effect Transistors. *J. Am. Chem. Soc.* **2003**, *125* (45), 13656–13657. https://doi.org/10.1021/ja0371810.

(12) Wu, J.-S.; Cheng, Y.-J.; Lin, T.-Y.; Chang, C.-Y.; Shih, P.-I.; Hsu, C.-S. Dithienocarbazole-Based Ladder-Type Heptacyclic Arenes with Silicon, Carbon, and Nitrogen Bridges: Synthesis, Molecular Properties, Field-Effect Transistors, and Photovoltaic Applications. *Adv. Funct. Mater.* **2012**, *22* (8), 1711–1722. https://doi.org/10.1002/adfm.201102906.

(13) Ma, Y.; Zheng, Q.; Yin, Z.; Cai, D.; Chen, S.-C.; Tang, C. Ladder-Type Dithienonaphthalene-Based Donor–Acceptor Copolymers for Organic Solar Cells. *Macromolecules* **2013**, *46* (12), 4813–4821. https://doi.org/10.1021/ma400696e.

(14) Yuan, Z.; Xiao, Y.; Qian, X. A Design Concept of Planar Conjugated Ladder Oligomers of Perylene Bisimides and Efficient Synthetic Strategy via Regioselective Photocyclization. *Chem. Commun.* **2010**, *46* (16), 2772–2774. https://doi.org/10.1039/B925605A.

(15) Sosorev, A. Yu. Charge-Transfer Complexes of Linear and Ladder-Type Conjugated Polymers as Promising Organic Narrow-Gap Semiconductors. *J. Exp. Theor. Phys.* **2022**, *135* (1), 100–106. https://doi.org/10.1134/S106377612207007X.

(16) Wang, M.; Fu, S.; Petkov, P.; Fu, Y.; Zhang, Z.; Liu, Y.; Ma, J.; Chen, G.; Gali, S. M.; Gao, L.; Lu, Y.; Paasch, S.; Zhong, H.; Steinrück, H.-P.; Cánovas, E.; Brunner, E.; Beljonne, D.; Bonn, M.; Wang, H. I.; Dong, R.; Feng, X. Exceptionally High Charge Mobility in Phthalocyanine-Based Poly(Benzimidazobenzophenanthroline)-Ladder-Type Two-Dimensional Conjugated Polymers. *Nat. Mater.* **2023**, *22* (7), 880–887. https://doi.org/10.1038/s41563-023-01581-6.

(17) Tian, H.; Deng, Y.; Pan, F.; Huang, L.; Yan, D.; Geng, Y.; Wang, F. A Feasibly Synthesized Ladder-Type Conjugated Molecule as the Novel High Mobility n-Type Organic Semiconductor. *J. Mater. Chem.* **2010**, *20* (37), 7998–8004. https://doi.org/10.1039/C0JM01173H.

(18) Huang, W.; Zhang, H.; Ma, J.; Chen, M.; Zhu, H.; Wang, W. Ladder-Type Conjugated Oligomers Prepared by the Scholl Oxidative Cyclodehydrogenation Reaction: Synthesis, Characterization and Application in Field Effect Transistors. *J. Mater. Chem. C* **2015**, *3* (24), 6200–6208. https://doi.org/10.1039/C5TC00354G.

(19) Lee, J.; Li, H.; Kalin, A. J.; Yuan, T.; Wang, C.; Olson, T.; Li, H.; Fang, L. Extended Ladder-Type Benzo[k]Tetraphene-Derived Oligomers. *Angew. Chem. Int. Ed.* **2017**, *56* (44), 13727–13731. https://doi.org/10.1002/anie.201707595.

(20) Mallory, F. B.; Butler, K. E.; Evans, A. C.; Brondyke, E. J.; Mallory, C. W.; Yang, C.; Ellenstein, A. Phenacenes: A Family of Graphite Ribbons. 2. Syntheses of Some

[7]Phenacenes and an [11]Phenacene by Stilbene-like Photocyclizations. *J. Am. Chem. Soc.* **1997**, *119* (9), 2119–2124. https://doi.org/10.1021/ja9638418.

(21) Kaji, Y.; Kawasaki, N.; Lee, X.; Okamoto, H.; Sugawara, Y.; Oikawa, S.; Ito, A.; Okazaki, H.; Yokoya, T.; Fujiwara, A.; Kubozono, Y. Low Voltage Operation in Picene Thin Film Field-Effect Transistor and Its Physical Characteristics. *Appl. Phys. Lett.* **2009**, *95* (18), 183302. https://doi.org/10.1063/1.3257373.

(22) Williams, A. T. R.; Winfield, S. A.; Miller, J. N. Relative Fluorescence Quantum Yields Using a Computer-Controlled Luminescence Spectrometer. *Analyst* **1983**, *108* (1290), 1067–1071. https://doi.org/10.1039/AN9830801067.

(23) Fisher, L. Jr.; Vázquez, R. J.; Howell, M.; Muthike, A. K.; Orr, M. E.; Jiang, H.; Dodgen, B.; Lee, D. R.; Lee, J. Y.; Zimmerman, P.; Goodson, T. I. Investigation of Thermally Activated Delayed Fluorescence in Donor–Acceptor Organic Emitters with Time-Resolved Absorption Spectroscopy. *Chem. Mater.* **2022**, *34* (5), 2161–2175. https://doi.org/10.1021/acs.chemmater.1c03668.

(24) Villabona-Monsalve, J. P.; Varnavski, O.; Palfey, B. A.; Goodson, T. Two-Photon Excitation of Flavins and Flavoproteins with Classical and Quantum Light. *J. Am. Chem. Soc.* **2018**, *140* (44), 14562–14566. https://doi.org/10.1021/jacs.8b08515.

(25) Villabona-Monsalve, J. P.; Burdick, R. K.; Goodson, T. I. Measurements of Entangled Two-Photon Absorption in Organic Molecules with CW-Pumped Type-I Spontaneous Parametric Down-Conversion. *J. Phys. Chem. C* **2020**, *124* (44), 24526–24532. https://doi.org/10.1021/acs.jpcc.0c08678.

(26) Rieger, R.; Müllen, K. Forever Young: Polycyclic Aromatic Hydrocarbons as Model Cases for Structural and Optical Studies. *J. Phys. Org. Chem.* **2010**, *23* (4), 315–325. https://doi.org/10.1002/poc.1644.

(27) Cocchi, C.; Prezzi, D.; Ruini, A.; Caldas, M. J.; Molinari, E. Anisotropy and Size Effects on the Optical Spectra of Polycyclic Aromatic Hydrocarbons. *J. Phys. Chem. A* **2014**, *118* (33), 6507–6513. https://doi.org/10.1021/jp503054j.

(28) Lefler, K. M.; Brown, K. E.; Salamant, W. A.; Dyar, S. M.; Knowles, K. E.; Wasielewski, M. R. Triplet State Formation in Photoexcited Slip-Stacked Perylene-3,4:9,10-Bis(Dicarboximide) Dimers on a Xanthene Scaffold. *J. Phys. Chem. A* **2013**, *117* (40), 10333–10345. https://doi.org/10.1021/jp4083008.

(29) Jones, A. L.; Gish, M. K.; Zeman, C. J. I.; Papanikolas, J. M.; Schanze, K. S. Photoinduced Electron Transfer in Naphthalene Diimide End-Capped Thiophene Oligomers. *J. Phys. Chem. A* **2017**, *121* (50), 9579–9588. https://doi.org/10.1021/acs.jpca.7b09095.

(30) Laquai, F.; Mishra, A. K.; Ribas, M. R.; Petrozza, A.; Jacob, J.; Akcelrud, L.; Müllen, K.; Friend, R. H.; Wegner, G. Photophysical Properties of a Series of Poly(Ladder-Type Phenylene)s. *Adv. Funct. Mater.* **2007**, *17* (16), 3231–3240. https://doi.org/10.1002/adfm.200700450.

(31) Zheng, L.; Polizzi, N. F.; Dave, A. R.; Migliore, A.; Beratan, D. N. Where Is the Electronic Oscillator Strength? Mapping Oscillator Strength across Molecular Absorption Spectra. *J. Phys. Chem. A* **2016**, *120* (11), 1933–1943. https://doi.org/10.1021/acs.jpca.6b00692.

(32) Zhang, G. P.; Zong, X. F. Effects of Electron Interactions on the Oscillator Strengths in One-Dimensional Systems: A Density-Matrix Renormalization Group Approach. *Chem. Phys. Lett.* **1999**, *308* (3), 289–294. https://doi.org/10.1016/S0009-2614(99)00638-7.

(33) Eshun, A.; Cai, Z.; Awies, M.; Yu, L.; Goodson, T. I. Investigations of Thienoacene Molecules for Classical and Entangled Two-Photon Absorption. *J. Phys. Chem. A* **2018**, *122* (41), 8167–8182. https://doi.org/10.1021/acs.jpca.8b06312.

(34) Keller, B.; Cai, Z.; Muthike, A. K.; Sahu, P. K.; Kim, H.; Eshun, A.; Zimmerman, P. M.; Zhang, D.; Goodson, T. I. Investigating the Optical Properties of Thiophene Additions to S-Indacene Donors with Diketopyrrolopyrrole, Isoindigo, and Thienothiophene Acceptors. *J. Phys. Chem. C* **2018**, *122* (48), 27713–27733. https://doi.org/10.1021/acs.jpcc.8b08567.

(35) Zheng, T.; Cai, Z.; Ho-Wu, R.; Yau, S. H.; Shaparov, V.; Goodson, T. I.; Yu, L. Synthesis of Ladder-Type Thienoacenes and Their Electronic and Optical Properties. *J. Am. Chem. Soc.* **2016**, *138* (3), 868–875. https://doi.org/10.1021/jacs.5b10175.

(36) Sandoval, J. S.; Haley, M. M.; Goodson, T. I. Nonlinear Optical Properties of Bis(Dehydrobenzoannuleno)Benzenes: An Experimental and Computational Approach. *J. Phys. Chem. A* **2025**, *129* (5), 1240–1251. https://doi.org/10.1021/acs.jpca.4c06285.

(37) Mandal, H.; Ogunyemi, O. J.; Nicholson, J. L.; Orr, M. E.; Lalisse, R. F.; Rentería-Gómez, Á.; Gogoi, A. R.; Gutierrez, O.; Michaudel, Q.; Goodson, T. Linear and Nonlinear Optical Properties of All-*Cis* and All-*Trans* Poly(*p*-Phenylenevinylene). *J. Phys. Chem. C* **2024**, *128* (6), 2518–2528. https://doi.org/10.1021/acs.jpcc.3c07082.

(38) Mandal, H.; Giri, S. K.; Jovanovski, S.; Varnavski, O.; Zagorska, M.; Ganczarczyk, R.; Chiang, T.-M.; Schatz, G. C.; Goodson, T. I. Impact of Classical and Quantum Light on Donor–Acceptor–Donor Molecules. *J. Phys. Chem. Lett.* **2024**, *15* (37), 9493–9501. https://doi.org/10.1021/acs.jpclett.4c01948.

(39) Drobizhev, M.; Stepanenko, Y.; Rebane, A.; Wilson, C. J.; Screen, T. E. O.; Anderson, H. L. Strong Cooperative Enhancement of Two-Photon Absorption in Double-Strand Conjugated

Porphyrin Ladder Arrays. *J. Am. Chem. Soc.* **2006**, *128* (38), 12432–12433. https://doi.org/10.1021/ja0649623.

(40) Jia, J.; Wu, X.; Zhang, X.; Wang, Y.; Yang, J.; Fang, Y.; Song, Y. Effect of Intramolecular Charge Transfer on Nonlinear Optical Properties of Chalcone Derivatives: A Visual Description of the Charge Transfer Process. *Phys. Chem. Chem. Phys.* **2022**, *24* (2), 955–965. https://doi.org/10.1039/D1CP04567A.

(41) Wang, W.; Mao, Y.; Yang, Z.; Chen, M. Theoretical Study on Photoinduced Charge Transfer in One-Photon and Two-Photon Absorption of Branching Oligofluorenes. *Spectrochim. Acta. A. Mol. Biomol. Spectrosc.* **2024**, *309*, 123826. https://doi.org/10.1016/j.saa.2023.123826.

(42) Mageswari, G. V.; Chitose, Y.; Tsuchiya, Y.; Lin, J.-H.; Adachi, C. Rational Molecular Design for Balanced Locally Excited and Charge- Transfer Nature for Two-Photon Absorption Phenomenon and Highly Efficient TADF-Based OLEDs. *Angew. Chem.* **2025**, *137* (8), e202420417. https://doi.org/10.1002/ange.202420417.

(43) Upton, L.; Harpham, M.; Suzer, O.; Richter, M.; Mukamel, S.; Goodson, T. I. Optically Excited Entangled States in Organic Molecules Illuminate the Dark. *J. Phys. Chem. Lett.* **2013**, *4* (12), 2046–2052. https://doi.org/10.1021/jz400851d.

(44) Varnavski, O.; Giri, S. K.; Chiang, T.-M.; Zeman, C. J.; Schatz, G. C.; Goodson, T. Colors of Entangled Two-Photon Absorption. *Proc. Natl. Acad. Sci.* **2023**, *120* (35), e2307719120. https://doi.org/10.1073/pnas.2307719120.

(45) Burdick, R. K.; Varnavski, O.; Molina, A.; Upton, L.; Zimmerman, P.; Goodson, T. I. Predicting and Controlling Entangled Two-Photon Absorption in Diatomic Molecules. *J. Phys. Chem. A* **2018**, *122* (41), 8198–8212. https://doi.org/10.1021/acs.jpca.8b07466.

(46) Schlawin, F.; Dorfman, K. E.; Fingerhut, B. P.; Mukamel, S. Manipulation of Two-Photon-Induced Fluorescence Spectra of Chromophore Aggregates with Entangled Photons: A Simulation Study. *Phys. Rev. A* **2012**, *86* (2), 023851. https://doi.org/10.1103/PhysRevA.86.023851.

(47) Roslyak, O.; Marx, C. A.; Mukamel, S. Nonlinear Spectroscopy with Entangled Photons: Manipulating Quantum Pathways of Matter. *Phys. Rev. A* **2009**, *79* (3), 033832. https://doi.org/10.1103/PhysRevA.79.033832.

(48) Schlawin, F.; Dorfman, K. E.; Mukamel, S. Entangled Two-Photon Absorption Spectroscopy. *Acc. Chem. Res.* **2018**, *51* (9), 2207–2214. https://doi.org/10.1021/acs.accounts.8b00173.

(49) Tabakaev, D.; Djorović, A.; La Volpe, L.; Gaulier, G.; Ghosh, S.; Bonacina, L.; Wolf, J.-P.; Zbinden, H.; Thew, R. T. Spatial Properties of Entangled Two-Photon Absorption. *Phys. Rev. Lett.* **2022**, *129* (18), 183601. https://doi.org/10.1103/PhysRevLett.129.183601.

(50) Guzman, A. R.; Harpham, M. R.; Süzer, Ö.; Haley, M. M.; Goodson, T. G. I. Spatial Control of Entangled Two-Photon Absorption with Organic Chromophores. *J. Am. Chem. Soc.* **2010**, *132* (23), 7840–7841. https://doi.org/10.1021/ja1016816.

(51) Kang, G.; Nasiri Avanaki, K.; Mosquera, M. A.; Burdick, R. K.; Villabona-Monsalve, J. P.; Goodson, T. I.; Schatz, G. C. Efficient Modeling of Organic Chromophores for Entangled Two-Photon Absorption. *J. Am. Chem. Soc.* **2020**, *142* (23), 10446–10458. https://doi.org/10.1021/jacs.0c02808.

(52) Lee, D.-I.; Goodson, T. Entangled Photon Absorption in an Organic Porphyrin Dendrimer. *J. Phys. Chem. B* **2006**, *110* (51), 25582–25585. https://doi.org/10.1021/jp066767g.

(53) Rani, C.; Goodson, T. I. Enhanced Exciton Coherence Time and Correlation with Probability of Absorption of Classical and Entangled Light in Quantum-Confined Systems. *J. Phys. Chem. C* **2024**, 128, 29, 12151–12163. https://doi.org/10.1021/acs.jpcc.4c01747.

(54) Ogunyemi, O. J.; Rani, C.; Varnavski, O.; Wajahath, R.; Norscia, M.; Malaikal, B.; Qiu, Y.; Sun, S.; Gu, Y.; Mukamel, S.; Wasielewski, M. R.; Goodson, T. I. Understanding the Correlation of the Quantum Dephasing Time and Entangled Photon Interaction in Crystalline Tetracene Derivatives. *J. Phys. Chem. C* **2024**, *128* (47), 20287–20296. https://doi.org/10.1021/acs.jpcc.4c05907.

(55) Sim, M.; Shin, J.; Shim, C.; Kim, M.; Jo, S. B.; Kim, J.-H.; Cho, K. Dependence of Exciton Diffusion Length on Crystalline Order in Conjugated Polymers. *J. Phys. Chem. C* **2014**, *118* (2), 760–766. https://doi.org/10.1021/jp409776s.

(56) Lunt, R. R.; Giebink, N. C.; Belak, A. A.; Benziger, J. B.; Forrest, S. R. Exciton Diffusion Lengths of Organic Semiconductor Thin Films Measured by Spectrally Resolved Photoluminescence Quenching. *J. Appl. Phys.* **2009**, *105* (5), 053711. https://doi.org/10.1063/1.3079797.

(57) Zhang, Y.; Yuan, Y.; Wang, P.; Gao, H.; Qin, Z.; Liu, D.; Zhang, X.; Gao, C.; Fang, H.-H.; Hu, W.; Dong, H. Long Exciton Diffusion Length in High Mobility Emissive Organic Semiconductor. *J. Phys. Chem. C* **2024**, *128* (8), 3431–3437. https://doi.org/10.1021/acs.jpcc.4c00234.

(58) A. Leonard, A.; A. Mosquera, M.; O. Jones, L.; Cai, Z.; J. Fauvell, T.; S. Kirschner, M.; J. Gosztola, D.; C. Schatz, G.; D. Schaller, R.; Yu, L.; X. Chen, L. Photophysical Implications of Ring Fusion, Linker Length, and Twisting Angle in a Series of Perylenediimide–

Thienoacene Dimers. *Chem. Sci.* **2020**, *11* (27), 7133–7143. https://doi.org/10.1039/D0SC02862B.

(59) Sudeep, P. K.; James, P. V.; Thomas, K. G.; Kamat, P. V. Singlet and Triplet Excited-State Interactions and Photochemical Reactivity of Phenyleneethynylene Oligomers. *J. Phys. Chem. A* **2006**, *110* (17), 5642–5649. https://doi.org/10.1021/jp0603637.

(60) Hayes, S. C.; Silva, C. Analysis of the Excited-State Absorption Spectral Bandshape of Oligofluorenes. *J. Chem. Phys.* **2010**, *132* (21), 214510. https://doi.org/10.1063/1.3432602.

(61) Muthike, A. K.; Awais, M. A.; Wang, C.; Orr, M. E.; Almeida, N. M. S.; North, S. C.; Yu, L.; Wilson, A. K.; Goodson, T. G. I. Effect of Long-Lived Ground-State Diradicaloids on the Photophysics of Semiladder Thiophene-Based Polymer Aggregates for Organic Light-Emitting Transistor Applications. *ACS Appl. Energy Mater.* **2024**, *7* (11), 4904–4918. https://doi.org/10.1021/acsaem.4c00685.

(62) Carlotti, B.; K. Madu, I.; Kim, H.; Cai, Z.; Jiang, H.; K. Muthike, A.; Yu, L.; M. Zimmerman, P.; Goodson, T. Activating Intramolecular Singlet Exciton Fission by Altering π-Bridge Flexibility in Perylene Diimide Trimers for Organic Solar Cells. *Chem. Sci.* **2020**, *11* (33), 8757–8770. https://doi.org/10.1039/D0SC03271A.

(63) Madu, I. K.; Jiang, H.; Laventure, A.; Zimmerman, P. M.; Welch, G. C.; Goodson, T. I. Impact of Ring-Fusion on the Excited State Decay Pathways of N-Annulated Perylene Diimides. *J. Phys. Chem. C* **2021**, *125* (19), 10500–10515. https://doi.org/10.1021/acs.jpcc.1c01964.

(64) Whitaker, W.; Sazanovich, I. V.; Kwon, Y.; Jeon, W.; Kwon, M. S.; Orr-Ewing, A. J. Characterization of the Reversible Intersystem Crossing Dynamics of Organic Photocatalysts Using Transient Absorption Spectroscopy and Time-Resolved Fluorescence Spectroscopy. *J. Phys. Chem. A* **2023**, *127* (51), 10775–10788. https://doi.org/10.1021/acs.jpca.3c04780.

(65) Ahmed, R.; Manna, A. K. Tailoring Intersystem Crossing of Perylenediimide through Chalcogen-Substitution at Bay-Position: A Theoretical Perspective. *J. Chem. Phys.* **2022**, *157* (21), 214301. https://doi.org/10.1063/5.0126428.

(66) Muthike, A. K.; Carlotti, B.; Madu, I. K.; Jiang, H.; Kim, H.; Wu, Q.; Yu, L.; Zimmerman, P. M.; Goodson, T. I. The Role of the Core Attachment Positioning in Triggering Intramolecular Singlet Exciton Fission in Perylene Diimide Tetramers. *J. Phys. Chem. B* **2021**, *125* (19), 5114–5131. https://doi.org/10.1021/acs.jpcb.1c02534.

(67) Ahmed, R.; Manna, A. K. Origins of Molecular-Twist-Triggered Intersystem Crossing in Functional Perylenediimides: Singlet–Triplet Gap versus Spin–Orbit Coupling. *J. Phys. Chem. A* **2022**, *126* (38), 6594–6603. https://doi.org/10.1021/acs.jpca.2c03455.

(68) Mehrdad, Z.; Noll, A.; Grabner, E.-W.; Schmidt, R. Sensitization of Singlet Oxygen via Encounter Complexes and via Exciplexes of Ππ* Triplet Excited Sensitizers and Oxygen. *Photochem. Photobiol. Sci.* **2002**, *1* (4), 263–269. https://doi.org/10.1039/B111677K.

(69) Schweitzer, C.; Mehrdad, Z.; Noll, A.; Grabner, E.-W.; Schmidt, R. Mechanism of Photosensitized Generation of Singlet Oxygen during Oxygen Quenching of Triplet States and the General Dependence of the Rate Constants and Efficiencies of O2(1Σg+), O2(1Δg), and O2(3Σg-) Formation on Sensitizer Triplet State Energy and Oxidation Potential. *J. Phys. Chem. A* **2003**, *107* (13), 2192–2198. https://doi.org/10.1021/jp026189d.

(70) Fan, Q.; Ni, W.; Chen, L.; Gurzadyan, G. G.; Xiao, Y. Singlet Relaxation Dynamics and Long Triplet Lifetimes of Thiophene-Coupled Perylene Diimides Dyads: New Insights for High Efficiency Organic Solar Cells. *Chin. Chem. Lett.* **2020**, *31* (11), 2965–2969. https://doi.org/10.1016/j.cclet.2020.06.018.

(71) Shivhare, R.; Moore, G. J.; Hofacker, A.; Hutsch, S.; Zhong, Y.; Hambsch, M.; Erdmann, T.; Kiriy, A.; Mannsfeld, S. C. B.; Ortmann, F.; Banerji, N. Short Excited-State Lifetimes Mediate Charge-Recombination Losses in Organic Solar Cell Blends with Low Charge-Transfer Driving Force. *Adv. Mater.* **2022**, *34* (22), 2101784. https://doi.org/10.1002/adma.202101784.

(72) Burdett, J. J.; Bardeen, C. J. The Dynamics of Singlet Fission in Crystalline Tetracene and Covalent Analogs. *Acc. Chem. Res.* **2013**, *46* (6), 1312–1320. https://doi.org/10.1021/ar300191w.

(73) Wu, T. C.; Thompson, N. J.; Congreve, D. N.; Hontz, E.; Yost, S. R.; Van Voorhis, T.; Baldo, M. A. Singlet Fission Efficiency in Tetracene-Based Organic Solar Cells. *Appl. Phys. Lett.* **2014**, *104* (19), 193901. https://doi.org/10.1063/1.4876600.

(74) Jang, H.-J.; Bittle, E. G.; Zhang, Q.; Biacchi, A. J.; Richter, C. A.; Gundlach, D. J. Electrical Detection of Singlet Fission in Single Crystal Tetracene Transistors. *ACS Nano* **2019**, *13* (1), 616–623. https://doi.org/10.1021/acsnano.8b07625.

(75) Basel, B. S.; Zirzlmeier, J.; Hetzer, C.; Phelan, B. T.; Krzyaniak, M. D.; Reddy, S. R.; Coto, P. B.; Horwitz, N. E.; Young, R. M.; White, F. J.; Hampel, F.; Clark, T.; Thoss, M.; Tykwinski, R. R.; Wasielewski, M. R.; Guldi, D. M. Unified Model for Singlet Fission within a Non-Conjugated Covalent Pentacene Dimer. *Nat. Commun.* **2017**, *8* (1), 15171. https://doi.org/10.1038/ncomms15171.

(76) Zirzlmeier, J.; Lehnherr, D.; Coto, P. B.; Chernick, E. T.; Casillas, R.; Basel, B. S.; Thoss, M.; Tykwinski, R. R.; Guldi, D. M. Singlet Fission in Pentacene Dimers. *Proc. Natl. Acad. Sci.* **2015**, *112* (17), 5325–5330. https://doi.org/10.1073/pnas.1422436112.

(77) Casanova, D. Electronic Structure Study of Singlet Fission in Tetracene Derivatives. *J. Chem. Theory Comput.* **2014**, *10* (1), 324–334. https://doi.org/10.1021/ct4007635.

Supplementary Figures

Figure S3.1: Schematic diagram of the nanosecond transient absorption setup

Figure S3.2: Kinetic of the ground state bleaching

Figure S3.3: Kinetic of the ESA 1

Figure S3.4: Kinetic of the purged ESA 2

Figure S3.5: Molecular orbital of BTp 5

Figure S3.6: Molecular orbital of BTp 7

Figure S3.7: Molecular orbital of BTp 9

Figure S3.8: Molecular orbital of BTp 11

Table S3.1: Electronic calculation of the BTp 5

Table S3.2: Electronic calculation of the BTp 7

Table S3.3: Electronic calculation of the BTp 9

Table S3.4: Electronic calculation of the BTp 11

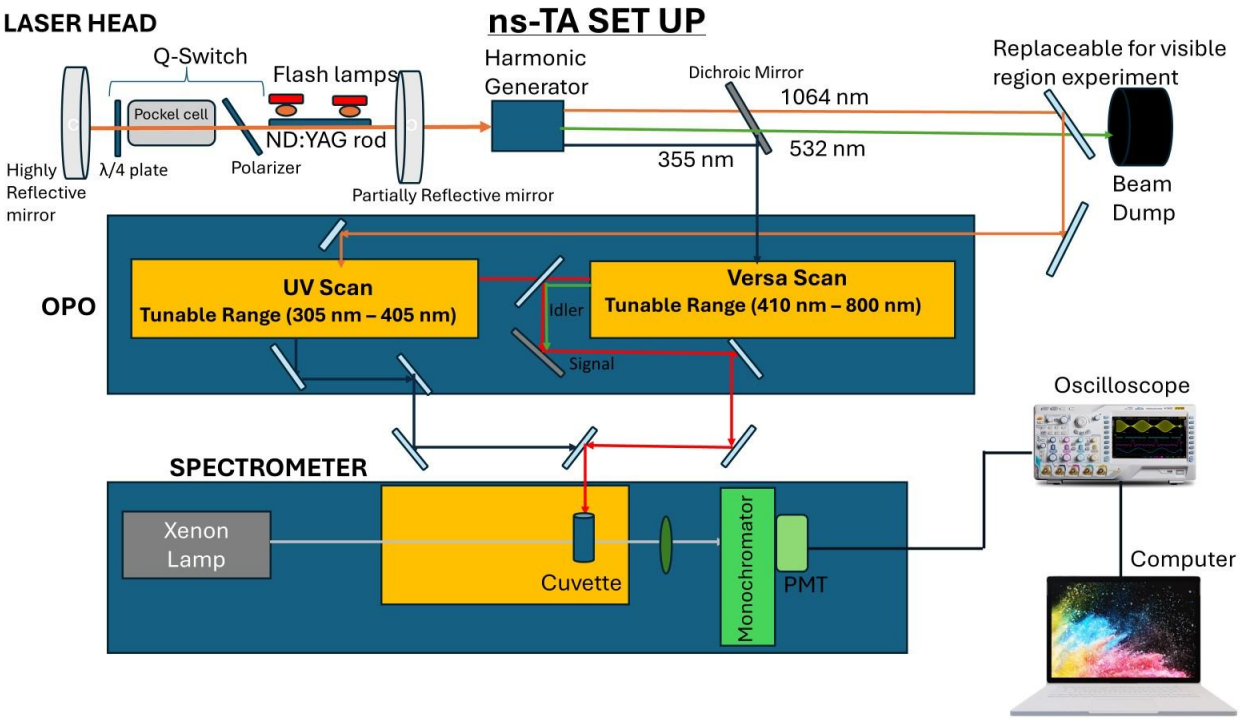


Figure S3.1: Schematic diagram of the nanosecond transient absorption setup

Kinetics of the ground state bleach

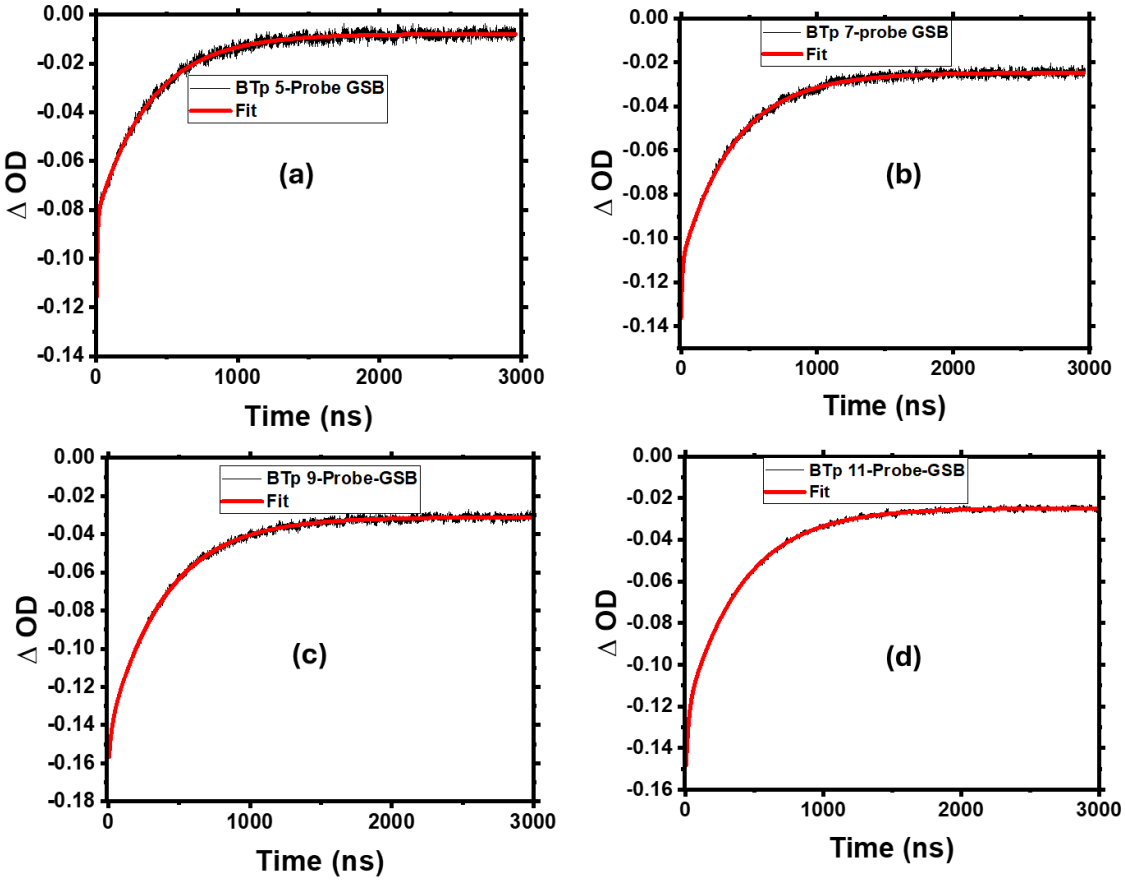


Figure S3.2: Kinetic of the ground state bleaching of the (a) BTp 5 at 310 nm (b) BTp 7 at 330 nm (c) BTp 9 at 355 nm (d) BTp 11 at 363 nm

Kinetic of the excited state absorption (ESA 1)

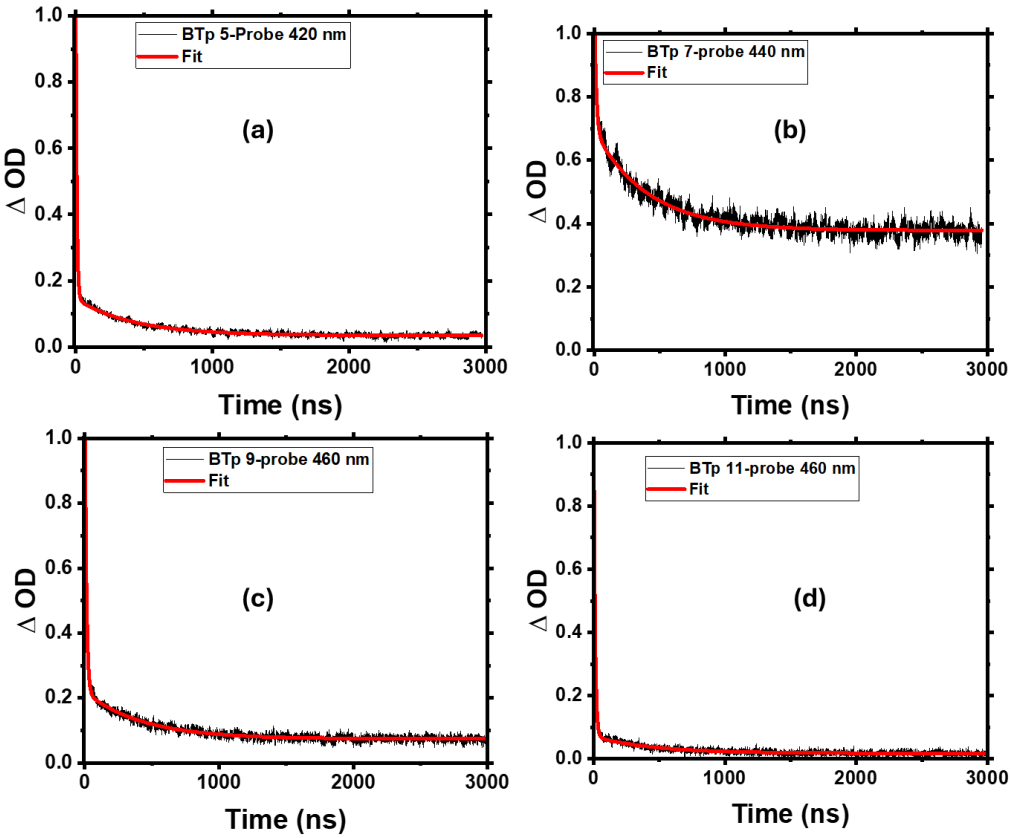


Figure S3.3: Kinetic of the ESA 1 (a) BTp 5 at 310 nm (b) BTp 7 at 330 nm (c) BTp 9 at 355 nm (d) BTp 11 at 363 nm

Kinetic of the excited state absorption Purged (ESA 2)

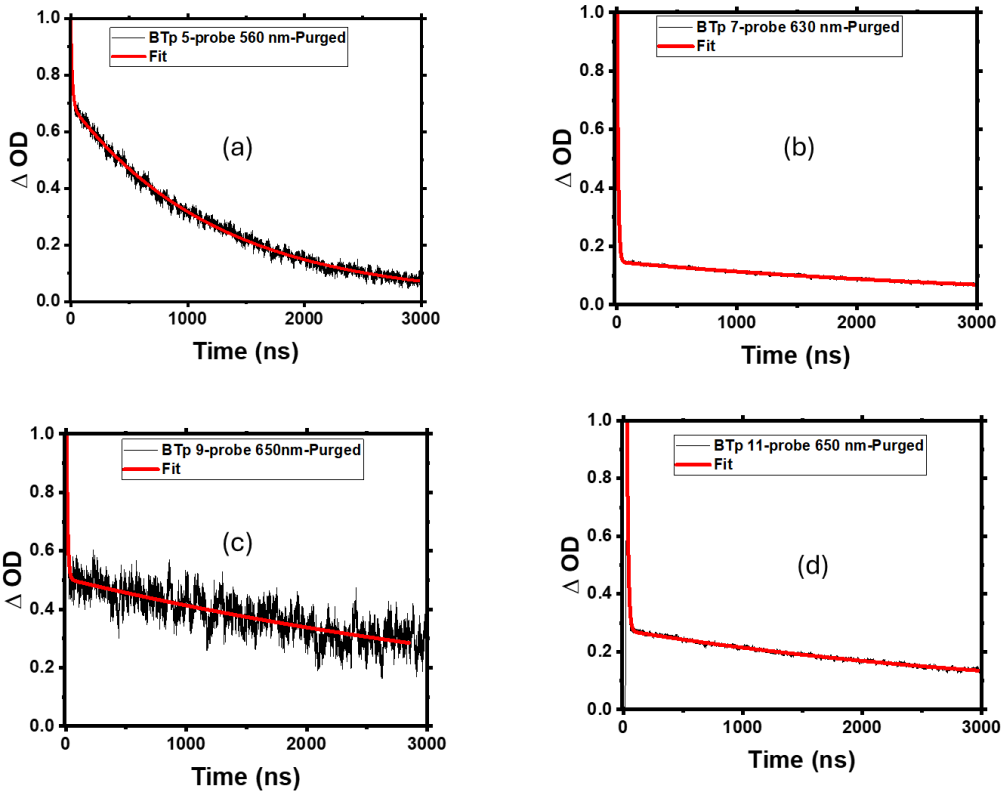


Figure S3.4: Kinetic of the purged ESA 2 (a) BTp 5 at 310 nm (b) BTp 7 at 330 nm (c) BTp 9 at 355 nm (d) BTp 11 at 363 nm

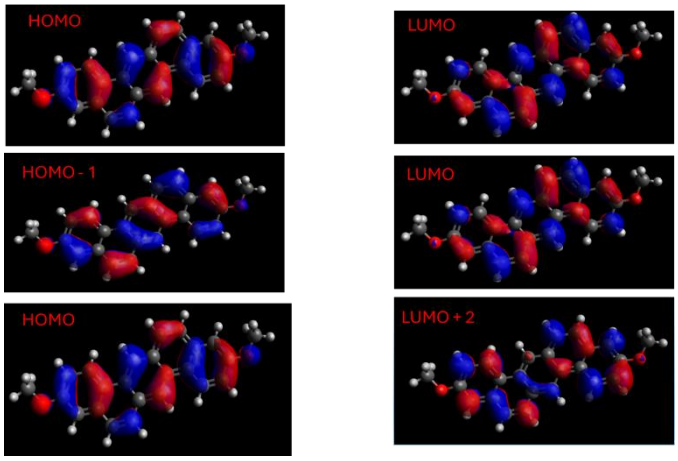


Figure S3.5: Molecular orbital of BTp 5

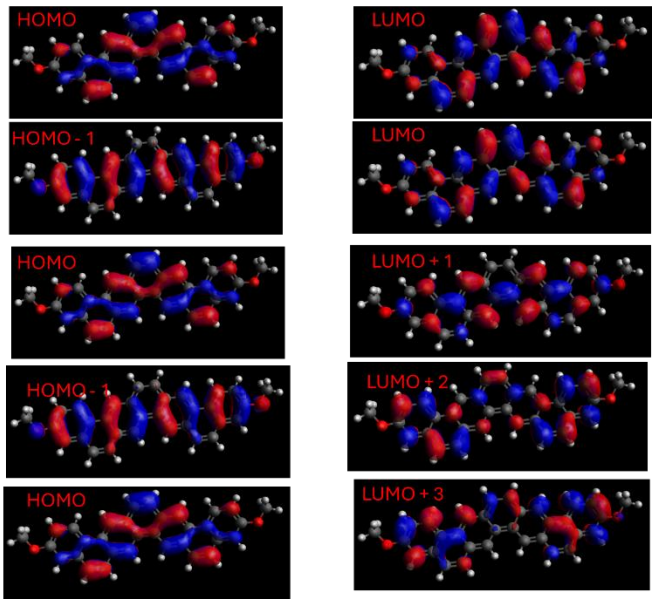


Figure S3.6: Molecular orbital of BTp 7

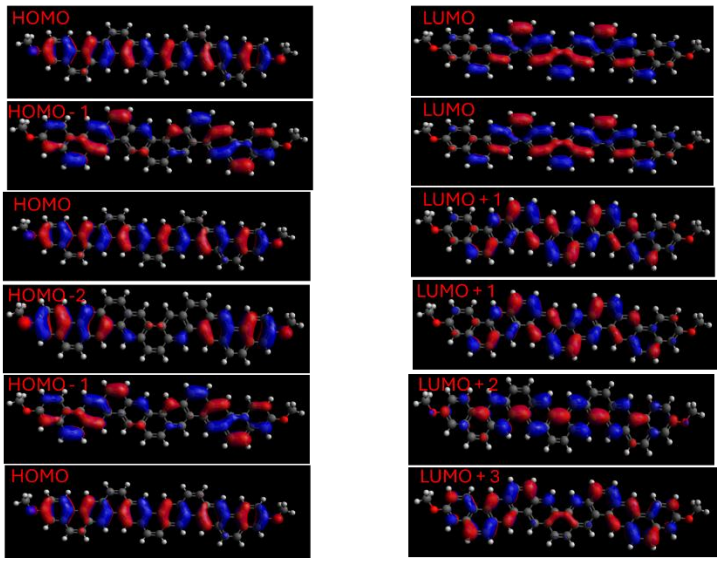


Figure S3.7: Molecular orbital of BTp 9

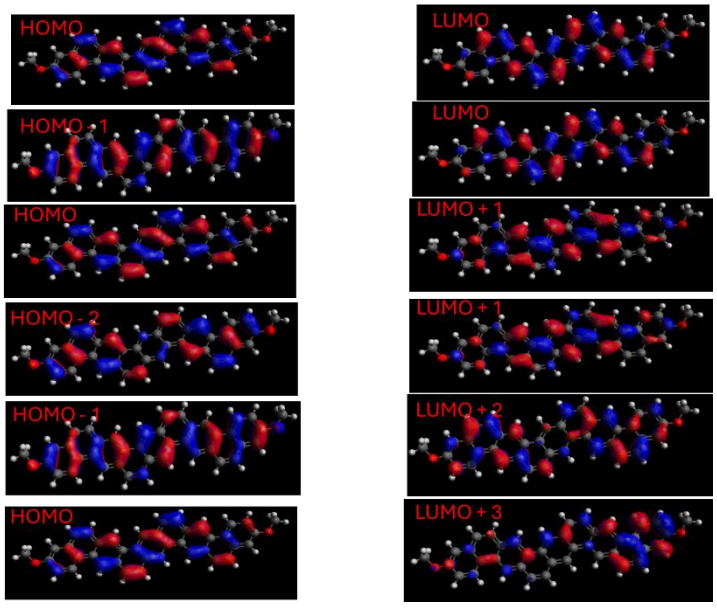


Figure S3.8: Molecular orbital of BTp 11

Theoretical Calculation

Table S3.1: Electronic calculation of the BTp 5

ABSORPTION SPECTRUM VIA TRANSITION ELECTRIC DIPOLE MOMENTS FOR BTp 5

State	Energy (cm-1)	Wavelength (nm)	fosc (au**2)	T2 (au)	TX (au)	TY (au)	TZ (au)
1	26527.0	377.0	0.016301654	0.20231	0.22233	-0.04789	0.38805
2	28910.9	345.9	0.019741492	0.22480	0.47382	-0.01441	-0.00946
3	32596.4	306.8	0.000000180	0.00000	0.00105	-0.00014	0.00084
4	33116.6	302.0	0.475120365	4.72317	-1.92968	0.16641	-0.98580
5	34030.9	293.9	1.847554875	17.87309	4.19971	-0.08632	-0.47759
6	34077.0	293.5	0.000002228	0.00002	-0.00460	0.00010	0.00058
7	34925.4	286.3	0.000000435	0.00000	0.00202	-0.00004	-0.00018
8	36175.1	276.4	0.000000008	0.00000	-0.00025	0.00002	-0.00013
9	38337.8	260.8	0.000000157	0.00000	0.00115	-0.00007	-0.00009

10	39073.0	255.9	0.357145776	3.00915	-1.70997	0.08473	-0.27926
11	39579.2	252.7	0.000000019	0.00000	-0.00018	0.00005	-0.00036
12	40098.2	249.4	0.001198026	0.00984	-0.08319	-0.00209	0.05395
13	40842.5	244.8	0.072213852	0.58208	0.68908	0.01167	-0.32728
14	42252.1	236.7	0.000000039	0.00000	0.00050	-0.00005	0.00024
15	43256.6	231.2	0.004275837	0.03254	-0.14196	0.01595	-0.11016
16	43735.6	228.6	0.873961631	6.57860	-2.55924	0.09725	-0.13942

Table S3.2: Electronic calculation of the BTp 7

ABSORPTION SPECTRUM VIA TRANSITION ELECTRIC DIPOLE MOMENTS FOR BTp 7

State	Energy (cm-1)	Wavelength (nm)	fosc (au**2)	T2 (au)	TX (au)	TY (au)	TZ (au)
1	23446.4	426.5	0.004068487	0.05713	0.02472	0.09945	-0.21593
2	25386.1	393.9	0.099037019	1.28433	0.99407	-0.52821	-0.13098

3	28565.2	350.1	0.292107494	3.36651	1.60949	-0.85500	-0.21224
4	28591.1	349.8	0.086305831	0.99377	-0.09927	-0.41493	0.90097
5	29412.3	340.0	2.022964627	22.64304	4.17424	-2.21721	-0.55018
6	29768.9	335.9	0.010640747	0.11768	-0.03315	-0.14352	0.30980
7	30521.8	327.6	0.739006713	7.97101	-2.47670	1.31547	0.32639
8	30960.8	323.0	0.022908719	0.24359	0.05189	0.20512	-0.44590
9	32708.1	305.7	0.016128848	0.16234	-0.04283	-0.17058	0.36250
10	33101.6	302.1	0.223260991	2.22044	-1.30730	0.69412	0.17211
11	34213.1	292.3	0.106851415	1.02817	0.88961	-0.47232	-0.11692
12	35020.4	285.5	0.000936827	0.00881	0.00213	0.02864	-0.08934
13	35502.4	281.7	0.008632068	0.08004	0.02800	0.11825	-0.25549
14	36334.1	275.2	0.021120289	0.19136	-0.38381	0.20372	0.05053
15	36764.6	272.0	0.526637102	4.71582	1.90493	-1.01196	-0.25099
16	37552.7	266.3	0.028869468	0.25309	0.04889	0.20524	-0.45670

Table S3.3: Electronic calculation of the BTp 9

ABSORPTION SPECTRUM VIA TRANSITION ELECTRIC DIPOLE MOMENTS FOR BTp 9

State	Energy (cm-1)	Wavelength (nm)	fosc (au**2)	T2 (au)	TX (au)	TY (au)	TZ (au)
1	22785.8	438.9	0.000517466	0.00748	0.04250	-0.05506	0.05137
2	24190.8	413.4	0.210687101	2.86723	-1.48460	0.69907	0.41774
3	26507.3	377.3	0.009055131	0.11246	-0.28933	0.16774	0.02476
4	27390.8	365.1	0.014294435	0.17181	-0.33610	0.23692	-0.05206
5	27539.5	363.1	1.292107408	15.44605	3.20567	-2.23476	0.41902
6	27799.9	359.7	2.397174385	28.38779	4.67094	-2.30052	-1.13036
7	28261.1	353.8	0.052384729	0.61023	-0.66528	0.24513	0.32794
8	29162.0	342.9	0.060962423	0.68821	-0.70490	0.43739	0.00271
9	30383.6	329.1	0.013231055	0.14336	0.32021	-0.20001	-0.02874
10	30670.3	326.0	0.058584323	0.62884	-0.69179	0.31545	0.22528

11	31340.6	319.1	0.008370865	0.08793	0.25987	-0.14282	0.00138
12	32127.4	311.3	0.024806304	0.25419	-0.39039	0.07444	0.31023
13	32256.3	310.0	0.350175892	3.57394	-1.65433	0.84969	0.33935
14	32782.1	305.0	0.020399120	0.20486	0.40108	-0.20563	-0.04133
15	33389.9	299.5	0.037353515	0.36829	-0.52417	0.29976	0.06069
16	33433.8	299.1	0.448527065	4.41650	1.80855	-1.06281	-0.12682

Table S4: Electronic calculation of the BTp 11

ABSORPTION SPECTRUM VIA TRANSITION ELECTRIC DIPOLE MOMENTS FOR BTp 11

State	Energy (cm-1)	Wavelength (nm)	fosc (au**2)	T2 (au)	TX (au)	TY (au)	TZ (au)
1	21609.0	462.8	0.002133856	0.03251	-0.02637	-0.07515	0.16176
2	22437.6	445.7	1.086357961	15.93942	3.45628	-1.87840	-0.68203
3	24280.3	411.9	0.000223011	0.00302	0.03624	-0.03523	0.02166
4	24718.5	404.6	0.000213632	0.00285	0.03433	-0.00197	-0.04078

5	25560.4	391.2	0.042584043	0.54847	0.27465	0.21823	-0.65224
6	26333.4	379.7	2.105784087	26.32581	4.41655	-2.54124	-0.60163
7	26392.4	378.9	0.261062117	3.25642	1.43175	-0.40715	-1.02016
8	26954.0	371.0	0.319164329	3.89822	1.71290	-0.87183	-0.45181
9	27659.5	361.5	0.204437075	2.43327	1.35265	-0.73072	-0.26391
10	27693.4	361.1	0.357302059	4.24751	-1.77601	1.00622	0.28429
11	28028.3	356.8	0.335055764	3.93546	1.71895	-0.92223	-0.36080
12	28859.2	346.5	0.940691529	10.73094	2.83640	-1.53551	-0.57269
13	29143.7	343.1	0.014134722	0.15967	-0.33605	0.20509	-0.06837
14	29495.2	339.0	0.019440878	0.21699	-0.40435	0.21489	0.08551
15	30068.6	332.6	0.012609396	0.13806	0.31908	-0.16291	-0.09850
16	30140.5	331.8	0.001599214	0.01747	0.12165	-0.04360	-0.02771
17	30466.3	328.2	0.003782715	0.04088	0.13836	-0.11086	0.09717

Chapter Four

Understanding the Correlation of the Quantum Dephasing Time and Entangled Photon Interaction in Crystalline Tetracene Derivatives

4.1. Author Contribution Statement

This chapter describes the result and conclusion of the collaborative work done by Professor Theodore G. Goodson III's group, Department of Chemistry and Macromolecular Science & Engineering, University of Michigan, Ann Arbor; Professor Shaul Mukamel, Department of Chemistry, University of California, Irvine, and Professor Michael R. Wasielewski, Department of Chemistry, Applied Physics Program, and Center for Molecular Quantum Transduction, Northwestern University. In this thesis, I worked on the two-photon absorption (TPA) and entangled two-photon absorption (ETPA), as well as the data analysis and writing of the manuscript. Rani, C worked on the Near Field Scanning Optical Microscope experiment, and Varnavski, O assisted with the manuscript review. Norscia II, M, Wajahath, R and Brock Malaikal assisted with the data analysis. Yunfan Qiu from Professor Michael R. Wasielewski's group synthesized the samples and characterized them. Shichao Sun and Yonghao Gu from Professor Shaul Mukamel's group worked on the electronic structure calculation.

This collaborative research is published in the *Journal of Physical Chemistry C* – citation: Ogunyemi, O. J., Rani, C., Varnavski, O., Wajahath, R., Norscia, M., Malaikal, B., ... & Goodson III, T. (2024). Understanding the Correlation of the Quantum Dephasing Time and Entangled Photon Interaction in Crystalline Tetracene Derivatives. *The Journal of Physical Chemistry C*, *128*(47), 20287-20296

4.2. Abstract

Quantum-to-quantum transduction is the coherent exchange of information between quantum systems, which is an essential element of quantum information science (QIS). Molecular architectures provide unmatched flexibility for tailoring the properties that are critical to quantum transduction, and molecular synthesis affords the opportunity to build novel molecular materials from the bottom-up. Singlet fission (SF) in organic chromophore solids provides a potential means of executing photon-to-spin quantum transduction because absorption of a single photon results in formation of four entangled spins that constitute a triplet pair state (TT). We have demonstrated that SF in single crystals of 5,12-bis(tricyclohexylsilylethynyl)-tetracene (TCHS-tetracene) produces a long-lived quintet state ^{5}(TT) that provides a promising new route to multi-qubit systems for QIS. Here, we investigate the interaction of classical and entangled photons (EPs) with TCHS-tetracene as well as the related TIPS-tetracene and tetracene to assess the molecular properties required for quantum transduction. From the classical two-photon absorption (TPA) experiment, we observed that TCHS-tetracene and TIPS-tetracene have a higher TPA cross-section than tetracene. The entangled two-photon absorption (EPTA) cross-section of TCHS-tetracene and TIPS-tetracene (6.914×10^{-19} cm^2/molecule and 5.057×10^{-19} cm^2/molecule, respectively) are about an order of magnitude larger than that of tetracene (5.146×10^{-20} cm^2/molecule) making TCHS-tetracene and TIPS-tetracene excellent candidates for demonstrating photon-to-spin transduction using singlet fission. We also observed a longer coherence time for the TCHS-tetracene in comparison to the tetracene molecular systems investigated which suggests its suitability for possible QIS applications.

4.3. Introduction

One of the important aspects of quantum information science (QIS) is quantum transduction, which involves the coherent exchange of information between quantum systems.[1,2] Diverse qubit candidates such as nitrogen vacancy centers in diamonds and spin-correlated radical ion pairs have been studied.[2–5] For example, photo-driven electron transfer from a molecular donor to an acceptor produces an entangled spin qubit pair that can be employed in quantum sensing.[6] Important parameters for defining a good qubit system are embodied in the DiVincenzo criteria, one of which is the ability of the qubit system to have a sufficiently long spin coherence time (T_2) to allow manipulation of the spins needed to execute quantum gate operations.[7] Molecular qubits are gaining interest because of their structural tunability and ease in manipulating electronic spins using microwave frequency radiation.[2,8–10] Photons are important carriers of quantum information because they can serve as propagating qubits that encode information using linear momentum, polarization and energy for storage and communication.[2,7] For quantum transduction to be established, there must be coherent transfer of information between the stationary material qubits and the propagating qubits (photons).[11]

In order to explore quantum transduction from photons to material system, specific quantum states of light such as entangled photon pairs can be used.[12,13] Entangled photons (EP) are a twin pair of photons namely signal and idler which are highly quantum correlated. As a result, the properties of the quantum state of each photon cannot be described independently of each other.[13,14] In our previous works, we have investigated the interaction of EPs with various molecular system using the entangled two photon absorption (ETPA) spectroscopic technique.[2,14–21] Strong entanglement fidelity during the two-photon excitation process has been demonstrated.[22,23] It was also found that ETPA provides the opportunities to access the states with high electronic

entanglement in molecular systems.[22] Entangled photon pair state parameters (such as degree of entanglement) can be experimentally well characterized using different quantum interferometry or joint spectral correlation methods.[24–27] These states can be also quantitatively controlled by specific control "knobs" such as entanglement time,[13,14,28–30] inter-photon delay in the pair[17,29,31–33] or by joint spectrum manipulation.[14,26]

EPs pairs can be generated via spontaneous parametric down conversion (SPDC).[14,28,34] The SPDC process involves the interaction of a strong beam with frequency (ω_p) with a second order (χ^2) nonlinear crystal resulting in the generation of twin photons (signal and idler) of lower energy that are highly correlated.[29,30] Furthermore, unlike classical light (photons) which are limited by their time-bandwidth uncertainty, EPs have strong temporal correlation and high frequency-time control.[13] Understanding the interaction of molecular systems with classical and EPs is important for exploring their suitability to execute quantum transduction. EPs opens opportunities in controlling the quantum transduction at molecular level as they possess the ability to transfer their discrete photonic states to the molecular system.[35] As a result of the high correlation observed in EPs, they can be utilized as propagating qubits to induce transduction in a molecular qubit system.[36]

The generation of entangled multi-spin systems that can serve as multi-qubit systems is important in QIS. This can be accomplished using singlet fission wherein photoexcitation of one molecule of an electronically coupled pair results in down conversion of the singlet exciton to two triplet excitons, proving that the triplet exciton energy is approximately half that of the singlet exciton.[37] If the resulting ^{1}(TT) state is sufficiently long lived, spin evolution occurs to produce the corresponding ^{5}(TT) state that has four entangled unpaired spins,[38–41] which can serve as a 4-qubit system that can be manipulated using microwave radiation.

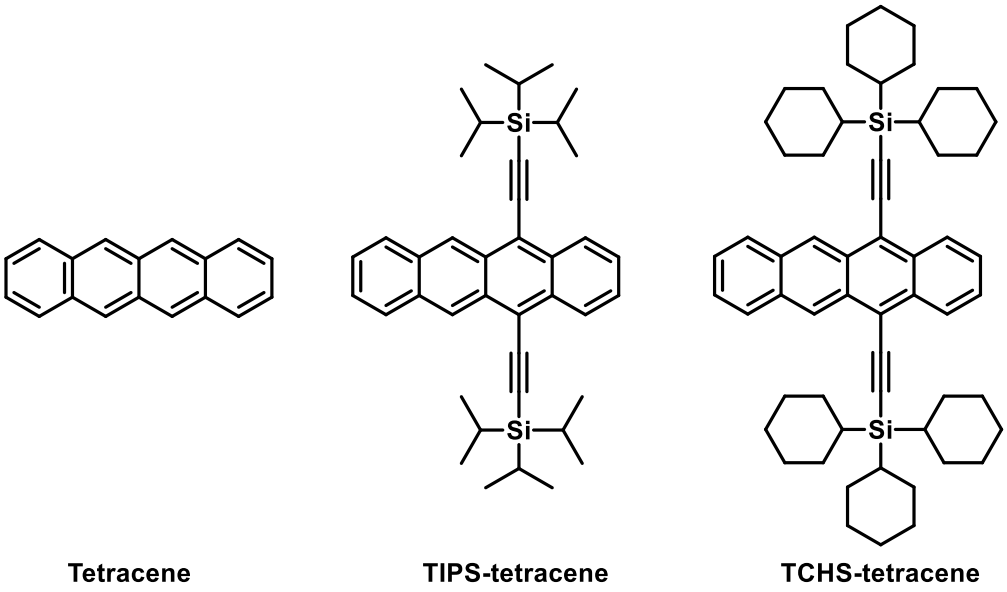


Figure 4.1. The structures of the tetracene, TIPS-tetracene and TCHS-tetracene.

Previous studies have shown that the ^{5}(TT) can be observed at cryogenic temperatures within tetracene dimers.[42] Wasielewski and co-workers recently reported studies on 5,12-bis(tricyclohexylsilylethynyl)-tetracene (TCHS-tetracene, **Figure 4.1**), whose large side groups are designed to engineering single crystal structures in which TCHS-tetracene molecules are positioned next to one another to form non-covalent dimers that are isolated from neighboring dimers in the crystal structure. Photoexcitation of single crystals of TCHS-tetracene produces a high yield of the ^{5}(TT) multiexciton state with an enhanced population lifetime T_{pop} = 130 μs at 5 K and a spin coherence lifetime T_2 = 3μs at 10 K. The value of T_2 increased to 10 μs at 10 K using a Carr-Purcell-Meiboom-Gill microwave pulse sequence to decouple the ^{5}(TT) state from the spin bath.[36]

However, to gain a full insight on the dynamic of the ^{5}(TT) states, it is important that we understand what happens in the initial S_1 state because it is the state that gives rise to the triplet state via singlet fission. The coherence time is important in QIS because it determines the time

frame in which the coherent interaction of light-matter can occur.[43,44] A longer coherence time of the S_1 state can provide insight into the ability of accessing the ^{5}(TT) quintet states in molecular systems. In this paper, we will describe the interaction of classical and EPs on tetracene, TIPS-tetracene, and TCHS-tetracene, the latter two molecules being candidates for generating highly spin correlated molecular qubit systems for quantum transduction in QIS applications. Furthermore, we utilized the femtosecond two-photon Near Scan Optical Microscope (NSOM) experiment to determine the coherence time of the S_1 state of the tetracene molecular systems at room temperature to establish its relationship with the lifetime of the ^{5}(TT) states which was measured using Time Resolved Electron Paramagnetic Resonance (TREPR) spectroscopy as reported by Wasielewski and co-workers.[36] This study focuses on understanding the relationship between the magnitude of interaction of the EPs with the tetracene molecular systems and the correlation with the coherence time of the S_1 state to determine the possibility of accessing the ^{5}(TT) states using EPs which can be utilized to drive future QIS applications.

4.4. Experimental Section

4.4.1. Sample Preparation.

Tetracene was purchased from Sigma-Aldrich, while TIPS-tetracene and TCHS-tetracene were synthesized using methods reported previously by Wasielewski and co-workers.[36] In the dark, an empty vial was weighed and approximately 1 mg of each sample was measured into the vial wrapped in aluminum foil. A known volume of tetrahydrofuran (THF) was added into three vials containing the tetracene, TIPS-tetracene and TCHS-tetracene, respectively. The solution was stirred and kept in the dark and used for the classical and entangled two-photon absorption experiment. For the NSOM experiment, the drop-casting method was used to prepare the film and kept under vacuum to ensure the removal of the solvents.

4.4.2. Absorption and Steady State Emission

Tetracene, TIPS-tetracene and TCHS-tetracene were dissolved in tetrahydrofuran (THF) and the absorption and steady state emission were measured. An Agilent 8341 spectrometer was used to measure the absorption using a 1 cm pathlength cuvette. A FluoroMax-4 fluorimeter was used to measure the emission with an integration time of 0.1 s and slit size of 1.0 nm.

4.4.3. Entangled Two Photon Absorption Measurements (ETPA)

The setup used for the ETPA experiment had been described by Villabona-Monsalve and co-workers.[14] A 405 nm continuous wave (cw) laser (CrystaLaser Inc. ,CL-2000) was used as our light source for the ETPA setup. The entangled light was generated from a type 1 beta barium borate (BBO) crystal via the spontaneous parametric down conversion process using the 405 nm pump from the cw laser. The entangled photons (signal and idler generated of 810 nm respectively) were focused into the 1 cm cuvette containing the sample using a convex lens and the entangled photons transmitted were focused onto an avalanche photodiode (Laser component COUNT-250N) after passing a band pass filter to prevent any fluorescence generated. Zinc *meso*-tetraphenylporphyrin (ZnTPP) was used as a standard in calibrating the system with toluene as the solvent. To measure the ETPA, THF was used for calibration and establishing the baseline with the transmitted entangled photon rate to be about 5.0 x 10^6 input photon flux. Upon establishing the baseline, the tetracene samples were introduced in the dark into the cuvette and the EPs transmitted were measured by adjusting the motorized neutral density (ND) filter to control the photon flux thereby obtaining series of five different measurements. The loss observed in the EPs flux due to the ETPA is compared with the established baseline. The slope of linear fit plot of the rate of the ETPA (counts/s) as a function of the input photon flux is used to calculate the ETPA cross-section.

4.4.4. Two Photon Absorption (TPA)

The classical TPA experiment was done using a Spectra-Physics Ti:Sapphire laser with 80 MHz repetition rate, 100 fs pulses, adjustable from 760-830 nm. All experiments were carried out in the dark using a 1 cm path length cuvette, the samples were excited at 800 nm, and the fluorescence was collected using a photomultiplier (Hamamatsu R7518P) and Hamamatsu photon counting unit. Coumarin 307 dissolved in methanol was used as a standard in this experiment. The emission detection wavelengths were 509, 539, and 539 nm for the tetracene, TIPS-tetracene and TCHS-tetracene, respectively. The input photon flux from the laser was controlled using a neutral density filter and a power dependency scan was done to obtain a dependency which was used for the experiment. The plot of the log of the fluorescence counts per second versus the log of the input photon flux (mW) was obtained and the intercept obtained was used in calculating the TPA cross-section.

4.4.5. Time-Resolved Near-Field Scanning Optical Microscopy (NSOM)

The experimental technique developed by Goodson and co-workers was used to determine the coherence time of the tetracene, TIPS-tetracene and TCHS-tetracene.[44–46] The coherence time experiment was done using NSOM with excitation from a Spectra-Physics Mai Tai laser, which generates 124 fs pulses at 800 nm. To get the topographic and fluorescence image, a near-field scanning technique with optical fiber tip has been used. Two-photon NSOM works on interference phenomena, where two-phase locked laser pulses interfere with the molecular polarization providing information about the coherent oscillations.[44,47]

4.4.6. Fluorescence Quantum Yields

Fresh samples of the tetracene, TIPS-tetracene and TCHS-tetracene were dissolved in THF in the dark. C485 dissolved in methanol was used as the fluorescence standard. The absorption of

the different dilutions was measured using the Agilent 8341 spectrometer with a 1 cm path length cuvette. Tetracene was excited at 437 nm, while TIPS-tetracene and TCHS-tetracene were all excited at 535 nm. Using the same dilutions prepared for the three tetracene samples, the emission was measured with a FluoroMax-4 fluorimeter and the area under the curve was plotted and calculated using Origin software. The fluorescence quantum yields of the Tetracene molecular systems studied were calculated using the Williams method.[48]

4.4.7. Theoretical Calculations

Time-dependent density functional theory (TDDFT) calculations for tetracene, TIPS-tetracene and TCHS-tetracene were performed using Gaussian 16 computational software to simulate the first excited singlet states (S_1). The ground state geometry of tetracene and TIPS-tetracene was optimized using DFT with the B3LYP functional and the 6-311g(d,p) basis set. The geometry of TCHS-tetracene was taken from its crystal structure.[17] The excited states were computed with time-dependent density functional theory (TDDFT) using the Tamm-Dancoff approximation (TDA), employing the same density functional and basis set used in the geometry optimization. The S_1 states are $\pi - \pi^*$ excitations and the highest occupied molecular orbital (HOMO) and lowest unoccupied molecular orbital (LUMO) involved in the S_1 excitations are obtained from Kohn-Sham orbitals in ground state density functional theory.

4.5. Result

4.5.1. Absorption and Emission Spectroscopy of Tetracene Systems

The absorption spectra of tetracene, TIPS-tetracene and TCHS-tetracene shown in **Figure 4.2A** exhibit maxima at 475, 535, and 535 nm, respectively. The fundamental peaks of the three molecules corresponding to their absorption maxima are attributed to the π-π* HOMO-LUMO transitions. The extended conjugation of TIPS-tetracene and TCHS-tetracene result in a red shift

of their absorption maxima relative to that of tetracene. The emission spectra of tetracene, TIPS-tetracene and TCHS-tetracene have maxima at 480, 539, and 539 nm, respectively (**Figure 4.2B**), and the latter two are similarly red shifted relative to tetracene. The fluorescence quantum yields of tetracene, TIPS-tetracene and TCHS-tetracene are 0.16, 0.65, and 0.71, respectively.

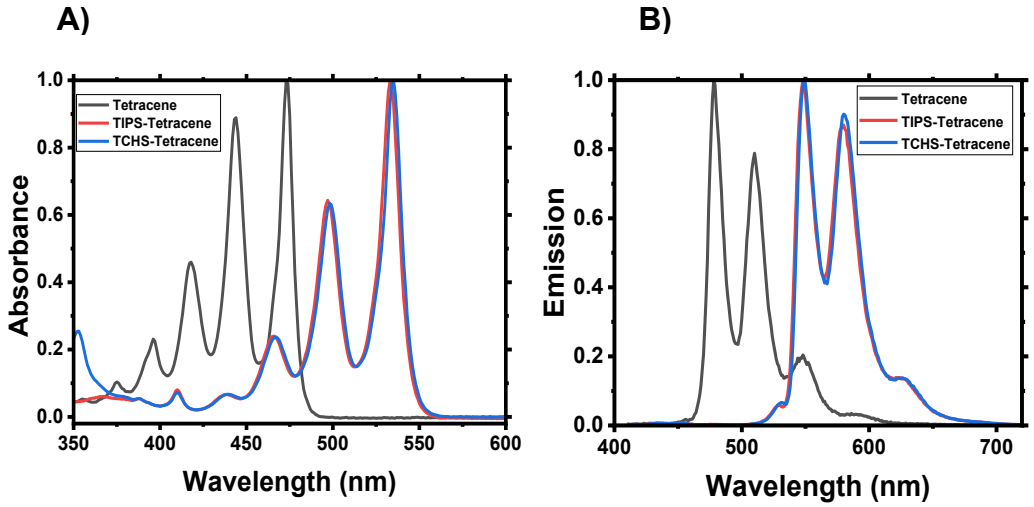


Figure 4.2. (A) Absorption and (B) steady-state emission spectra of tetracene, TIPS-tetracene and TCHS-tetracene.

4.5.2. Time Resolved Electron Paramagnetic Resonance (TREPR)

In the previous study, Wasielewski and co-workers probed the spins state in a single crystal of TCHS-tetracene using TREPR spectroscopy.[36] From this study, we were able to identify two strongly correlated peaks that originates from the transition in $m_s = 0$ to $m_s = \pm 1$ sublevels which based on the Rabi frequency calculated was assigned the ^{5}(TT) state; while the four outer peaks with two different orientations were assigned the uncorrelated triplets, ^{3}T which are formed by the dissociation of the correlated triplet pair. Thus, by utilizing a single crystal, it was possible to isolate the correlated ^{5}(TT) peaks and investigate the decoherence mechanism and spin dynamic

using pulsed-EPR spectroscopy. The temperature dependence study showed the ^{5}(TT) peaks are observed even at room temperature (293K) for the TCHS-tetracene unlike the TIPS-tetracene in which the ^{5}(TT) peaks were observed below 150 K.[49] The T_{pop} of the ^{5}(TT) state in the TCHS-tetracene was 87 ns at room temperature. The T_2 of the ^{5}(TT) state in the TCHS-tetracene was 3 μs at 10 K which is four times longer than the T_2 of the ^{5}(TT) state which is 750 ns in the TIPS-tetracene at 5 K.[36,50] This longer T_2 of the TCHS-tetracene enables greater than 270 spin-flip operations before decoherence occurs, highlighting the importance of the ^{5}(TT) as a promising spin qubit candidate.[36]

4.5.3. Electronic Structure Calculations of Tetracene Systems

The lowest singlet excited states (S_1) of the three molecules are π-π* HOMO-LUMO transitions. The excitation energies of the S_1 of Tetracene, TIPS-tetracene and TCHS-tetracene are 460.73 nm (2.6931 eV), 525.52 nm (2.3595 eV) and 515.91 nm (2.4032 eV) respectively, comparable with experimental results (472 nm, 535 nm, 535 nm respectively). The transition electric dipoles between ground state and S1 of tetracene, TIPS-tetracene and TCHS-tetracene were estimated from spectral data to be 3.03 Debye, 6.32 Debye and 6.25 Debye respectively. **Figure 3** shows the HOMO and LUMO orbital energy level for the tetracene, TIPS-tetracene and TCHS tetracene. The electron density is observed on the tetracene architecture as seen in the LUMO. The HOMO (π orbitals) and LUMO (π* orbitals) in the TIPS-tetracene and TCHS-tetracene are partially delocalized in the carbon-carbon triple bond in the side chain, causing a red shift of the S_1 state energies.

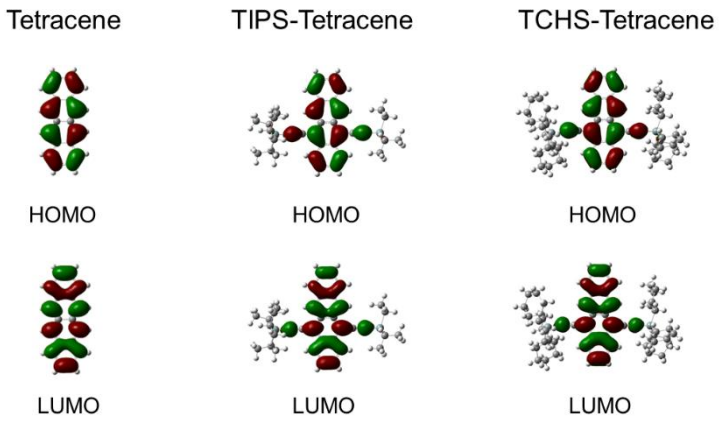


Figure 4.3. Molecular orbitals of the tetracene, TIPS-tetracene and TCHS-tetracene

4.5.4. Classical Two-Photon Absorption of Tetracene Systems

In this study, we first investigated the nonlinear interaction of the tetracene molecular systems with classical light using the two-photon absorption (TPA) spectroscopic technique. TPA is a non-linear optical process involving the simultaneous absorption of two photons that accesses a given state using half the energy of the corresponding one photon absorption process and thus gives rise to interesting photophysical properties of the materials.[51] The technique used in measuring the TPA cross-section in this work had been described by our previous work.[2,19,44,52] A linear fit with the slope 2 was obtained from the logarithm plot of the fluorescence intensity (counts/s) versus the input photon intensity (mW) as seen in **Figure 4.4A**. The red-shift was observed in the two-photon emission spectra of the TIPS-tetracene and TCHS-tetracene in comparison to the bare tetracene (**Figure 4.44B**). The magnitude of the TPA cross-section has been reported to increase with increasing transition dipole moment.[51] This correlates strongly with our experimental data in which we observed an increase in the TPA cross-section for the TIPS-tetracene and TCHS-tetracene with higher transition dipole moment relative to the parent tetracene. The transition dipole moment for tetracene, TIPS-tetracene and TCHS-tetracene was

calculated to be 3.03 Debye, 6. 32 Debye and 6.25 Debye, respectively (**Table 4.1**).

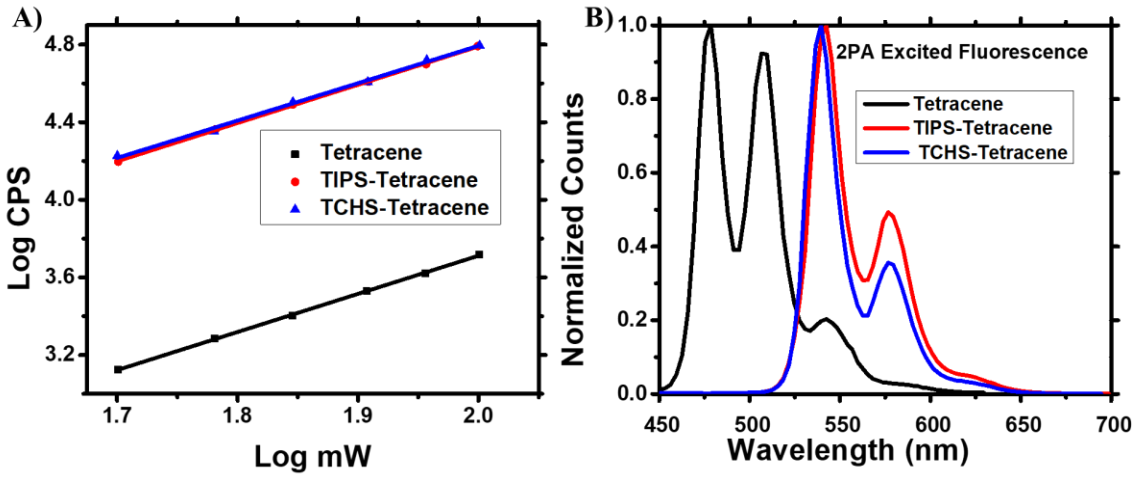


Figure 4.4 (A) Two-photon intensity dependence spectra; and (B) Two-photon excited fluorescence spectra for tetracene, TIPS-tetracene, and TCHS-tetracene

Table 4.1. Table showing the TPA cross-section of the tetracene, TIPS-tetracene and TCHS-tetracene.

Compound	**Concentration (M)**	**δ (GM)**	**μ (Debye)**	**Φ_F**
tetracene	2.90×10^{-4}	0.54	3.03	0.16
TIPS-tetracene	4.81×10^{-5}	9.55	6.32	0.65
TCHS-tetracene	4.93×10^{-5}	10.7	6.25	0.71

δ-TPA cross-section; μ- Transition dipole moment; Φ_F- Fluorescence Quantum yield

From the classical two-photon absorption experiment, we observed that the TIPS-tetracene and TCHS-tetracene have TPA cross-sections that are orders of magnitude higher than unsubstituted tetracene. The TPA cross-section for tetracene, TIPS-tetracene and TCHS-tetracene is 0.54 GM, 9.55 GM and 10.7 GM, respectively, with the latter exhibiting the highest cross-section. The increase in the number of π electrons had been reported to influence the magnitude of

the TPA cross-section.[51] This corelates with our experimental result in which we observe a high TPA cross-section in the TIPS-tetracene and TCHS-tetracene with extended conjugation relative to the bare tetracene. Furthermore, the magnitude of the TPA cross-section depends on the charge transfer (CT) character of the excited state.[19,53,54] Thus, we anticipate a substantial charge transfer property in the TCHS-tetracene which shows the highest TPA cross-section.

4.5.5. Entangled Two-Photon Absorption (ETPA)

In order to explore the possibility of accessing the ^{5}(TT) states with EPs, we need to first investigate the magnitude of interaction of the EPs with the tetracene, TIPS-tetracene and TCHS-tetracene using the ETPA spectroscopic technique.[2,14,19,55] The ETPA cross-section is determined quantum mechanically for an entangled twin state and can be given as the following eq (4.1):[22,28]

$$\sigma_e = \frac{\pi}{4A_eT_e}\omega_1\omega_2\langle S_e^2\rangle g_e(\omega_f) \qquad \text{(Equation 4.1)}$$

where A_e is the entanglement area and T_e is the entanglement time between the photon pair and g_e is the lineshape fucntion. In eq 4.1, $\langle S_e^2\rangle$ is the rotationally averaged ETPA strength of the molecule which depends on the transition dipole moment and the detuning energy of the molecule.[22,28]

Table 4.2: Table showing the ETPA cross-section of the tetracene, TIPS-tetracene and TCHS-tetracene.

Compound	**Concentration (M)**	**ETPA (cm^2/molecule)**
tetracene	2.34 x10^{-4}	5.146 x 10^{-20}
TIPS-tetracene	5.05 x10^{-5}	5.057 x 10^{-19}
TCHS-tetracene	7.22 x10^{-5}	6.914 x 10^{-19}

The ETPA cross-section of the TIPS-tetracene and TCHS-tetracene is observed to increase with

increasing dipole moment in comparison to the bare tetracene. From our experimental finding, the ETPA cross-section of the TIPS-tetracene and TCHS-tetracene are about an order of magnitude higher than the unsubstituted tetracene (**Table 4.2**). The ETPA rate in tetracene, TIPS-tetracene and TCHS-tetracene is shown in **Figure 4.5**. The TCHS-tetracene is observed to have the highest ETPA cross-section. Based on the increased magnitude in interaction of EPs with the TIPS-tetracene and TCHS-tetracene in comparison to the parent tetracene; our goal is to access the ^{5}(TT) quintet state with EPs using these molecular engineered tetracene system, which is an important aspect we are currently addressing.

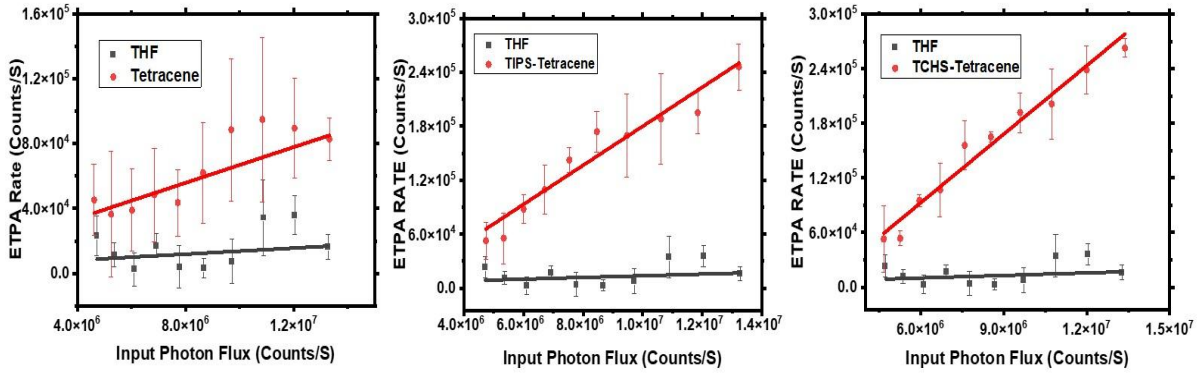


Figure 4.5. Rate of the ETPA absorption of the tetracene, TIPS-tetracene and TCHS-tetracene.

4.5.6. Coherence Time measured with Femtosecond Near-Field Optical Microscope

Time-resolved two-photon NSOM was used to calculate the exciton coherence time of all the forms of tetracene, TIPS-tetracene, and TCHS-tetracene at room temperature. NSOM allow excitation and interrogation of small particles separated by 10-20 nm and their corresponding photoluminescence image can be recorded. The exciton coherence time can be calculated on the basis of quantum intereference phenomena beween the laser pulses and sample. **Figure 4.6** shows the NSOM images of tetracene and TIPS-tetracene in a 500 × 500 nm area. From the fluorescence image (**Figures 4.6A and 4.6C**), structures that are a few nanometers in length for both tetracene

and TIPS-tetracene can be seen on film. An average of 4000 counts for the fluorescence emission were observed from both the samples. The power dependence of the fluorescence emission was also checked to confirm two-photon absorption in tetracene and TIPS-tetracene. The corresponding topographic image has also been observed (**Figure 4.6B and 4.6D**), which confirms that the film is not uniform, and the sample is randomly distributed on the glass substrate. However, from the fluorescence image, a few nanometer particles of both samples can be seen. Similarly, NSOM images have also been recorded for TCHS-tetracene (**Figure 4.7**). An average fluorescence emission count of 5000 was observed from TCHS-tetracene, which is higher than

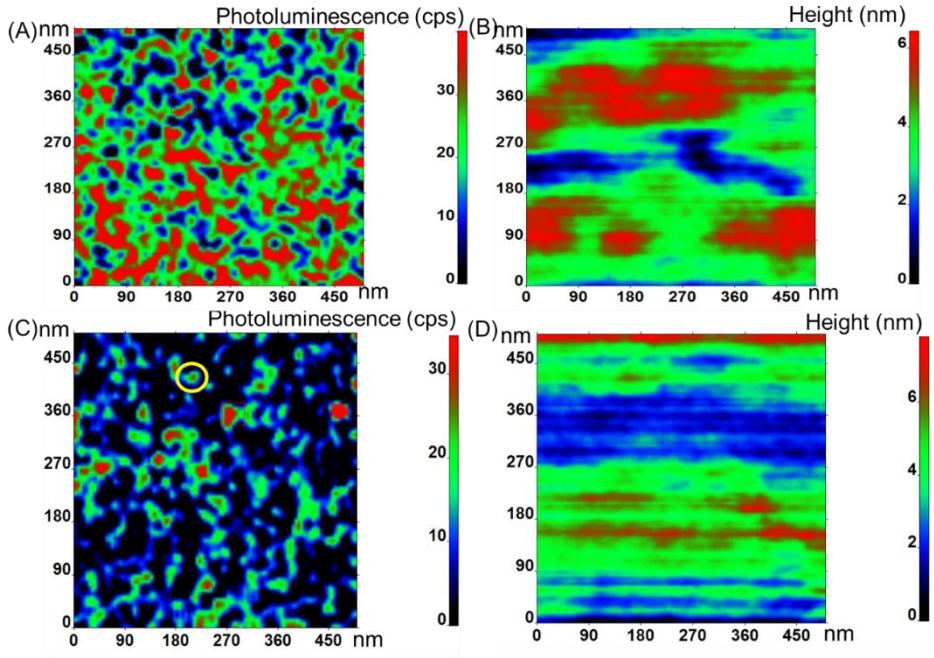


Figure 4.6. (A) NSOM images of tetracene obtained from the two-photon Fluorescence profile on a 500 × 500 nm area and (C) NSOM images of TIPS-tetracene obtained from the two-photon Fluorescence profile on a 500 × 500 nm area. (B) Corresponding AFM profile of the tetracene. and (D) Corresponding AFM profile of the TIPS-tetracene.

observed for tetracene and TIPS-tetracene. The fluorescence image of TCHS-tetracene shows ~30 nm structures, which are almost in the same size range as those of tetracene and TIPS-tetracene

(**Figure 4.6A and 4.6C**). The topographic image of TCHS-tetracene (**Figure 4.7B**) also confirms that the film is not uniform, and the sample is randomly distributed on the surface of the substrate. From the topographic image, it can be said that the sample shrinks at the center of the glass substrate and the film is not very uniform. However, from the fluorescence image we still observe small particles. In order to conduct the time-resolved measurement and to calculate the coherence times of tetracene, TIPS-tetracene, and TCHS-tetracene, the optical fiber tip was focused on the small particles by fixing the X and Y coordinates in the NSOM software. In the time-resolved measurements, shorts scans were repeated in the different time-scale ranges to get the longer time-

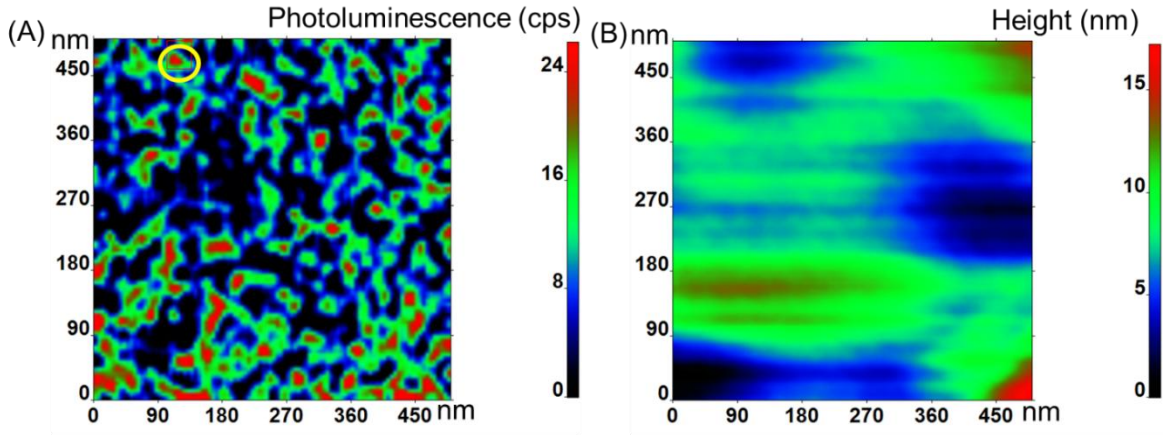


Figure 4.7. NSOM Images of TCHS-tetracene obtained from the two-photon NSOM, (A) Fluorescence profile on a 500 × 500 nm area, (B) Corresponding AFM profile on the same area.

resolved data. Oscillations in the time-resolved photoluminescence amplitude continuously decrease with time because the wavefunction loses coherence. **Figure 4.8A** shows the photoluminescence amplitude as a function of interpulse delay for the laser autocorrelator function. The inset of **Figure 4.8A** shows the photoluminescence oscillation amplitude at short times.

To obtain the photoluminescence amplitude, the minimum of the oscillation has been subtracted from the maxima of the oscillation (maxima-minima). The inset shows that the

photoluminescence signal oscillates with a 2.7 fs period. The coherent time or dephasing time has been calculated by exponential fitting the photoluminescence amplitude decay. The autocorrelation function decay (ACF or laser response) is 88 fs.

From the exponential fitting, the interference/exciton decay times for tetracene and TIPS-tetracene are 80.5 ± 5.4 fs and 83.5 ± 5.4 fs, respectively (**Figure 4.8B**), which is shorter than the ACF. The shorter exciton decay time of tetracene and TIPS-tetracene confirms that the electronic coherence created in the molecule upon photoexcitation is lost very fast. On the other hand, the exciton decay time for TCHS-tetracene (**Figure 4.8C**) is 126 fs, which is longer than the ACF.

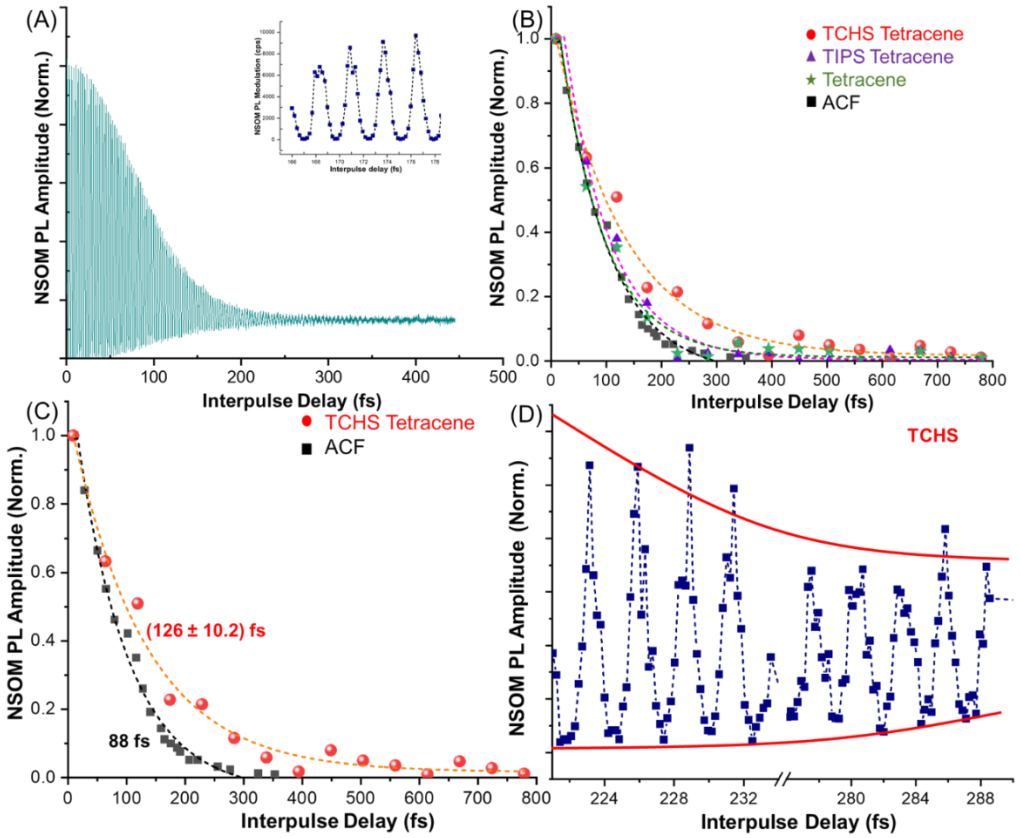


Figure 4.8. (A) NSOM photoluminescence modulation as a function of the interpulse delay for autocorrelation function (blue curve), inset represents the photoluminescence oscillation for TCHS-tetracene in the range of (166 – 180) fs. (B) Normalized photoluminescence modulation amplitude of the Tetracene (green star), TIPS-tetracene (purple triangle), and TCHS-tetracene (red spheres) as a function of the interpulse delay time. Dashed lines indicate the best fitting result to the single decay exponential function. Grey squares (blue dotted line) show the autocorrelation function. (C) Normalized photoluminescence modulation amplitude of the TCHS-tetracene, (D) Photoluminescence oscillations for TCHS-tetracene.

Figure 4.8D shows the fluorescence oscillations of TCHS-tetracene decays with the inter-pulse delay time in the range from (221-234) fs and (276-289) fs. The decay in fluorescence oscillations confirms that the system loses its coherence with the laser pulse and no interference phenomena is observed.

4.6. Discussion

From the steady state experiment, we observed the red-shift in the absorption and emission spectra of the TCHS-tetracene and TIPs-tetracene relative to the bare tetracene. This is due to the presence of the extended conjugation which arises due to the carbon-carbon triple bond of the alkyne group attached to the engineered TCHS-tetracene and TIPS-tetracene. We confirmed this from the electronic structure calculations which shows the electron density in the bare tetracene; however, we observed the partial delocalization of electrons in the triple bond (alkyne group) side chain in the TCHS-tetracene and TIPS-tetracene showing the extension of the conjugated system. From our theoretical calculation, the excitation wavelength calculated are 460.73 nm, 525.52 nm and 515.91 nm are consistent with our experimental absorption maxima of the tetracene, TIPS-tetracene and TCHS-tetracene are 472 nm, 535 nm, 535 nm respectively. Furthermore, our theoretical calculation showed that the TIPS-tetracene and TCHS-tetracene have a higher transition dipole moment of in comparison to the bare tetracene.

The TCHS-tetracene and TIPS-tetracene both absorb classical light in an order of magnitude ten times (10x) higher than the bare tetracene molecule as seen from the calculated TPA cross-section. This high TPA cross-section of the TCHS-tetracene and the TIPS-tetracene can be attributed to their increased transition dipole moment and changes in charge transfer character. The TCHS-tetracene with the bulky group has the highest TPA cross-section which is an indicator of its high charge transfer properties. The charge transfer character of the excited state is also an important parameter that have been investigated for efficient singlet fission processes.[56–59]

Furthermore, we investigated the coherence lifetime of this two-photon excited state (S_1) at room temperature using the two-photon NSOM spectroscopic technique to probe the feasibility of accessing multiexciton states. We anticipate that the longer the coherence time of the two-photon

excited state (S_1) can be beneficial for quantum transduction to the entangled spin states.[60] We observed that the TCHS-tetracene has a longer coherence lifetime at room temperature which is higher compared to other tetracene molecules investigated. The longer coherence time of S_1 state observed in the TCHS-tetracene might be correlated with the higher population of the ^{5}(TT) reported in ref.[36] The T_2 value for tetracene itself was not reported. Tetracene serves as a model for designing molecular systems with longer quintet state T_2 lifetimes. However, we predict that the T_2 lifetime will be shorter in comparison to TIPS-tetracene and TCHS-tetracene. Molecules with longer NSOM dephasing times possess longer T_2 lifetimes as in the case of TIPS-tetracene and TCHS-tetracene compared to tetracene itself. However, in order to access the ^{5}(TT) quintet state, a longer dephasing lifetime of the S_1 state is required. Thus, the shorter dephasing time of the TIPS-tetracene correlates with the shorter T_2 lifetime of the quintet state in comparison to the TCHS-tetracene.

We anticipated that for quantum transduction to be achieved using EPs, high absorption rate of EPs by the molecular system would be advantageous. From our experimental result, we observed that the TCHS-tetracene has the highest ETPA cross-section than the other tetracene molecular system investigated. Chanchal and co-workers in a recent study suggested that the ETPA cross-section may increase with increase in the radiative lifetime of the excited state.[45] This implies that as the coherence lifetime increases, the probability of absorbing more EPs may increase and hence might leads to an increase in its population of the excited state. The bulky group in the TCHS-tetracene enables its tetracene core to be relatively isolated from each other resulting to weak interchromophore packing which enables it to be shielded to some degree from its environment and maintains excited state coherence for a longer time. In contrast, tetracene and TIPS-tetracene have either no or less sterically demanding groups,

respectively, resulting in stronger interchromophore coupling, which results in more rapid loss of coherence. Long coherence lifetime of the excited state (S_1) is beneficial for coherent formation of the entangled triplet pair.[60] This could form the mechanism of quantum transduction from entangled photons to the entangled triplet pair which might further over time leads to the observation of the ^{5}(TT) quintet state. The high ETPA cross-section in the TCHS-tetracene may indicate the elevated absorption rate and high population of the excited state which might facilitate observing the signatures of transduction the using EPs. Hence, the longer coherence lifetime, and higher magnitude of the TPA and ETPA cross-section suggest that TCHS-tetracene is an excellent candidate for exploiting entanglement transduction via SF.

4.7. Conclusion

From our experimental and theoretical investigation of the three tetracene systems it appears that the TCHS-tetracene has many parameters that are consistent with the enhanced capabilities for entanglement transduction. The high ETPA cross-section observed in the TCHS-tetracene suggests increased interactions with the EPs which may be useful to study the quantitative entanglement parameters in the process of entanglement transduction from photon pair to the molecular spin system. Dominant excited state in ETPA involves significant electronic entanglement, suggesting strong entanglement fidelity in ETPA process. Additionally, the longer coherence lifetime of the S_1 state in the TCHS-tetracene provides further reason for observing the coherent transfer of quantum information to the spin states. We anticipate that due to the stronger interaction of the EPs with the TCHS-tetracene; the ^{5}(TT) quintet state can be accessed with the EPs via singlet fission for potential QIS applications which is an area we are currently working on.

REFERENCES

(1) Harvey, S. M.; Wasielewski, M. R. Photogenerated Spin-Correlated Radical Pairs: From Photosynthetic Energy Transduction to Quantum Information Science. *J. Am. Chem. Soc.* **2021**, *143* (38), 15508–15529. https://doi.org/10.1021/jacs.1c07706.

(2) Villabona-Monsalve, J. P.; Tcyrulnikov, N. A.; Lorenzo, E. R.; LaBine, N.; Burdick, R.; Krzyaniak, M. D.; Young, R. M.; Wasielewski, M. R.; Goodson, T. I. Two-Photon Absorption in Electron Donor–Acceptor Dyads and Triads Using Classical and Entangled Photons: Potential Systems for Photon-to-Spin Quantum Transduction. *J. Phys. Chem. C* **2022**, *126* (14), 6334–6343. https://doi.org/10.1021/acs.jpcc.2c00830.

(3) Mani, T. Molecular Qubits Based on Photogenerated Spin-Correlated Radical Pairs for Quantum Sensing. *Chem. Phys. Rev.* **2022**, *3* (2), 021301. https://doi.org/10.1063/5.0084072.

(4) Bar-Gill, N.; Pham, L. M.; Jarmola, A.; Budker, D.; Walsworth, R. L. Solid-State Electronic Spin Coherence Time Approaching One Second. *Nat. Commun.* **2013**, *4* (1), 1743. https://doi.org/10.1038/ncomms2771.

(5) Irber, D. M.; Poggiali, F.; Kong, F.; Kieschnick, M.; Lühmann, T.; Kwiatkowski, D.; Meijer, J.; Du, J.; Shi, F.; Reinhard, F. Robust All-Optical Single-Shot Readout of Nitrogen-Vacancy Centers in Diamond. *Nat. Commun.* **2021**, *12* (1), 532. https://doi.org/10.1038/s41467-020-20755-3.

(6) Palmer, J. R.; Williams, M. L.; Young, R. M.; Peinkofer, K. R.; Phelan, B. T.; Krzyaniak, M. D.; Wasielewski, M. R. Oriented Triplet Excitons as Long-Lived Electron Spin Qutrits in a Molecular Donor–Acceptor Single Cocrystal. *J. Am. Chem. Soc.* **2024**, *146* (1), 1089–1099. https://doi.org/10.1021/jacs.3c12277.

(7) DiVincenzo, D. P. The Physical Implementation of Quantum Computation. *Fortschritte Phys.* **2000**, *48* (9–11), 771–783. https://doi.org/10.1002/1521-3978(200009)48:9/11<771::AID-PROP771>3.0.CO;2-E.

(8) Bayliss, S. L.; Deb, P.; Laorenza, D. W.; Onizhuk, M.; Galli, G.; Freedman, D. E.; Awschalom, D. D. Enhancing Spin Coherence in Optically Addressable Molecular Qubits through Host-Matrix Control. *Phys. Rev. X* **2022**, *12* (3), 031028. https://doi.org/10.1103/PhysRevX.12.031028.

(9) Pazera, G. J.; Krzyaniak, M. D.; Wasielewski, M. R. Pulse Sequences for Manipulating the Spin States of Molecular Radical-Pair-Based Electron Spin Qubit Systems for Quantum Information Applications. *J. Chem. Phys.* **2023**, *158* (20), 204118. https://doi.org/10.1063/5.0145278.

(10) Mao, H.; Pažėra, G. J.; Young, R. M.; Krzyaniak, M. D.; Wasielewski, M. R. Quantum Gate Operations on a Spectrally Addressable Photogenerated Molecular Electron Spin-Qubit Pair. *J. Am. Chem. Soc.* **2023**, *145* (11), 6585–6593. https://doi.org/10.1021/jacs.3c01243.

(11) Lauk, N.; Sinclair, N.; Barzanjeh, S.; Covey, J. P.; Saffman, M.; Spiropulu, M.; Simon, C. Perspectives on Quantum Transduction. *Quantum Sci. Technol.* **2020**, *5* (2), 020501. https://doi.org/10.1088/2058-9565/ab788a.

(12) Mukamel, S.; Freyberger, M.; Schleich, W.; Bellini, M.; Zavatta, A.; Leuchs, G.; Silberhorn, C.; Boyd, R. W.; Sánchez-Soto, L. L.; Stefanov, A. *et al*. Roadmap on Quantum Light Spectroscopy. *J. Phys. B At. Mol. Opt. Phys.* **2020**, *53* (7), 072002. https://doi.org/10.1088/1361-6455/ab69a8.

(13) Dorfman, K. E.; Schlawin, F.; Mukamel, S. Nonlinear Optical Signals and Spectroscopy with Quantum Light. *Rev. Mod. Phys.* **2016**, *88* (4), 045008. https://doi.org/10.1103/RevModPhys.88.045008.

(14) Villabona-Monsalve, J. P.; Burdick, R. K.; Goodson, T. I. Measurements of Entangled Two-Photon Absorption in Organic Molecules with CW-Pumped Type-I Spontaneous Parametric Down-Conversion. *J. Phys. Chem. C* **2020**, *124* (44), 24526–24532. https://doi.org/10.1021/acs.jpcc.0c08678.

(15) Kang, G.; Nasiri Avanaki, K.; Mosquera, M. A.; Burdick, R. K.; Villabona-Monsalve, J. P.; Goodson, T. I.; Schatz, G. C. Efficient Modeling of Organic Chromophores for Entangled Two-Photon Absorption. *J. Am. Chem. Soc.* **2020**, *142* (23), 10446–10458. https://doi.org/10.1021/jacs.0c02808.

(16) Burdick, R. K.; Varnavski, O.; Molina, A.; Upton, L.; Zimmerman, P.; Goodson, T. I. Predicting and Controlling Entangled Two-Photon Absorption in Diatomic Molecules. *J. Phys. Chem. A* **2018**, *122* (41), 8198–8212. https://doi.org/10.1021/acs.jpca.8b07466.

(17) Lee, D.-I.; Goodson, T. Entangled Photon Absorption in an Organic Porphyrin Dendrimer. *J. Phys. Chem. B* **2006**, *110* (51), 25582–25585. https://doi.org/10.1021/jp066767g.

(18) Eshun, A.; Cai, Z.; Awies, M.; Yu, L.; Goodson, T. I. Investigations of Thienoacene Molecules for Classical and Entangled Two-Photon Absorption. *J. Phys. Chem. A* **2018**, *122* (41), 8167–8182. https://doi.org/10.1021/acs.jpca.8b06312.

(19) Mandal, H.; Ogunyemi, O. J.; Nicholson, J. L.; Orr, M. E.; Lalisse, R. F.; Rentería-Gómez, Á.; Gogoi, A. R.; Gutierrez, O.; Michaudel, Q.; Goodson, T. I. Linear and Nonlinear Optical Properties of All-Cis and All-Trans Poly(p-Phenylenevinylene). *J. Phys. Chem. C* **2024**, *128* (6), 2518–2528. https://doi.org/10.1021/acs.jpcc.3c07082.

(20) Villabona-Monsalve, J. P.; Varnavski, O.; Palfey, B. A.; Goodson, T. I. Two-Photon Excitation of Flavins and Flavoproteins with Classical and Quantum Light. *J. Am. Chem. Soc.* **2018**, *140* (44), 14562–14566. https://doi.org/10.1021/jacs.8b08515.

(21) Burdick, R. K.; Schatz, G. C.; Goodson, T. Enhancing Entangled Two-Photon Absorption for Picosecond Quantum Spectroscopy. *J. Am. Chem. Soc.* **2021**, *143* (41), 16930–16934. https://doi.org/10.1021/jacs.1c09728.

(22) Varnavski, O.; Giri, S. K.; Chiang, T.-M.; Zeman, C. J.; Schatz, G. C.; Goodson, T. Colors of Entangled Two-Photon Absorption. *Proc. Natl. Acad. Sci.* **2023**, *120* (35), e2307719120. https://doi.org/10.1073/pnas.2307719120.

(23) Jiang, X.-H.; Chen, P.; Qian, K.-Y.; Chen, Z.-Z.; Xu, S.-Q.; Xie, Y.-B.; Zhu, S.-N.; Ma, X.-S. Quantum Teleportation Mediated by Surface Plasmon Polariton. *Sci. Rep.* **2020**, *10* (1), 11503. https://doi.org/10.1038/s41598-020-67773-1.

(24) Bouchard, F.; Sit, A.; Zhang, Y.; Fickler, R.; Miatto, F. M.; Yao, Y.; Sciarrino, F.; Karimi, E. Two-Photon Interference: The Hong–Ou–Mandel Effect. *Rep. Prog. Phys.* **2020**, *84* (1), 012402. https://doi.org/10.1088/1361-6633/abcd7a.

(25) Shi, L.; Galvez, E. J.; Alfano, R. R. Photon Entanglement Through Brain Tissue. *Sci. Rep.* **2016**, *6* (1), 37714. https://doi.org/10.1038/srep37714.

(26) Fedorov, M. V.; Miklin, N. I. Schmidt Modes and Entanglement. *Contemp. Phys.* **2014**, *55* (2), 94–109. https://doi.org/10.1080/00107514.2013.878554.

(27) Lum, D. J.; Mazurek, M. D.; Mikhaylov, A.; Parzuchowski, K. M.; Wilson, R. N.; Jimenez, R.; Gerrits, T.; Stevens, M. J.; Cicerone, M. T.; Camp, C. H. Witnessing the Survival of Time-Energy Entanglement through Biological Tissue and Scattering Media. *Biomed. Opt. Express* **2021**, *12* (6), 3658–3670. https://doi.org/10.1364/BOE.423743.

(28) Kang, G.; Nasiri Avanaki, K.; Mosquera, M. A.; Burdick, R. K.; Villabona-Monsalve, J. P.; Goodson, T. I.; Schatz, G. C. Efficient Modeling of Organic Chromophores for Entangled Two-Photon Absorption. *J. Am. Chem. Soc.* **2020**, *142* (23), 10446–10458. https://doi.org/10.1021/jacs.0c02808.

(29) Eshun, A.; Varnavski, O.; Villabona-Monsalve, J. P.; Burdick, R. K.; Goodson, T. I. Entangled Photon Spectroscopy. *Acc. Chem. Res.* **2022**, *55* (7), 991–1003. https://doi.org/10.1021/acs.accounts.1c00687.

(30) Schlawin, F.; Dorfman, K. E.; Mukamel, S. Entangled Two-Photon Absorption Spectroscopy. *Acc. Chem. Res.* **2018**, *51* (9), 2207–2214. https://doi.org/10.1021/acs.accounts.8b00173.

(31) Tabakaev, D.; Montagnese, M.; Haack, G.; Bonacina, L.; Wolf, J.-P.; Zbinden, H.; Thew, R. T. Energy-Time-Entangled Two-Photon Molecular Absorption. *Phys. Rev. A* **2021**, *103* (3), 033701. https://doi.org/10.1103/PhysRevA.103.033701.

(32) Varnavski, O.; Goodson, T. I. Two-Photon Fluorescence Microscopy at Extremely Low Excitation Intensity: The Power of Quantum Correlations. *J. Am. Chem. Soc.* **2020**, *142* (30), 12966–12975. https://doi.org/10.1021/jacs.0c01153.

(33) Dayan, B.; Pe'er, A.; Friesem, A. A.; Silberberg, Y. Two Photon Absorption and Coherent Control with Broadband Down-Converted Light. *Phys. Rev. Lett.* **2004**, *93* (2), 023005. https://doi.org/10.1103/PhysRevLett.93.023005.

(34) Burdick, R. K.; Villabona-Monsalve, J. P.; Mashour, G. A.; Goodson, T. Modern Anesthetic Ethers Demonstrate Quantum Interactions with Entangled Photons. *Sci. Rep.* **2019**, *9* (1), 11351. https://doi.org/10.1038/s41598-019-47651-1.

(35) Zhong, C.; Han, X.; Jiang, L. Microwave and Optical Entanglement for Quantum Transduction with Electro-Optomechanics. *Phys. Rev. Appl.* **2022**, *18* (5), 054061. https://doi.org/10.1103/PhysRevApplied.18.054061.

(36) Jacobberger, R. M.; Qiu, Y.; Williams, M. L.; Krzyaniak, M. D.; Wasielewski, M. R. Using Molecular Design to Enhance the Coherence Time of Quintet Multiexcitons Generated by Singlet Fission in Single Crystals. *J. Am. Chem. Soc.* **2022**, *144* (5), 2276–2283. https://doi.org/10.1021/jacs.1c12414.

(37) Smith, M. B.; Michl, J. Singlet Fission. *Chem. Rev.* **2010**, *110* (11), 6891–6936. https://doi.org/10.1021/cr1002613.

(38) Bae, Y. J.; Zhao, X.; Kryzaniak, M. D.; Nagashima, H.; Strzalka, J.; Zhang, Q.; Wasielewski, M. R. Spin Dynamics of Quintet and Triplet States Resulting from Singlet Fission in Oriented Terrylenediimide and Quaterrylenediimide Films. *J. Phys. Chem. C* **2020**, *124* (18), 9822–9833. https://doi.org/10.1021/acs.jpcc.0c03189.

(39) Pace, N. A.; Rugg, B. K.; Chang, C. H.; Reid, O. G.; Thorley, K. J.; Parkin, S.; Anthony, J. E.; Johnson, J. C. Conversion between Triplet Pair States Is Controlled by Molecular Coupling in Pentadithiophene Thin Films. *Chem. Sci.* **2020**, *11* (27), 7226–7238. https://doi.org/10.1039/D0SC02497J.

(40) Tayebjee, M. J. Y.; Sanders, S. N.; Kumarasamy, E.; Campos, L. M.; Sfeir, M. Y.; McCamey, D. R. Quintet Multiexciton Dynamics in Singlet Fission. *Nat. Phys.* **2017**, *13* (2), 182–188. https://doi.org/10.1038/nphys3909.

(41) Basel, B. S.; Zirzlmeier, J.; Hetzer, C.; Phelan, B. T.; Krzyaniak, M. D.; Reddy, S. R.; Coto, P. B.; Horwitz, N. E.; Young, R. M.; White, F. J. *et al*. Unified Model for Singlet Fission

within a Non-Conjugated Covalent Pentacene Dimer. *Nat. Commun.* **2017**, *8* (1), 15171. https://doi.org/10.1038/ncomms15171.

(42) Lin, L.-C.; Smith, T.; Ai, Q.; Rugg, B. K.; Risko, C.; Anthony, J. E.; Damrauer, N. H.; Johnson, J. C. Multiexciton Quintet State Populations in a Rigid Pyrene-Bridged Parallel Tetracene Dimer. *Chem. Sci.* **2023**, *14* (41), 11554–11565. https://doi.org/10.1039/D3SC03153E.

(43) Press, D.; Ladd, T. D.; Zhang, B.; Yamamoto, Y. Complete Quantum Control of a Single Quantum Dot Spin Using Ultrafast Optical Pulses. *Nature* **2008**, *456* (7219), 218–221. https://doi.org/10.1038/nature07530.

(44) Ricci, F.; Marougail, V.; Varnavski, O.; Wu, Y.; Padgaonkar, S.; Irgen-Gioro, S.; Weiss, E. A.; Goodson, T. I. Enhanced Exciton Quantum Coherence in Single CsPbBr3 Perovskite Quantum Dots Using Femtosecond Two-Photon Near-Field Scanning Optical Microscopy. *ACS Nano* **2021**, *15* (8), 12955–12965. https://doi.org/10.1021/acsnano.1c01615.

(45) Rani, C.; Goodson, T. I. Enhanced Exciton Coherence Time and Correlation with Probability of Absorption of Classical and Entangled Light in Quantum-Confined Systems. *J. Phys. Chem. C* **2024**, *128* (29), 12151–12163. https://doi.org/10.1021/acs.jpcc.4c01747.

(46) Varnavski, O.; Kim, T.; Cai, Z.; Yu, L.; Goodson, T. I. Inhomogeneity of the Ultrafast Excited State Dynamics in Organic Photovoltaic Materials Measured at Nanoscale. *J. Phys. Chem. C* **2018**, *122* (38), 22201–22209. https://doi.org/10.1021/acs.jpcc.8b08023.

(47) Ricci, F.; Mandal, H.; Wajahath, M.; Burdick, R. K.; Villabona-Monsalve, J. P.; Hussain, S.; Goodson, T. I. Investigations of Coherence in Perovskite Quantum Dots with Classical and Quantum Light. *J. Phys. Chem. C* **2023**, *127* (7), 3579–3593. https://doi.org/10.1021/acs.jpcc.2c08455.

(48) Williams, A. T. R.; Winfield, S. A.; Miller, J. N. Relative Fluorescence Quantum Yields Using a Computer-Controlled Luminescence Spectrometer. *The Analyst* **1983**, *108* (1290), 1067. https://doi.org/10.1039/an9830801067.

(49) Weiss, L. R.; Bayliss, S. L.; Kraffert, F.; Thorley, K. J.; Anthony, J. E.; Bittl, R.; Friend, R. H.; Rao, A.; Greenham, N. C.; Behrends, J. Strongly Exchange-Coupled Triplet Pairs in an Organic Semiconductor. *Nat. Phys.* **2017**, *13* (2), 176–181. https://doi.org/10.1038/nphys3908.

(50) Bayliss, S. L.; Weiss, L. R.; Kraffert, F.; Granger, D. B.; Anthony, J. E.; Behrends, J.; Bittl, R. Probing the Wave Function and Dynamics of the Quintet Multiexciton State with Coherent Control in a Singlet Fission Material. *Phys. Rev. X* **2020**, *10* (2), 021070. https://doi.org/10.1103/PhysRevX.10.021070.

(51) Pawlicki, M.; Collins, H. A.; Denning, R. G.; Anderson, H. L. Two-Photon Absorption and the Design of Two-Photon Dyes. *Angew. Chem. Int. Ed.* **2009**, *48* (18), 3244–3266. https://doi.org/10.1002/anie.200805257.

(52) Cai, Z.; Vázquez, R. J.; Zhao, D.; Li, L.; Lo, W.; Zhang, N.; Wu, Q.; Keller, B.; Eshun, A.; Abeyasinghe, N. *et al*. Two Photon Absorption Study of Low-Bandgap, Fully Conjugated Perylene Diimide-Thienoacene-Perylene Diimide Ladder-Type Molecules. *Chem. Mater.* **2017**, *29* (16), 6726–6732. https://doi.org/10.1021/acs.chemmater.7b01512.

(53) Muthike, A. K.; Awais, M. A.; Wang, C.; Orr, M. E.; Almeida, N. M. S.; North, S. C.; Yu, L.; Wilson, A. K.; Goodson, T. G. I. Effect of Long-Lived Ground-State Diradicaloids on the Photophysics of Semiladder Thiophene-Based Polymer Aggregates for Organic Light-Emitting Transistor Applications. *ACS Appl. Energy Mater.* **2024**, *7* (11), 4904–4918. https://doi.org/10.1021/acsaem.4c00685.

(54) Upton, L.; Harpham, M.; Suzer, O.; Richter, M.; Mukamel, S.; Goodson, T. I. Optically Excited Entangled States in Organic Molecules Illuminate the Dark. *J. Phys. Chem. Lett.* **2013**, *4* (12), 2046–2052. https://doi.org/10.1021/jz400851d.

(55) Lee, D.-I.; Goodson, T. Entangled Photon Absorption in an Organic Porphyrin Dendrimer. *J. Phys. Chem. B* **2006**, *110* (51), 25582–25585. https://doi.org/10.1021/jp066767g.

(56) He, G.; Busby, E.; Appavoo, K.; Wu, Q.; Xia, J.; Campos, L. M.; Sfeir, M. Y. Charge Transfer States Impact the Triplet Pair Dynamics of Singlet Fission Polymers. *J. Chem. Phys.* **2020**, *153* (24), 244902. https://doi.org/10.1063/5.0029858.

(57) Garoni, E.; Zirzlmeier, J.; Basel, B. S.; Hetzer, C.; Kamada, K.; Guldi, D. M.; Tykwinski, R. R. Two-Photon Absorption in Pentacene Dimers: The Importance of the Spacer Using Upconversion as an Indirect Route to Singlet Fission. *J. Am. Chem. Soc.* **2017**, *139* (40), 14017–14020. https://doi.org/10.1021/jacs.7b08287.

(58) Lukman, S.; Chen, K.; Hodgkiss, J. M.; Turban, D. H. P.; Hine, N. D. M.; Dong, S.; Wu, J.; Greenham, N. C.; Musser, A. J. Tuning the Role of Charge-Transfer States in Intramolecular Singlet Exciton Fission through Side-Group Engineering. *Nat. Commun.* **2016**, *7* (1), 13622. https://doi.org/10.1038/ncomms13622.

(59) M. Hart, S.; Ruchira Silva, W.; R. Frontiera, R. Femtosecond Stimulated Raman Evidence for Charge-Transfer Character in Pentacene Singlet Fission. *Chem. Sci.* **2018**, *9* (5), 1242–1250. https://doi.org/10.1039/C7SC03496B.

(60) Chan, W.-L.; Berkelbach, T. C.; Provorse, M. R.; Monahan, N. R.; Tritsch, J. R.; Hybertsen, M. S.; Reichman, D. R.; Gao, J.; Zhu, X.-Y. The Quantum Coherent Mechanism for Singlet Fission: Experiment and Theory. *Acc. Chem. Res.* **2013**, *46* (6), 1321–1329. https://doi.org/10.1021/ar300286s.

Chapter Five

Linear and Nonlinear Optical Properties of All-*cis* and All-*trans* Poly(*p*-phenylene vinylene)

5.1. Author Contribution Statement

This chapter describes the result and conclusion of the collaborative work done by Professor Theodore G. Goodson III's group, Department of Chemistry and Macromolecular Science & Engineering, University of Michigan, Ann Arbor; and Professor Quentin Michaudel, Department of Chemistry, Texas A&M University. In this study, I worked on the two-photon absorption (TPA) and entangled two-photon absorption (ETPA) experiment and contributed in the writing of the manuscript. Mandal, Haraprasad and Meghan E. Orr worked on the upconversion, time-correlated singled photon counting and the femtosecond transient absorption experiment, in addition to the manuscript writing. The synthesis of the samples was done by Jake L. Nicholson from Professor Quentin Michaudel group, while the electronic structure calculation was done by Ángel Rentería-Gómez, Achyut R. Gogoi, Osvaldo Gutierrez.

This collaborative research is published in the *Journal of Physical Chemistry C* – citation: Mandal, Haraprasad, Olusayo J. Ogunyemi, Jake L. Nicholson, Meghan E. Orr, Remy F. Lalisse, Ángel Rentería-Gómez, Achyut R. Gogoi, Osvaldo Gutierrez, Quentin Michaudel, and Theodore Goodson III. "Linear and Nonlinear Optical Properties of All-cis and All-trans Poly (p-phenylenevinylene)." *The Journal of Physical Chemistry C* 128, no. 6 (2024): 2518-2528.

5.2. Abstract

Poly(*p*-phenylenevinylene) (PPV) is a staple of the family of conjugated polymers with desirable optoelectronic properties for applications including light-emitting diodes (LEDs) and photovoltaic devices. Although the significant impact of olefin geometry on the steady-state optical properties of PPVs has been extensively studied, PPVs with precise stereochemistry have yet to be investigated using nonlinear optical spectroscopy for quantum sensing, as well as light harvesting for biological applications. Herein, we report our investigation of the influence of olefin stereochemistry on both linear and nonlinear optical properties through the synthesis of all-*cis* and all-*trans* PPV copolymers. We performed two-photon absorption (TPA) using a classical and entangled light source and compared both classical TPA and entangled two-photon absorption (ETPA) cross sections of these stereodefined PPVs. Whereas the TPA cross section of the all-*trans* PPV was expectedly higher than that of all-*cis* PPV, presumably because of the larger transition dipole moment, the opposite trend was measured via ETPA, with the all-*cis* PPV exhibiting the highest ETPA cross section. DFT calculations suggest that this difference might stem from the interaction of entangled photons with lower-lying electronic states in the all-*cis* PPV variant. Additionally, we explored the photoinduced processes for both *cis* and *trans* PPVs through time-resolved fluorescence upconversion and femtosecond transient absorption techniques. This study revealed that the sensitivity of PPVs in two-photon absorption varies with classical versus quantum light and can be modulated through the control of the geometry of the repeating alkenes, which is a key stepping stone toward their use in quantum sensing, bioimaging, and the design of polymer-based light-harvesting systems.

5.3. Introduction

Over the years, there has been increased interest in utilizing conjugated polymers with unique electroluminescence properties for applications in organic light-emitting diodes (OLEDs) in display technologies, organic semiconductors in photovoltaic cells for energy conversion and in energy storage devices, and as solid-state laser materials.[1,2] Among these, the properties of poly(*p*-phenylene vinylene) (PPV) and its derivatives have been extensively studied, which has paved the way for their use in optical devices and bulk-heterojunction solar cells.[3–8] PPVs consist of alternating *p*-phenylene and vinylene subunits with higher stability compared to polyacetylene and more flexibility compared to polyphenylene.[2,4] The parent unsubstituted PPV has a band gap of 2.5 eV with a broad spectrum in the visible region, both features that can be modulated through structural derivatization, which is crucial for implementation into photoluminescence devices.[9] The structure and conformation of conjugated polymers is known to determine the fluorescence lifetime, photoluminescence efficiency, as well as electron and charge mobilities in resulting devices. For example, the alkenes in the PPV backbone can exhibit either *cis* or *trans* configurations, which dictates the overall chain conformation. High *trans* content typically results in rod-like structures that favor π-π stacking and therefore aggregation, whereas high *cis* content leads to more coiled and twisted structures with reduced conjugation length.[10–12] Both π–π stacking and conjugation length drastically affect the charge transport mobility of the polymer along with the composition of its backbone. It has been observed that polymers with linear backbones have higher charge transfer properties than polymers with flexible or wave-like backbone.[13,14] The modularity of synthetic methods[1,2] to modify the PPV scaffold via copolymerization or post polymerization functionalization have permitted the synthesis of numerous derivatives with improved conjugation length, solubility, and packing along the polymer backbone through the

addition of non-conjugated carbon bridges or conjugated π-linkers. Efficient packing leads to improved optical, charge transport and sensing properties.[15–19] In addition to being pursued for applications discussed above (OLED, photovoltaics, etc.), PPV also exhibits biocompatibility, low toxicity, and high fluorescence quantum yields making them promising fluorophores for bioimaging applications.[20] For example, in a recent study by Tanja Junkers and co-workers, amphiphilic PPV copolymers were synthesized to form fluorescent micelles for drug delivery that were imaged using classical light and laser scanning confocal microscopy.[21]

The use of PPV materials in nonlinear optical (NLO) applications is especially intriguing, since NLO effects can be exploited for optical communication, frequency doubling and tripling, and photorefractive effect.[22,23] While several studies have allowed the identification of the structural parameters of organic materials responsible for NLO,[24-26] it remains crucial to design new organic chromophores to further understand and optimize NLO phenomena prior to their technological implementation. Of particular interest, some organic materials have been shown recently to exhibit NLO phenomena sensitive to the use of entangled photons.[27-30] The two entangled photons generated by the process of spontaneous parametric down-conversion (SPDC) share a coupled eigenstate where the properties of each of the photons cannot be isolated separately.[31,32] Unlike classical two-photon absorption (TPA), strong temporal and spatial correlations of the entangled photon pair lead to the simultaneous absorption of the two photons (figure 1), at the condition that the absorption occurs within a time window known as the entanglement time, T_e.[29,33] And, this phenomenon is known as entangled-two photon absorption (ETPA). Unlike classical TPA where the TPA has a quadratic on input photon flux, theoretical studies have shown that ETPA rate exhibits a linear dependence on the excitation flux [28,30]. This linear dependency is dominant only when the flux intensities are sufficiently low.[34,35] Entangled

two-photon absorption therefore allows for improved resolution and sensitivity at lower excitation flux compared to classical TPA, which is promising for applications in quantum sensing, optical communication, and bioimaging.[32] Because of their synthetic versatility, the PPV family offers a lot of opportunities to investigate the relationships between the precise molecular structure of organic materials and NLO behaviors with both classical and entangled light.

Accessing PPVs with >99% *cis* alkenes has been a longstanding synthetic challenge due to the thermodynamic bias for the *trans* vinylene phenylene motif,[1,2] which has limited nonlinear spectroscopy studies to PPVs with mostly *trans* alkenes or *cis*/*trans* mixtures. For example, Lavrentiev *et al.* theoretically investigated the low-lying electronic structure of PPV,[36] while Guo and Shih extensively studied the low-lying two-photon excited states in TPA spectroscopy with substituted and unsubstituted PPVs.[37] Ghosh *et al.* explored the exciton dynamics and formation mechanism of polymeric nanostructures based on poly(2-methoxy-5-(2'-ethylhexyloxy)-*p*-phenylene vinylene) (MEH-PPV) by using a femtosecond Ti:sapphire pulse laser as the light source.[38] In addition, De Boni *et al*. reported the degenerate non-linear absorption spectrum of MEH-PPV in chloroform using a femtosecond Z-scan technique.[39] The TPA cross-section spectrum of poly(2-methoxy-5-(2′2′-ethylhexyloxy)-1,4-phenylenevinylene) was also determined by Oliveria *et al.*[40] using a white-light continuum (WLC) Z-scan technique.

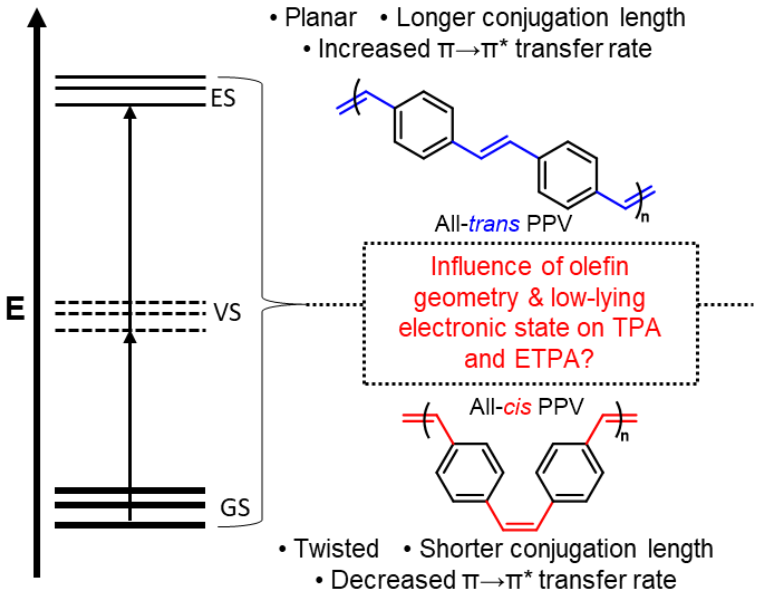


Figure 5.1. Schematic energy diagram of a two-photon absorption process happens from ground state (GS) through virtual state (VS) to two-photon excited state (ES). The olefin geometry of all-trans PPV and all-cis PPV investigated here is also shown.

Herein, we discuss our investigation of the interaction of two diblock copolymers containing either an all-*cis* or an all-*trans* PPV segment (**Figure 5.1**) with both classical and entangled light in two-photon absorption. The diblock copolymers were synthesized via a stereoselective ring-opening metathesis polymerization (ROMP) of paracyclophane diene monomers used in combination with a norbornene imide derivative. We then measured the TPA and ETPA of both diblock copolymers and explored their photo-induced relaxation processes by time-resolved fluorescence up-conversion and femtosecond transient absorption techniques to investigate their intrachain charge transfer nature.

5.4. Experimental Section

5.4.1. Synthesis of Monomers and Polymers

Monomers **1** and **2** were synthesized according to literature procedures [41, 42] (see Supporting Information for more details). To synthesize all-*cis* block copolymer poly-*cis*-**1**-*b*-*cis*-**2**, monomer **1** (73.3 mg, 296.4 μmol, 30 equiv) was first measured into a reaction vial charged with a stir bar inside a nitrogen filled glove box. Ruthenium catalyst Ru-St (8.6 mg, 9.9 μmol, 1 equiv) dissolved in deoxygenated THF (0.10 mL) was then added to the vial and stirred for 1 h at room temperature. Into a second reaction vial containing monomer **2** and a stir bar, 0.08 mL of the mixture was then transferred. The reaction was run in the dark at 40 °C for 2 h before cooling to room temperature and quenching with excess ethyl vinyl ether (0.1 mL). After leaving for an additional 30 min at room temperature, two cycles of precipitation with addition of methanol, centrifugation, and decantation afforded the isolated polymer. After wrapping in aluminum foil and concentrating under reduced pressure, 23 mg of poly-*cis*-**1**-*b*-*cis*-**2** was then dissolved in 23 mL of DCM and irradiated for 1 h at room temperature using two 350 nm UV lamps placed 1 cm away from the sample to afford poly-*cis*-**1**-*b*-*trans*-**2**. The sample was wrapped in aluminum foil and concentrating under reduced pressure. All polymer samples were fully dried, kept wrapped in aluminum foil, and stored under an inert atmosphere at –20 °C.

5.4.2. Entangled Two-Photon Absorption

The entangled two photon absorption experimental setup which had been previously described was used for the purpose of this study.[43] Type I noncollinear spontaneous parametric down-conversion (SPDC) was generated using a Type I BBO crystal with a potable CW laser. The 405 nm light generated from the CW laser goes through a variable neutral density filter which is used to adjust the pump power into the BBO crystal, resulting in SPDC and entangled photon

production. After passing through the sample in the cuvette, the entangled photons are refocused via a band pass filter with a plano-convex lens before entering the avalanche photodiode (APD). A final band pass filter was introduced to remove any extra wavelength of light other than the entangled light that may have entered the system because of entangled photons (EP) interactions with the material that resulted in fluorescence or emission.

To measure the EP transmission rate using an APD, the ETPA experiment starts by introducing a pure chloroform into the cuvette. The variable neutral density filter (NDF) was used to optimize the power of the laser going into the BBO crystal and, as a result, the intensity of the entangled light that interacts with the sample can be controlled. To calibrate the stage, a maximum of 5.5 x 10^6 uncorrected photon counts per second (cps) is targeted. Once this maximum input photon rate is set, the ETPA scan is taken for a total of ten input photon rate values. After a baseline absorbance for the pure solvent has been found, the solvent is replaced with a diluted PPV dissolved in chloroform so that EP transmission can be measured again. The loss in EP transmission seen between the sample solution and pure solvent is due to ETPA absorption. At least three measurements are taken of each PPV to ensure the best signal-to-noise ratio. Since ETPA is done at such a low photon input intensity, it usually takes more than one measurement to get a stable set of readings.

5.5. Results and Discussion

5.5.1. Design and synthesis of PPVs for this study

To access stereodefined PPVs with either >99% *cis* or >99% *trans* alkenes, we relied on a two-step approach: First stereoretentive ring-opening metathesis polymerization (ROMP)[44-46] of paracyclophane diene monomers[47-51]would deliver an all-*cis* PPV segment, then selective photoisomerization of the PPV block would provide the all-*trans* congener.[52] To optimize the

solubility in organic solvents of both *cis* and *trans* PPVs, we designed block copolymers containing a solubilizing poly(norbornene imide) segment stitched to the stereodefined PPV. Additionally, 2-ethylhexyloxy side chains that are known to impart high solubility to conjugated polymers were selected as substituents of the PPV.[53] Adapting a protocol recently developed by Michaudel and coworkers,[10,54] two stereodefined copolymers were synthesized and isolated for two-photon absorption spectroscopy (**Figure 5.2**). The all-*cis* poly(norbornene imide) segment was first synthesized using a 30:1 ratio of monomer **1** to **Ru-St** initiator. Chain extension using 15 equivalents of monomer **2** followed by termination with excess ethyl vinyl ether afforded all-*cis* block copolymer poly-*cis*-**1**-*b*-*cis*-**2**. The *cis*-selectivity of the polymerization (>99%) was assessed using NMR spectroscopy (Figures S1,2). SEC analysis revealed a narrow dispersity ($Đ$ = 1.20) and good agreement between the theoretical and experimental number average molecular weight (**Figure S5.5 and Table S5.1**). Photoisomerization of the PPV block under UV light (350 nm) delivered the *trans* PPV variant poly-*cis*-**1**-*b*-*trans*-**2** with exquisite selectivity (>99% *trans* PPV) and no isomerization of the poly(norbornene imide) block as shown by NMR spectroscopy (Figures S3,4).

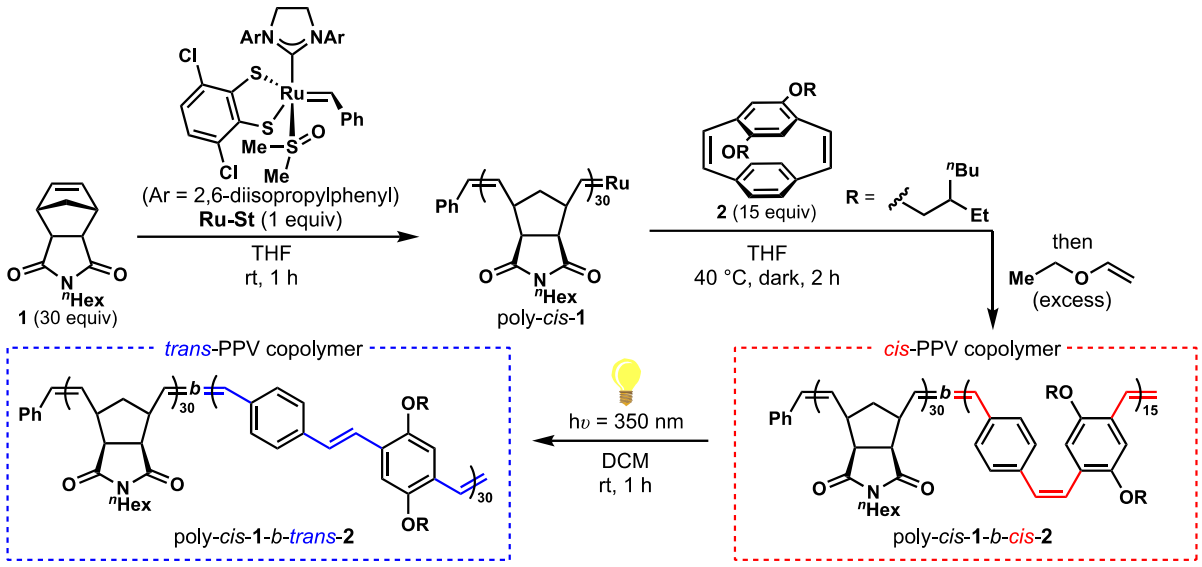


Figure 5.2. Synthesis of diblock copolymers containing either an all-*cis* or an all-*trans* PPV segment: Sequential stereoretentive ROMP of monomers **1** and **2** using catalyst **Ru-St** delivered poly-*cis*-**1**-*b*-*cis*-**2**. Subsequent PPV-selective photoisomerization afforded poly-*cis*-**1**-*b*-*trans*-**2**.

5.5.2. Steady-state absorption and emission:

UV-vis absorption measurements for poly-*cis*-**1**-*b*-*cis*-**2** and poly-*cis*-**1**-*b*-*trans*-**2** were carried out in chloroform at room temperature with maximum π–π* absorptions of 389 nm and 442 nm, respectively, indicating a red-shift after photoisomerization consistent with previous studies[10,54-56] (**Figure 5.3**). Interestingly, emission spectra for poly-*cis*-**1**-*b*-*cis*-**2** and poly-*cis*-**1**-*b*-*trans*-**2** collected following excitation at 389 and 442 nm, respectively, were almost identical. An emission maximum was observed at 517 nm in both spectra (**Figure 5.2**). In addition, another weak band at the region of 555 nm for both PPV samples was observed and is consistent with a previous report.[10] Relative quantum yields were determined, and poly-*cis*-**1**-*b*-*trans*-**2** was found to have a quantum yield 20% higher than poly-*cis*-**1**-*b*-*cis*-**2**. All steady-state results are summarized in Table 1. The narrower optical bandgap and higher quantum yield observed for poly-

cis-**1**-*b*-*trans*-**2** suggest a more efficient intramolecular charge transfer (ICT) compared to poly-*cis*-**1**-*b*-*cis*-**2.**

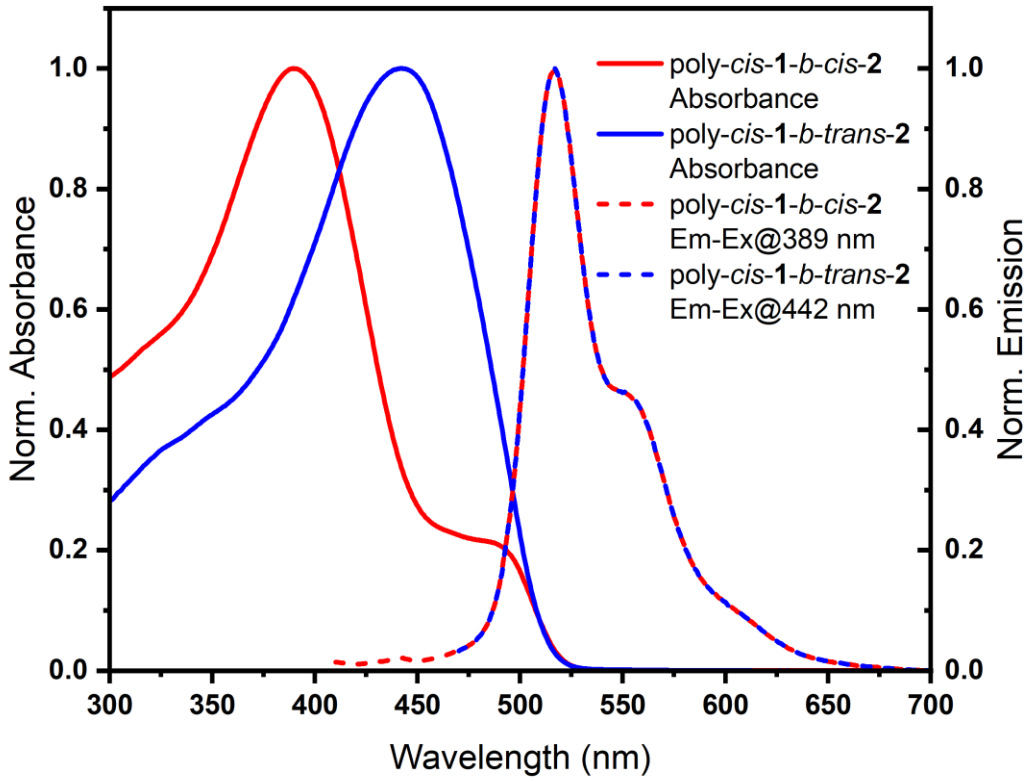


Figure 5.3. Normalized steady state absorption (C = 25.0 and 12.5 μg/mL, respectively) and emission (C = 4.2 and 1.6 ng/mL, respectively) spectra of poly-*cis*-**1**-*b*-*cis*-**2** and poly-*cis*-**1**-*b*-*trans*-**2** in chloroform. Excitations for poly-*cis*-**1**-*b*-*cis*-**2** and poly-*cis*-**1**-*b*-*trans*-**2** were 389 and 442 nm, respectively.

Table 5.1. Steady-state Absorption and Emission Properties of poly-*cis*-**1**-*b*-*cis*-**2** and poly-*cis*-**1**-*b*-*trans*-**2** in chloroform.

Samples	**Absorption (nm)**	**Emission (nm)**	**Φ_{fl} (%)**
poly-*cis*-**1**-*b*-*cis*-**2**	389	517, 555	36.3
poly-*cis*-**1**-*b*-*trans*-**2**	442	517, 555	56.5

5.5.3. Classical two-photon absorption

The nonlinear optical properties of poly-*cis*-**1**-*b*-*cis*-**2** and poly-*cis*-**1**-*b*-*trans*-**2** were then analyzed using classical TPA (λ_{exc} = 800 nm) with induced fluorescence detection to gain insight into the charge transfer characters. It has been observed that the transition probability of TPA increases with increasing ICT character.[57] The logarithmic plot of the intensity (counts per second) *versus* the laser power (mW) shows a linear fit with a slope value of about 2 for both PPV samples (**Figure 5.4A**). This indicates that a two-photon excitation process is allowed in both poly-*cis*-**1**-*b*-*cis*-**2** and poly-*cis*-**1**-*b*-*trans*-**2**. **Figure 5.4A** shows the power dependent two-photon excited fluorescence spectra while **Figure 5.4B** is the two-photon emission which correlates well with the steady-state emission spectra. The slope values obtained from the power-dependence logarithm plot was used to calculate the two-photon absorption cross section.[58] The TPA cross sections were calculated using the following equation:

$$\sigma_{sample} = \frac{10^{b_{sample}-b_{std}}\phi_{std}\sigma_{std}[c]_{std}n_{std}}{\phi_{sample}[c]_{sample}n_{sample}} \qquad \textbf{(Equation 5.1)}$$

where ϕ is the emission quantum yield, n is the solvent refractive index, b is the intercept in the linear fit of the quadratic power dependence, and [c] is the concentration. The two-photon

photoluminescence spectra were measured by exciting the sample at 800 nm and collecting the photoluminescence at 520 nm, the two-photon excited fluorescence maxima (**Figure 5.4B**). In all cases, the two-photon excited emission spectra are very similar to the one-photon steady state emission spectra (**Figure 5.3**). The TPA cross-section values for both poly-*cis*-**1**-*b*-*cis*-**2** and poly-*cis*-**1**-*b*-*trans*-**2** at the same concentration were found to be 11.4 GM and 1490 GM (1 Göppert-Mayer = 10^{-50} cm^4 s $photon^{-1}$) respectively, as listed in Table 2. The TPA cross-section for poly-*cis*-**1**-*b*-*trans*-**2** was found to be much higher than that of poly-*cis*-**1**-*b*-*cis*-**2** indicating efficient intramolecular charge transfer nature of poly-*cis*-**1**-*b*-*trans*-**2** which is useful for OLED, two-photon imaging, and photovoltaic applications. It has been observed that the transition probability of TPA increases with increasing ICT character.[57] This higher TPA cross-section was ascribed to the increased conjugation length and higher π–π interaction present in poly-*cis*-**1**-*b*-*trans*-**2** as a result of the more rodlike structure of the *trans* PPV segment, which allows for more effective charge mobility along the polymer backbone. In order to better understand the TPA cross-section in terms of dipole moments and the different TPA mechanisms, the random (classical) TPA expression can also be written as:[57]

$$\delta_R = \frac{B}{\hbar^2 \varepsilon_0^2} \omega_1^0 \omega_2^0 \delta(\varepsilon_f - \varepsilon_g - 2\omega_0) \times \left| \frac{1}{(\omega_0 + \varepsilon_g - \varepsilon_e) - ik_e/2} \mu_{fe}.e\mu_{eg}.e + \frac{1}{\omega_0 - \frac{ikg}{2}} \mu_{fg}.e\mu_{gg}.e + \frac{1}{\omega_0 - \frac{ikf}{2}} \mu_{ff}.e\mu_{fg}.e \right|^2 \quad \text{(Equation 5.2)}$$

The first term in Equation 5.2 describes TPA through an intermediate level. Alternatively, the second and third terms in Equation 5.2 describe TPA through the transition dipole pathway where the ground and final states are strongly coupled to each other. Therefore, in the transition dipole pathway intermediate states are not involved. Chouk *et al.* described that the transition dipole-

moment of *trans*-PPV is three times greater due to higher electron mobility created by a lower overall torsional level and higher planarity than *cis*-PPV.[59] We also calculated the transition dipole moment for all PPVs, which was found to be 2.59 and 0.23 Debye for poly-*cis*-**1**-*b*-*trans*-**2** and poly-*cis*-**1**-*b*-*cis*-**2** respectively. The strong dependence of the random TPA cross section on the transition dipole moment (Equation 5.2) therefore explains why poly-*cis*-**1**-*b*-*trans*-**2** has a greater TPA cross-section value compared to poly-*cis*-**1**-*b*-*cis*-**2**.

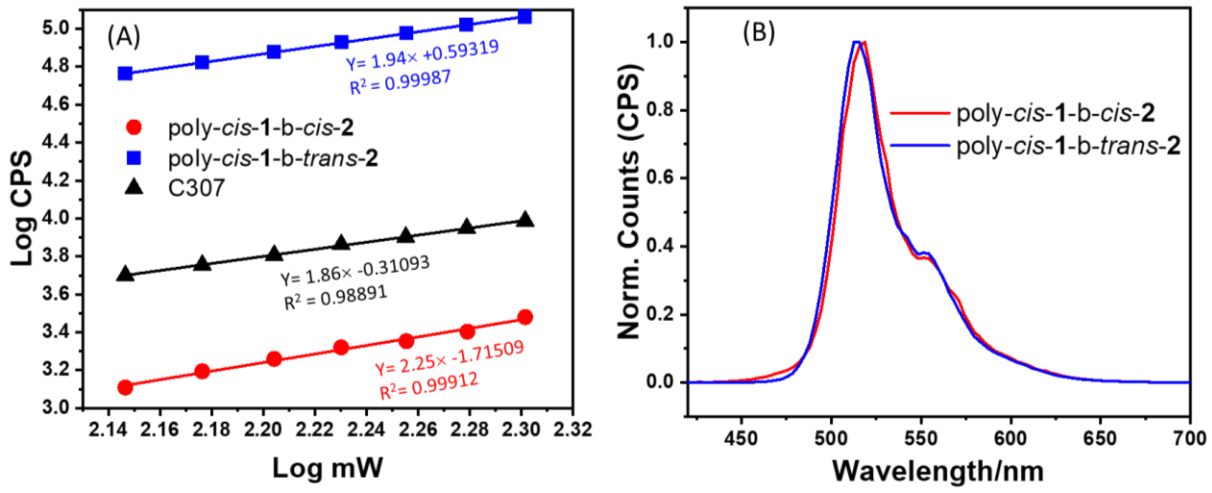


Figure 5.4. (A) Excitation power dependent classical TPA fluorescence (at 520 nm) and (B) two-photon excited fluorescence spectra of the investigated compounds. The excitation wavelength was 800 nm.

Table 4.2. Summary of Classical TPA Cross-sections of the Copolymers in Chloroform

Samples	**Concentration (M)**	**TPA (GM)**	**Cross-section**
poly-*cis*-**1**-*b*-*cis*-**2**	3.97×10^{-6}	11.4	
poly-*cis*-**1**-*b*-*trans*-**2**	3.97×10^{-6}	1490	

5.5.4. Time-resolved fluorescence up-conversion

In order to have insight into early time relaxation dynamics, time-resolved fluorescence studies of poly-*cis*-**1**-*b*-*cis*-**2** and poly-*cis*-**1**-*b*-*trans*-**2** were performed at the emission wavelength of 517 nm upon excitation at 400 nm, using fluorescence up-conversion technique (**Figure 5.5**). As shown in Figure 5, decay curves clearly show that there is a faster fluorescence decay for poly-*cis*-**1**-*b*-*trans*-**2** compared to poly-*cis*-**1**-*b*-*cis*-**2**. All the time profiles are tri-exponentially fit with a relatively fast rise component of ~0.153–0.166 ps and predominant slow components in ps time domain. All the fitted decay parameters are given in Table 3. Both poly-*cis*-**1**-*b*-*cis*-**2** and poly-*cis*-**1**-*b*-*trans*-**2** show almost identical rise times. However, the fluorescence decay lifetimes for both PPVs are different. For poly-*cis*-**1**-*b*-*trans*-**2**, the shorter time constant becomes faster from 155 ps to 28.1 ps along with a rise of very fast time constant [0.166 ps]. Again, the longer component changes from 604 ps to 413 ps indicates a decrease in radiative processes in the case of poly-*cis*-**1**-*b*-*trans*-**2** relative to poly-*cis*-**1**-*b*-*cis*-**2**. The decrease in radiative processes of the decay dynamics suggest the more efficient charge transfer occurs in poly-*cis*-**1**-*b*-*trans*-**2**.

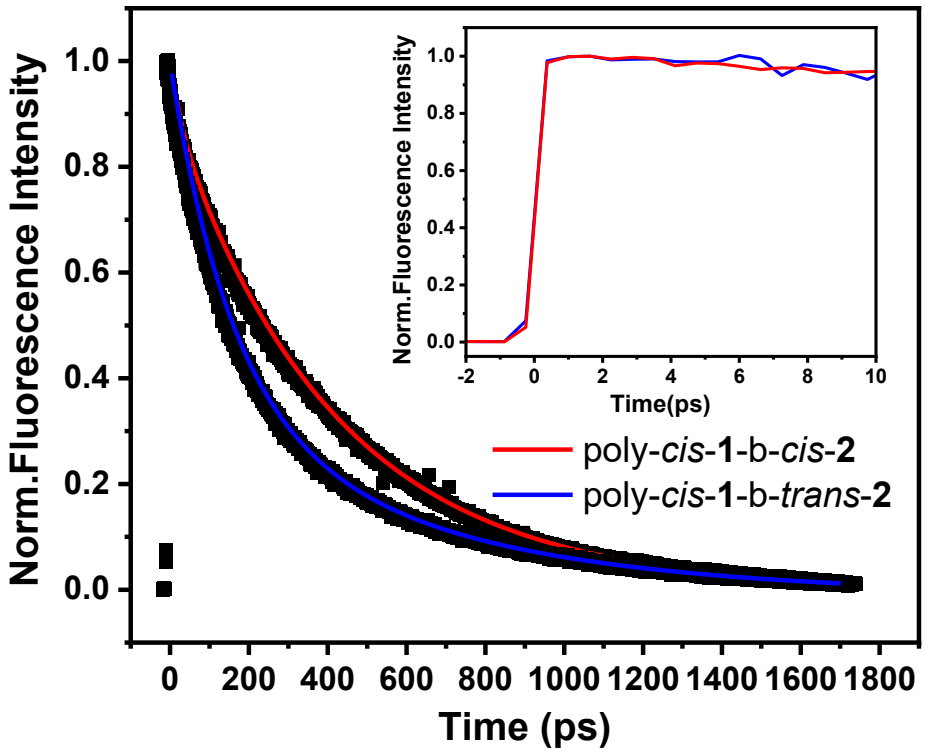


Figure 5.5. Fluorescence decay traces of poly-*cis*-**1**-*b*-*cis*-**2** and poly-*cis*-**1**-*b*-*trans*-**2** at the emissive wavelength of 517 nm after excitation at 400 nm. Inset are the emissive decay traces in 10 ps time window.

Table 5.3. Summary of the Fluorescence Up-conversion with both Copolymers[a]

Samples	**τ_1 (ps) (a_1%)**	**τ_2(ps) (a_2%)**	**τ_3(ps) (a_3%)**
poly-*cis*-**1**-*b*-*cis*-**2**	0.153 ± 0.004 (-100)	155 ± 1.22 (63)	604 ± 10.4 (37)
poly-*cis*-**1**-*b*-*trans*-**2**	0.166 ± 0.002 (-100)	28.1 ± 1.00 (10)	413 ± 0.66 (90)

[a]A negative amplitude indicates that the corresponding components are rise components.

5.5.5. Femtosecond Transient Absorption

To gain more insight into the charge carrier distribution in the excited state and their relaxation and recombination dynamics of both PPVs in a sub-picosecond to picosecond time scale, we further performed time-resolved transient absorption (TA) experiments. **Figure 5.6A, B** (**and Figure S5.8**) presents the time-resolved TA spectra of the excited state population following photoexcitation of the PPV samples in chloroform at room temperature. The pump source at 400 nm was used for both poly-*cis*-**1**-*b*-*cis*-**2** and poly-*cis*-**1**-*b*-*trans*-**2**, with probing of the entire visible region. The initial spectra consist of a stimulated emission (SE) around 500 nm (for poly-*cis*-**1**-*b*-*cis*-**2**) and 490 nm (poly-*cis*-**1**-*b*-*trans*-**2**) which overlaps with ground state bleach (GSB) for poly-*cis*-**1**-*b*-*cis*-**2** and poly-*cis*-**1**-*b*-*trans*-**2**, respectively, and the broad excited state absorption (ESA) band beyond 600 nm peaking at 724 and 750 nm for poly-*cis*-**1**-*b*-*cis*-**2** and poly-*cis*-**1**-*b*-*trans*-**2** respectively. A blue shift (like steady state emission spectra) and spectral narrowing of the SE peak is observed for poly-*cis*-**1**-*b*-*trans*-**2** relative to poly-*cis*-**1**-*b*-*cis*-**2**. **Figure 5.6C** shows the SE dynamics of poly-*cis*-**1**-*b*-*cis*-**2** and poly-*cis*-**1**-*b*-*trans*-**2** at 500 and 490 nm, respectively. **Figure 5.6D** shows the ESA dynamics of poly-*cis*-**1**-*b*-*cis*-**2** and poly-*cis*-**1**-*b*-*trans*-**2** at 724 and 750 nm, respectively. Inset of **Figure 5.6C & 5.6D** represents rise/decay dynamics in 20 ps time domain to get better understanding in ultrafast timescale. All SE decays were well fitted by bi-exponential functions with characteristic lifetime values of 7.5 ps (73%) & >1600 ps (27%) (greater than the experimental time window) for poly-*cis*-**1**-*b*-*cis*-**2** and 5.8 ps (78.8%) & 167 ps (21.2%) for poly-*cis*-**1**-*b*-*trans*-**2**, respectively, which nicely corroborates with the fluorescence decay time measured by the fluorescence upconversion technique. The shortening of time signifies the faster excited state energy/electron transfer which eventually makes the bleach recovery faster in case of poly-*cis*-**1**-*b*-*trans*-**2**. In addition, all ESA decays were also fitted biexponentially with lifetimes

values of 7.1 ps (67%) & 275 ps (33%) for poly-*cis*-**1**-*b*-*cis*-**2** at 724 nm; and 8.3 ps (64%) & 332 ps (36%) at 750 nm for poly-*cis*-**1**-*b*-*trans*-**2**, respectively. Instead of ESA decay, we can also see a very fast rise component with lifetime values of 0.249 ps (for poly-*cis*-**1**-*b*-*cis*-**2**) and 0.273 ps (for poly-*cis*-**1**-*b*-*trans*-**2**), respectively.

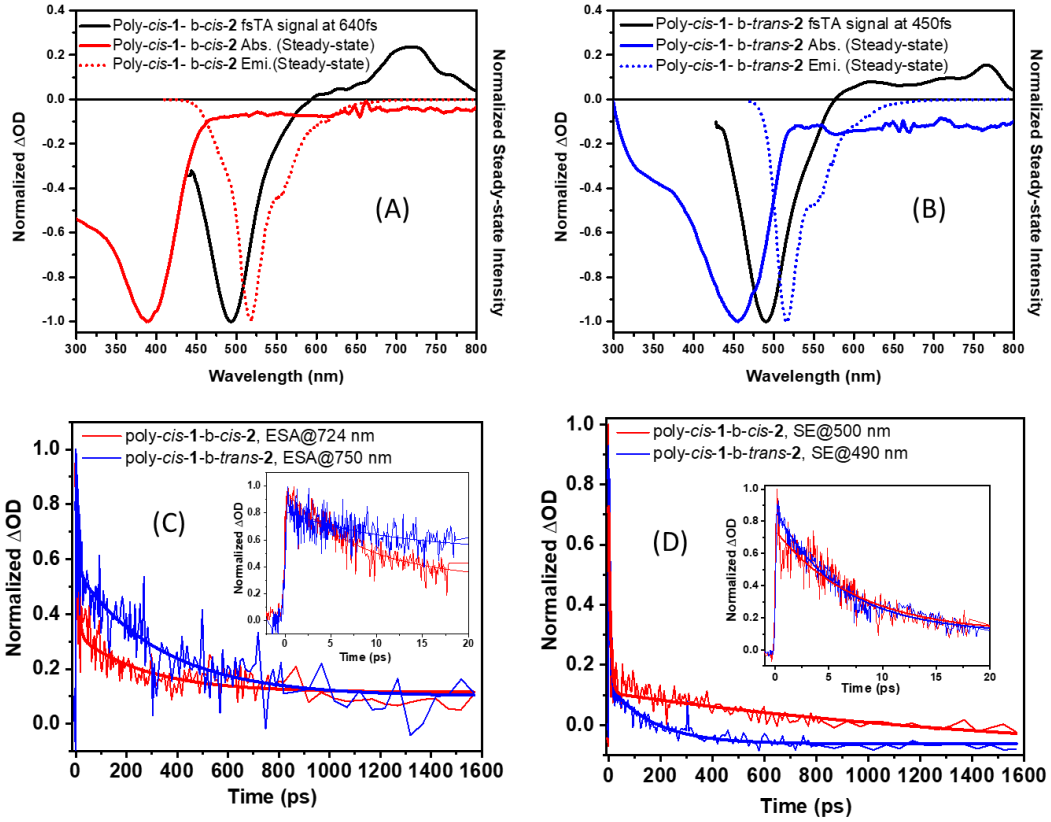


Figure 5.6. Femtosecond transient absorption spectra (*fs*TAS) for poly-*cis*-**1**-*b*-*cis*-**2** (A) and poly-*cis*-**1**-*b*-*trans*-**2** (B) corroborated with steady state absorption and emission spectra. Lower panel shows time traces of poly-*cis*-**1**-*b*-*cis*-**2** and poly-*cis*-**1**-*b*-*trans*-**2** in 1.6 ns and 20 ps (inset) time windows. The excitation wavelength for both compounds was 400 nm.

Table 5.4. Transient Absorption Data for poly-*cis*-**1**-*b*-*cis*-**2** and poly-*cis*-**1**-*b*-*trans*-**2**.[a]

Stimulated Emission dynamics			
Samples	**t_1 (ps), (a_1%)**		**t_2 (ps), (a_2%)**
poly-cis-**1**-b-cis-**2**	7.5 ± 0.38 (73)		>1600 ± 344 (27)
poly-*cis*-**1**-*b*-*trans*-**2**	5.8 ± 0.21 (78.8)		167 ± 22 (21.2)
Excited state absorption dynamics			
Samples	**t_1 (ps), (a_1%)**	**t_2 (ps), (a_2%)**	**t_3 (ps), (a_3%)**
poly-*cis*-**1**-b-*cis*-**2**	0.249±0.09 (-100)	7.1±0.56 (67)	275±77 (33)
poly-*cis*-**1**-*b*-*trans*-**2**	0.273±0.12 (-100)	8.3±0.52 (64)	332±64 (36)

[a]A negative amplitude indicates that the corresponding components are rise components.

All TA data listed in **Table 5.4** are consistent with literature reports:[60–64] The early relaxation originates from a strong coupling between electronic and vibrational states. Hence, the fast kinetic

processes are attributed to delocalized exciton states (sub ps) and vibrational cooling (few ps).[65] Subsequently, the excited state dynamics is dominated by intrachain charge/energy transfer on a characteristic timescale of tens of ps.[66,67] This electronic charge/energy transfer occurs prior to emission which generally stems from localized low-energy sites.[68–71]

In case of SE dynamics, the t_1 component [for poly-*cis*-**1**-*b*-*cis*-**2**, t_1 = 7.5 ps and for poly-*cis*-**1**-*b*-*trans*-**2**, t_2 = 5.8 ps] is assigned to the vibrational cooling of S1 state. Whereas the t_2 component [for poly-*cis*-**1**-*b*-*cis*-**2**, t_2 = >1600 ps and for poly-*cis*-**1**-*b*-*trans*-**2**, t_2 = 167 ps] is assigned for the relaxation time from S_1 to ground state (S_0). The shortening of time constant signifies the more efficient excited state energy/electron transfer which eventually makes the recombination faster in case of poly-*cis*-**1**-*b*-*trans*-**2** because of its effective conjugation length, high dipole moment, and increased π–π stacking compared to poly-*cis*-**1**-*b*-*cis*-**2**.

The three excited state components are characterized as hot S_1 (hot singlet state), S_1 (singlet state), and S_1 to ground state (S_0). The hot S_1 is short lived (249 fs for poly-*cis*-**1**-*b*-*cis*-**2** and 273 fs for poly-*cis*-**1**-*b*-*trans*-**2**) that is attributed to the initial excitation to the hot S_1 state of the PPVs. The hot S1 state decays very fast to the vibrationally relaxed S_1 state whose lifetime is found to be 7.1 ps for 8.3 ps for poly-*cis*-**1**-*b*-*cis*-**2** and poly-*cis*-**1**-*b*-*trans*-**2**, respectively. Finally, it recombines to ground state (S_0) with the time constant of 275 ps and 332 ps for poly-*cis*-**1**-*b*-*cis*-**2** and poly-*cis*-**1**-*b*-*trans*-**2**, respectively. The time scale of the ES decay of $S_1 - S_0$ is found to be very close to upconversion decay trace. It is important to note that the excited state decay for poly-*cis*-**1**-*b*-*trans*-**2** is relatively slower than poly-*cis*-**1**-*b*-*cis*-**2** which is due to the efficient charge transfer nature of poly-*cis*-**1**-*b*-*trans*-**2** and generation of a long-lived CT state which is beneficial for a light harvesting system.

5.5.6. Entangled-two photon absorption.

Entangled two-photon absorption, a non-linear optical process, was utilized to acquire a better understanding of how quantum light (non-classical) interacts with poly-*cis*-**1**-*b*-*cis*-**2** and poly-*cis*-**1**-*b*-*trans*-**2**. The mechanism for this transition involves the absorption of two entangled photons which are quantum correlated with each other and induce unique photophysics during the ETPA transition. In classical TPA, the two photons are not correlated with each other and so neither are the two absorption events since the two photons can be absorbed randomly. Hence, ETPA scales linearly with the input photon rate, rather than quadratically for classical TPA. The linear trend yields an enhancement in the absorption rate at low input intensities compared to classical TPA, allowing two-photon transitions to be probed at extremely small photon rates where the molecule cannot be damaged. Thus, this study enhances the molecular sensitivity in probing the photophysical characteristics of poly-*cis*-**1**-*b*-*cis*-**2** and poly-*cis*-**1**-*b*-*trans*-**2** with extremely low photon flux preventing photobleaching and light-mediated toxicity.

Figure 7 shows the ETPA rate as a function of input photon flux for poly-*cis*-**1**-*b*-*cis*-**2** and poly-*cis*-**1**-*b*-*trans*-**2** in chloroform. Both poly-*cis*-**1**-*b*-*cis*-**2** and poly-*cis*-**1**-*b*-*trans*-**2** absorbed entangled light in magnitude higher than the baseline as expected. Furthermore, at relatively similar concentrations, poly-*cis*-**1**-*b*-*cis*-**2** exhibited a higher ETPA absorption than poly-*cis*-**1**-*b*-*trans*-**2**. This finding implies that poly-*cis*-**1**-*b*-*cis*-**2** absorb entangled photons better than poly-*cis*-**1**-*b*-*trans*-**2** in chloroform solution. In general, ETPA cross-section, σ_e is given by:[72]

$$\sigma_e = \frac{2\pi}{(\hbar\varepsilon_0 c)^2 A_e T_e}\omega_i\omega_s\delta\left(\varepsilon_f - \varepsilon_i - \omega_i - \omega_s\right) \times \left|\left\{\sum_j \{D_{is}^{(j)} \frac{1-\exp\left[-iT_e\Delta_j^{(i)}\right]}{\Delta_j^i} + D_{si}^{(j)} \frac{1-\exp\left[-iT_e\Delta_j^{(s)}\right]}{\Delta_j^s}\}\right\}\right|^2 \qquad \text{(Equation 5.3)}$$

where $\hbar$ is Plank's constant, ε_0 is vacuum permittivity, c is the speed of light, A_e and T_e are entanglement area and entanglement time, respectively, ω_i and ω_s are the frequencies of the idler and signal photons, $\delta(\varepsilon_f - \varepsilon_i - \omega_i - \omega_s)$ enforces energy conservation, and ε_i are the energy eigenvalues of the ground and excited states, respectively, $D_{is}^{(j)} = < \Psi_i|e_i\mu|\Psi_j >< \Psi_j|e_s\mu|\Psi_f >$ gives the transition dipole matrix elements, and $\Delta_j^{(k)} = \varepsilon_j - \varepsilon_i - \omega_k$ is the detuning energy where k = i or s refers to the signal and idler photons. Like classical TPA, the ETPA cross-section is also directly proportional to the transition dipole moment, thus a similar trend in ETPA cross-section would be expected. Interestingly, the ETPA cross-section (**Table 5.5**) for poly-*cis*-**1**-*b*-*cis*-**2** (5 x 10^{-18} cm^2/molecule) was found to be twice as large as that of poly-*cis*-**1**-*b*-*trans*-**2** (2.2 x 10^{-18} cm^2/molecule) indicating that *cis*-PPV is more sensitive to entangled light which can be useful for quantum sensing and quantum imaging applications. The capability of these PPVs to absorb entangled light may be the cause of this opposite trend. However, the ETPA cross-section also depends on electronic energy levels of the molecule. Generally, in each molecule, there are certain electronic energy states which are not easily accessible by classical light but may be accessible with entangled light. It has been described by Chouk et al that *cis*-PPV has higher energy band gap and lower HOMO level than *trans*-PPV.[52] In our TD-DFT studies performed on *trans*- and *cis*-PPV, we observed a similar decrease in the HOMO energy level by -0.40 eV from *trans*- to *cis*-PPV (**Figures 5.8 and S5.9**), respectively. The decrease in the HOMO orbital energy coupled with the increase in energy of the LUMO and LUMO+1 orbitals increased the band gap of the *cis*-PPV. Interestingly, the HOMO-1 orbital also decreased in energy level by -0.12 eV (**Figure 5.8**). Presumably this lower-lying HOMO-1 electronic energy state could enable *cis*-PPV to absorb a substantial quantity of entangled two-photons, leading to a greater ETPA cross-section than *trans*-

PPV. To gain a better understanding as to why the *cis*-PPV observed a lower HOMO-1 energy level, we sought to simulate the amount of orbital delocalization in the *trans*- vs. *cis*-PPV systems by measurement of the orbital delocalization index (ODI) for HOMO and HOMO-1 orbitals. Interestingly, while both HOMO and HOMO-1 orbitals were lower in energy for the *cis*-PPV, less orbital delocalization was observed (**Tables S5.8 – S5.9**) contrary to what would be expected. As a result, single point calculations at the CAM-B3LYP-D3/6-311G(d,p)-SMD($CHCl_3$) level of theory were performed on the individual styrene (1)/(3) and 1,4-dimethoxy-2-vinylbenzene (2)/(4) fragments of *cis*- (**Figure S5.14**) and *trans*-PPV (**Figure S5.13**). Plotting the HOMO-1, HOMO, LUMO, and LUMO+1 energies of each fragment, we determined that the HOMO and HOMO-1 orbitals significantly decreased in energy from *trans*- to *cis*-PPV for the majority of fragments (**Figure S5.15**). The styrene fragment 1 (*trans*-PPV(1) vs. *cis*-PPV(1)) saw the largest decrease in HOMO orbital energy from *trans*- to *cis*-PPV ($\Delta E_{HOMO}(1)$ = -0.16 eV). The 1,4-dimethoxy-2-vinylbenzene fragment 2 (*trans*-PPV(2) vs. *cis*-PPV(2)) saw the largest decrease in HOMO-1 orbital energy from *trans*- to *cis*-PPV ($\Delta E_{HOMO-1}(2)$ = -0.32 eV), leading to a decrease in the entire *cis*-PPV HOMO-1 orbital energy (Table S10). These results suggest that the quantum interference between entangled photons and the interacting matter can provide changes to two-photon absorption signals that are not observed classically due to a lower lying HOMO-1 electronic state in *cis*-PPV.

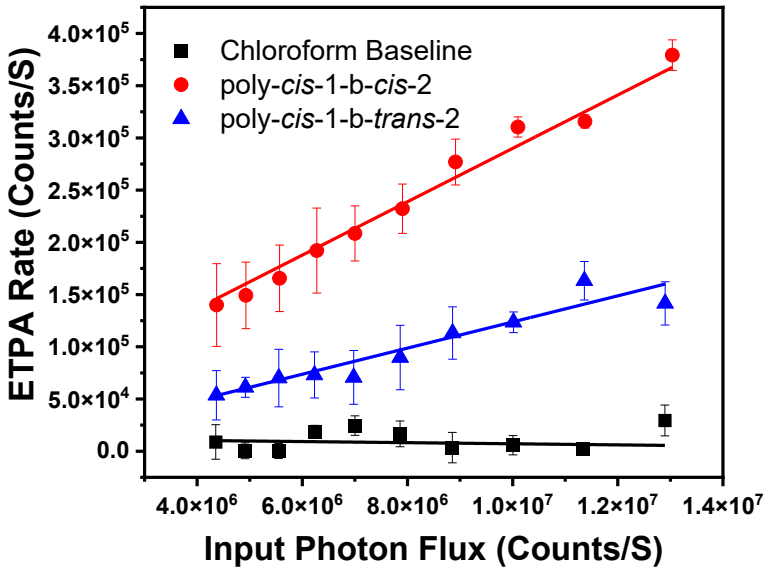


Figure 5.7. Entangled two-photon absorption as a function of input photon flux (i.e., excitation power) for poly-*cis*-**1**-*b*-*cis*-**2** and poly-*cis*-**1**-*b*-*trans*-**2** in chloroform solution.

ETPA scales linearly with the input photon flux, rather than quadratically for classical TPA. The linear trend yields an enhancement in the absorption rate at low input intensities compared to classical TPA. The ETPA rate is determined to be the difference between the photon counts per second transmitted through the solvent (chloroform) and the sample (PPVs) solution for a given input photon flux.

Table 5.5. ETPA Cross-sections for poly-*cis*-**1**-*b*-*cis*-**2** and poly-*cis*-**1**-*b*-*trans*-**2** in chloroform.

Samples	**Conc. (μM)**	**ETPA Cross-section (cm^2/molecule)**
poly-*cis*-**1**-*b*-*trans*-**2**	8.4	2.2×10^{-18}
poly-*cis*-**1**-*b*-*cis*-**2**	8.9	5.0×10^{-18}

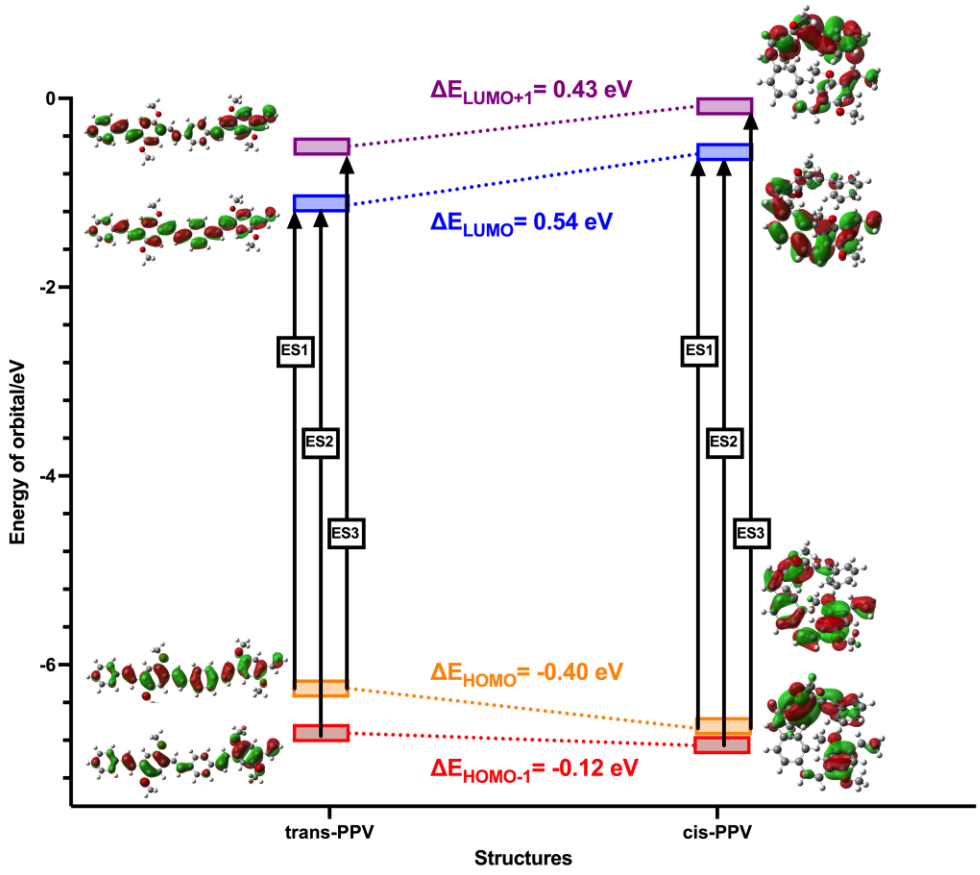


Figure 5.8. Frontier molecular HOMO−1 through LUMO+1 orbitals of *trans*- (left panel) and *cis*-PPV (right panel) calculated at the CAM-B3LYP-D3/6-311+G(d,p)-SMD($CHCl_3$) level of theory.

5.6. Conclusion

This comprehensive spectroscopic investigation of poly-*cis*-**1**-*b*-*cis*-**2** and poly-*cis*-**1**-*b*-*trans*-**2** demonstrates that the olefin geometry of the conjugated polymer significantly impacts the two-photon absorption properties. When TPA cross-sections are compared, poly-*cis*-**1**-*b*-*trans*-**2** has a greater classical TPA cross-section than poly-*cis*-**1**-*b*-*cis*-**2**, suggesting a more efficient intramolecular charge transfer, which is in line with our femtosecond transient absorption studies where we found a relatively long-lived CT state for poly-*cis*-**1**-*b*-*trans*-**2.** These findings might

have strong implications for the potential uses of PPVs as fluorophores. Indeed, while all-*trans* PPV might be suitable applications including OLED, two-photon imaging, and photovoltaic applications because of a more efficient intramolecular charge transfer, all-*cis* PPV appears to be more sensitive to entangled light (larger ETPA cross section), which is desirable for quantum sensing and quantum imaging applications. DFT calculations supports our hypothesis that the all-*cis* PPV variant possesses a lower lying HOMO-1 state comparatively to the all-*trans* congener, which suggests a more energetically favorable interaction with entangled photons that could result in the larger ETPA cross section observed experimentally. We anticipate that the ability to tune both classical TPA and non-classical ETPA cross sections through synthetic structural modification of the olefin geometry in PPVs will help inform future design of chromophores for applications in this field.

REFERENCES:

1. Zaquen, N., Lutsen, L., Vanderzande, D. & Junkers, T. Controlled/living polymerization towards functional poly(*p*-phenylene vinylene) materials. *Polym. Chem.* **2016**, *7*, 1355–1367.

2. Blayney, A. J., Perepichka, I. F., Wudl, F. & Perepichka, D. F. Advances and Challenges in the Synthesis of Poly(*p*-phenylene vinylene)-Based Polymers. *Isr. J. Chem.* **2014,** *54*, 674–688.

3. Burroughes, J. H.; Bradley, D. D. C.; Brown, A. R.; Marks, R. N.; Mackay, K.; Friend, R. H.; Burns, P. L.; Holmes, A. B. Light-Emitting Diodes Based on Conjugated Polymers. *Nature* **1990**, *347*, 539–541.

4. Halls, J. J. M.; Walsh, C. A.; Greenham, N. C.; Marseglia, E. A.; Friend, R. H.; Moratti, S. C.; Holmes, A. B. Efficient photodiodes from interpenetrating polymer networks. *Nature* **1995**, *376*, 498–500.

5. Kraft, A.; Grimsdale, C. A.; Holmes, B. A. Electroluminescent Conjugated Polymers-Seeing Polymers in a New Light. *Angew Chem Int Ed Engl*. **1998**, *37*, 402–428.

6. Freitag, M., Teuscher, J., Saygili, Y. *et al.* Dye-sensitized solar cells for efficient power generation under ambient lighting. *Nature Photon* **2017**, *11*, 372–378.

7. Grimsdale, A. C., Chan, K. L., Martin, R. E., Jokisz, P. G. & Holmes, A. B. Synthesis of light-emitting conjugated polymers for applications in electroluminescent devices. *Chem. Rev.* **2009**, *109*, 897–1091.

8. Brabec, C., Dyakonov, V. & Scherf WILEY-, U. *Organic photovoltaics: materials, device*

physics, and manufacturing technologies. (2011).

9. Friend, R. H.; Gymer, R. W.; Holmes, A. B.; Burroughes, J. H.; Marks, R. N.; Taliani, C.; Bradley, D. D. C.; Dos Santos, D. A.; Brédas, J. L.; Lögdlund, M.; Salaneck, W. R. Electroluminescence in conjugated polymers. *Nature* **1999***, 397*, 121–128.

10. Hsu, T. W., Kim, C. & Michaudel, Q. Stereoretentive Ring-Opening Metathesis Polymerization to Access All- cis Poly(p-phenylenevinylene)s with Living Characteristics. *J. Am. Chem. Soc***. 2020**, *142*, 11983–11987.

11. Shin, S.; Menk, F.; Kim, Y.; Lim, J.; Char, K.; Zentel, R.; Choi, T.-L. Living Light-Induced Crystallization-Driven Self-Assembly for Rapid Preparation of Semiconducting Nanofibers. *J. Am. Chem. Soc*. **2018**, *140*, 6088.

12. Wang, F.; He, F.; Xie, Z.; Li, M.; Hanif, M.; Gu, X.; Yang, B.; Zhang, H.; Lu, P.; Ma, Y. A Solution-Processible Poly(p-phenylene vinylene) without Alkyl Substitution: Introducing the cis- Vinylene Segments in Polymer Chain for Improved Solubility, Blue Emission, and High Efficiency. *J. Polym. Sci., Part A: Polym. Chem*. **2008**, *46*, 5242.

13. Lei, T., Dou, J. H., Cao, X. Y., Wang, J. Y. & Pei, J. Electron-Deficient Poly(p-phenylene vinylene) Provides Electron Mobility over 1 cm2 V-1 s-1 under Ambient Conditions. *J. Am. Chem. Soc.* **2013**, *135*, 12168–12171.

14. Osaka, I., Abe, T., Shinamura, S. & Takimiya, K. Impact of isomeric structures on transistor performances in naphthodithiophene semiconducting polymers. *J. Am. Chem. Soc.* **2011**, *133*, 6852–6860.

15. Chen, L. *et al.* From the Cover: Highly sensitive biological and chemical sensors based on

reversible fluorescence quenching in a conjugated polymer. *Proc. Natl. Acad. Sci. U. S. A.* **1999**, *96,* 12287.

16. Vanden Bout, D. A. *et al.* Discrete intensity jumps and intramolecular electronic energy transfer in the spectroscopy of single conjugated polymer molecules. *Science* **1997**, 277, 1074–1077.

17. Chaieb, A. *et al.* PL and EL properties of oligo (p-phenylene vinylene) (OPPV) derivatives and their applications in organic light-emitting diodes (OLED). *Opt. Mater. (Amst).* **2008**, *31*, 68–74.

18. Dilonardo, E. *et al.* Tailoring Optical Properties of Blue-Gap Poly(p-phenylene Vinylene)s for LEDs Applications. *Adv. Sci. Technol.* **2010**, *75*, 118–123.

19. Hu, D. *et al.* Collapse of stiff conjugated polymers with chemical defects into ordered, cylindrical conformations. *Nat.* **2000,** *405,*1030–1033.

20. Peters, M. *et al.* PPV-Based Conjugated Polymer Nanoparticles as a Versatile Bioimaging Probe: A Closer Look at the Inherent Optical Properties and Nanoparticle-Cell Interactions. *Biomacromolecules* **2016**, *17*, 2562–2571.

21. Zaquen, N. *et al.* Profluorescent PPV-Based Micellar System as a Versatile Probe for Bioimaging and Drug Delivery. *Biomacromolecules* **2016**, *17*, 4086–4094.

22. Garmire, Elsa. Nonlinear Optics in Daily Life. *Optics Express*, **2013**, *21*, 30532.

23. Verbiest, T.; Parsoons, A. Nonlinear Optical Properties of Polymeric Materials and Polymer Films: Recent Developments and Future Trends. Macromol. *Symp*. **1996**, *102*, 347–354.

24. Castet, F.; Rodriguez, V.; Pozzo, J.L.; Ducasse, L.; Plaque, A.; Champagne, B. Design and Characterization of Molecular Nonlinear Optical Switches. *Acc. Chem. Res*. **2013**, *46*, 2656–2665.

25. Li, D.Q; Ratner, M.A.; Marks, T.J. Molecular and Macromolecular Nonlinear Optical Materials. Probing Architecture/Electronic Structure/Frequency Doubling Relationships via an SCF-LCAO MECI .Pi. Electron Formalism. *J. Am. Chem. Soc*. **1988**, *110*, 1707– 1715.

26. Marder, S.R.; Kippelen, B.; Jen, A.K.Y. Design and Synthesis of Chromophores and Polymers for Electro-optic and Photorefractive Applications. *Nature*, **1997**, *388*, 845–851.

27. Saleh, B.; Jost, B.; Fei, H.B.; Teich, M. Entangled-Photon Virtual State Spectroscopy. *Phys. Rev. Lett*. **1998**, *80*, 33483.

28. Fei, H.B., Jost, B., Popescu, S., Saleh, B., Teich, M. Entanglement-Induced Two Photon Transparency. *Phys. Rev. Lett* **1997**, *78*, 1679

29. Eshun, A.; Gu, B.; Varnavski, O.; Asban, S.; Dorfman, KE.; Mukamel,S.; Goodson, T. Investigations of molecular optical properties using quantum light and Hong–Ou–Mandel interferometry. *J. Am. Chem. Soc.* **2021**, *143*, 9070–9081

30. Donehue, JE.; Varnavski, OP.; Cemborski, R.; Iyoda, M.; Goodson, T.; Probing coherence in synthetic cyclic light-harvesting pigments. *Journal of the American Chemical Society* **2011** *133*, 4819-4828.

31. Song, J.-A.; Peterson, G. I.; Bang, K.-T.; Ahmed, T. S.; Sung, J.-C.; Grubbs, R. H.; Choi, T. L. Ru-catalyzed, *cis*-selective ring opening metathesis polymerization of various monomers, including a dendronized macromonomer, and implications to enhanced shear

stability. *J. Am. Chem. Soc.* **2020**, *142*, 10438-10445.

32. Eshun, A.; Varnavski, O.; Villabona-Monsalve, J. P.; Burdick, R. K.; Goodson, III. T. "Entangled Photon Spectroscopy" *Acc. Chem. Res.* **2022**, *55*, 7, 991-1003.

33. Burdick, R. K.; Schatz, G. C.; Goodson, III. T. "Enhancing Entangled Two-Photon Absorption for Picosecond Quantum Spectroscopy ", *J. Am. Chem. Soc.* **2021**, *143*, 41, 16930-16934.

34. Varnavski,O.; Goodson, T. Two-photon fluorescence microscopy at extremely low excitation intensity: The power of quantum correlations. *Am. Chem. Soc*. **2020**, *142*, 12966–12975.

35. Varnavski, O.; Gunthardt, C.; Rehman, A.; Luker, G. D.; Goodson, III. T. "Quantum Light-Enhanced Two-Photon Imaging of Breast Cancer Cells" *J. Phys. Chem. Lett.* **2022**, *13*, 12, 2772-2781

36. M. Y. Lavrentiev, W. Barford, S. J. Martin and H. Daly. Theoretical investigation of the low-lying electronic structure of poly„p-phenylene vinylene. Phys. Rev. B: Condens. Matter Mater. Phys. **1999**, *59*, 9987–9994.

37. Guo, F.; Shih, Y. Z. Low-lying two-photon excitations in poly(*p*-phenylene vinylene) and its derivatives. Chemical Physics Letters **2003**, *370*, 572–577.

38. Ghosh, A.; Jana, B.; Chakraborty, S.; Maiti, S.; Jana, B.; Ghosh, H. N.; Patra, A. Exciton Dynamics and Formation Mechanism of MEH-PPV Polymer-Based Nanostructures. *J. Phys. Chem. C* **2017**, *121*, 21062–21072.

39. De Boni, L.; Andrade, A. A.; Correa, D. S.; Balogh, D. T.; Zilio, S. C.; Misoguti, L.;

Mendonca, C. R. Nonlinear absorption spectrum in MEH-PPV/Chloroform solution: A competition between two-photon and saturated absorption processes. *J. Phys. Chem. B* **2004**, *108*, 5221–5224.

40. Oliveira, S. L.; Correa, D. S.; De Boni, L.; Misoguti, L.; Zilio, S. C.; Mendonca, C. R. Two-photon absorption cross spectrum of a pi-conjugated polymer obtained using the white-light continuum Z-scan technique. *Appl. Phys. Lett.* **2006***, 88*, 021911.

41. Hancock, S. N,; Yuntawattana, N.; Valdez, S. M.; Michaudel, Q. Expedient synthesis and ring-opening metathesis polymerization of pyridinonorbornenes. *Polym. Chem.* **2022**, *12*, 5530-5535.

42. Lidster, B. J.; Behrendt, J. M.; Turner, M. L.; Monotelechelic poly(p-phenylenevinylene)s by ring opening metathesis polymerization. *Chem. Commun*. **2014**, *50*, 11867–11870.

43. Villabona-Monsalve, J. P.; Burdick, R. K.; Goodson, III. T. "Measurements of Entangled Two-Photon Absorption in Organic Molecules with CW-Pumped Type-I Spontaneous Parametric Down-Conversion", *J. Phys. Chem. C* **2020**, *124*, 24526-24532.

44. Khan, R. K. M.; Torker, S.; Hoveyda, A. H. Readily accessible and easily modifiable Ru-based catalysts for efficient and Z-selective ring-opening metathesis polymerization and ring-opening/cross-metathesis. *J. Am. Chem. Soc.* **2013**, *135*, 10258–10261.

45. Song, J.-A.; Peterson, G. I.; Bang, K.-T.; Ahmed, T. S.; Sung, J.-C.; Grubbs, R. H.; Choi, T. L. Ru-catalyzed, *cis*-selective ring opening metathesis polymerization of various monomers, including a dendronized macromonomer, and implications to enhanced shear stability. *J. Am. Chem. Soc.* **2020**, *142*, 10438–10445.

46. Kempel, S. J.; Hsu, T.-W.; Michaudel, Q. Stereoretentive olefin metathesis: A new avenue for the synthesis of all-*cis* poly(*p*-phenylene vinylene)s and stereodefined polyalkenamers. *Synlett*, **2021**, *32*, 851–857.

47. Yu, C.-Y.; Turner, M. L. Soluble Poly(*p*-phenylenvinylene)s through ring-opening metathesis polymerization. *Angew. Chem. Int. Ed***. 2006***, 45*, 7797–7800.

48. Yu, C.-Y.; Horie, M.; Spring, A. M.; Tremel, K.; Turner, M. L. Homopolymers and block copolymers of *p*-phenylenevinylene-2,5-diethylhexyloxy-*p*-phenylenevinylene and *m*-phenylenevinylene-2,5-diethylhexyloxy-*p*-phenylenevinylene by ring-opening metathesis polymerization. *Macromolecules* **2010**, *43*, 222–232.

49. Menk, F.; Mondeshki, M.; Dudenko, D.; Shin, S.; Schollmeyer, D.; Ceyhun, O.; Choi, T.-L.; Zentel, R. Reactivity studies of alkoxy-substituted [2.2]Paracyclophane-1,9-dienes and specific coordination of the monomer repeating unit during ROMP. *Macromolecules* **2015**, *48*, 7435–7445.

50. Lidster, B. J.; Kumar, D. R.; Spring, A. M.; Yu, C.-Y.; Helliwell, M.; Raftery, J.; Turner, M. L. Alkyl substituted [2.2]paracyclophane-1,9-dienes. *Org. Biomol. Chem.* **2016**, *14*, 6079–6087.

51. Kumar, D. R.; Lidster, B. J.; Adams, R. W.; Turner, M. L. Mechanistic investigation of the ring opening metathesis polymerisation of alkoxy and alkyl substituted paracyclophanedienes. *Polym. Chem.* **2017**, *8*, 3186–3194.

52. Shin, S.; Menk, F.; Kim, Y.; Lim, J.; Char, K.; Zentel, R.; Choi, T.-L. Living light-induced crystallization-driven self-assembly for rapid preparation of semiconducting nanofibers. *J.*

Am. Chem. Soc. **2018**, *140*, 6088–6094.

53. Gorman, C. B.; Ginsburg, E. J.; Grubbs, R. H. Soluble, highly conjugated derivatives of polyacetylene from the ring-opening metathesis polymerization of monosubstituted coclooctatetraenes: synthesis and the relationship between polymer structure and physical properties. *J. Am. Chem. Soc*.**1993**, *115*, 1397–1409.

54. Hsu, T.-W, Kempel, S. J., Michaudel, Q. All-cis poly(p-phenylene vinylene)s with high molar masses and fast photoisomerization rates obtained through stereoretentive ring-opening metathesis polymerization of [2,2]paracyclophane dienes with various aryl substituents. *J. Polym. Sci*. **2022**, *60*, 569–578.

55. Katayama, H.; Nagao, M.; Nishimura, T.; Matsui, Y.; Umeda, K.; Akamatsu, K.; Tsuruoka, T.; Nawafune, H.; Ozawa, F. Stereocontrolled synthesis and optical properties of all-*cis* poly(phenylene vinylenes) (PPVs): A method for direct patterning of PPVs. *J. Am. Chem. Soc.* **2005**, *127*, 4350–4353.

56. Moslin, R. M.; Espino, C. G.; Swager, T. M. Synthesis of conjugated polymers containing *cis*-phenylenevinylenes by titanium-mediated reductions. *Macromolecules* **2009**, *42*, 452–454.

57. Upton, L.; Harpham, M.; Suzer, O.; Richter, M.; Mukamel, S.; Goodson, T. Optically Excited Entangled States in Organic Molecules Illuminate the Dark. *J. Phys. Chem. Lett*. **2013**, *4*, 2046–2052.

58. Villabona-Monsalve, J. P., Varnavski, O., Palfey, B. A. & Goodson, T. Two-Photon Excitation of Flavins and Flavoproteins with Classical and Quantum Light. *J. Am. Chem.*

Soc. **2018**, *140*, 14562–14566.

59. Chouk, R.; Bergaoui, M., Jaballah, N.; Majdoub, M.; Khalfaoui, M. Shedding light on structural, optoelectronic and charge transport properties of PPV stereoisomers for multilayer OLED application: A first principle computational studies. *J. Mol. Liq.* **2019,** *284*, 193–202.

60. Peng, Z. & Yu, L. Synthesis of conjugated polymers containing ionic transition metal complexes. *J. Am. Chem. Soc.***1996,** *118*, 3777–3778.

61. Wang, Q., Wang, L., Yu, L. Synthesis and unusual physical behavior of a photorefractive polymer containing tris (bipyridyl) ruthenium (II) complexes as a photosensitizer and exhibiting a low. *J. Am. Chem. Soc.* **1998***, 120,* 12860–12868.

62. Wang, Q. & Yu, L. Conjugated polymers containing mixed-ligand ruthenium(II) complexes. Synthesis, characterization, and investigation of photoconductive properties. *J. Am. Chem. Soc.* **2000**, *122*, 11806–11811.

63. Sumpter, B. G. *et al.* Computational study of the structure, dynamics, and photophysical properties of conjugated polymers and oligomers under nanoscale confinement. *ACS Publ.* **2005**, *109*, 7671–7685.

64. Correia, H., Ramos, M. Modelling the effect of nonplanarity on charge transport along conjugated polymer chains. *Materials Science and Engineering C* **2007**, *27,* 1133–1137.

65. Ghosh, A. *et al.* Exciton Dynamics and Formation Mechanism of MEH-PPV Polymer-Based Nanostructures. *J. Phys. Chem. C* **2017**, *121*, 21062–21072.

66. Meskers, S. C. J., Janssen, R. A. J., Haverkort, J. E. M., & Wolter, J. H. Relaxation of photo-

excitations in films of oligo- and poly- (para-phenylene vinylene) derivatives. *Chemical Physics* **2000**, *260*, 415–439.

67. Herz, L. M., Silva, C., Grimsdale, A. C., Müllen, K. & Phillips, R. T. Time-dependent energy transfer rates in a conjugated polymer guest-host system. *Phys. Rev. B – Condens. Matter Mater. Phys.* **2004** ,*70*, 1–9.

68. Nguyen, T. Q., Wu, J., Doan, V., Schwartz, B. J. & Tolbert, S. H. Control of energy transfer in oriented conjugated polymer-mesoporous silica composites. *Science* **2000**, *288*, 652–656.

69. Carlotti, B.; Cai, Z.; Kim, H.; Sharapov, V.; Madu, I. K.; Zhao, D.; Chen, W.; Zimmerman, P. M.; Yu, L.; Goodson, T., III Charge Transfer and Aggregation Effects on the Performance of Planar vs Twisted Nonfullerene Acceptor Isomers for Organic Solar Cells. *Chem. Mater*. **2018**, *30*, 4263−4276.

70. Madu, I. K.; Muller, E. W.; Kim, H.; Shaw, J.; Burney-Allen, A. A.; Zimmerman, P.; Jeffries-el, M.; Goodson, T., III Heteroatom and Side Chain Effects on the Optical and Photophysical Properties: Ultrafast and Nonlinear Spectroscopy of New Naphtho[1,2-b:5,6-b′]difuran Donor Polymers. *J. Phys. Chem. C* **2018**, *122*, 17049−17066.

71. Keller, B.; McLean, A.; Kim, B. G.; Chung, K.; Kim, J.; Goodson, T., III Ultrafast Spectroscopic Study of Donor-Acceptor Benzodithiophene Light Harvesting Organic Conjugated Polymers. *J. Phys. Chem. C* **2016**, *120*, 9088−9096.

72. Eshun, A.; Cai, Z.; Awies, M.; Yu, L.; Goodson III, T. Investigations of thienoacene molecules for classical and entangled two-photon absorption. *The Journal of Physical Chemistry A* **2018**, *122*, 8167–8182.

Supplementary information

Experimental Procedures

General Reagent Information

General Analytical Information

Monomer Synthesis

Scheme S5.1. Synthesis of monomer **2**

Diblock Copolymer Synthesis

Figure S5.1. ^{1}H NMR (400 MHz, $CDCl_3$) spectrum of poly-*cis*-**1**-*b*-*cis*-**2**

Figure S5.2. ^{13}C NMR (125 MHz, $CDCl_3$) spectrum of poly-*cis*-**1**-*b*-*cis*-**2**

Figure S5.3: ^{1}H NMR (400 MHz, $CDCl_3$) spectrum of poly-*cis*-**1**-*b*-*trans*-**2**

Figure S5.4: ^{13}C NMR (125 MHz, $CDCl_3$) Spectrum of poly-*cis*-**1**-*b*-*trans*-**2**

Size Exclusion Chromatography

Table S5.1. Molecular weight and dispersity values for poly-*cis*-**1**-*b*-*cis*-**2**

Figure S5.5. Size exclusion chromatography trace of poly-*cis*-**1**-*b*-*cis*-**2**

Quantum Yield Calculations

Equation S1

Figure S5.6. Integrated emission intensity vs. absorbance for poly-*cis*-**1**-*b*-*cis*-**2** and Coumarin 153 standard

Figure S5.7. Integrated emission intensity vs. absorbance for poly-*cis*-**1**-*b*-*trans*-**2** and Fluorescein standard

Femtosecond Transient Absorption Spectra

Figure S5.8. Femtosecond transient absorption spectra for poly-*cis*-**1**-*b*-*cis*-**2** and poly-*cis*-**1**-*b*-*trans*-**2**

Computational analysis of *trans*- and *cis*-PPV

Figure S5.9. Boltzmann weighted UV-Vis spectra of (a) *trans*- and (b) *cis*-PPV calculated at the CAM-B3LYP/6-311+G(d,p) level of theory in chloroform (SMD)

Figure S5.10. Boltzmann weighted UV-Vis spectra of (a) *trans*- and (b) *cis*-PPVcalculated at the B3LYP/6-311+G(d,p) level of theory in chloroform (SMD)

Figure S5.11. Boltzmann weighted UV-Vis spectra of (a) *trans*- and (b) *cis*-PPV calculated at the M06-2X/6-311+G(d,p) level of theory in chloroform (SMD)

Fragmentation model

Figure S5.12. Single point calculations for the HOMO and HOMO-1 orbitals for the *trans*- (left panel) and *cis*-PPV (right panel) calculated at the CAM-B3LYP-D3/6-311G(d,p)-SMD($CHCl_3$) level of theory

Figure S5.13. Single point calculations for the HOMO and HOMO-1 orbitals for the *trans*-PPV fragments calculated at the CAM-B3LYP-D3/6-311G(d,p)-SMD($CHCl_3$)

level of theory

Figure S5.14. Single point calculations for the HOMO and HOMO-1 orbitals for the *cis*-PPV fragments calculated at the CAM-B3LYP-D3/6-311G(d,p)-SMD ($CHCl_3$) level of theory

Figure S5.15. Comparison of the HOMO and HOMO-1 orbitals for the *trans/cis*-PPV fragments calculated at the CAM-B3LYP-D3/6-311G(d,p)-SMD ($CHCl_3$) level of theory

Two-Photon Absorption (TPA)

Time-Resolved Fluorescence Up-Conversion

Femtosecond Transient Absorption

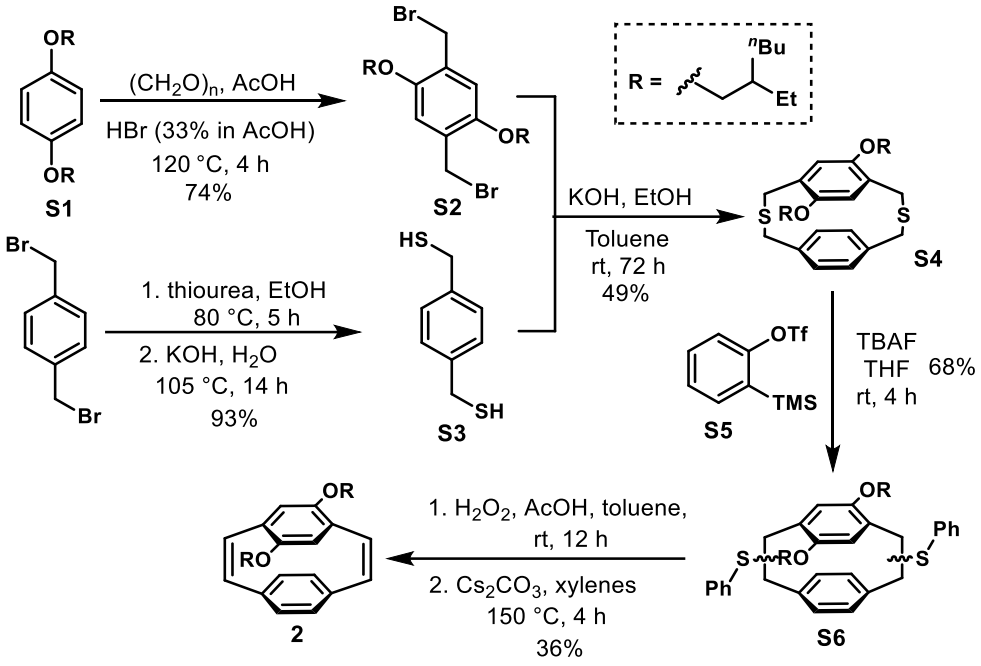
Computational Method

Time-Dependent Density Functional Theory (TD-DFT

General Reagent Information: All reactions were carried out under an inert nitrogen atmosphere with dry solvents under anhydrous conditions unless otherwise stated. Dry dichloromethane (DCM), diethyl ether (Et_2O), tetrahydrofuran (THF), and toluene (PhMe) were obtained by passing the previously degassed solvents through activated alumina columns. Synthesis of polymers using stereoretentive ruthenium catalyst was carried out in a nitrogen-filled glove box (SG1800/750TS-F, VIGOR). Reagents were purchased at the highest commercial quality and used without further purification, unless otherwise stated. Yields refer to chromatographically and spectroscopically (^{1}H NMR) homogeneous material, unless otherwise stated. Reactions were monitored by thin layer chromatography (TLC) carried out on 250 μm SiliCycle SiliaPlate™ silica plates (F254), using UV light as the visualizing agent. Flash silica gel chromatography was performed using SiliCycle SiliaFlash® Irregular Silica Gel (60 Å, particle size 40–63 μm). The polymer was isolated after precipitation using an Eppendorf 5804 centrifuge.

General Analytical Information: The polymer sample was analyzed using a Tosoh EcoSec HLC 8320GPC system with a TSKgel SuperHM-M column and a TSKgel SuperH-RC column at a flow rate of 0.40 mL/min at 40 °C. THF stabilized with BHT was used as the eluent and the number-average molecular weight (M_n), weight-average molecular weight (M_w), and dispersity ($Đ$) for the polymer were calculated from a UV chromatogram against a TSKgel polystyrene standard. NMR spectra were recorded on Bruker Avance Neo 400 and Bruker Avance 500 instruments and were calibrated using residual undeuterated solvent as an internal reference ($CHCl_3$ @ 7.26 ppm ^{1}H NMR, 77.16 ppm ^{13}C NMR). The following abbreviations were used to explain NMR peak multiplicities: s = singlet, d = doublet, t = triplet, q = quartet, m = multiplet, br = broad.

Monomer Synthesis:



Scheme S1. Synthesis of monomer **2**.

N-*n*Hexyl *exo*-norbornene diimide (1). Compound 1 was synthesized following literature procedure reported by Michaudel and coworkers and the spectroscopic data for this compound were identical to those reported in the literature.[1] ^{1}H NMR (500 MHz, $CDCl_3$) δ 6.28 (s, 2 H), 3.45 (t, J = 7.6 Hz, 2 H), 3.27 (s, 2 H), 2.66 (s, 2 H), 1.59–1.47 (m, 3 H), 1.33–1.21 (m, 7 H), 0.86 (t, J = 6.7 Hz, 3 H).

1,4-Di(2-ethylhexyloxy)benzene (S1). Compound **S1** was synthesized following literature procedure reported by Lozano and co-workers and the spectroscopic data for this compound were identical to those reported in the literature.[2] ^{1}H NMR (400 MHz, $CDCl_3$) δ 6.82 (s, 4 H), 3.79 (d,

J = 5.8 Hz, 2 H), 3.78 (d, *J* = 6.1 Hz, 2 H) 1.75–1.62 (m, 2 H), 1.54–1.24 (m, 16 H), 0.93–0.87 (t, 12 H) ppm.

1,4-Bis(bromomethyl)-2,5-di(2-ethylhexyloxy)benzene (S2). Synthesis of compound **S2** was adapted from literature procedure reported by Lozano and coworkers.[2] **S1** (10.0 g, 30.0 mmol, 1.0 equiv) and paraformaldehyde (3.6 g, 120 mmol, 4.0 equiv) were added to a 500 mL round bottom flask, then a solution of HBr (33 wt% in acetic acid, 20 mL) diluted in an additional 140 mL of acetic acid was added slowly. A condenser was adapted onto the flask and the reaction mixture was stirred at 120 °C for 4 h. Once cooled to room temperature, the mixture was poured into water (200 mL) at 0 °C. The precipitated solid was filtered and washed with water several times. The solid residues were then washed with MeOH (3 × 20 mL), and compound **S2** was isolated as an off-white solid (11.6 g, 22.3 mmol, 74%). The spectroscopic data for this compound were identical to those reported in the literature.[1] ^{1}H NMR (400 MHz, $CDCl_3$) δ 6.84 (s, 2H), 4.51 (s, 4H), 3.87 (d, *J* = 5 Hz, 4H), 1.75–1.62 (m, 2H), 1.54–1.24 (m, 16H), 0.93–0.87 (t, 12H) ppm.

1,4-Bis(thiolatomethyl)benzene (S3). Compound **S3** was synthesized following literature procedure reported by Turner and co-workers and the spectroscopic data for this compound were identical to those reported in the literature.[3] ^{1}H NMR (400 MHz, $CDCl_3$) δ 7.28 (s, 4 H), 3.73 (d, *J* = 7.5 Hz, 4 H), 1.75 (t, *J* = 7.5 Hz, 2 H) ppm.

5,8-Di(2-ethylhexyloxy)-2,11-dithia[3,3]paracyclophane (S4). Compound **S4** was synthesized following literature procedure reported by Turner and co-workers and the spectroscopic data for this compound were identical to those reported in the literature.[4] ^{1}H NMR (400 MHz, $CDCl_3$) δ 6.96 (d, *J* = 8 Hz, 2 H), 6.89 (d, *J* = 8 Hz, 2 H), 6.42 (s, 2 H), 4.26 (d, *J* = 15 Hz, 2 H), 3.89–3.83

(m, 2 H), 3.82 (d, J = 15 Hz, 2 H), 3.76 (d, J = 15 Hz, 2 H), 3.68–3.62 (m, 2 H), 3.36 (d, J = 15 Hz, 2 H), 1.79–1.72 (m, 2 H), 1.68–1.33 (m, 16 H), 1.06–0.92 (m, 12 H) ppm.

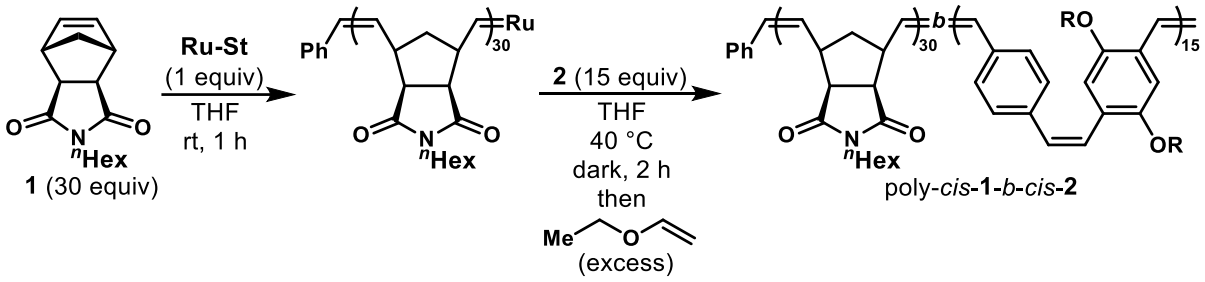
2-(trimethylsilyl)phenyl trifluoromethanesulfonate (**S5**). Benzyne precursor **S5** was prepared according to literature procedure reported by Turner and co-workers and the spectroscopic data for this compound were identical to those reported in the literature.[3] ^{1}H NMR (400 MHz, $CDCl_3$) δ 7.54 (dd, J = 7.5, 1.9 Hz, 1 H), 7.44 (ddd, J = 8.3, 7.3, 1.9 Hz, 1 H), 7.38–7.31 (m, 2 H), 0.37 (s, 9 H) ppm.

Dithiaparacyclophane Isomers (S6). Compound **S6** was synthesized following literature procedure reported by Turner and co-workers and the spectroscopic data for this compound were identical to those reported in the literature.[4]

4,7-Di(2-ethylhexyloxy)-[2.2]paracyclophane-1,9-diene (2). Compound **2** was synthesized following literature procedure reported by Turner and co-workers and the spectroscopic data for this compound were identical to those reported in the literature.[4] ^{1}H NMR (400 MHz, $CDCl_3$) δ 7.10 (d, J = 10 Hz, 2 H), 6.90 (d, J = 10 Hz, 2 H), 6.80 (d, J = 8 Hz, 2 H), 6.48 (d, J = 8 Hz, 2 H), 5.77 (s, 2 H), 3.72–3.65 (m, 2 H), 3.65–3.58 (m, 2 H), 1.77–1.59 (m, 2 H), 1.59–1.25 (m, 16 H), 1.04–0.79 (m, 12 H) ppm.

Diblock Copolymer Synthesis:

Poly-*cis*-**1**-*b*-*cis*-**2**:



A solution of ruthenium catalyst **Ru-St** (8.6 mg, 9.9 μmol, 1 equiv) in deoxygenated THF (0.10 mL) was added to a reaction vial containing monomer **1** (73.3 mg, 296.4 μmol, 30 equiv) and a stir bar inside a nitrogen filled glove box. The reaction was stirred inside the glove box for 1 h at room temperature, and then 0.08 mL of the mixture was transferred to a second reaction vial containing monomer **2** (52.2 mg, 113.3 μmol, 15 equiv) and a stir bar. The mixture was stirred for 2 h at 40 °C in the dark inside the glovebox. The reaction was allowed to cool to room temperature, and then quenched with excess ethyl vinyl ether (0.1 mL) and left for 30 min at room temperature. The polymer was isolated by performing two cycles of precipitation with addition of methanol, centrifugation, and decantation. The isolated polymer was wrapped in aluminium foil and concentrated under reduced pressure before being stored under an inert atmosphere at –20 °C to prevent any undesired photoisomerization. ^{1}H NMR (400 MHz, $CDCl_3$) δ 7.21 (s, 4 H), 6.75 (s, 2 H), 6.64 (d, J = 12.3 Hz, 2 H), 6.49 (d, J = 12.3 Hz, 2 H), δ 5.60-5.37 (m, 4 H), 3.51–2.87 (m, 16 H), 2.37–1.95 (m, 2 H), 1.56–1.46 (m, 6 H), 1.41–1.13 (m, 30 H), 0.90–0.77 (m, 18 H) ppm. ^{13}C NMR (125 MHz, $CDCl_3$) δ 178.6, 178.4, 178.2, 150.5, 136.5, 133.5, 129.4, 128.9, 126.2, 125.5, 114.0, 71.4, 52.6, 52.4, 41.9, 41.6, 39.4, 39.0, 38.9, 31.5, 30.6, 29.1, 27.8, 26.7, 26.6, 24.0, 23.2, 22.7, 14.2, 14.1, 11.1 ppm.

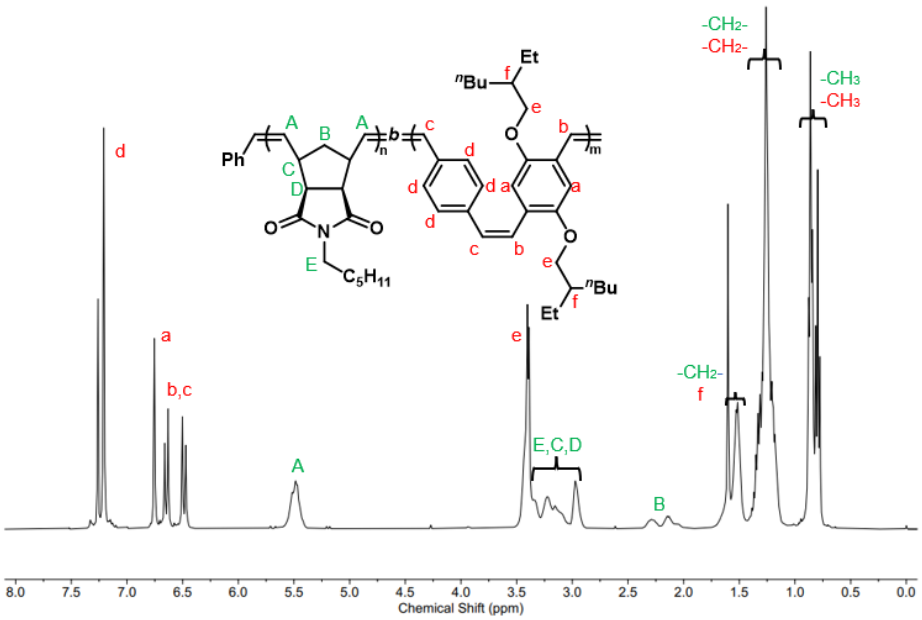


Figure S5.1. ^{1}H NMR (400 MHz, $CDCl_3$) spectrum of poly-*cis*-**1**-*b*-*cis*-**2**.

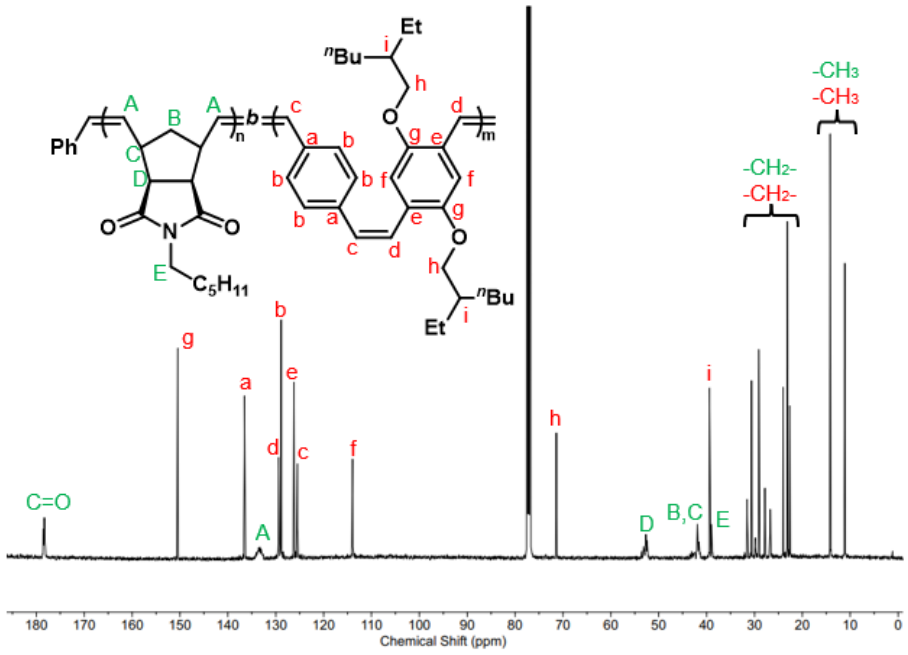
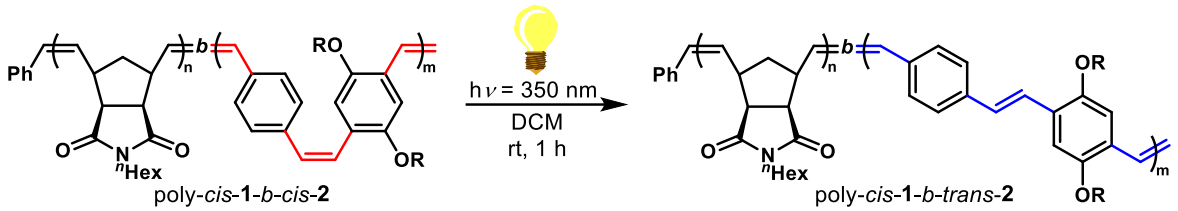


Figure S5.2. ^{13}C NMR (125 MHz, $CDCl_3$) spectrum of poly-*cis*-**1**-*b*-*cis*-**2**.

Poly-*cis*-**1**-*b*-*trans*-**2**:



A solution (23 mg in 23 mL, C = 1 mg/mL) of poly-*cis*-**1**-*b*-*cis*-**2** was irradiated in DCM using two 350 nm UV lamps placed 1 cm away from the sample for 1 hour at room temperature to give poly-*cis*-**1**-*b*-*trans*-**2**. The sample was wrapped in aluminium foil and concentrated under reduced pressure before being stored under an inert atmosphere at –20 °C. ^{1}H NMR (400 MHz, $CDCl_3$) δ 7.65–7.30 (m, 6 H), 7.22–6.80 (m, 4 H), δ 5.68–5.26 (m, 4 H), 4.05–3.73 (m, 4 H), 3.51–2.87 (m, 12 H), 2.37–1.95 (m, 2 H), 1.93–1.79 (m, 2 H), 1.71–1.20 (m, 34 H), 1.04–0.80 (m, 18 H) ppm. ^{13}C NMR (125 MHz, $CDCl_3$) δ 178.6, 178.4, 178.2, 151.5, 137.4, 133.5, 128.6, 127.1, 127.0, 123.5, 110.5, 72.1, 52.6, 52.4, 41.9, 41.6, 40.0, 39.0, 38.9, 31.5, 31.2, 29.5, 27.8, 26.7, 26.6, 24.4, 23.2, 22.7, 14.3, 14.1, 11.5 ppm.

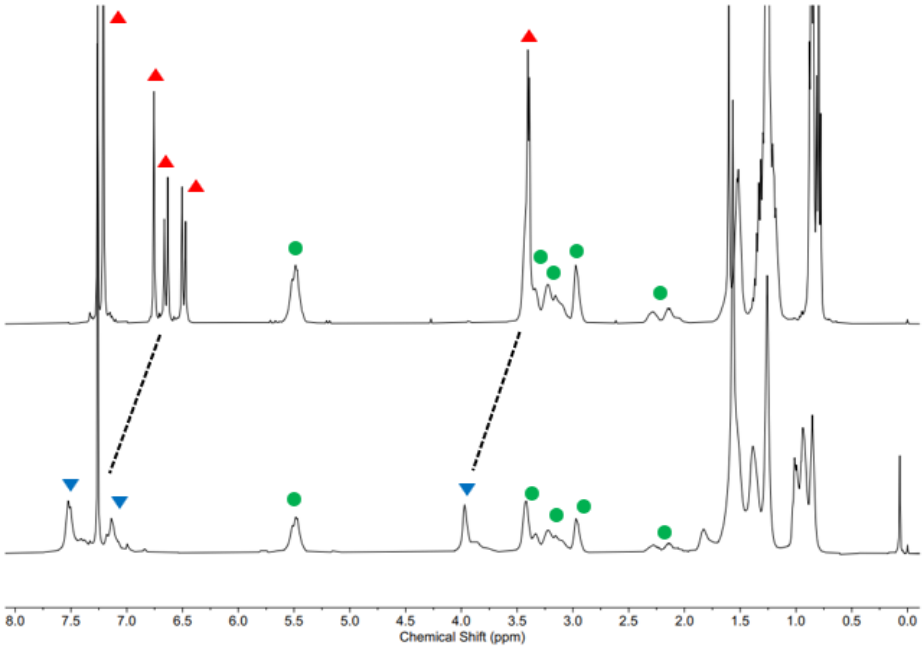


Figure S5.3. ^{1}H NMR (400 MHz, $CDCl_3$) spectra showing change in chemical shifts after photoisomerization of poly-*cis*-**1**-*b*-*cis*-**2** (red/green) to give poly-*cis*-**1**-*b*-*trans*-**2** (blue/green).

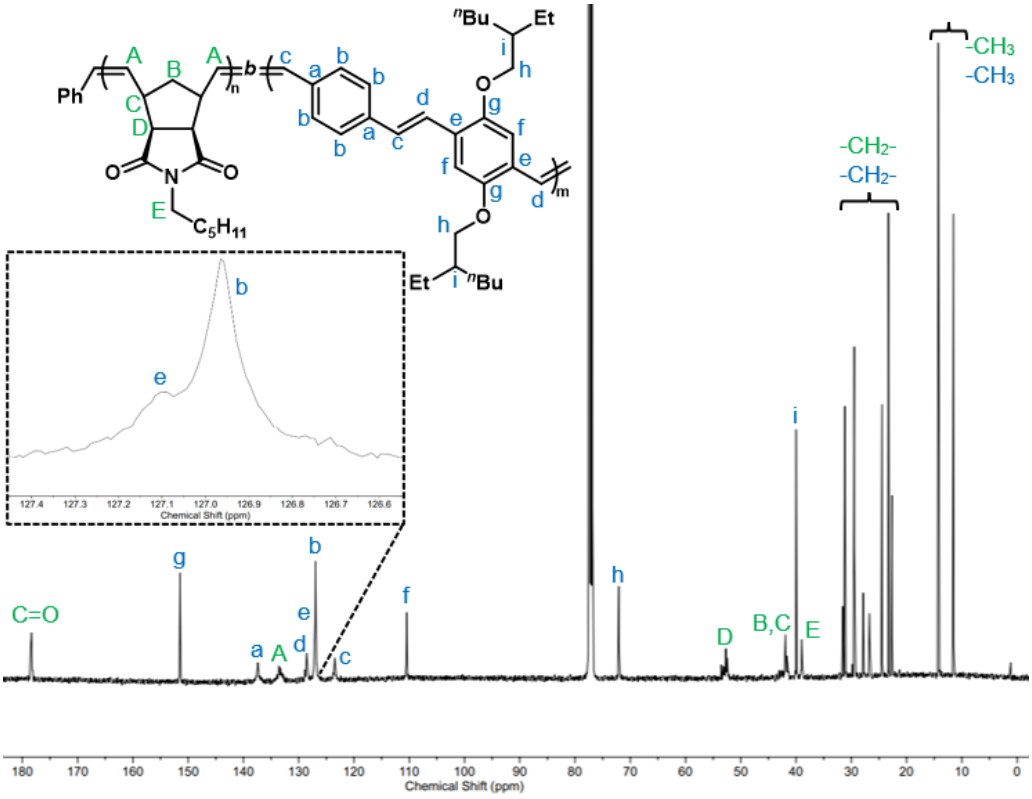


Figure S5.4. ^{13}C NMR (125 MHz, $CDCl_3$) spectrum of poly-*cis*-**1**-*b*-*trans*-**2**.

Size Exclusion Chromatography:

Table S5.1. Molecular weight and dispersity values for poly-*cis*-**1**-*b*-*cis*-**2**.

Block copolymer	Target n,m	M_n^{theor} (kg/mol)	M_n^{exp} (kg/mol)	$Đ$
poly-*cis*-**1**-*b*-*cis*-**2**	30,15	14.5	16.3	1.20

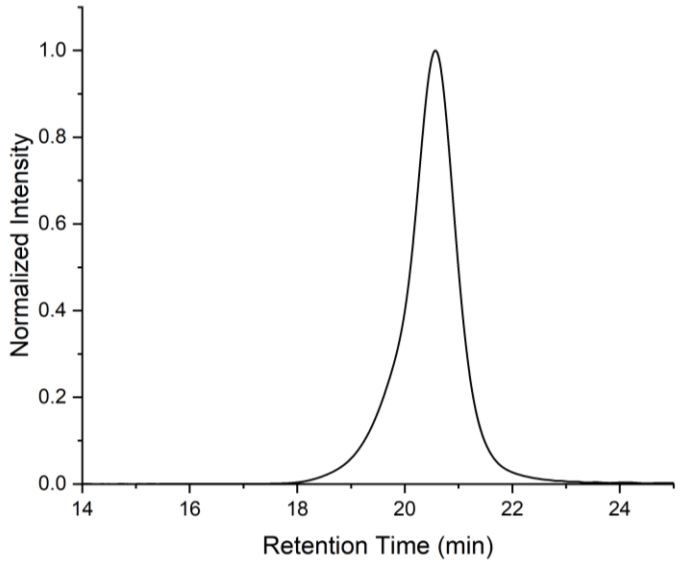


Figure S5.5. Size exclusion chromatography trace of poly-*cis*-**1**-*b*-*cis*-**2**.

Quantum Yield Calculations:

Fluorescence quantum yields were measured in dilute solutions of poly-*cis*-**1**-*b*-*cis*-**2** and poly-*cis*-**1**-*b*-*trans*-**2** in chloroform ($\eta = 1.45$) against either Coumarin 153 in ethanol ($\Phi_{fl} = 0.53$, $\eta = 1.36$) for poly-*cis*-**1**-*b*-*cis*-**2** or fluorescein in aq. NaOH (C = 0.1 M, $\Phi_{fl} = 0.89$, $\eta = 1.33$) for poly-*cis*-**1**-*b*-*trans*-**2**. Absorbance measurements were kept below 0.04 to reduce possible reabsorption effects. Fluorescence quantum yields were calculated based on the gradients (slope) of the plot of integrated emission versus absorbance at λ_{ex} using **Equation S1**.[4]

$$\Phi_{sample} = \Phi_{standard} \times \left(\frac{Gradient_{sample}}{Gradient_{standard}}\right) \times \left(\frac{\eta_{sample}}{\eta_{standard}}\right)^2 \qquad \textbf{(Equation S1)}$$

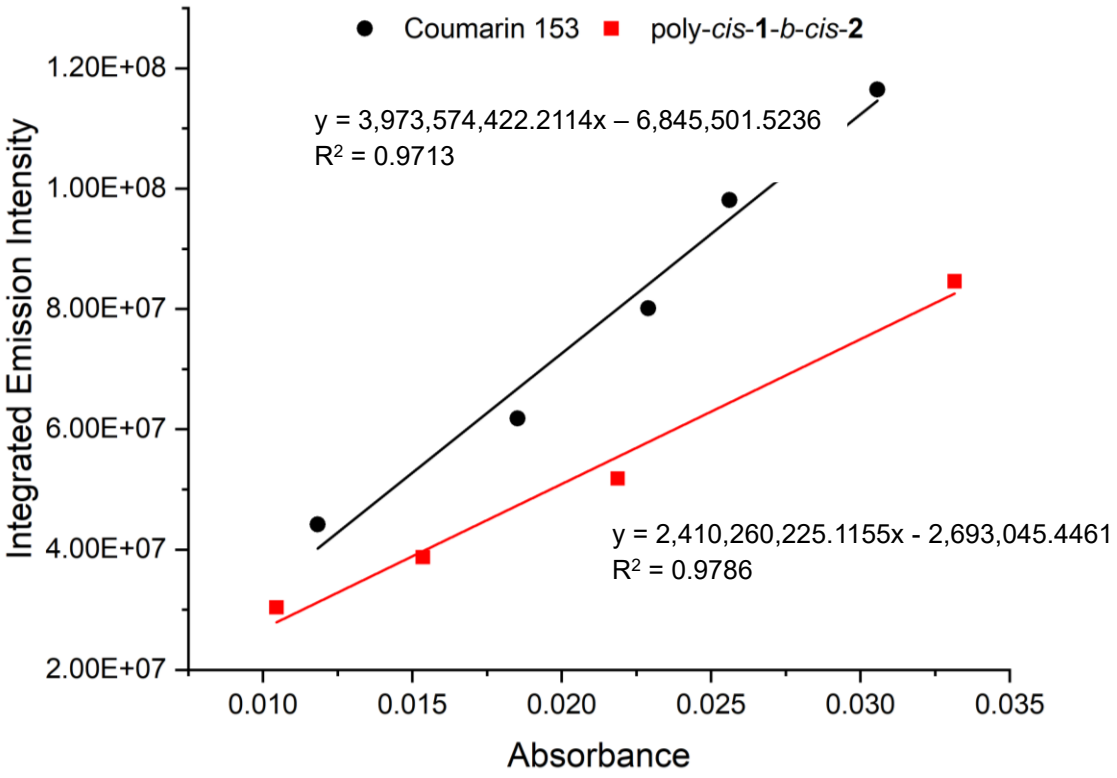


Figure S5.6. Plot of integrated emission intensity vs. absorbance for poly-*cis*-**1**-*b*-*cis*-**2** and Coumarin 153 (λ_{ex} = 385 nm).

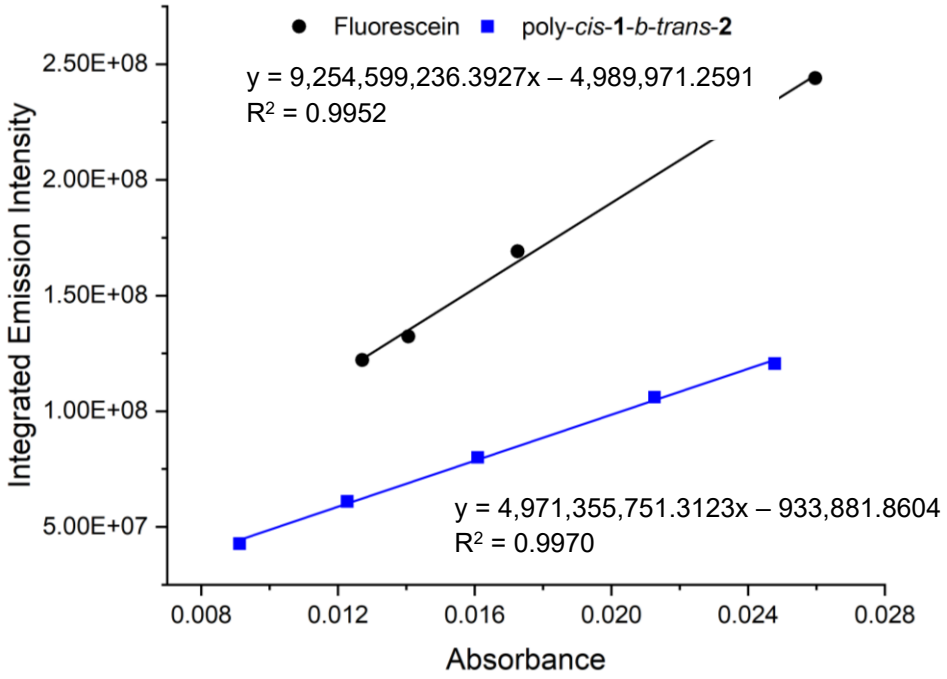


Figure S5.7. Plot of integrated emission intensity vs. absorbance for poly-*cis*-**1**-*b*-*trans*-**2** and Fluorescein (λ_{ex} = 455 nm).

Femtosecond Transient Absorption Spectra:

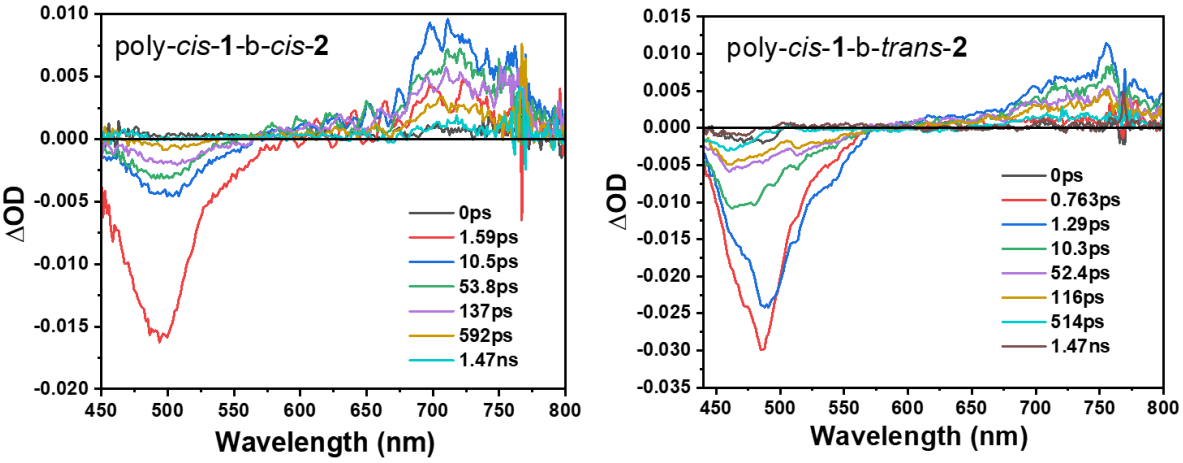


Figure S5.8. Femtosecond transient absorption spectra (*fs*TAS) for poly-*cis*-**1**-*b*-*cis*-**2** (A) and poly-*cis*-**1**-*b*-*trans*-**2** (B) at different delay times in chloroform.

Computational analysis of *trans*- and *cis*-PPV

The *trans*- and *cis*-PPV's were optimized using a two-step protocol of a conformational search with the OPLS3e[6] forcefield followed by a higher-level density functional theory (DFT) optimization at the CAM-B3LYP-D3/6-311+G(d,p)-SMD($CHCl_3$) level of theory.[7] For each system, a suggested structure was constructed, and an exhaustive conformational analysis was performed to generate 20 different starting conformations with the OPLS3e force field. using the Macromodel package of Schrodinger 23.[8] The 20 conformations were subjected to ground-state geometry optimizations carried out with the CAM-B3LYP density functional with the 6-311+G(d,p) basis set and GD3 empirical dispersion. Solvent effects were simulated in chloroform with the solvation model density method (SMD). All ground-state geometry optimizations were performed with Gaussian 16.[9] The stationary points from these efforts were then carried on to the subsequent UV−Vis studies performed at the same CAM-B3LYP-D3/6-311+G(d,p)-SMD($CHCl_3$) level of theory reported in the main manuscript. Higher-level optimizations and UV-Vis calculations were repeated with the B3LYP and M06-2X[10] functionals for comparison. Boltzmann weighted UV-Vis plots using the relative free energy (Tables S2 – S7) for *trans*- and *cis*-PPV were generated at the three different levels of theory (Figure S9 – S11).

At all levels of theory we found very similar observations in the TD-DFT simulations (Figure S9 – S11). For *trans*-PPV, one distinct UV-Vis excitation was observed at 413 (CAM-B3LYP-D3), 531 (B3LYP-D3), and 412 nm (M06-2X-D3) corresponding to one HOMO – LUMO singlet excitation (ES1, Figure S9(a) – S11(a)). The UV-Vis absorption peaks for *cis*-PPV were blue-shifted at 309 (CAM-B3LYP-D3), 369 (B3LYP-D3), and 311 nm (M06-2X-D3) when compared to *trans*-PPV (Figure S9(b) – S11(b)) correlating with experimental findings. At each

level of theory, three distinct UV-Vis excitations were observed ES1 (HOMO – LUMO), ES2 (HOMO-1 – LUMO), and ES3 (HOMO – LUMO+1) illustrated in Figure 7.

Table S5.2. Energetic data for the top 20 conformations of *trans*-PPV calculated at the CAM-B3LYP-D3/6-311+G(d,p) level of theory in chloroform (SMD)

Conformation	Relative enthalpy at zero temperature (kcal/mol)	Relative enthalpy at 298 K (kcal/mol)	Relative free energy at 298 K (kcal/mol)
1	0.1	0.1	1.5
2	0.3	0.3	1.9
3	0.2	0.2	1.6
4	0.3	0.3	2.0
5	0.3	0.2	2.0
6	0.1	0.1	1.2
7	0.0	0.0	1.0
8	0.1	0.2	1.0
9	0.1	0.2	1.1
10	0.1	0.1	1.1
11	0.1	0.1	1.5
12	0.2	0.1	1.7
13	0.1	0.1	1.4
14	0.0	0.0	1.3
15	0.0	0.1	0.0
16	0.4	0.2	2.4

17	0.1	0.1	1.3
18	0.4	0.2	2.2
19	0.3	0.2	1.7
20	0.3	0.2	2.2

Table S5.3. Energetic data for the top 20 conformations of *trans*-PPV calculated at the B3LYP-D3/6-311+G(d,p) level of theory in chloroform (SMD)

Conformation	Relative enthalpy at zero temperature (kcal/mol)	Relative enthalpy at 298 K (kcal/mol)	Relative free energy at 298 K (kcal/mol)
1	0.2	0.1	0.7
2	0.1	0.1	0.6
3	0.1	0.1	1.0
4	0.1	0.1	0.7
5	0.0	0.0	0.1
6	0.1	0.2	0.2
7	0.1	0.1	0.7
8	0.1	0.1	0.2
9	0.1	0.1	0.3
10	REPEAT OF 3	REPEAT OF 3	REPEAT OF 3
11	0.3	0.3	0.7
12	0.0	0.0	0.0
13	0.0	0.0	0.4
14	0.2	0.2	0.3
15	0.0	0.0	0.3

16	0.1	0.1	0.5
17	0.1	0.0	0.6
18	0.4	0.3	1.6
19	0.4	0.2	1.4
20	0.3	0.2	0.8

Table S5.4. Energetic data for the top 20 conformations of *trans*-PPV calculated at the M06-2X-D3/6-311+G(d,p) level of theory in chloroform (SMD)

Conformation	Relative enthalpy at zero temperature (kcal/mol)	Relative enthalpy at 298 K (kcal/mol)	Relative free energy at 298 K (kcal/mol)
1	0.3	0.3	0.9
2	0.1	0.1	0.6
3	0.0	0.0	0.2
4	0.1	0.1	0.4
5	REPEAT OF 2	REPEAT OF 2	REPEAT OF 2
6	0.0	0.0	0.2
7	0.1	0.1	0.8
8	0.1	0.1	0.4
9	0.2	0.2	0.8
10	0.0	0.1	0.1
11	0.1	0.2	0.5
12	0.1	0.1	0.6
13	0.1	0.1	0.3
14	0.0	0.0	0.3

15	0.0	0.0	0.6
16	0.0	0.0	0.2
17	0.1	0.1	0.5
18	0.1	0.1	0.0
19	0.2	0.1	0.5
20	0.2	0.1	0.1

Table S5.5. Energetic data for the top 20 conformations of *cis*-PPV calculated at the CAM-B3LYP-D3/6-311+G(d,p) level of theory in chloroform (SMD)

Conformation	Relative enthalpy at zero temperature (kcal/mol)	Relative enthalpy at 298 K (kcal/mol)	Relative free energy at 298 K (kcal/mol)
1	0.3	0.0	0.9
2	0.1	0.0	0.3
3	0.0	0.0	0.0
4	0.1	0.1	1.4
5	0.0	1.2	1.6
6	0.0	1.2	0.8
7	0.1	0.5	2.3
8	0.1	0.5	2.2
9	0.2	1.1	2.9
10	0.0	1.2	2.2
11	0.1	1.3	2.5
12	0.1	1.5	2.3
13	0.1	2.8	3.0

14	0.0	1.5	1.8
15	0.0	2.4	2.9
16	0.0	1.9	2.2
17	0.1	2.0	1.6
18	0.1	2.4	1.7
19	0.2	2.5	2.1
20	0.2	2.8	1.7

Table S5.6. Energetic data for the top 20 conformations of *cis*-PPV calculated at the B3LYP-D3/6-311+G(d,p) level of theory in chloroform (SMD)

Conformation	Relative enthalpy at zero temperature (kcal/mol)	Relative enthalpy at 298 K (kcal/mol)	Relative free energy at 298 K (kcal/mol)
1	0.0	0.0	0.6
2	0.0	0.0	0.2
3	0.0	0.0	0.0
4	Failed	Failed	Failed
5	Failed	Failed	Failed
6	1.1	1.3	1.0
7	0.4	0.3	1.7
8	0.4	0.3	1.4
9	1.4	1.4	2.4
10	1.2	1.2	1.9
11	1.1	1.3	1.0
12	1.5	1.5	2.0

13	2.7	2.7	2.7
14	1.9	2.0	2.4
15	2.6	2.5	3.5
16	2.0	2.1	1.8
17	2.1	2.2	1.6
18	2.5	2.6	1.8
19	2.6	2.7	2.1
20	2.8	2.9	1.8

Table S5.7. Energetic data for the top 20 conformations of *cis*-PPV calculated at the M06-2X-D3/6-311+G(d,p) level of theory in chloroform (SMD)

Conformation	Relative enthalpy at zero temperature (kcal/mol)	Relative enthalpy at 298 K (kcal/mol)	Relative free energy at 298 K (kcal/mol)
1	0.4	0.5	0.2
2	0.3	0.4	0.0
3	0.0	0.0	0.7
4	0.2	0.1	1.2
5	1.5	1.7	1.2
6	1.2	1.5	0.4
7	0.7	0.6	1.1
8	0.8	0.7	1.1
9	1.5	1.6	2.0
10	1.0	1.1	1.6
11	2.1	1.8	3.9

12	3.1	2.6	5.4
13	4.2	4.5	2.5
14	2.3	2.4	2.3
15	2.9	3.1	2.7
16	2.9	3.0	3.5
17	2.8	3.0	2.7
18	3.9	4.1	2.2
19	3.8	4.1	1.9
20	4.0	4.4	1.8

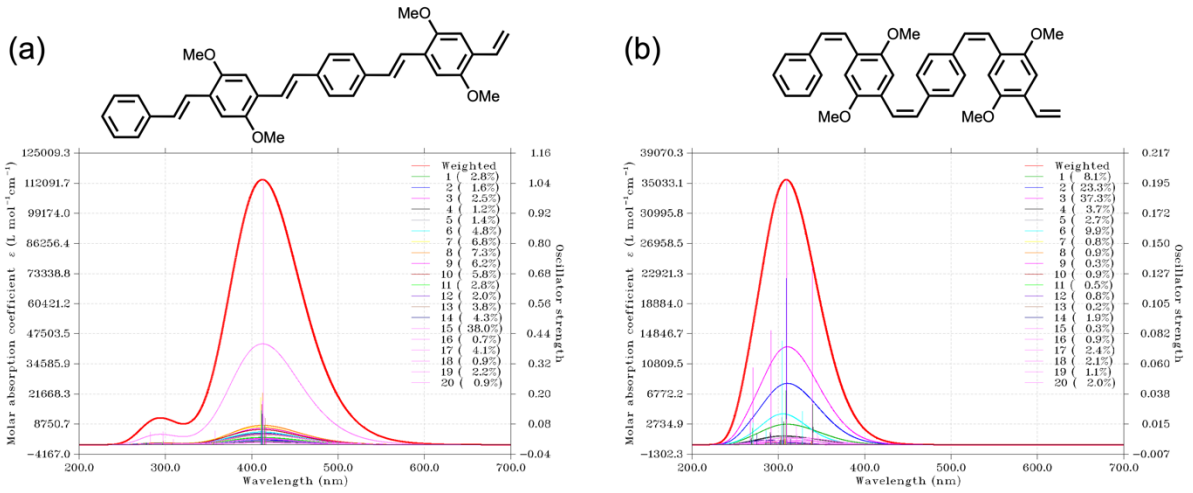


Figure S5.9. Boltzmann weighted UV-Vis spectra of (a) *trans*- and (b) *cis*-PPV calculated at the CAM-B3LYP/6-311+G(d,p) level of theory in chloroform (SMD)

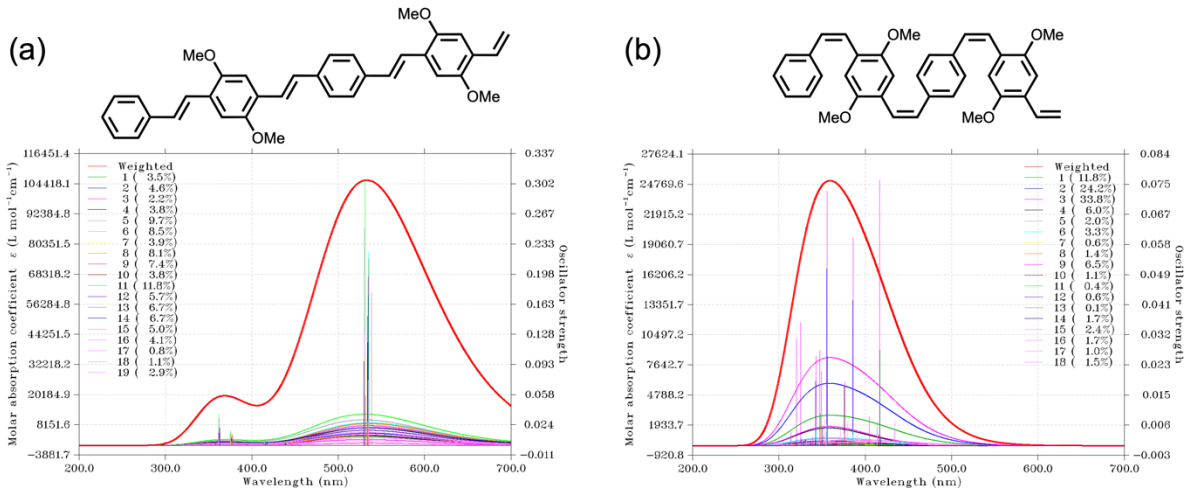


Figure S5.10. Boltzmann weighted UV-Vis spectra of (a) *trans*- and (b) *cis*-PPV calculated at the B3LYP/6-311+G(d,p) level of theory in chloroform (SMD)

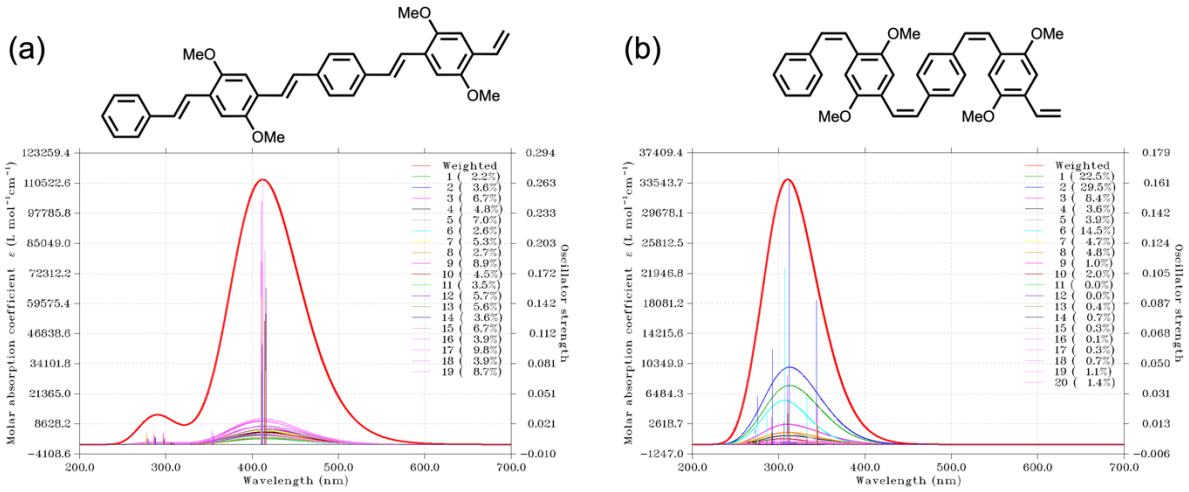


Figure S5.11. Boltzmann weighted UV-Vis spectra of (a) *trans*- and (b) *cis*-PPV calculated at the M06-2X/6-311+G(d,p) level of theory in chloroform (SMD)

Fragmentation model

In order to understand the magnitude of orbital delocalization the lowest energy conformations for the *trans*- (conformation 15) and *cis*-PPV (conformation 3) optimized at the CAM-B3LYP-D3 level of theory in chloroform (SMD) were taken for analysis. Single point calculations of the *trans*- and *cis*-PPV conformations were performed at the CAM-B3LYP-D3/6-311G(d,p)-SMD($CHCl_3$) level of theory, excluding diffuse functions for further analysis with Multiwfn 3.8.[11] To evaluate the extent of spatial delocalization of the HOMO and HOMO-1 orbitals for *trans*- and *cis*-PPV we used the orbital delocalization index (ODI).[12] ODI is useful in quantifying the spatial delocalization of a particular molecular orbital, where the lower the ODI value corresponds to more orbital delocalization. Intriguingly, while the HOMO (by -0.40 eV) and HOMO-1 (by -0.12 eV) orbitals of *cis*-PPV were lower in energy, less orbital delocalization was observed (Tables S8 – S9).

To discern the change in energy for the HOMO/HOMO-1 orbitals, single point calculations were performed on the individual styrene (1)/(3) and 1,4-dimethoxy-2-vinylbenzene (2)/(4) fragments of *trans*- (Figure S13) and *cis*-PPV (Figure S14). Plotting the HOMO-1, HOMO, LUMO, and LUMO+1 energies of each fragment, a marked decrease in energy was observed in the HOMO/HOMO-1 orbitals *trans*- to *cis*-PPV for the majority of fragments (Figure S15). We determined that HOMO/HOMO-1 energies of the individual fragments led to the decrease in their orbital energy from *trans*- to *cis*-PPV complexes (Table S10).

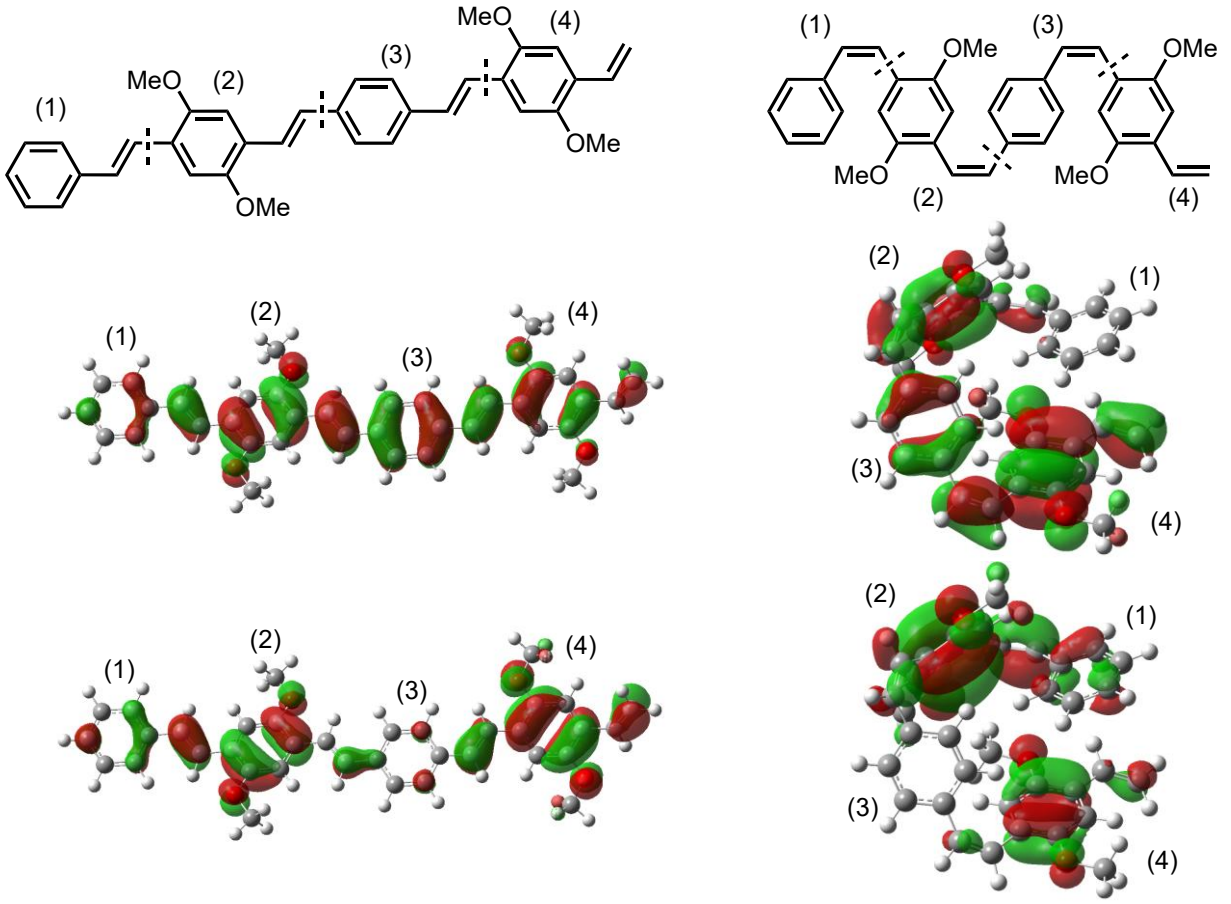


Figure S5.12. Single point calculations for the HOMO and HOMO-1 orbitals for the *trans*- (left panel) and *cis*-PPV (right panel) calculated at the CAM-B3LYP-D3/6-311G(d,p)-SMD($CHCl_3$) level of theory

Table S5.8. Fragment orbital composition analysis for the HOMO/HOMO-1 orbitals for the *trans*-PPV(1), *trans*-PPV(2), *trans*-PPV(3), and *trans*-PPV(4) fragments indicated in Figure S12 calculated at the CAM-B3LYP-D3/6-311G(d,p)-SMD($CHCl_3$) level of theory

trans-PPV	Energy level (eV)	*trans*-PPV(1)	*trans*-PPV(2)	*trans*-PPV(3)	*trans*-PPV(4)
HOMO	-6.18	12.47%	41.28%	26.87%	19.37%

HOMO ODI	N/A	3.48	3.48	3.48	3.48
HOMO-1	-6.65	12.49%	26.58%	11.15%	49.76%
HOMO-1 ODI	N/A	3.94	3.94	3.94	3.94

Table S5.9. Fragment orbital composition analysis for the HOMO/HOMO-1 orbitals for the *cis*-PPV(1), *cis*-PPV(2), *cis*-PPV(3), and *cis*-PPV(4) fragments indicated in Figure S12 calculated at the CAM-B3LYP-D3/6-311G(d,p)-SMD($CHCl_3$) level of theory

cis-PPV	Energy level (eV)	*cis*-PPV(1)	*cis*-PPV(2)	*cis*-PPV(3)	*cis*-PPV(4)
HOMO	-6.58	3.04%	16.72%	21.92%	58.31%
HOMO ODI	N/A	4.63	4.63	4.63	4.63
HOMO-1	-6.78	12.93%	63.93%	2.52%	20.61%
HOMO-1 ODI	N/A	5.34	5.34	5.34	5.34

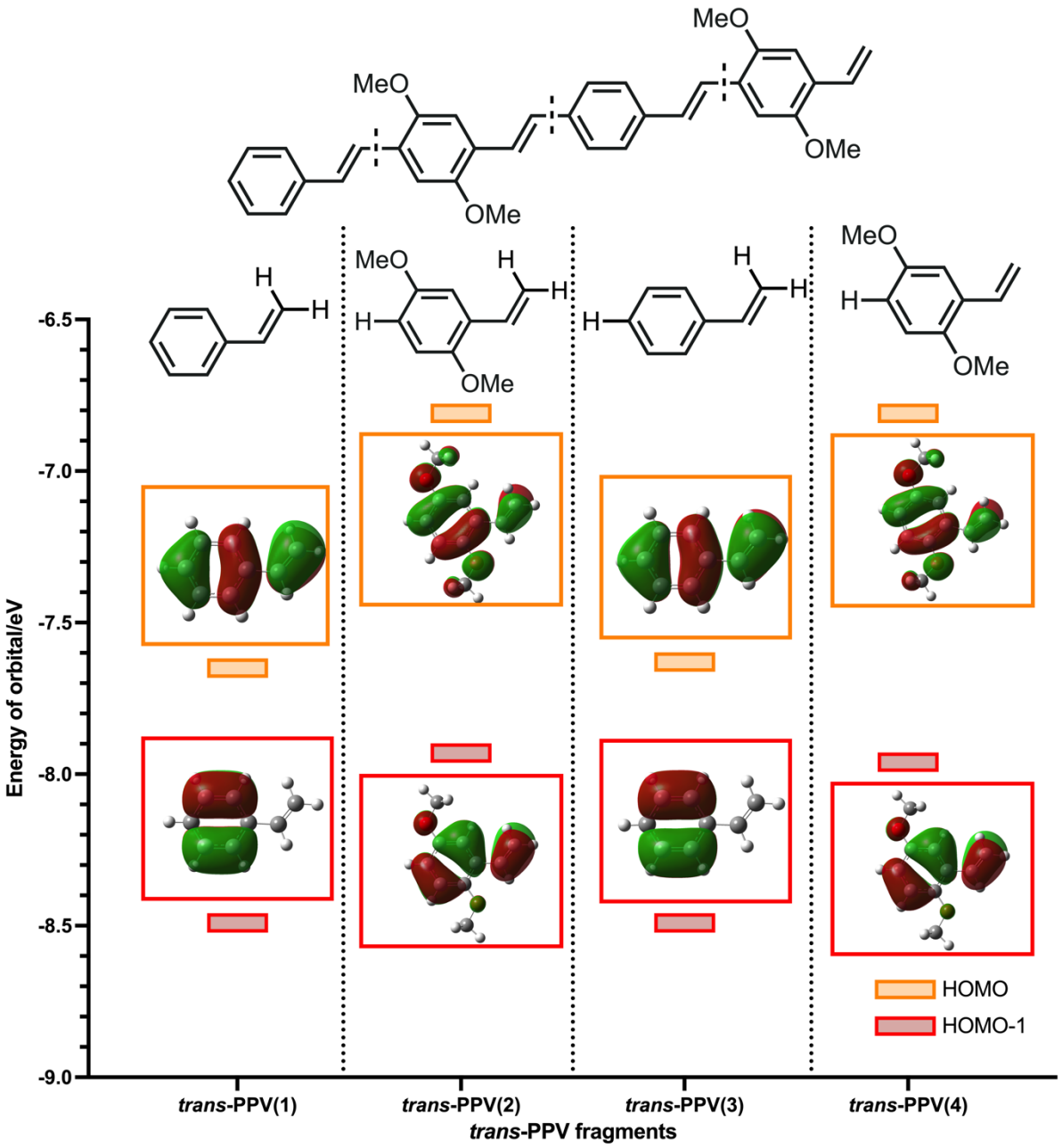


Figure S5.13. Single point calculations for the HOMO and HOMO-1 orbitals for the *trans*-PPV fragments calculated at the CAM-B3LYP-D3/6-311G(d,p)-SMD($CHCl_3$) level of theory

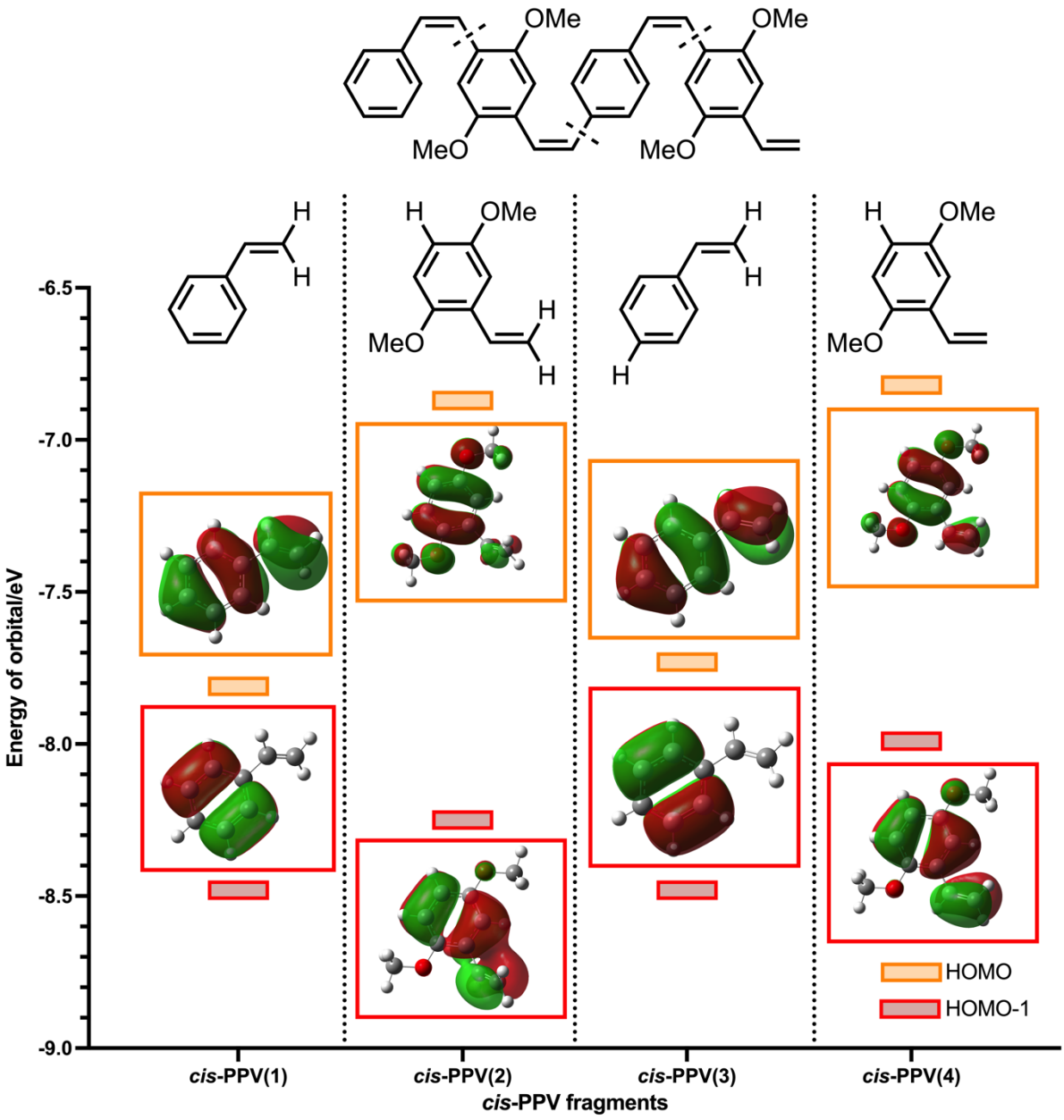


Figure S5.14. Single point calculations for the HOMO and HOMO-1 orbitals for the *cis*-PPV fragments calculated at the CAM-B3LYP-D3/6-311G(d,p)-SMD($CHCl_3$) level of theory

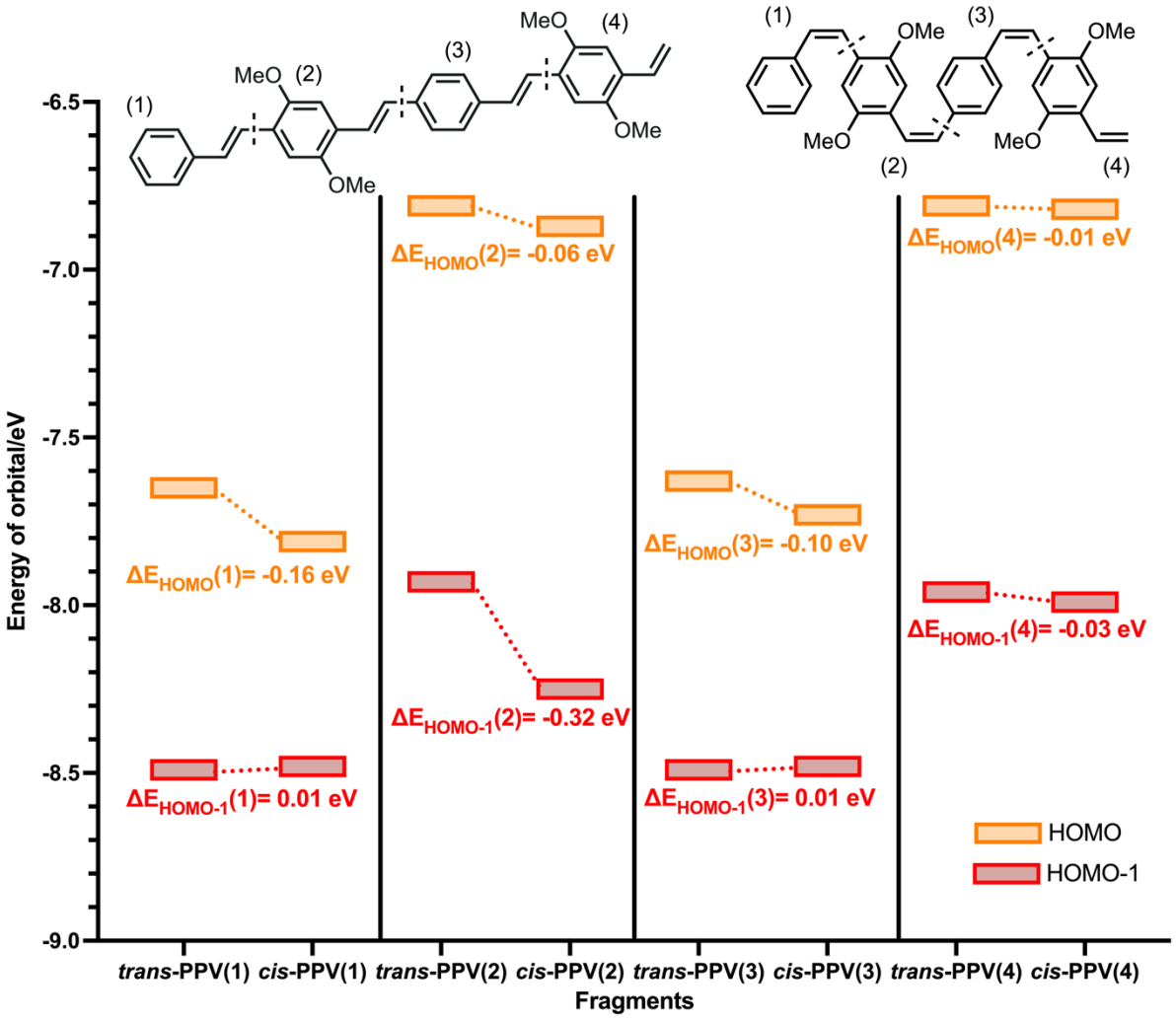


Figure S5.15. Comparison of the HOMO and HOMO-1 orbitals for the *trans/cis*-PPV fragments calculated at the CAM-B3LYP-D3/6-311G(d,p)-SMD($CHCl_3$) level of theory

Table S5.10. Change in energy for the HOMO/HOMO-1 orbitals from the *trans*- to *cis*-PPV fragments calculated at the CAM-B3LYP-D3/6-311G(d,p)-SMD($CHCl_3$) level of theory

	Fragment 1	Fragment 2	Fragment 3	Fragment 4	Total of all fragments	Full *cis*-/*trans*-PPV
ΔE_{HOMO} (eV)	-0.16	-0.06	-0.10	-0.01	-0.33	-0.40
ΔE_{HOMO-1}	0.01	-0.32	0.01	-0.03	-0.33	-0.12

Steady-state absorption and emission

The absorption and emission measurements were carried out in dilute chloroform solutions. Absorption spectra were collected on a Shimadzu UV-2600 UV-visible spectrophotometer using 1.0 cm path length quartz cuvettes. Fluorescence measurements were collected on a Horiba FluoroMax 4 spectrofluorometer with entrance and exit slits set to 2.0 nm and an integration time of 0.1 s.

Two-Photon Absorption (TPA)

The TPA cross-section of liquid samples were determined using the two-photon induced fluorescence technique employing two-photon power-dependent fluorescence intensity. TPA was performed with a mode-locked Ti:Sapphire laser (Spectra-Physics Millenia) adjustable from 760 to 830 nm, producing 110 fs output pulses at an 80 MHz repetition rate. For the current investigation, all liquid samples contained in 1 cm quartz cuvette were excited at 800 nm and generated fluorescence collected in the perpendicular direction to the incident beam using a Hamamatsu photomultiplier tube and photocounting unit. The emission detection wavelengths

were set to be 520 nm for poly-*cis*-**1**-*b*-*cis*-**2** and poly-*cis*-**1**-*b*-*trans*-**2** by Newport Oriel Cornerstone monochromator. Using a neutral density filter, the input power was varied, and the TPA cross-sections were calculated by comparing with known standard solution. For this measurement, we used Coumarin 307 ($\delta = 28$)[13] standard solution in methanol as a reference.

Time-Resolved Fluorescence Up-Conversion.

The detailed experimental setup used for the measurements of femtosecond fluorescence upconversion previously described by Goodson and co-workers was used in this study.[14] The study of fluorescence upconversion for poly-*cis*-**1**-*b*-*cis*-**2** and poly-*cis*-**1**-*b*-*trans*-**2** were performed at an up-converted wavelength of 346.7 nm using a FOG- 100 system (CDP Instruments, Inc.). A mode-locked Ti:Sapphire (Tsunami, Spectra Physics) laser source of 800 nm (~ 700 mW) was used as a fundamental beam. The fundamental beam was frequency doubled by passing it through a β-barium borate (BBO) nonlinear crystal. By second harmonic generation, 400 nm light was produced which acted as the excitation source for the sample in solution phase (1 mm thick rotating sample cell). The remaining 800 nm gate beam was directed to a gold-coated retroreflector mirror connected to a 2 ns optical delay line, before being focused together with the fluorescence on a 0.5 mm Type I BBO crystal. The angle of the crystal was adjusted to the phase-matching conditions at the fluorescence wavelength of interest. The upconverted signal which induced a delay in time by adjusting the path length of the gate beam. Both the gate and the sample fluorescence passed through a BBO crystal. Sum frequency generation occurred when the gate pulse entered the BBO crystal at the same time as the sample fluorescence. As delay is introduced to the gate beam, fluorescence decay can be detected. The detected (up-converted) light is collected by a monochromator and a photomultiplier tube (R1527P, Hamamatsu).

Femtosecond Transient Absorption

The femtosecond transient experimental setup contained a Spectra-Physics ultrafast amplified laser system. The Spectra-Physics ultrafast amplified laser system contained a Millennia Pro laser (continuous wave at 532nm with a power of 4.3W) that was used to pump Spectra-Physics Tsunami Ti:Sapphire mode-locked laser (pulsed at 790nm, output power: 250mW, repetition rate: 80MHz, approximate pulse width: 80fs) and Empower Q-switched laser (pulsed at 527nm, output power: 8W, repetition rate: 1kHz, approximate pulse width: 200ns) were used to pump a Spitfire Amplifier laser to generate an amplified 790nm output beam with: an approximate pulse width of 110 fs; repetition rate of 1kHz; and approximate output power of 1W. The 790nm amplified femtosecond pulse was directed into a beamsplitter, where approximate 15% of the pulse was used to generate the probe beam for fs-TA experiment and other roughly 85% was used to pump a Spectra-Physics Optical Parametric Amplifier (OPA). After the beamsplitter and OPA, both probe and pump beams were directed into an Ultrafast System Inc. Helios fs-TA optical setup. Specifically, the pump beam was directed into an optical chopper and focused onto samples in a quartz cuvette with a 2mm path length. The samples were liquid solutions all PPV prepared in chloroform and had an optical density ranging from 0.5–0.8 for experiments. The probe beam was directed through a computer-controlled delay line and focused onto a 3mm sapphire plate that generated a white light continuum. The probe beam/white light continuum and sample signal was directed and focused onto an Ocean Optics spectrometer and charge-coupled device (CCD), which collected the difference in absorbance signal (ΔA) as a result of the pump being on versus off due to the optical chopper. The Helios software, by Ultrafast Systems Inc., was used for data acquisition and the data analysis was done using Surface Xplorer and Origin Pro software.

Computational Method

Time-Dependent Density Functional Theory (TD-DFT)

Shorter models of the all-*trans*- and all-*cis*-PPV segments were optimized using a two-step protocol of a conformational search with the OPLS3e forcefield followed optimization using a higher-level of theory in chloroform with the SMD solvation model [i.e., SMD($CHCl_3$) - CAM-B3LYP-D3/6-311+G(d,p)]. Frequency analysis was then used to characterize stationary points as minima followed by subsequent UV−vis studies at the same level of theory.

References

1. Hancock, S. N,; Yuntawattana, N.; Valdez, S. M.; Michaudel, Q. Expedient synthesis and ring-opening metathesis polymerization of pyridinonorbornenes. *Polym. Chem.* **2022**, *12*, 5530-5535.
2. Padron, S.; Patlan, R.; Gutierrez, J.; Santos, N.; Eubanks, T.; Lozano, K. Production and Characterization of Hybrid BEH-PPV/PEO Conjugated Polymer Nanofibers by Forcespinning™. *J. Appl. Polym. Sci.* **2012**, *125*, 3610–3616.
3. Lidster, B. J.; Kumar, D. R.; Spring, A. M.; Yu, C.-Y.; Helliwell, M.; Raftery, J.; Turner, M. L. Alkyl substituted [2.2]paracyclophane-1,9-dienes. *Org. Biomol. Chem.* **2016**, *14*, 6079–6087.
4. Lidster, B. J.; Behrendt, J. M.; Turner, M. L.; Monotelechelic poly(*p*-phenylenevinylene)s by ring opening metathesis polymerization. *Chem. Commun.* **2014**, *50*, 11867–11870.
5. Würth, C.; Grabolle, M.; Pauli, J.; Spieles, M.; Resch-Genger, U. Relative and absolute determination of fluorescence quantum yields of transparent samples. *Nat. Protoc.* **2013**, *8*, 1535–1550.
6. Harder, E.; Damm, W.; Maple, J.; Wu, C.; Reboul, M.; Xiang, J. Y.; Wang, L.; Lupyan, D.; Dahlgren, M. K.; Knight, J. L.; Kaus, J. W.; Cerutti, D. S.; Krilov, G.; Jorgensen, W. L.; Abel, R.; Friesner, R. A. OPLS3: A Force Field Providing Broad Coverage of Drug-like Small Molecules and Proteins. *Journal of Chemical Theory and Computation* **2016**, 12, 281-296.
7. (a) Yanai, T.; Tew, D. P; Handy, N. C. A new hybrid exchange–correlation functional using the Coulomb-attenuating method (CAM-B3LYP). *Chemical Physics Letters* **2004**, 393, 51-57. (b) Becke, A. D. Density-functional thermochemistry. III. The role of exact exchange.

The Journal of Chemical Physics **1993**, 98, 5648-5652. (c) Kim, K.; Jordan, K. D. Comparison of Density Functional and MP2 Calculations on the Water Monomer and Dimer. *The Journal of Physical Chemistry* **1994**, 98, 10089-10094. (d) Stephens, P. J.; Devlin, F. J.; Chabalowski, C. F.; Frisch, M. J. Ab Initio Calculation of Vibrational Absorption and Circular Dichroism Spectra Using Density Functional Force Fields. *The Journal of Physical Chemistry* **1994**, 98, 11623-11627. (e) Grimme, S.; Antony, J.; Ehrlich, S.; Krieg, H. A consistent and accurate ab initio parameterization of density functional dispersion correction (DFT-D) for the 94 elements H-Pu. *J. Chem. Phys*. **2010**, 132, 154104. (f) Clark, T.; Chandrasekhar, J.; Spitznagel, G. W.; Schleyer, P. V. R. Efficient diffuse function-augmented basis sets for anion calculations. III. The 3-21+G basis set for first-row elements, Li-F. *J. Comput. Chem*. **1983**, 4, 294-301. (g) Krishnan, R., Binkley, J. S., Seeger, R., Pople, J. A. Self-consistent molecular orbital methods. XX. A basis set for correlated wave functions. *J. Chem. Phys.* **1980**, 72, 650-654. (h) Miertuš, S.; Scrocco, E.; Tomasi, J. Electrostatic interaction of a solute with a continuum. A direct utilization of AB initio molecular potentials for the prevision of solvent effects. *Chemical Physics* **1981**, 55, 117-129. (i) Miertuš, S.; Tomasi, J. Approximate evaluations of the electrostatic free energy and internal energy changes in solution processes. *Chemical Physics* **1982**, 65, 239-245. (j) Pascual-ahuir, J. L.; Silla, E.; Tuñon, I. GEPOL: An improved description of molecular surfaces. III. A new algorithm for the computation of a solvent-excluding surface. *Journal of Computational Chemistry* **1994**, 15, 1127-1138.

8. **Schrödinger Release 2023-2**: MacroModel, Schrödinger, LLC, New York, NY, 2023.
9. Frisch, M. J.; Trucks, G. W.; Schlegel, H. B.; Scuseria, G. E.; Robb, M. A.; Cheeseman, J. R.; Scalmani, G.; Barone, V.; Petersson, G. A.; Nakatsuji, H.; Li, X.; Caricato, M.;

Marenich, A. V.; Bloino, J.; Janesko, B. G.; Gomperts, R.; Mennucci, R.; ian, H. P.; Ortiz, D. V.; Izmaylov, A. F.; Sonnenburg, J. L.; Williams-Young, D.; Ding, F.; Lipparini, F.; Egidi, F.; Goings, J.; Peng, B.; Petrone, A.; Henderson, T.; Ranasinghe, D.; Zakrzewski, V. G.; Gao, J.; Rega, N.; Zheng, G.; Liang, W.; Hada, M.; Ehara, M.; Toyota, K.; Fukuda, R.; Hasegawa, J.; Ishida, M.; Nakajima, T.; Honda, Y.; Kitao, O.; Nakai, H.; Vreven, T.; Throssell, K.; Montgomery, J. A., Jr.; Peralta, J. E.; Ogliaro, F.; Bearpark, M. J.; Heyd, J. J.; Brothers, E. N.; Kudin, K. N.; Staroverov, V. N.; Keith, T. A.; Kobayashi, R.; Normand, J.; Raghavachari, K.; Rendell, A. P.; Burant, J. C.; Iyengar, S. S.; Tomasi, J.; Cossi, M.; Millam, J. M.; Klene, M.; Adamo, C.; Cammi, R.; Ochterski, J. W.; Martin, R. L.; Morokuma, K.; Farkas, O.; Foresman, J. B.; Fox, D. J. Gaussian 16, Rev. A.03, Gaussian, Inc.: Wallingford CT, 2016.

10. (a) Zhao, Y.; Truhlar, D. G. The M06 Suite of Density Functionals for Main Group Thermochemistry, Thermochemical Kinetics, Noncovalent Interactions, Excited States, and Transition Elements: Two New Functionals and Systematic Testing of Four M06- Class Functionals and 12 Other Function. *Theor. Chem. Acc.* **2008**, 120, 215–241. (b) Zhao, Y.; Truhlar, D. G. Density Functionals with Broad Applicability in Chemistry. *Acc. Chem. Res.* **2008**, 41, 157–167.
11. Lu, T.; Chen, F. Multiwfn: A Multifunctional Wavefunction Analyzer. *J. Comput. Chem*. **2012**, 33, 580−592.
12. Lu, T.; Chen F. Calculation of Molecular Orbital Composition. *Acta Chimica Sinica* **2011**, 69, 2393-2406

13. Melnikov, S. A, Serdobintsev, Yu. P., Vedyaykin, D.A., and Khodorkovskii, A.M., Two-photon absorption cross section for Coumarins 102, 153 and 307. *Journal of Physics: Conf. Series* **2017**, *917*, 062029.
14. Ricci, F.; Mandal, H.; Wajahath, M.; Burdick, R.; Villabona-Monsalve, J.P.; Hussain, S.;Goodson, T. Investigations of Coherence in Perovskite Quantum Dots with Classical and Quantum Light. *J. Phys. Chem. C* **2023**, *127*, 7, 3579–3593

Chapter Six

Enhancing Reverse Intersystem Crossing Through Higher-Lying Triplet States in Engineered Indacenodithieno[3,2-b]thiophene (IDTT)-Based Molecular Systems

6.1. Author Contribution Statement

In this thesis chapter, I have done majority of the work including experimental, data analysis and writing of the manuscript. The chapter describes the work and results from the collaborative research by Professor Theodore Goodson III (Department of Macromolecular Science and Engineering, University of Michigan, Ann Arbor, and Department of Chemistry, University of Michigan, Ann Arbor), and Professor Wei You (Department of Chemistry, University of North Carolina at Chapel Hill, Chapel Hill, NC). I would also like to acknowledge Bishal Saha, Juan Juan S. Sandoval, Alexander Stark and Professor Paul Zimmerman for the electronic calculation and data interpretation. Also, I acknowledge Sara D. Jovanovski and Professor Benedetta for the two-photon absorption data and analysis; additionally, Zhong Xiaowei from Professor Wei You group synthesized and characterized the samples.

The manuscript based on this work is currently in preparation for submission to the *Journal of the American Chemical Society*. As a result, certain details may be refined prior to submission, and the final published version may differ in emphasis from the content presented in this dissertation. The author information for this study is: Olusayo J. Ogunyemi, Zhong Xiaowei, Sara D. Jovanovski, Benedetta Carlotti, Bishal Saha, Juan S. Sandoval, Alexander Stark, Paul Zimmerman, Wei You and Theodore Goodson III. (To be submitted to *J. Am. Chem. Soc*.)

6.2. Abstract

Advancing thermally activated delayed fluorescence (TADF) materials requires precise control over excited-state energetics and coupling pathways to promote efficient reverse intersystem crossing (rISC). Here, we report the synthesis of a series of ladder-type indacenodithieno[3,2-b]thiophene (IDTT) molecular systems, monomer (M1), dimer (D1), and trimer (T1) that reveal how systematic extension of the fused core IDTT units modulates spin dynamics and charge-transfer character. Increasing the number of IDTT units from M1 to T1 lowers the energy of higher-lying triplet states and strengthens their electronic coupling with the emissive singlet (S_1), thereby directly enhancing rISC. Transient absorption spectroscopy shows that T1 exhibits the fastest K_{rISC} (6.8 x 10^6 s^{-1}) and the highest delayed fluorescence yield (Φ_{TADF} = 19%), providing clear experimental evidence for efficient TADF in this series. TD-DFT calculations corroborate these results, identifying strong spin-orbit coupling (SOC ≈ 0.8 cm^{-1}) between the charge-transfer singlet state (^{1}CT) and a higher-lying locally excited triplet (^{3}LE, T_3) as the key rISC channel in T1. Concurrently, the enhanced intramolecular charge-transfer nature of T1 manifests in a ~25-fold increase in classical two-photon absorption cross-section (δ_{TPA}) and nearly an order-of-magnitude enhancement in entangled two-photon absorption cross-section (σ_e) relative to M1, revealing the mechanistic connection between charge-transfer strength, nonlinear optical response, and spin conversion dynamics. Our findings provide mechanistic insight into the crucial role of higher-lying triplet states in governing TADF efficiency. By tuning the electronic structure of ladder-type IDTT frameworks from M1 to T1, we demonstrate a rational strategy for enhancing K_{rISC} and delayed fluorescence via singlet-triplet electronic coupling. This work defines clear structure-property relationships for charge transfer-mediated spin conversion and offers a design approach to

engineering high-performance TADF emitters for next-generation optoelectronic and quantum photonic applications.

6.2.3. Introduction

According to spin statistics, in electroluminescence three triplet states are formed for every singlet state thereby limiting the internal quantum efficiency (η_{IQE}) of fluorescence-based organic light emitting diodes (OLEDs) to 25 %.[1,2] Hence, there has been significant interest in Thermally Activated Delayed Fluorescence (TADF) involving the up-conversion of non-emissive triplet excitons into emissive singlet exciton to achieve high η_{IQE} for efficient OLED device applications.[3–8] For effective utilization of the triplet excitons, fast reverse intersystem crossing (rISC) rates from the triplet to singlet state is very important to outcompete bimolecular exciton annihilation processes such as triplet-triplet annihilation (TTA).[9–11] Achieving high rates of rISC involves molecular modification to reduce the energy gap (ΔE_{ST}) between the lowest triplet (T_1) and lowest singlet (S_1) excited states and increasing the spin orbit coupling (SOC) between these states (eqn 1).[2,4,12–19] Conventional TADF-type materials are based on molecules with increased CT properties containing Donor (D)-Acceptor (A) moieties which allows the spatial separation of the HOMO and LUMO in the D-A system thereby reducing the ΔE_{ST}.[20–25] Most recently, multiresonance (MR)-TADF materials have also been developed to localize the HOMO and LUMO on different atoms of the same molecule which suppress the excited state relaxation, reduce wide broadening, increase the SOC and enhance the K_{rISC}.[5,26–30] The rate of reverse intersystem crossing (K_{rISC}) can be theoretically described within the framework of Fermi's golden rule, where $\hbar$ is the reduced Planck constant. According to this model, K_{rISC} is proportional to the square of the

SOC matrix element between the singlet and triplet states, ($<S_1|\hat{H}_{SO}|T_1>$), and the Franck-Condon weighted density of states (ρFC), as shown in Equation 1:[6]

$$K_{rISC} = \frac{2\pi}{h}\ \rho FC|<S_1|\hat{H}_{SO}|T_1>|^2 \quad \ldots (1)$$

However, even when SOC is favorable, for rISC to occur, the ΔE_{ST} needs to be sufficiently small (typically below ~0.2 eV) to allow upconversion of the triplet into the emissive singlet. There have been debates on other mechanisms of TADF, particularly involving the role of higher lying triplet excited states in contributing to K_{rISC}.[31–34] One of such mechanisms that has gained increasing attention is spin-vibronic coupling (SVC), a second-order process in which vibrational motions facilitate coupling between electronic excited states.[31,32,35,36] In contrast to the conventional first-order model, where rISC is governed solely by SOC between the S_1 and T_1, SVC enables additional pathways by involving thermally accessible higher triplet states (T_n, n > 1). If the T_n state possesses orbital character distinct from that of the S_1 state, or for instance, a locally excited (^{3}LE) triplet interacts with a charge-transfer singlet (^{1}CT), then the SOC between T_n and S_1 can be significantly enhanced, in accordance with El-Sayed's rule.[34,36] This sequence of thermally driven population transfer followed by a spin-allowed transition can accelerate rISC even in cases where direct coupling between T_1 and S_1 is inefficient. Recent investigations on MR-TADF materials have shown that the rISC via SVC from the $T_1 \rightarrow T_2$ (or T_n) $\rightarrow S_1$ is the main pathway for the TADF other than the direct $T_1 \rightarrow S_1$.[37–40] This mechanism is favored due to the reduced SOC between the S_1 and the T_1 as a result of their identical transition orbital distribution. The enhanced SOC between the T_2 (or T_n) and the S_1 makes the rISC more efficient.

Cheon et al. revealed that the slow K_{rISC} in DABNA-1 (a-typical MR-TADF material) arises from a combination of a small SOC between the S_1 and T_1 states (~ 0.036 cm^{-1}) and a large T_1-T_2

energy gap (~ 0.62 eV), which suppresses second-order SVC. In contrast, they reported that structural modifications in pBP-DABNA-Me introduce multiple localized triplet (^{3}LE) states in close energetic proximity to S_1 and T_1. These additional ^{3}LE states exhibited significantly larger SOC values (up to 0.204 cm^{-1}), effectively enhancing SVC and enabling a much faster K_{rISC}.[41]

The efficiency in the K_{rISC} arises because the ^{1}CT spin can interact more strongly with a ^{3}LE state that lies close in energy, enabling a spin-flip transition. Intersystem crossing (ISC) between ^{1}CT and ^{3}CT states is slow and inefficient relative to ISC between ^{1}CT and ^{3}LE in D-A TADF molecules.[42,43] Hence, in these molecular systems, the ^{1}CT show strong SOC with close lying ^{3}LE states.[42,44,45] In elucidating the mechanism of TADF, it has been shown in several reports that the ^{3}LE is the essential triplet state that dictates the ΔE_{ST} and the K_{rISC} in TADF emitters where direct coupling between ^{1}CT and ^{3}CT states remains inefficient.[46,47] This was also confirmed in the work of Franca et al. who utilized nanosecond transient absorption (ns-TA) spectroscopy to demonstrate the role of a triplet local exciton (^{3}LE) state in facilitating TADF in spiro-linked acridine anthracenone derivative 10-phenyl-10*H*,10′*H*-spiro[acridine-9,9′-anthracen]-10′-one (ACRSA).[48]

In this work, we demonstrated that increasing the conjugation length of ladder-type indacenodithieno[3,2-b]thiophene (IDTT)-based (Monomer (M1), Dimer (D1), and Trimer (T1)) molecular systems through molecular engineering significantly enhances the K_{rISC} by involving higher-lying triplet states. Our work provides fundamental insight into controlling the interplay between ^{3}CT and ^{3}LE triplet states for efficient $^3\text{CT} \rightarrow {}^1\text{CT}$ rISC . We further demonstrated high delayed fluorescence quantum yield (Φ_{TADF}) with increasing number of core IDTT units from the M1 to T1 providing evidence of TADF in these molecules. Using time-resolved spectroscopy supported by TD-DFT calculations, we uncover a unique energetic and electronic configuration in

T1, where multiple triplet states with distinct ^{3}LE character lie below the ^{1}CT, resulting in enhanced SOC coupling and high K_{rISC}. Additionally, our experimental data show significant enhancement in intramolecular charge-transfer (ICT) character from M1 to T1, which is confirmed by the increase in two-photon absorption (TPA) cross-section. This work provides critical insight into tuning energies of higher-lying ^{3}LE triplet states for increased K_{rISC}, thereby establishing a clear design framework for achieving high TADF efficiency in ladder-type IDTT-based systems.

6.4. Methods and Materials

6.4.1. Absorption and Emission

The steady state absorption spectra of M1, D1 and D1 in chloroform were measured using the Agilent Cary 60 UV-Visible spectrometer with a xenon lamp having a detection range from 190 nm to 1100 nm. A cuvette with a path length of 1cm was used for all measurements. The emission spectra were obtained using a FluoroMax-4 fluorimeter with an integration time of 0.1 s and a slit size of 1.0 nm.

6.4.2. Fluorescence Quantum Yield

Williams comparative method was used in measuring the fluorescence quantum yields of M1, D1 and T1.[49,50] As a result of their different emissive properties, Coumarin 307 dissolved in methanol was used as the standard for the monomer while Rhodamine B in ethanol was used as the standard for the dimer and trimer compounds. The same procedure was repeated to measure the quantum yield of the nitrogen purged samples.

6.4.3. Classical Two Photon Absorption

Two-Photon Excited Fluorescence (TPEF) techniques described by Goodson and co-workers was used to determine the TPA cross-section (δ_{TPA}) of the monomer, dimer and trimer.[51,52] The mode-locked Ti:Sapphire tsunami laser was used to generate the femtosecond pulses utilized

to excite the sample at 800 nm which was dissolved in a 1cm path length cuvette. The TPA emission scan was performed by collecting the fluorescence using the cornerstone Oriel monochromator which is connected to Hamamatsu photomultiplier detector and a counting unit. We utilized the neutral density filter to adjust the photon flux from the laser and the fluorescence counts as a function of the input photon flux was determined. Coumarin 307 was used as the standard for the monomer while Rhodamine B was used as the standard for the dimer and trimer compounds. The TPA slope was obtained by plotting the logarithmic graph of the fluorescence versus the input photon flux. The 880 nm excitation TPA measurement for M1 and 1040 nm excitation TPA experiment for D1 and T1 were accomplished by utilizing a fs tunable amplified laser system as described earlier with a similar methodolodgy.[53] Rhodamine B was used as a standard for these measurements.

6.4.4. Entangled Two Photon Absorption

The entangled two photon absorption (ETPA) experimental setup utilized had been described previously by Villabona and co-workers.[54,55] The pump source for the ETPA experiment is the 405 nm continuous wave (cw) light generated from the CrystaLaser Inc. (CL-2000) laser. Entangled photon pairs were generated via spontaneous parametric down-conversion (SPDC) using a type-I Beta Barium Borate (BBO) crystal, pumped by the 405 nm laser beam. The resulting entangled photons (signal and idler wavelengths with 800 nm, respectively) were focused into a 1 cm quartz cuvette containing the sample using a convex lens. After transmission through the sample, the entangled photons passed through a band-pass filter to eliminate any fluorescence background before detection by an avalanche photodiode (Laser Components COUNT-250N). Zinc meso-tetraphenylporphyrin in toluene served as a calibration standard. Chloroform was used to establish a baseline by measuring the transmitted entangled photon (EP) rate at an incident

photon flux of approximately 5.0 x10^6 photons per second. Following baseline determination, the M1, D1 and T1 in chloroform were introduced into the 1 cm cuvette. The transmitted EP rate was recorded at five different incident photon flux levels by adjusting a motorized neutral density (ND) filter. The decrease in transmitted photon counts due to ETPA was evaluated relative to the established baseline. The ETPA cross-section was calculated from the slope of a linear fit of the ETPA-induced count rate (counts/s) plotted against the incident photon flux.

6.4.5. Nanosecond Transient Absorption Spectroscopy

The excited state dynamics of the transient species in the IDTT-based oligomers were determined using nanosecond transient absorption spectroscopy. Nd:YAG (neodymium-doped yttrium aluminum garnet) laser with 10 Hz repetition rate was used as the excitation source, pumping a tunable GWU Optical Parametric Oscillator (OPO) system. The xenon flash lamps excited the Nd:YAG rods producing a fundamental output at 1064 nm. This beam was subsequently directed into a harmonic generator containing a KDP crystal to produce second and third harmonic wavelengths at 532 nm and 355 nm, which then enters the OPO. The tunable OPO (from 305 nm to 2300 nm) was used to generate the desired pump in the UV, visible and even the IR region which goes into the LP980 Edinburg spectrometer. The OPO was directed into an Edinburgh LP980 spectrometer, which houses the probe light source, sample compartment, and monochromator for spectral detection. The spectrometer was calibrated using a standard solution of $Ru(bpy)_3^{2+}$. The pump wavelength was set to 435 nm, 520 nm and 525 nm for M1, D1 and T1 respectively. The transmitted probe light was converted into an electrical signal via a photodetector connected to an oscilloscope, and the corresponding changes in absorbance were recorded using the LP980 software. By plotting the transient absorption changes against wavelength and time, the excited state dynamics of the transient absorbing species were determined

6.4.6. Femtosecond Transient Absorption Spectroscopy

A regenerative amplified titanium:sapphire laser system (Spitfire Pro, Spectra-Physics, 1 kHz repetition rate) produced a 790 nm (~110 fs) laser pulse with an output of approximately 800 mW. 90% of the output was utilized to pump an optical parametric amplifier (Spectra-Physics) to generate a 400 nm pump pulse. The white-light probe was generated by focusing the remaining 10% of the output to a calcium fluoride or sapphire crystal, spanning from 380 to 700 nm and 450 to 800 nm, respectively. Then, the 400 nm pump and probe beams were directed to an Ultrafast System Inc. Helios fs-TA optical setup. A mechanical chopper was used to block every other pump pulse. The pump and pulse beams were focused onto a 2 mm quartz cuvette containing the sample, stirred with a magnetic stir bar. Samples were diluted to a maximum absorbance of ~0.4 at their λ_{max}. After passing through the sample, the white-light probe is centered on a charge–coupled device (Ocean Optics), and the data was acquired by the Helios software (Ultrafast Systems Inc.)

The TA signal was collected using a parallel ($\Delta A_{\parallel}$) and perpendicular ($\Delta A_{\perp}$) pump-probe polarizations. The isotropic TA signal, $I(\lambda, \Delta t)$, dependent on the wavelength (λ) and pump-probe time delay (Δt) was calculated as:

$$I(\lambda, \Delta t) = \frac{\Delta A_{\parallel} + 2\Delta A_{\perp}}{3} \quad (1)$$

The global analysis was performed using the Glotaran software package (Equation 1), assuming a parallel kinetic model. The time-resolved data was fitted to a set of N exponential functions where the amplitude varies as a function of the wavelength, calculated as (Equation 2):

$$I(\lambda, \Delta t) = \sum_j^N DAS_j(\lambda)\ (e^{-\Delta t/\tau_j}) \quad (2)$$

where τ_j is the lifetime of the j exponential decaying component, and $DAS_j(\lambda)$ is the spectral amplitude or decay-associated spectra. In this way, each decay–associated spectra describe the spectral changes that occur in the time-resolved data with an associated time constant τ_j.

6.4.7. TD-DFT Calculations

Geometry optimization for the monomer, dimer and trimer was carried out using the B3LYP hybrid functional with the 6-31G* basis set. The B3LYP method combines Becke's three-parameter exchange functional (B3) with the Lee-Yang-Parr (LYP) correlation functional. B3LYP includes a fraction of exact Hartree-Fock exchange and accounts for electron correlation effects, making it well-suited for geometry optimization and electronic structure studies of organic π-conjugated system. The polarization functions of 6-31G* allow for better modelling of molecular orbitals and geometry, especially in non-planar systems or molecules with heteroatoms like sulfur. It provides a good compromise between accuracy and computational cost and is frequently used for geometry optimization. For TDDFT calculations cc-pVTZ basis set was used which includes three functions per valence orbital, improving correlation treatment and excitation energy predictions. It is well-suited for TDDFT studies, providing better accuracy in excited-state calculations than 6-31G*. It could help here to refine the excited-state properties obtained from TDDFT calculations and check the convergence of excitation energies with respect to basis set size.

6.5. Result

6.5.1. Synthesis

The synthetic routes for the IDTT based molecules are shown in **Chart 6.1**. **M1** was synthesized following a reported procedure.[56] Monobromination of **M1** using N-

bromosuccinimide (NBS) afforded M1-Br in an 88% yield. Direct borylation of **M1** with 1.5 equivalents of 4,4,5,5-tetramethyl-1,3,2-dioxaborolane (HBpin) produced a mixture of mono- and di-borylated products. This crude mixture was used directly in the following Suzuki coupling step without purification. The final products, **D1** and **T1**, were isolated in yields of 32% and 36%, respectively. Detailed syntheses can be found in the SI.

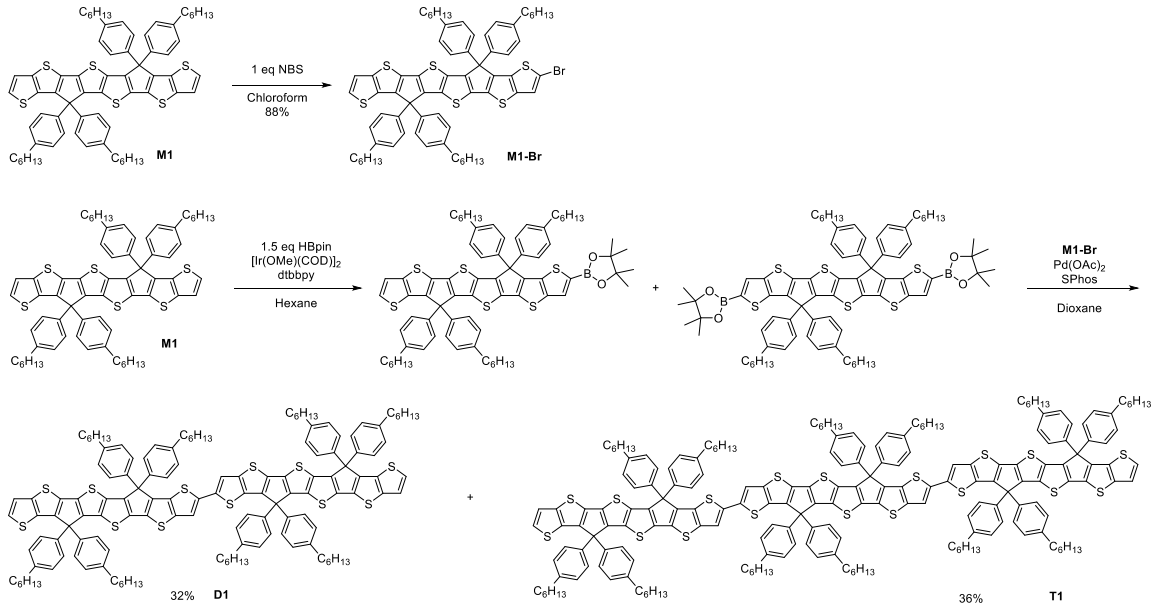


Chart 6.1: Synthetic route for M1, D1 and T1

6.5.2. Absorption and Emission

The steady-state absorption spectra of M1, D1 and T1 are shown in **Figure 6.1A**. All the three oligothiophene based molecules exhibit absorption bands at higher energy in the range of 200 nm to 350 nm, as well as broad absorption band at lower energy in the visible region between 360 nm and 700 nm. The absorption maxima of M1, D1 and T1 corresponding to their π-π* transitions were determined to be 435 nm, 520 nm and 525 nm, respectively (**Table 6.1**). Increasing the number of core monomeric units results in clear bathochromic shifts in the

absorption maxima indicative of enhanced electronic delocalization and efficient vibrational coupling. Emission spectra of the oligothiophenes show a red-shift maxima upon increasing the number of the core monomeric units, ranging from 450 nm to 800 nm (**Figure 6.1B**). The emission-maxima of M1, D1 and T1 are 490 nm, 585 nm and 593 nm respectively (**Table 6.1**). The large stoke shifts in these oligomers suggest notable differences in ground and excited-state geometries, consistent with large excited-state reorganization energies and changes in dipole moment upon electronic excitation.[57]

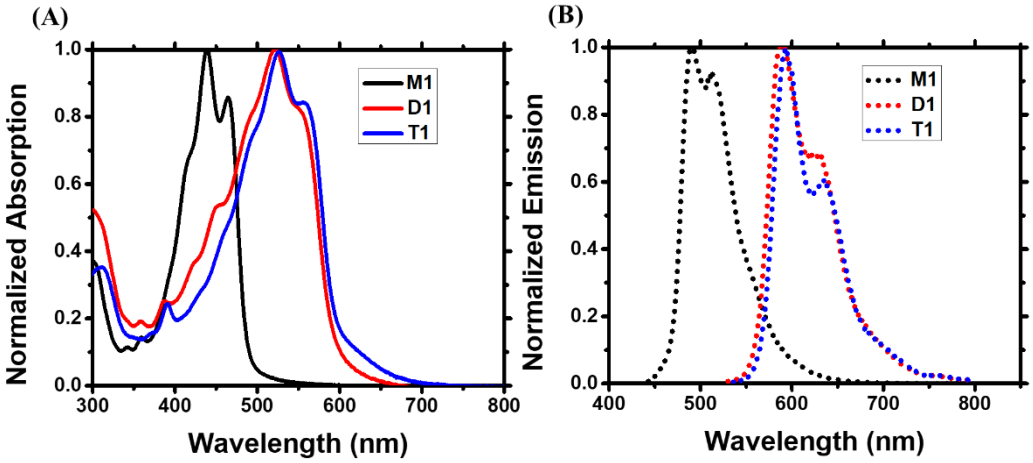


Figure 6.1 (A) Absorption spectra of M1, D1 and T1 (B) Emission spectra of M1, D1 and T1 in chloroform.

M1 exhibits a fluorescence quantum yield (Φ_F) of 47 % in air equilibrated solution, which increases to 54 % under oxygen-free conditions obtained through nitrogen purging (Φ_{PF}). D1, containing two linearly fused oligothiophene units, shows a Φ_F of 34 % with Φ_{PF} increasing to 43 %. T1 exhibits a Φ_F of 36 % with a substantial increase in the Φ_{PF} determined to be 52 %. This enhanced fluorescence quantum yields under oxygen-free conditions suggest the presence of delayed fluorescence components, which are critical for TADF mechanisms.[58,59]

Table 6.1: Steady state properties of the M1, D1 and T1

Compound	λ_{abs} (nm)	λ_{ems} (nm)	$E_{singlet}$ (eV)	(f_{osc})	Φ_F (%)	Φ_{PF} (%)
M1	438	490	2.77	1.59	47	54
D1	520	585	2.09	3.64	34	43
T1	525	593	1.88	5.28	36	52

λ_{abs} = Absorption maxima, λ_{ems} = Emission maxima and f_{osc} = Oscillator strength, Φ_f = Fluorescence quantum yield, Φ_{PF} = Purged fluorescence quantum yield

6.5.3. Electronic Structure Calculations

The calculated excited state energy for the S_1 and their corresponding oscillator strength is shown in **Table 6.1**. The intensity of the lowest-energy transitions, quantified by the oscillator strength (f_{osc}), increases with the number of fused oligothiophene units. Specifically, M1 exhibits an oscillator strength of 1.59, which increases to 3.64 for D1 and 5.28 for T1. This trend reflects a systematic increase in transition dipole moment and transition probability, arising from the extended conjugation, stronger vibronic coupling between the oligothiophene units and more delocalized frontier molecular orbitals. Our TD-DFT calculations show the reduction of the singlet excited state (S_1) energy as we extend the thiophenes rings from the monomer to the trimer. Molecular orbital analysis reveals distinct differences in the electronic distribution of the oligothiophene series as the number of core monomeric units increases. For M1, the HOMO and LUMO are largely confined to the central thiophene moiety, indicating a localized electronic structure with limited conjugation length. In contrast, D1 and T1 systems exhibit a progressive extension of both the HOMO and LUMO across the fused thiophene backbone, consistent with enhanced π-delocalization and stronger electronic coupling between the monomeric subunits.

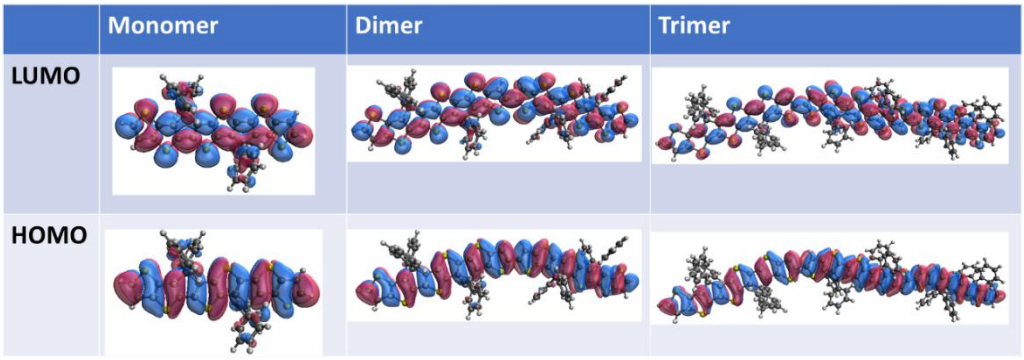


Figure 6.2: Molecular orbital of the M1, D1 and T1

6.5.4. Two-Photon Absorption

The nonlinear optical response (NLO) of the oligothiophenes were determined using the two-photon excited fluorescence (TPEF) technique.[60,61] Two-photon absorption cross sections (δ_{TPA}) were extracted from fluorescence intensity power dependences. The δ_{TPA} is highly sensitive to molecular symmetry and extent of excited-state charge delocalization[62–65]. Log-log plots of emission intensity versus excitation power exhibit slopes of approximately 2 for M1, D1, and T1, confirming a two-photon excitation process (**Figure 6.3**). Measurements were initially performed using 800 nm excitation.

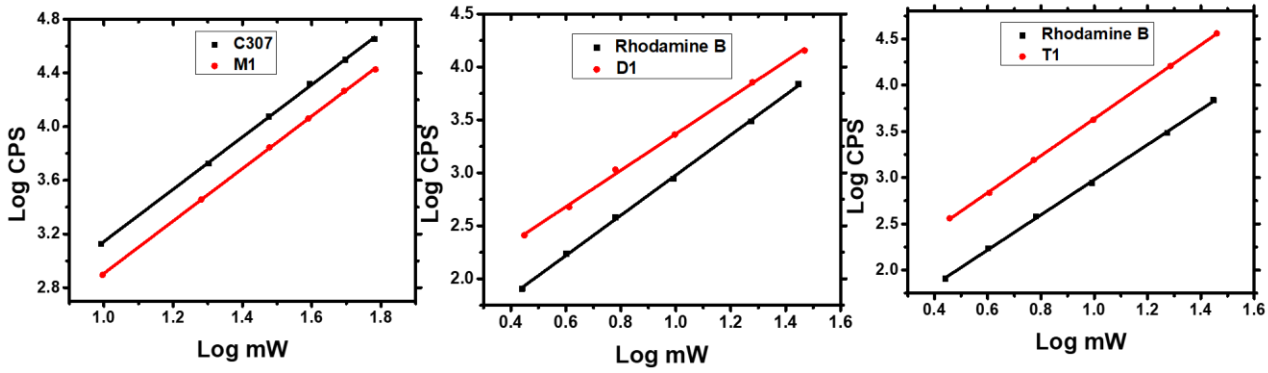


Figure 6.3: Plot of the classical 800 nm excitation TPA of M1, D1 and T1

The δ_{TPA} increases significantly across the oligomer series (**Table 6.2**), from 57.1 GM for M1 to 190 GM for D1 and 1450 GM for T1. Relative to M1 and D1, T1 displays enhancements of approximately 25-fold and 10-fold, respectively. The enhancement in the δ_{TPA} correlates with the increase in f_{osc} across the series (**Table 6.1**). The δ_{TPA} of M1 is comparable to reported values for extended thienoacene systems, including fused benzothiophene derivatives with larger π-conjugated frameworks (FBT-11R, FBT 15R and FBT 21R).[66] The larger δ_{TPA} observed for T1 reflects stronger electronic coupling of the three coupled thiophene units.

To further assess the nonlinear response near the one-photon absorption maxima, additional classical TPA measurements were performed using excitation wavelengths corresponding to twice the absorption peak energies. M1 was excited at 880 nm, consistent with its absorption maximum at 440 nm, while D1 and T1 were excited at 1040 nm, corresponding to absorption maxima at 520 and 525 nm, respectively. Log-log plots of TPA signal versus excitation power yield slopes of approximately 2 for all three compounds, confirming two-photon absorption under resonant excitation conditions (**Figure 6.4**).

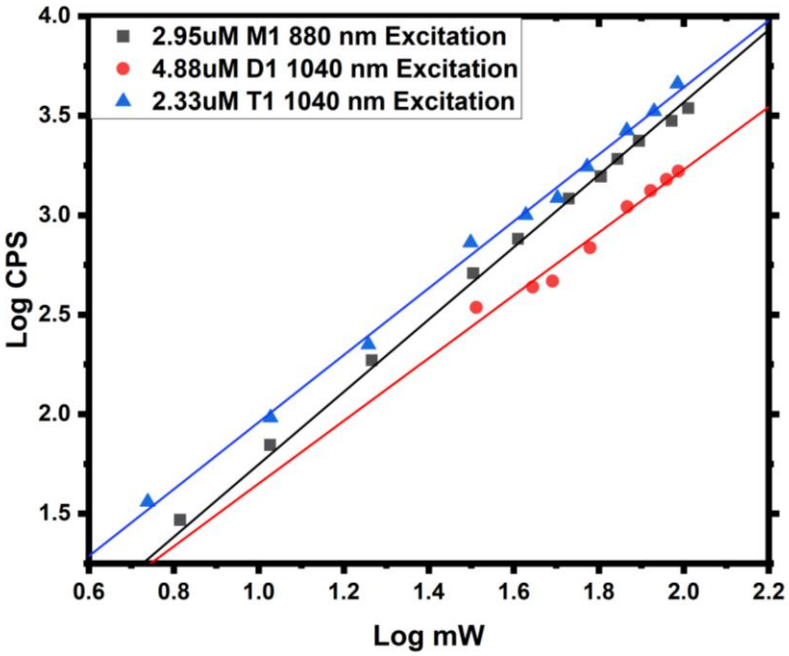


Figure 6.4. Plot of the classical 880 nm excitation TPA of M1, and 1040 nm excitation TPA of D1 and T1

The δ_{TPA} at resonant excitation are summarized in **Table 6.2**. At resonance, δ_{TPA} values of 8.75 GM (M1), 6.51 GM (D1), and 20.6 GM (T1) were obtained, which are lower than the corresponding values measured at 800 nm excitation. This clearly demonstrates that the off-resonant excitation produces a stronger two-photon response across the oligomer series. The trend from monomer to trimer is preserved, with T1 exhibiting the largest enhancement, highlighting the cumulative effect of increasing conjugation on the two-photon absorption. This highlights the unusually strong off-resonant two-photon response in these systems, reflecting the presence of more efficient two-photon pathways accessed under 800 nm excitation, as discussed in detail in the Discussion section.

Table 6.2. Classical TPA cross-sections at 800 nm excitation and at resonance (maxima one photon absorption spectra) for M1, D1, T1

Compound	TPA $\delta_{800\ nm}$ (GM)	TPA $\delta_{at\ res.}$ (GM)
M1	57	8.75
D1	190	6.51
T1	1450	20.6

6.5.5. Entangled Two-Photon Absorption Spectroscopy

The magnitude of the interaction of M1, D1 and T1 with quantum light was determined using entangled two-photon absorption (ETPA) spectroscopy. The entangled photons (signal and idler), generated via spontaneous parametric down-conversion (SPDC), enable selective molecular excitation through quantum states that are not accessible using classical light sources.[67–69] Unlike classical TPA, which exhibits a quadratic dependence on input intensity, ETPA scales linearly with the incident photon flux. **Figure 6.5** shows the ETPA rate as a function of the input photon flux for M1, D1 and T1. The corresponding ETPA cross-sections (σ_{ETPA}), determined experimentally,

are summarized in **Table 6.3** and show systematic increase with the number of oligothiophene units.

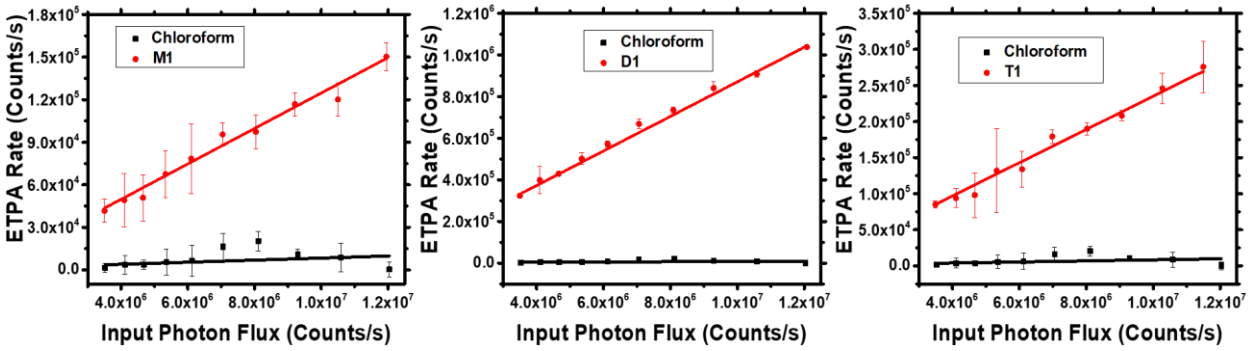


Figure 6.5: ETPA rate of M1, D1 and T1 in chloroform.

M1 exhibits a σ_{ETPA} of 8.23 x10^{-19} (cm^2/molecule). Upon increasing the thiophene units, the σ_e increases to 3.87 x10^{-18} (cm^2/molecule) for D1, and further increases to 4.17 x10^{-18} (cm^2/molecule) in T1, representing almost one order-of-magnitude enhancement compared to M1. The increase in the σ_{ETPA} from M1 to both D1 and T1 indicates strong electronic coupling between thiophene units upon oligomer extension. This enhanced coupling facilitates greater charge delocalization and more allowed transition pathways, leading to stronger light-matter interaction with entangled photons.

Table 6.3: Entangled TPA cross-section for the investigated compounds in chloroform.

Compound	Conc (M)	σ_{ETPA}(cm^2/molecule)
M1	2.61 x10^{-5}	8.23 x10^{-19}
D1	3.78 x10^{-5}	3.67 x10^{-18}
T1	9.47 x10^{-6}	4.17 x10^{-18}

6.5.6. Femtosecond transient absorption spectroscopy

Femtosecond transient absorption (fsTA) was used to determine the electronic excited state dynamics of the compounds studied in this work. **Figure 6.6** (a) and (b) presents the fsTA spectra of the chromophores, pumped at 400 nm. After photoexcitation, the (a) monomer exhibits a negative ground-state bleach (GSB) that mirrors the ground-state absorption between 410-500 nm alongside a broad positive excited-state absorption (ESA) from 500-700 nm. The stimulated emission (SE) band lies between 450 and 600 nm and overlaps with the GSB and the ESA. The trimer presents similar features: (i) a negative GSB that mirrors the ground-state absorption from 480-600 nm, (ii) an overlap between GSB, SE, and ESA from 580-640 nm, and (iii) a broad and strong ESA above 600 nm.

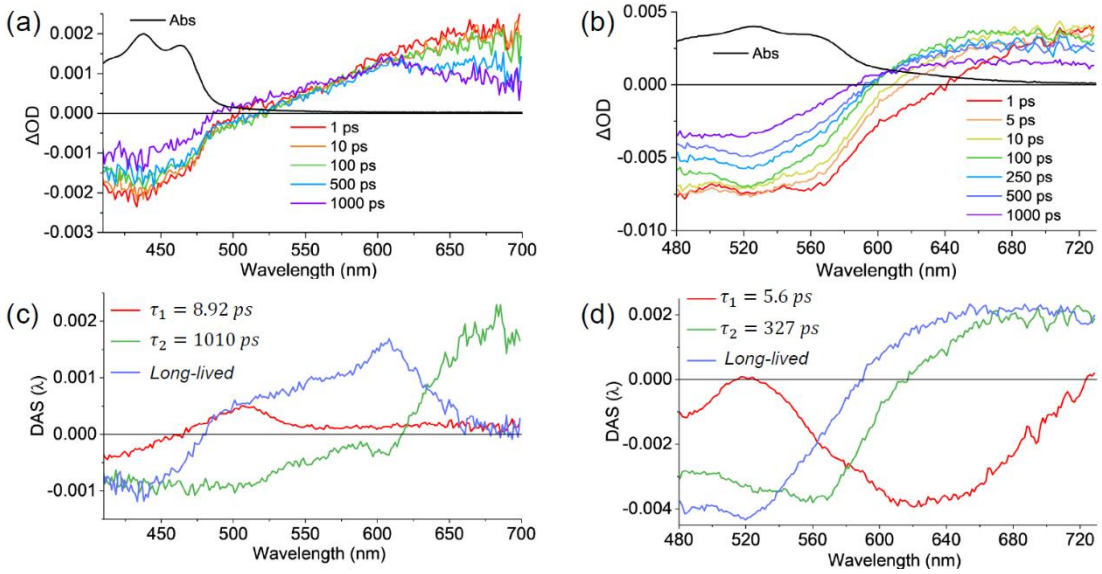


Figure 6.6. fsTA spectra at different time delays for (a) monomer and (b) trimer. The excitation wavelength was set to 400 nm. The absorption spectra are shown in black solid lines. Decay-associated spectra, DAS, and their corresponding time constants, τ for (c) monomer and (d) trimer.

Global analysis was used to analyze the time-resolved data. The data was fitted using a set of decaying components or decay-associated spectra DAS_j (λ) with an associated time constant, presented in **Figure 6.6** (c) and (d). For both cases, we identified three components. The first component, represented in red, is attributed to solvent and intramolecular excited state reorganization, and internal conversion to the lowest singlet excited state. The second component, presented in green, shows the emergence of new ESA bands above 600 nm and a loss of SE. This component is assigned to the intersystem crossing from the lowest singlet electronic state to a triplet state. The third component, represented in blue, corresponds to a long-lived component that is beyond the 1.5 ns delay stage of our instrument. This component is associated with the spectral signatures of a triplet state, and its decay is beyond the instrumental capabilities.

We observed an increase in the ISC rate from monomer to trimer. This trend is consistent with computational calculations indicating an increase in spin-orbit coupling and a reduction in the energy gap between the singlet and triplet states. The ISC rate is nearly 3 times faster for the trimer (1/327 ps^{-1}) relative to the monomer (1/1010 ps^{-1}).

6.5.7. Nanosecond transient absorption spectroscopy

Nanosecond transient absorption (nsTA) spectroscopy was utilized to probe the long-lived excited states and transient intermediates, under both air-saturated and nitrogen-purged conditions. The negative ΔOD observed at wavelengths corresponding to the steady-state absorption maxima is assigned to GSB, indicating depopulation of the ground state. As shown in **Figure 6.7**, the GSB for M1, D1, and T1 occurs at 435, 520, and 525 nm, respectively. Positive ΔOD bands were assigned to ESA arising from the transient population of singlet or triplet excited states, observed at 600, 670, and 680 nm for M1, D1, and T1, respectively.

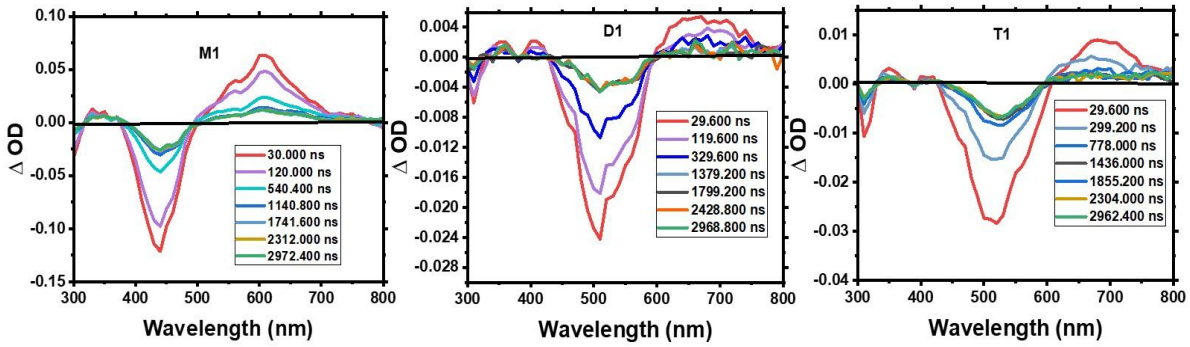


Figure 6.7: Nanosecond transient absorption spectra of M1, D1 and T1 in chloroform.

The time-resolved studies clearly reveal the distinct contributions of singlet and triplet states to the excited-state dynamics of the oligothiophene series. The biexponential decay observed in the kinetic traces, with fast (τ_1) and slow (τ_2) components, indicates the presence of multiple relaxation pathways. The fast components (τ_1) were determined to be 9.1 ns for M1, 13.1 ns for D1, and 6.3 ns for T1. The fast components, on the order of several nanoseconds, remained essentially unaffected by oxygen, suggesting that they arise primarily from singlet-state relaxation and short-lived charge-transfer processes.

In contrast, the slow components exhibited pronounced oxygen sensitivity, with lifetimes extending into the microsecond range under nitrogen-purged conditions. This behavior confirms the involvement of triplet states and demonstrates that the triplet population can be effectively stabilized in the absence of quenching. The decay rate of the purged M1, D1 and T1 were 2.7 x10^5 s^{-1}, 2.9 x10^5 s^{-1} and 5.0 x10^5 s^{-1} respectively.

To quantify the efficiency of triplet-to-singlet conversion, reverse intersystem crossing rates (K_{rISC}) were determined using delayed fluorescence quantum yields (Φ_{TADF}). This approach, widely employed in emission-based measurements, calculates Φ_{TADF} from the difference in

fluorescence quantum yields under nitrogen-purged and air-equilibrated conditions.[70–72] By incorporating both the contributions of the triplet excited state and delayed fluorescence, the K_{rISC} values were derived following the method established by Vásquez and co-workers (**eqn 2**).[73]

$$K_{rISC} = \Phi_{TADF} \text{ x } k_{triplet} \qquad \ldots (2)$$

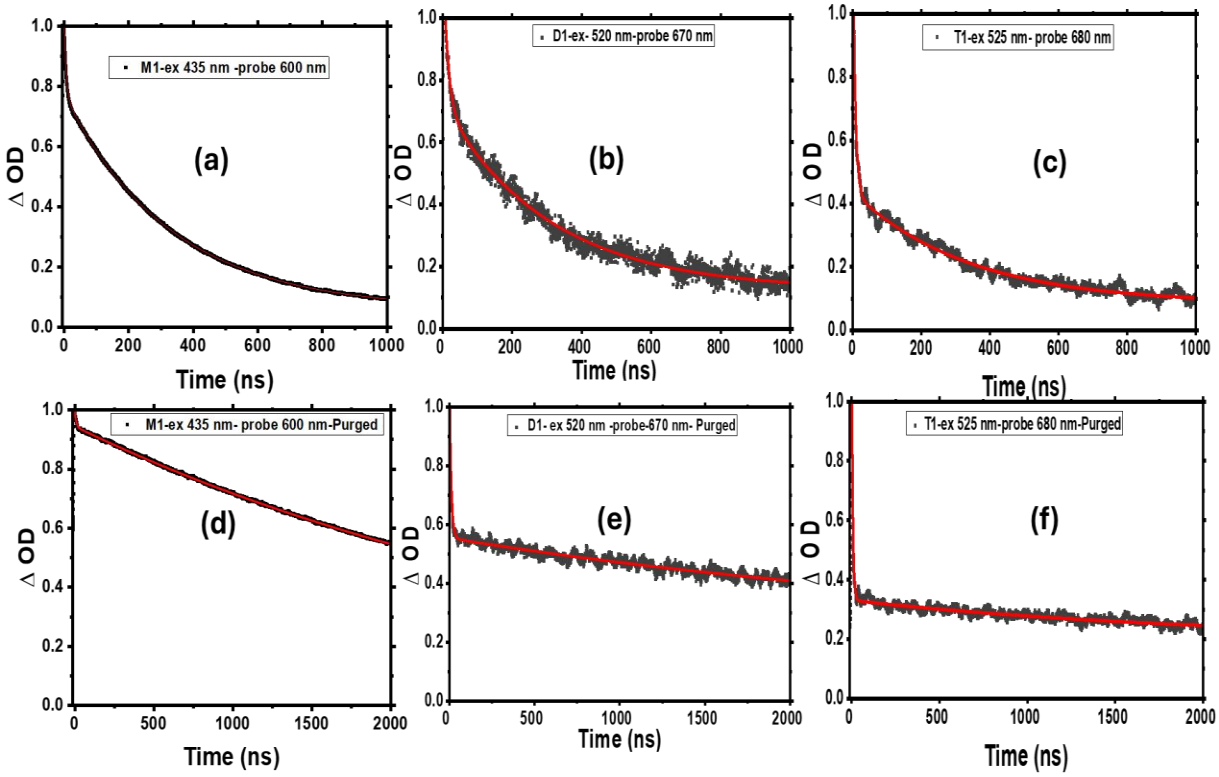


Figure 6.8: Transient absorption decay kinetic of the chromophores in chloroform: M1 probed at 600 nm (a) unpurged, (d) purged; D1 probed at 670 nm (b) unpurged (e) purged ; and T1 probed at 680 nm (c) unpurged and (f) purged

The calculated reverse K_{rISC} for the oligothiophene series increase with oligomer length. The monomer (M1) exhibits a K_{rISC} of 1.9 x 10^6 s^{-1}, the dimer (D1) 2.6 x 10^6 s^{-1}, and the trimer

(T1) 8.0 x 10^6 s^{-1} (**Table 6.4**). The trimer shows an approximately fourfold enhancement relative to the monomer, indicating more efficient triplet-to-singlet conversion. All three compounds display K_{rISC} values above 10^5 s^{-1}, within the range reported for efficient TADF-active chromophores, supporting their classification as TADF-capable materials.[73]

Table 6.4: Decay lifetimes and K_{rISC} of the chromophores

	ESA		**ESA Purged**		**Φ_{TADF} (%)**	**$k_{Triplet}$ (s^{-1}) Purged**	**k_{rISC} (s^{-1})**
	(τ_1) ns	**(τ_2) ns**	**(τ_1) ns**	**(τ_2) µs**			
M1	9.1	330	8.9	3.6	7	2.7 x10^5	1.9 x10^6
D1	13.1	325	10.1	3.5	9	2.9 x10^5	2.6 x10^6
T1	6.3	340	6.2	2.0	16	5.0 x10^5	8.0 x10^6

$k_{Triplet}$ = decay rate of the ESA purged ($1/\tau_2$), $\Phi_{TADF} = \Phi_{PF} - \Phi_F$ (see **Table 6.1**)

6.6. Discussion

The red-shift in the steady-state absorption and emission data indicating increased electronic coupling along the oligothiophene backbone. The large shift observed when moving from M1 to D1 reflects the strong coupling between adjacent thiophene units, which lowers the energy of the lowest singlet transition by allowing the excited-state charge density to extend beyond a single repeat unit. The broadening of the absorption bands observed in D1 and T1, relative to M1, is attributed to increased vibronic coupling and a higher density of accessible excited states arising from effective electronic interactions.

Experimentally, the D1 and the T1 shows similar steady state absorption and emission properties with absorption maxima at 520 nm and 526 nm, respectively (**Figure 6.1**). This similarity is

attributed to the localized nature of the lowest-energy $S_0 \rightarrow S_1$ transition, which primarily involves frontier orbitals confined to individual monomer units or small segments of the oligomer. Consequently, extending the conjugation from D1 to T1 produces only a modest bathochromic shift. Additionally, steady state experiments show that M1 displays high Φ_F, which increases moderately upon oxygen removal from the solution. In contrast, both D1 and T1 exhibit reduced Φ_F, but show notably larger enhancements when deoxygenated (Φ_{PF}). The increase in Φ_{PF} efficiency in oxygen-free environments strongly indicates the involvement of delayed fluorescence pathways and triplet states in the emissive mechanism.

The order-of-magnitude increase in the δ_{TPA} from monomer M1 to trimer T1 provides direct experimental evidence for significantly stronger electronic coupling in the fully fused oligomer. Our analysis reveals that this enhancement is governed by the strong coupling of key electronic transitions within a dominant $S_0 \rightarrow S_1 \rightarrow S_2$ pathway.

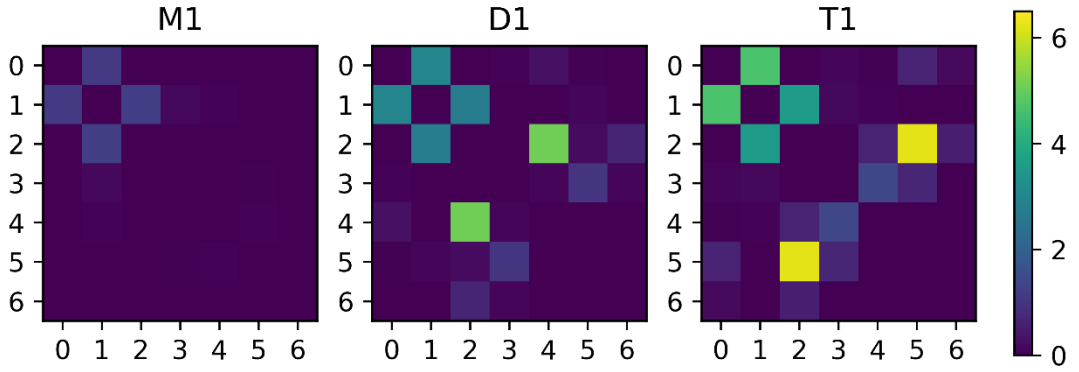


Figure 6.9. Excited-to-excited state transition matrices of Monomer Dimer and Trimer for the first 6 excited states. Each element in the matrix corresponds to the oscillator strength of the electronic transition

The δ_{TPA} for T1 was calculated to be 1450 GM, representing a 25-fold and 10-fold increase over M1 and D1, respectively, despite the nearly identical one-photon absorption maxima of D1

(520 nm) and T1 (525 nm). The δ_{TPA} scales with the square of the transition dipole moment, which is quantified by the oscillator strength.[60,65,79] The calculated oscillator strengths confirm this trend, increasing from 1.59, 3.64 and 5.28 for the M1, D1 and T1 respectively. The transition matrices (**Fig. 6.9**) show a clear increase in the oscillator strength of the $S_0 \rightarrow S_1$ transition and, more importantly, in the strength of the $S_1 \rightarrow S_2$ excited-state coupling. The dimer D1 exhibits a significant increase in both values compared to M1, but the trimer T1 shows the largest change. In T1, the $S_0 \rightarrow S_1$ transition is the most intense ($f_{0,1} = 5.28$), and the $S_1 \rightarrow S_2$ coupling is the strongest in the series ($f_{1,2} \approx 3.60$). This strong coupling in T1 is the key factor that enhances the probability of absorbing the second photon further contributing to the increased cross-section.

Interestingly, we observed a difference in the magnitude of the δ_{TPA} when we excited the molecules at their one-photon absorption maxima. The rate of the two-photon absorption process depends on the energy difference between the virtual intermediate state and a real excited-state. For D1 and T1, excitation at 800 nm results in a virtual state that is close in energy to the S_1 state This proximity allows the second photon absorption to be efficiently driven by the strong $S_1 \rightarrow S_2$ coupling, which is most pronounced in T1 ($f_{1,2} \approx 3.60$) resulting in the high δ_{TPA}. For the monomer M1, the same 800 nm excitation also brings its virtual state near the S_1 state, enhancing its δ_{TPA} relative to excitation at its one-photon maximum. Conversely, excitation at 1040 nm for D1 and T1, or at 880 nm for M1, corresponds to their respective one-photon maxima, the virtual state is farther from the S_1 energy, reducing the efficiency of the $S_1 \rightarrow S_2$ coupling pathway and leading to the lower measured δ_{TPA} values. The magnitude of δ_{TPA} is known to correlate with charge-transfer character, which is directly enhanced by the strong electronic coupling in the extended fused-core systems.[74–78] This significant enhancement arises from the extended

conjugation and rigid backbone of the three fused IDTT cores in T1, minimizing torsional disorder, and reduces inhomogeneous broadening. which enhances the resonant contribution to the two-photon absorption process.[80]

Additionally, while frontier molecular orbital analysis suggests a locally excited (LE) character for the excited state (**Figure 6.10)**, the dramatic enhancement of the δ_{TPA} cross-section in the trimer T1 provides critical, insight into its electronic structure. The magnitude of δ_{TPA} is a measure of charge-transfer (CT) character, as it scales with the change in dipole moment between the ground and excited states. The exceptionally high δ_{TPA} of T1, therefore, indicates that the excited state possesses significant CT contributions. This suggests evidence of a hybrid excited state with strong LE-CT mixing. This hybrid character, facilitated by strong electronic coupling across the fused cores, is likely a key factor enabling efficient spin-vibronic coupling with nearby triplet states for reverse intersystem crossing.[81–86]

Further insight into the excited state properties of the IDTT series was determined utilizing quantum entangled spectroscopic technique. Prior studies have demonstrated the triplet-selective nature of ETPA, wherein fac-Ir(ppy) photocatalysts exhibit predominant population of pure triplet states under entangled excitation conditions, contrasting with the mixed singlet-triplet population observed in classical TPA.[87,88] These findings imply that the ETPA mechanism offers more efficient direct population of triplet states. The σ_e of T1 determined to be 4.17 $x10^{-18}$ (cm^2/molecule) is about an order of magnitude higher than that of M1 (8.23 $x10^{-19}$ (cm^2/molecule)) consistent with stronger electronic coupling and more delocalized excited states. In T1, the S_1 state is strongly coupled to higher-lying triplet states, particularly T_3, via enhanced spin-orbit coupling (SOC ~ 0.8 cm^{-1}), which arises from increased CT character and π-delocalization. The σ_e of D1 is

significantly higher than M1 possibly due to the enhanced spin orbital mixing of the lowest singlet excited state with the higher triplet excited state (T_2). In addition, the σ_e has been determined to be dependent on the transition dipole moment and the detuning energy of the molecule.[54,68,89,90] This is consistent with the experimental observation for the IDTT based molecules. T1 with three thiophene subunits exhibits greater electronic coupling and enhanced f_{osc} correlating with the high σ_e compared to the M1. This reflects a more polarized and delocalized excited-state wavefunction in T1, arising from increased π-conjugation across the thiophene units. The charge redistribution enhances the polarizability and transition strength, both of which directly affect the entangled two-photon absorption response.

TD-DFT calculations provided detailed insight into the electronic structure the nature of the singlet and triplet energies of the M1, D1 and T1. Natural Transition Orbital (NTO) analysis confirms that the higher-lying triplet states are predominantly of locally exciton (^{3}LE) character with no significant change in the electron density in the Highest Occupied Natural Transition Orbital (HONTO) and Lowest Unoccupied Natural Transition Orbital (LUNTO).

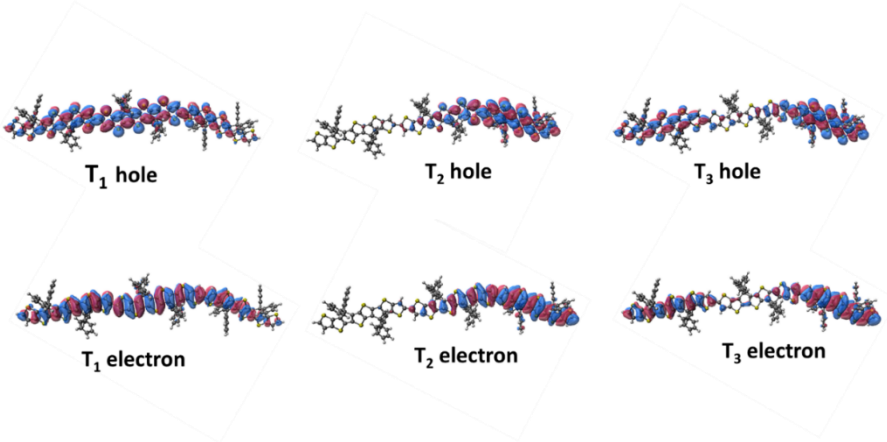


Figure 6.10: NTO for the triplet excited state of T1

The HONTO and LUNTO for the singlet and triplet excited state for M1 and D1 are shown in **Figure S5** and **Figure S7**. The NTO of the triplet excited state for the T1 is shown in **Figure 6.10 and Figure S8**. The calculated SOC matrix elements between the S_1 and various ^{3}LE triplet states (T_1, T_2, T_3) provide critical insight into the mechanisms underlying the enhanced TADF efficiency observed with increasing number of IDTT units. For M1, the dominant SOC is between S_1 and T_1, with a value of 0.80 cm^{-1}. This indicates these two states are strongly coupled, the high $S_1 \rightarrow T_1$ energy gap of 1.03 eV makes the TADF process relatively inefficient. In the D1, the SOC between the S_1 and T_1 decreases suggesting reduced coupling. However, the S_1 is strongly coupled to the T_2 with a SOC of 0.67 cm^{-1} as seen in the D1. Upon incorporating more IDTT core moieties via molecular engineering in T1, we observed significant redistribution of SOC contributions where the coupling between S_1 and T_1 drastically diminishes to 0.06 cm^{-1}, while the interaction with higher-lying triplet states increases, with S_1-T_3 coupling reaching 0.77 cm^{-1}. This change suggests that in T1, efficient rISC does not primarily proceed via the lowest triplet state (T_1) but rather through the ^{3}LE (T_3) state closest lying to S_1 (see **Figure 6.11**). The T_3 state acts as intermediate, facilitating SVC pathways that accelerate the upconversion of triplet excitons to the emissive singlet. This mechanism is consistent with the observed high Φ_{TADF} and rapid K_{rISC} in T1, highlighting the critical role of higher triplet states with strong SOC in promoting efficient TADF in extended IDTT-based molecular systems.

Table 6.5: Spin orbit coupling and transition states involved for M1, DI and T1

Transition States	M1 (SOC) cm^{-1}	D1(SOC) cm^{-1}	T1(SOC) cm^{-1}
$S_1 \rightarrow T_1$	0.80	0.12	0.06
$S_1 \rightarrow T_2$	0.001	0.67	0.23
$S_1 \rightarrow T_3$	0.005	0.10	0.77

Our nanosecond transient absorption (ns-TA) measurements directly quantify the triplet dynamics and thermally activated delayed fluorescence (TADF) that govern the K_{rISC}. The presence of delayed fluorescence, confirmed by the increase in photoluminescence quantum yield under nitrogen purging, provides clear evidence of an active TADF mechanism. This efficiency, however, varies dramatically across the series, revealing a structure-dependent activation pathway.

We utilized our ns-TA technique to demonstrate the role of the triplet excited state and Φ_{TADF} in enhancing the K_{rISC}. The presence of delayed fluorescence as detemined from the purged fluorescence quantum yield suggests evidences of TADF mechanisms. M1 exhibits the lowest Φ_{TADF} of 7 % demonstrating minimal involvement of the triplet excited state contributing to the overall radiative process. Under nitrogen purged conditions, the triplet lifetime (τ_2) for M1 was determined to be 3.6 µs with $k_{triplet}$ of 2.7 x10^5 s^{-1}. The calculated K_{rISC} of M1 was found to be 1.9 x10^6 s^{-1} which is lower compared to that of D1 and T1 (**Table 6.4**). This is attributed to the large S_1-T_1 energy gap (ΔE_{ST}) of 1.09 eV in M1, which poses a thermodynamic barrier for efficient thermal activation of K_{rISC} (**Figure 6.11**). As seen from **Table 6.5**, the S_1 has a low SOC of 0.001 cm^{-1} with the closest lying ^{3}LE state (T_2). The energy gap between the S_1 and T_2 is about 0.29 eV. This low SOC between the S_1 and T_2 in M1 contributes to the low K_{rISC}. The strong SOC (0.80 cm^{-}

[1]) between S_1 and T_1 orbitals and the large ΔE_{ST}, as revealed by TD-DFT calculation, further confirm the limiting TADF properties in M1.

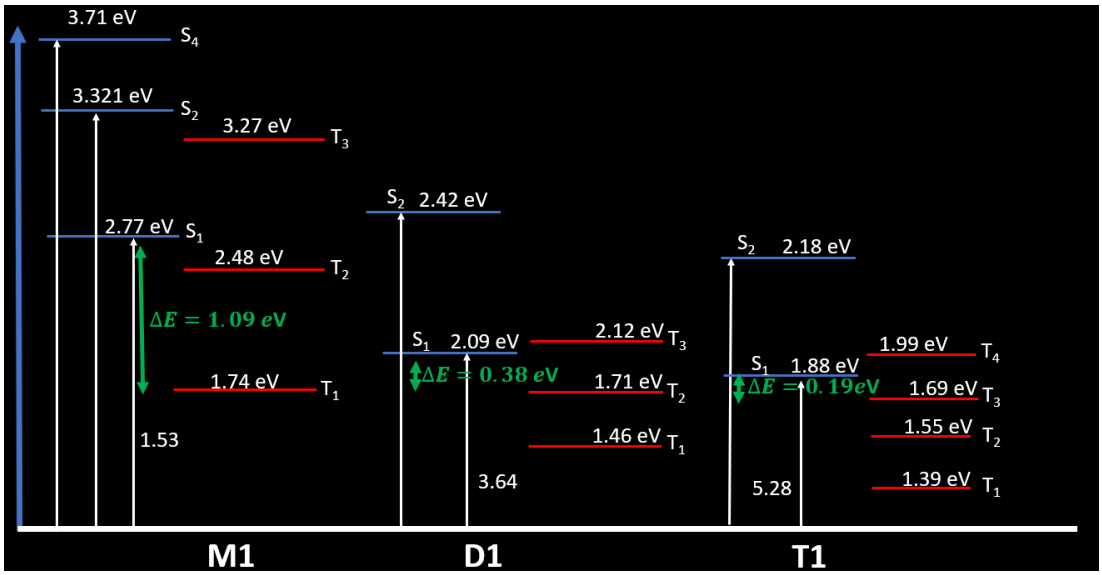


Figure 6.11: Excited state energies as obtained from the TD-DFT calculations of M1, D1 and T1.

In contrast, D1 showed significant difference compared to M1. The τ_2 was measured to be 3.5 µs, with a $k_{triplet}$ of 2.7 x10^5 s^{-1}. The Φ_{TADF} yield increased slightly to 9 %, resulting in a K_{rISC} of 2.6 x10^6 s^{-1}, which is a 1.2-fold enhancement relative to M1. Although, the energy gap between the S_1 and T_1 is relatively larger (0.63 ev), there is less SOC of 0.12 cm^{-1} between these two states. This enhancement in the K_{rISC} of D1 relative to the M1 is attributed to a reduced ΔE_{ST} of 0.38 eV between S_1 and T_2, arising from increased delocalization and more effective spin-orbit mixing. The calculated SOC between S_1 and T_2 is 0.66 cm^{-1}. The small energy gap between the T_1 and T_2 of 0.25 eV, contributes to enhance SVC between these two states which enhances the K_{rISC} comparatively to the M1. The accessible (^{3}LE) T_2 states, coupled with stronger SOC provides a more favorable thermodynamic and orbital environment for triplet-to-singlet conversion. The T1

exhibited the most efficient triplet dynamics among the series. The triplet lifetime was shortened to 2.0 μs with a higher $k_{triplet}$ of 5.0 x10^5 s^{-1}, accompanied by a substantial increase in Φ_{TADF} determined to be 16 %. This translated to a high K_{rISC} of 8.0 x10^6 s^{-1}, representing a 3.5-fold increase over M1. The enhanced performance in T1 is rationalized by a smaller energy separation ΔE_{ST} (0.19 eV) between S_1 and the strongly coupled (^{3}LE) T_3 state. Incorporating three thiophene monomeric units in the T1 reduces the energy of higher lying triplet excited state (T_3), which strongly coupled to the S_1 with a SOC magnitude of approximately 0.8 cm^{-1} as seen in **Figure 6.11**. The resulting increase in SOC and triplet state density with multiple low lying ^{3}LE states lowers the activation barrier for upconversion, enabling more efficient harvesting of triplet excitons into emissive singlets. Vásquez and co-workers established that typical TADF materials posseses $K_{rISC} \geq 10^5$ s^{-1} consistent with high external quantum efficiency (EQE) in devices.[59] The T1 possesses K_{rISC} comparable to typical TADF chromophores providing evidence of its efficient delayed fluorescence properties.

Analysis of the fs-TA data reveals a dramatically enhanced intersystem crossing (ISC) rate in the trimer, which directly supports the observation of efficient reverse intersystem crossing (RISC) in the ns-TA experiment. The fs-TA dynamics exhibit a long-lived component persisting beyond the nanosecond timescale, which we definitively attribute to the formation of a triplet excited state. Critically, the ISC rate is nearly 3 times faster for the trimer (1/327 ps^{-1}) relative to the monomer (1/1010 ps^{-1}), indicating a highly efficient spin-flipping process into the triplet states. This accelerated forward ISC is a key prerequisite for the observed high RISC rate, as both processes are governed by the same underlying electronic coupling. The trend is consistent with computational calculations indicating an increase in spin-orbit coupling and a reduction in the

energy gap (ΔE_{ST}) between the singlet and triplet states. Consequently, the rapid population of the triplet state via enhanced forward ISC establishes a substantial triplet reservoir, enabling the thermally activated RISC back to the singlet state that is central to the trimer's delayed emission properties.

A deeper mechanistic understanding of the reverse intersystem crossing (RISC) process in the IDTT-based emitters emerges from consideration of the higher-lying triplet states. In addition to the lowest triplet (T_1), the T_2 and T_3 states play a critical role as intermediate states that mediate the upconversion pathway to the emissive S_1 state.[91] When the energetic separation between T_1 and T_2 is sufficiently small (~0.2 - 0.3 eV), efficient internal equilibration among the triplet states becomes possible. Recent theoretical and experimental studies have shown that such near-degeneracy of the triplet states strongly favors a spin-vibronic coupling mechanism, wherein SOC and non-adiabatic coupling act cooperatively to enhance intersystem crossing rates. In this case, the presence of energetically accessible T_2/T_3 states provides additional bridging channels for RISC, thereby lowering the activation barrier for upconversion to S_1. The effect is particularly pronounced in molecular systems where the lowest singlet state exhibits significant charge-transfer character, as this facilitates SOC-driven mixing with the higher-lying triplets that retain more localized (LE) character.[92]

To understand the trend in reverse intersystem crossing rates, we investigated the coupling within the triplet manifold using TDA-TDDFT calculations. In the monomer M1, weak coupling between T_1 and T_2 (0.005 cm^{-1}) alongside a large S_1-T_1 energy gap and minimal S_1-T_2 SOC results in a low K_{rISC}. Conversely, in the dimer D1, we observe strong intramolecular coupling between the triplet states, particularly $T_1 \rightarrow T_2$ (2.11 cm^{-1}) and $T_2 \rightarrow T_3$ (2.38 cm^{-1}). This strong

triplet coupling pathway, combined with significant SOC between S_1 and T_2 (0.67 cm^{-1}), facilitates a faster K_{rISC}. The most significant enhancement occurs in the trimer T1. Here, the SOC between S_1 and T_3 is the strongest in the series (0.77 cm^{-1}). Furthermore, the triplet states are strongly coupled, with major contributions from $T_1 \rightarrow T_2$ (2.20 cm^{-1}) and $T_2 \rightarrow T_3$ (1.15 cm^{-1}). This combination of robust S_1- T_3 SOC and a well-coupled triplet manifold creates the most efficient pathway for reverse intersystem crossing, leading to the highest measured K_{rISC}.

The enhancement in the K_{rISC} observed in T1 relative to M1 highlights the impact of SOC in facilitating more efficient triplet-to-singlet upconversion. Prior work by França et al. demonstrated that efficient TADF in spiro-linked acridine anthracenone molecular sysytem arises from coupling between a localized triplet (^{3}LE) state and charge-transfer (^{1}CT/^{3}CT) states mediated by a small ΔE_{ST} and favorable SOC.[93] Our experimental data reveal a similar mechanistic pathway in T1. Specifically, our SOC calculations show that direct $S_1 \rightarrow T_1$ coupling is minimal (0.06 cm^{-1}) with $\Delta E_{S1\text{-}T1}$ of 0.49 eV, while the coupling of $S_1 \rightarrow T_3$ increases to 0.77 cm^{-1} with $\Delta E_{S1\text{-}T3}$ of 0.19 eV, indicating that the high K_{rISC} in T1 is not dominated by the lowest triplet but is instead mediated by a higher-lying triplet state with partial LE character. Furthermore, previous studies on donor-acceptor-type TADF emitters, such as TPCzTPA and TPCz2NP, have highlighted the critical role of orbital separation and charge-transfer character in modulating ΔE_{ST} and facilitating efficient reverse intersystem crossing (rISC). In these systems, the HOMO was localized on electron-rich donor units, while the LUMO extended across the acceptor framework (TPN), resulting in partial spatial separation. Our NTO analysis revealed the presence of multiple low-lying ^{3}LE state with enhanced SOC between S_1. Particularly, SOC values between S_1 and T_3 were calculated to be significantly higher than those between S_1 and T_1 confirming the

involvement of higher-lying triplet states as key contributors to TADF.[94] This effect of the ^{3}LE as an efficient intermediate state in enhancing the rISC is supported by experimental data as seen in the case of D1 and T1 in comparison to M1. Additionally, the higher density of energetically accessible triplet states in T1, arising from increased conjugation and electronic coupling, enhances the probability of finding near-resonant T_n levels with favorable orbital overlap and symmetry with S_1. The evidence of high K_{rISC} determined by the ns-TA method is consistent with the high δ_{TPA} and σ_e obtained for the T1. This is indicative of high CT and enhance intersystem crossing to the triplet state facilitated by the heavy atom effect of the IDTT repeating units in T1. Our experimental data suggest that the K_{rISC} process is mediated not solely by proximity in energy levels, but by the nature of the triplet states involved as shown in T1. By fine-tuning conjugation length, electronic delocalization, and spin-state interactions, chromophores such as T1 can be developed as functional building blocks for next-generation TADF emitters and nonlinear optical materials.

6.7. Conclusion

Our work establishes a clear design strategy for increasing electronic coupling and K_{rISC} via molecular engineering. The Trimmer exhibits about a 25 -fold increase in the TPA cross-section relative to the momomeric unit indicating significant enhancement in the CT properties. This increase in CT strength is directly correlated with greater electronic delocalization and stronger electronic coupling, both of which are known to facilitate rISC by reducing energy mismatches and enhancing state mixing. Consistent with this, our time-resolved spectroscopic results reveal significant enhancements in both KrISC and ΦTADF as the number of core indacenodithieno[3,2-b]thiophene units is synthetically increased from M1 to T1. In particular, T1 exhibits the highest

TADF efficiency, which we attribute to the cooperative effects of enhanced CT, stronger coupling between the emissive singlet state and multiple locally excited triplet (^{3}LE) states, and improved orbital overlap. Importantly, TD-DFT calculations confirm that efficient rISC in T1 does not proceed through direct S_1 - T_1 coupling but instead involves the higher-lying T_3 state, which lies in close energetic proximity to S_1. The strong SOC between S_1 and T_3, combined with the CT-induced vibronic mixing, leads to the observed acceleration of K_{rISC}. This work provides new mechanistic insight and design principles for developing high-performance TADF materials for OLEDs, organic lasers, and emerging quantum optoelectronic technologies.

References

(1) Diesing, S.; Zhang, L.; Zysman-Colman, E.; Samuel, I. D. W. A Figure of Merit for Efficiency Roll-off in TADF-Based Organic LEDs. *Nature* **2024**, *627* (8005), 747–753. https://doi.org/10.1038/s41586-024-07149-x.

(2) Liu, Y.; Li, C.; Ren, Z.; Yan, S.; Bryce, M. R. All-Organic Thermally Activated Delayed Fluorescence Materials for Organic Light-Emitting Diodes. *Nat. Rev. Mater.* **2018**, *3* (4), 1–20. https://doi.org/10.1038/natrevmats.2018.20.

(3) Jeon, S. O.; Lee, K. H.; Kim, J. S.; Ihn, S.-G.; Chung, Y. S.; Kim, J. W.; Lee, H.; Kim, S.; Choi, H.; Lee, J. Y. High-Efficiency, Long-Lifetime Deep-Blue Organic Light-Emitting Diodes. *Nat. Photonics* **2021**, *15* (3), 208–215. https://doi.org/10.1038/s41566-021-00763-5.

(4) Chen, X.-K.; Kim, D.; Brédas, J.-L. Thermally Activated Delayed Fluorescence (TADF) Path toward Efficient Electroluminescence in Purely Organic Materials: Molecular Level Insight. *Acc. Chem. Res.* **2018**, *51* (9), 2215–2224. https://doi.org/10.1021/acs.accounts.8b00174.

(5) Wu, X.; Su, B.-K.; Chen, D.-G.; Liu, D.; Wu, C.-C.; Huang, Z.-X.; Lin, T.-C.; Wu, C.-H.; Zhu, M.; Li, E. Y.; Hung, W.-Y.; Zhu, W.; Chou, P.-T. The Role of Host–Guest Interactions in Organic Emitters Employing MR-TADF. *Nat. Photonics* **2021**, *15* (10), 780–786. https://doi.org/10.1038/s41566-021-00870-3.

(6) Zhao, Z.; Yan, S.; Ren, Z. Regulating the Nature of Triplet Excited States of Thermally Activated Delayed Fluorescence Emitters. *Acc. Chem. Res.* **2023**, *56* (14), 1942–1952. https://doi.org/10.1021/acs.accounts.3c00175.

(7) Hu, Y. X.; Miao, J.; Hua, T.; Huang, Z.; Qi, Y.; Zou, Y.; Qiu, Y.; Xia, H.; Liu, H.; Cao, X.; Yang, C. Efficient Selenium-Integrated TADF OLEDs with Reduced Roll-Off. *Nat. Photonics* **2022**, *16* (11), 803–810. https://doi.org/10.1038/s41566-022-01083-y.

(8) Cui, L.-S.; Gillett, A. J.; Zhang, S.-F.; Ye, H.; Liu, Y.; Chen, X.-K.; Lin, Z.-S.; Evans, E. W.; Myers, W. K.; Ronson, T. K.; Nakanotani, H.; Reineke, S.; Bredas, J.-L.; Adachi, C.; Friend, R. H. Fast Spin-Flip Enables Efficient and Stable Organic Electroluminescence from Charge-Transfer States. *Nat. Photonics* **2020**, *14* (10), 636–642. https://doi.org/10.1038/s41566-020-0668-z.

(9) Einzinger, M.; Zhu, T.; de Silva, P.; Belger, C.; Swager, T. M.; Van Voorhis, T.; Baldo, M. A. Shorter Exciton Lifetimes via an External Heavy-Atom Effect: Alleviating the Effects of Bimolecular Processes in Organic Light-Emitting Diodes. *Adv. Mater.* **2017**, *29* (40), 1701987. https://doi.org/10.1002/adma.201701987.

(10) Reineke, S.; Schwartz, G.; Walzer, K.; Leo, K. Reduced Efficiency Roll-off in Phosphorescent Organic Light Emitting Diodes by Suppression of Triplet-Triplet Annihilation. *Appl. Phys. Lett.* **2007**, *91* (12), 123508. https://doi.org/10.1063/1.2786840.

(11) Lee, J.; Jeong, C.; Batagoda, T.; Coburn, C.; Thompson, M. E.; Forrest, S. R. Hot Excited State Management for Long-Lived Blue Phosphorescent Organic Light-Emitting Diodes. *Nat. Commun.* **2017**, *8* (1), 15566. https://doi.org/10.1038/ncomms15566.

(12) Franca, L. G.; Long, Y.; Li, C.; Danos, A.; Monkman, A. The Critical Role of Nπ* States in the Photophysics and Thermally Activated Delayed Fluorescence of Spiro Acridine-Anthracenone. *J. Phys. Chem. Lett.* **2021**, *12* (5), 1490–1500. https://doi.org/10.1021/acs.jpclett.0c03314.

(13) Goswami, S.; Gish, M. K.; Wang, J.; Winkel, R. W.; Papanikolas, J. M.; Schanze, K. S. π-Conjugated Organometallic Isoindigo Oligomer and Polymer Chromophores: Singlet and Triplet Excited State Dynamics and Application in Polymer Solar Cells. *ACS Appl. Mater. Interfaces* **2015**, *7* (48), 26828–26838. https://doi.org/10.1021/acsami.5b09041.

(14) Fang, F.; Zhu, L.; Li, M.; Song, Y.; Sun, M.; Zhao, D.; Zhang, J. Thermally Activated Delayed Fluorescence Material: An Emerging Class of Metal-Free Luminophores for Biomedical Applications. *Adv. Sci.* **2021**, *8* (24), 2102970. https://doi.org/10.1002/advs.202102970.

(15) Hirata, S.; Sakai, Y.; Masui, K.; Tanaka, H.; Lee, S. Y.; Nomura, H.; Nakamura, N.; Yasumatsu, M.; Nakanotani, H.; Zhang, Q.; Shizu, K.; Miyazaki, H.; Adachi, C. Highly Efficient Blue Electroluminescence Based on Thermally Activated Delayed Fluorescence. *Nat. Mater.* **2015**, *14* (3), 330–336. https://doi.org/10.1038/nmat4154.

(16) Xie, Y.; Li, Z. Thermally Activated Delayed Fluorescent Polymers. *J. Polym. Sci. Part Polym. Chem.* **2017**, *55* (4), 575–584. https://doi.org/10.1002/pola.28448.

(17) Hosokai, T.; Matsuzaki, H.; Nakanotani, H.; Tokumaru, K.; Tsutsui, T.; Furube, A.; Nasu, K.; Nomura, H.; Yahiro, M.; Adachi, C. Evidence and Mechanism of Efficient Thermally Activated Delayed Fluorescence Promoted by Delocalized Excited States. *Sci. Adv.* **2017**, *3* (5), e1603282. https://doi.org/10.1126/sciadv.1603282.

(18) S. Nobuyasu, R.; S. Ward, J.; Gibson, J.; A. Laidlaw, B.; Ren, Z.; Data, P.; S. Batsanov, A.; J. Penfold, T.; R. Bryce, M.; B. Dias, F. The Influence of Molecular Geometry on the Efficiency of Thermally Activated Delayed Fluorescence. *J. Mater. Chem. C* **2019**, *7* (22), 6672–6684. https://doi.org/10.1039/C9TC00720B.

(19) Balijapalli, U.; Nagata, R.; Yamada, N.; Nakanotani, H.; Tanaka, M.; D'Aléo, A.; Placide, V.; Mamada, M.; Tsuchiya, Y.; Adachi, C. Highly Efficient Near-Infrared Electrofluorescence from a Thermally Activated Delayed Fluorescence Molecule. *Angew. Chem. Int. Ed.* **2021**, *60* (15), 8477–8482. https://doi.org/10.1002/anie.202016089.

(20) Nobuyasu, R. S.; Ren, Z.; Griffiths, G. C.; Batsanov, A. S.; Data, P.; Yan, S.; Monkman, A. P.; Bryce, M. R.; Dias, F. B. Rational Design of TADF Polymers Using a Donor–Acceptor

Monomer with Enhanced TADF Efficiency Induced by the Energy Alignment of Charge Transfer and Local Triplet Excited States. *Adv. Opt. Mater.* **2016**, *4* (4), 597–607. https://doi.org/10.1002/adom.201500689.

(21) P, K. P. C.; Rayappa Naveen, K.; Hur, J. Acceptor–Donor–Acceptor Based Thermally Activated Delayed Fluorescent Materials: Structure–Property Insights and Electroluminescence Performances. *Mater. Chem. Front.* **2024**, *8* (3), 769–784. https://doi.org/10.1039/D3QM01125A.

(22) Karthik, D.; Jung, Y. H.; Lee, H.; Hwang, S.; Seo, B.-M.; Kim, J.-Y.; Han, C. W.; Kwon, J. H. Acceptor–Donor–Acceptor-Type Orange–Red Thermally Activated Delayed Fluorescence Materials Realizing External Quantum Efficiency Over 30% with Low Efficiency Roll-Off. *Adv. Mater.* **2021**, *33* (18), 2007724. https://doi.org/10.1002/adma.202007724.

(23) Wex, B.; R. Kaafarani, B. Perspective on Carbazole-Based Organic Compounds as Emitters and Hosts in TADF Applications. *J. Mater. Chem. C* **2017**, *5* (34), 8622–8653. https://doi.org/10.1039/C7TC02156A.

(24) Aydemir, M.; Xu, S.; Chen, C.; Bryce, M. R.; Chi, Z.; Monkman, A. P. Photophysics of an Asymmetric Donor–Acceptor–Donor′ TADF Molecule and Reinterpretation of Aggregation-Induced TADF Emission in These Materials. *J. Phys. Chem. C* **2017**, *121* (33), 17764–17772. https://doi.org/10.1021/acs.jpcc.7b06299.

(25) Jia, J.-H.; Liang, D.; Yu, R.; Chen, X.-L.; Meng, L.; Chang, J.-F.; Liao, J.-Z.; Yang, M.; Li, X.-N.; Lu, C.-Z. Coordination-Induced Thermally Activated Delayed Fluorescence: From Non-TADF Donor–Acceptor-Type Ligand to TADF-Active Ag-Based Complexes. *Chem. Mater.* **2020**, *32* (1), 620–629. https://doi.org/10.1021/acs.chemmater.9b04585.

(26) Wu, X.; Ni, S.; Wang, C.-H.; Zhu, W.; Chou, P.-T. Comprehensive Review on the Structural Diversity and Versatility of Multi-Resonance Fluorescence Emitters: Advance, Challenges, and Prospects toward OLEDs. *Chem. Rev.* **2025**, *125* (14), 6685–6752. https://doi.org/10.1021/acs.chemrev.5c00021.

(27) Naveen, K. R.; Oh, J. H.; Lee, H. S.; Kwon, J. H. Tailoring Extremely Narrow FWHM in Hypsochromic and Bathochromic Shift of Polycyclo-Heteraborin MR-TADF Materials for High-Performance OLEDs. *Angew. Chem.* **2023**, *135* (32), e202306768. https://doi.org/10.1002/ange.202306768.

(28) Wu, S.; Zhang, L.; Wang, J.; Kumar Gupta, A.; Samuel, I. D. W.; Zysman-Colman, E. Merging Boron and Carbonyl Based MR-TADF Emitter Designs to Achieve High Performance Pure Blue OLEDs. *Angew. Chem.* **2023**, *135* (28), e202305182. https://doi.org/10.1002/ange.202305182.

(29) Jin, P.; Wei, X.; Yin, B.; Xu, L.; Guo, Y.; Zhang, C. Stepwise Charge/Energy Transfer in MR-TADF Molecule-Doped Exciplex for Ultralong Persistent Luminescence Activated with Visible Light. *Adv. Mater.* **2024**, *36* (30), 2400158. https://doi.org/10.1002/adma.202400158.

(30) Wang, X.-Z.; Xing, S.; Xiao, X.; Yuan, L.; Hou, Z.-Y.; Zheng, Y.-X. Axial Chiral Biphenyl MR-TADF Enantiomers for Efficient Narrowband Circularly Polarized Electroluminescence. *Adv. Funct. Mater.* **2025**, *35* (1), 2412044. https://doi.org/10.1002/adfm.202412044.

(31) Etherington, M. K.; Gibson, J.; Higginbotham, H. F.; Penfold, T. J.; Monkman, A. P. Revealing the Spin–Vibronic Coupling Mechanism of Thermally Activated Delayed Fluorescence. *Nat. Commun.* **2016**, *7* (1), 13680. https://doi.org/10.1038/ncomms13680.

(32) Gibson, J.; Monkman, A. P.; Penfold, T. J. The Importance of Vibronic Coupling for Efficient Reverse Intersystem Crossing in Thermally Activated Delayed Fluorescence Molecules. *ChemPhysChem* **2016**, *17* (19), 2956–2961. https://doi.org/10.1002/cphc.201600662.

(33) Penfold, T. J.; Gindensperger, E.; Daniel, C.; Marian, C. M. Spin-Vibronic Mechanism for Intersystem Crossing. *Chem. Rev.* **2018**, *118* (15), 6975–7025. https://doi.org/10.1021/acs.chemrev.7b00617.

(34) Keruckiene, R.; A. Vaitusionak, A.; I. Hulnik, M.; A. Berezianko, I.; Gudeika, D.; Macionis, S.; Mahmoudi, M.; Volyniuk, D.; Valverde, D.; Olivier, Y.; Lin Woon, K.; V. Kostjuk, S.; Reineke, S.; V. Grazulevicius, J.; Sini, G. Is a Small Singlet–Triplet Energy Gap a Guarantee of TADF Performance in MR-TADF Compounds? Impact of the Triplet Manifold Energy Splitting. *J. Mater. Chem. C* **2024**, *12* (10), 3450–3464. https://doi.org/10.1039/D3TC04397E.

(35) Lv, L.; Yuan, K.; Zhao, T.; Dai, G. Intrinsic Analysis of Thermally Activated Delayed Fluorescence (TADF) for Ag(I) Complex Based on the Path Integral Approach: Origin of the Effective Spin-Flipping Channel and Vibrational Spin-Orbit Coupling Effect. *J. Phys. Chem. A* **2022**, *126* (38), 6695–6709. https://doi.org/10.1021/acs.jpca.2c05209.

(36) Dos Santos, J. M.; Hall, D.; Basumatary, B.; Bryden, M.; Chen, D.; Choudhary, P.; Comerford, T.; Crovini, E.; Danos, A.; De, J.; Diesing, S.; Fatahi, M.; Griffin, M.; Gupta, A. K.; Hafeez, H.; Hämmerling, L.; Hanover, E.; Haug, J.; Heil, T.; Karthik, D.; Kumar, S.; Lee, O.; Li, H.; Lucas, F.; Mackenzie, C. F. R.; Mariko, A.; Matulaitis, T.; Millward, F.; Olivier, Y.; Qi, Q.; Samuel, I. D. W.; Sharma, N.; Si, C.; Spierling, L.; Sudhakar, P.; Sun, D.; Tankelevičiūtė, E.; Duarte Tonet, M.; Wang, J.; Wang, T.; Wu, S.; Xu, Y.; Zhang, L.; Zysman-Colman, E. The Golden Age of Thermally Activated Delayed Fluorescence Materials: Design

and Exploitation. *Chem. Rev.* **2024**, *124* (24), 13736–14110. https://doi.org/10.1021/acs.chemrev.3c00755.

(37) Cheon, H.-J.; Woo, S.-J.; Baek, S.-H.; Lee, J.-H.; Kim, Y.-H. Dense Local Triplet States and Steric Shielding of a Multi-Resonance TADF Emitter Enable High-Performance Deep-Blue OLEDs. *Adv. Mater.* **2022**, *34* (50), 2207416. https://doi.org/10.1002/adma.202207416.

(38) Stavrou, K.; Danos, A.; Hama, T.; Hatakeyama, T.; Monkman, A. Hot Vibrational States in a High-Performance Multiple Resonance Emitter and the Effect of Excimer Quenching on Organic Light-Emitting Diodes. *ACS Appl. Mater. Interfaces* **2021**, *13* (7), 8643–8655. https://doi.org/10.1021/acsami.0c20619.

(39) Zhang, Y.; Wei, J.; Zhang, D.; Yin, C.; Li, G.; Liu, Z.; Jia, X.; Qiao, J.; Duan, L. Sterically Wrapped Multiple Resonance Fluorophors for Suppression of Concentration Quenching and Spectrum Broadening. *Angew. Chem. Int. Ed.* **2022**, *61* (2), e202113206. https://doi.org/10.1002/anie.202113206.

(40) Braveenth, R.; Lee, H.; Park, J. D.; Yang, K. J.; Hwang, S. J.; Naveen, K. R.; Lampande, R.; Kwon, J. H. Achieving Narrow FWHM and High EQE Over 38% in Blue OLEDs Using Rigid Heteroatom-Based Deep Blue TADF Sensitized Host. *Adv. Funct. Mater.* **2021**, *31* (47), 2105805. https://doi.org/10.1002/adfm.202105805.

(41) Cheon, H.-J.; Woo, S.-J.; Baek, S.-H.; Lee, J.-H.; Kim, Y.-H. Dense Local Triplet States and Steric Shielding of a Multi-Resonance TADF Emitter Enable High-Performance Deep-Blue OLEDs. *Adv. Mater.* **2022**, *34* (50), 2207416. https://doi.org/10.1002/adma.202207416.

(42) Dance, Z. E. X.; Mickley, S. M.; Wilson, T. M.; Ricks, A. B.; Scott, A. M.; Ratner, M. A.; Wasielewski, M. R. Intersystem Crossing Mediated by Photoinduced Intramolecular Charge

Transfer: Julolidine−Anthracene Molecules with Perpendicular π Systems. *J. Phys. Chem. A* **2008**, *112* (18), 4194–4201. https://doi.org/10.1021/jp800561g.

(43) dos Santos, P. L.; Dias, F. B.; Monkman, A. P. Investigation of the Mechanisms Giving Rise to TADF in Exciplex States. *J. Phys. Chem. C* **2016**, *120* (32), 18259–18267. https://doi.org/10.1021/acs.jpcc.6b05198.

(44) Lim, B. T.; Okajima, S.; Chandra, A. K.; Lim, E. C. Radiationless Transitions in Electron Donor-Acceptor Complexes: Selection Rules for S1 → T Intersystem Crossing and Efficiency of S1 → S0 Internal Conversion. *Chem. Phys. Lett.* **1981**, *79* (1), 22–27. https://doi.org/10.1016/0009-2614(81)85280-3.

(45) Marian, C. M. Mechanism of the Triplet-to-Singlet Upconversion in the Assistant Dopant ACRXTN. *J. Phys. Chem. C* **2016**, *120* (7), 3715–3721. https://doi.org/10.1021/acs.jpcc.6b00060.

(46) Santos, P. L.; Ward, J. S.; Data, P.; Batsanov, A. S.; Bryce, M. R.; Dias, F. B.; Monkman, A. P. Engineering the Singlet–Triplet Energy Splitting in a TADF Molecule. *J. Mater. Chem. C* **2016**, *4* (17), 3815–3824. https://doi.org/10.1039/C5TC03849A.

(47) Data, P.; Pander, P.; Okazaki, M.; Takeda, Y.; Minakata, S.; Monkman, A. P. Dibenzo[a,j]Phenazine-Cored Donor–Acceptor–Donor Compounds as Green-to-Red/NIR Thermally Activated Delayed Fluorescence Organic Light Emitters. *Angew. Chem. Int. Ed.* **2016**, *55* (19), 5739–5744. https://doi.org/10.1002/anie.201600113.

(48) Franca, L. G.; Long, Y.; Li, C.; Danos, A.; Monkman, A. The Critical Role of Nπ* States in the Photophysics and Thermally Activated Delayed Fluorescence of Spiro Acridine-Anthracenone. *J. Phys. Chem. Lett.* **2021**, *12* (5), 1490–1500. https://doi.org/10.1021/acs.jpclett.0c03314.

(49) Williams, A. T. R.; Winfield, S. A.; Miller, J. N. Relative Fluorescence Quantum Yields Using a Computer-Controlled Luminescence Spectrometer. *The Analyst* **1983**, *108* (1290), 1067. https://doi.org/10.1039/an9830801067.

(50) Fisher, L. Jr.; Vázquez, R. J.; Howell, M.; Muthike, A. K.; Orr, M. E.; Jiang, H.; Dodgen, B.; Lee, D. R.; Lee, J. Y.; Zimmerman, P.; Goodson, T. I. Investigation of Thermally Activated Delayed Fluorescence in Donor–Acceptor Organic Emitters with Time-Resolved Absorption Spectroscopy. *Chem. Mater.* **2022**, *34* (5), 2161–2175. https://doi.org/10.1021/acs.chemmater.1c03668.

(51) Cai, Z.; Vázquez, R. J.; Zhao, D.; Li, L.; Lo, W.; Zhang, N.; Wu, Q.; Keller, B.; Eshun, A.; Abeyasinghe, N.; Banaszak-Holl, H.; Goodson, T. I.; Yu, L. Two Photon Absorption Study of Low-Bandgap, Fully Conjugated Perylene Diimide-Thienoacene-Perylene Diimide Ladder-Type Molecules. *Chem. Mater.* **2017**, *29* (16), 6726–6732. https://doi.org/10.1021/acs.chemmater.7b01512.

(52) Villabona-Monsalve, J. P.; Tcyrulnikov, N. A.; Lorenzo, E. R.; LaBine, N.; Burdick, R.; Krzyaniak, M. D.; Young, R. M.; Wasielewski, M. R.; Goodson, T. Two-Photon Absorption in Electron Donor–Acceptor Dyads and Triads Using Classical and Entangled Photons: Potential Systems for Photon-to-Spin Quantum Transduction. *J. Phys. Chem. C* **2022**, *126* (14), 6334–6343. https://doi.org/10.1021/acs.jpcc.2c00830.

(53) Jovanovski, S. D.; Sandoval, J. S.; Goodson, S.; Mishra, A.; Ince, M.; Martínez-Díaz, M. V.; Torres, T.; Goodson, T. I. The Effect of Symmetry Breaking on the Nonlinear and Quantum Optical Properties of Novel Zinc Phthalocyanine Dendrimer Systems. *J. Phys. Chem. A* **2025**, *129* (41), 9568–9582. https://doi.org/10.1021/acs.jpca.5c05870.

(54) Villabona-Monsalve, J. P.; Burdick, R. K.; Goodson, T. I. Measurements of Entangled Two-Photon Absorption in Organic Molecules with CW-Pumped Type-I Spontaneous Parametric Down-Conversion. *J. Phys. Chem. C* **2020**, *124* (44), 24526–24532. https://doi.org/10.1021/acs.jpcc.0c08678.

(55) Villabona-Monsalve, J. P.; Varnavski, O.; Palfey, B. A.; Goodson, T. I. Two-Photon Excitation of Flavins and Flavoproteins with Classical and Quantum Light. *J. Am. Chem. Soc.* **2018**, *140* (44), 14562–14566. https://doi.org/10.1021/jacs.8b08515.

(56) Li, T.; Dai, S.; Ke, Z.; Yang, L.; Wang, J.; Yan, C.; Ma, W.; Zhan, X. Fused Tris(Thienothiophene)-Based Electron Acceptor with Strong Near-Infrared Absorption for High-Performance As-Cast Solar Cells. *Adv. Mater.* **2018**, *30* (10), 1705969. https://doi.org/10.1002/adma.201705969.

(57) Mandal, H.; Giri, S. K.; Jovanovski, S.; Varnavski, O.; Zagorska, M.; Ganczarczyk, R.; Chiang, T.-M.; Schatz, G. C.; Goodson, T. I. Impact of Classical and Quantum Light on Donor–Acceptor–Donor Molecules. *J. Phys. Chem. Lett.* **2024**, *15* (37), 9493–9501. https://doi.org/10.1021/acs.jpclett.4c01948.

(58) Fisher, L. Jr.; Vázquez, R. J.; Howell, M.; Muthike, A. K.; Orr, M. E.; Jiang, H.; Dodgen, B.; Lee, D. R.; Lee, J. Y.; Zimmerman, P.; Goodson, T. I. Investigation of Thermally Activated Delayed Fluorescence in Donor–Acceptor Organic Emitters with Time-Resolved Absorption Spectroscopy. *Chem. Mater.* **2022**, *34* (5), 2161–2175. https://doi.org/10.1021/acs.chemmater.1c03668.

(59) Vázquez, R. J.; Yun, J. H.; Muthike, A. K.; Howell, M.; Kim, H.; Madu, I. K.; Kim, T.; Zimmerman, P.; Lee, J. Y.; III, T. G. New Direct Approach for Determining the Reverse Intersystem Crossing Rate in Organic Thermally Activated Delayed Fluorescent (TADF)

Emitters. *J. Am. Chem. Soc.* **2020**, *142* (18), 8074–8079. https://doi.org/10.1021/jacs.0c01225.

(60) Villabona-Monsalve, J. P.; Varnavski, O.; Palfey, B. A.; Goodson, T. Two-Photon Excitation of Flavins and Flavoproteins with Classical and Quantum Light. *J. Am. Chem. Soc.* **2018**, *140* (44), 14562–14566. https://doi.org/10.1021/jacs.8b08515.

(61) Villabona-Monsalve, J. P.; Tcyrulnikov, N. A.; Lorenzo, E. R.; LaBine, N.; Burdick, R.; Krzyaniak, M. D.; Young, R. M.; Wasielewski, M. R.; Goodson, T. I. Two-Photon Absorption in Electron Donor–Acceptor Dyads and Triads Using Classical and Entangled Photons: Potential Systems for Photon-to-Spin Quantum Transduction. *J. Phys. Chem. C* **2022**, *126* (14), 6334–6343. https://doi.org/10.1021/acs.jpcc.2c00830.

(62) Pawlicki, M.; Collins, H. A.; Denning, R. G.; Anderson, H. L. Two-Photon Absorption and the Design of Two-Photon Dyes. *Angew. Chem. Int. Ed.* **2009**, *48* (18), 3244–3266. https://doi.org/10.1002/anie.200805257.

(63) Cai, Z.; Vázquez, R. J.; Zhao, D.; Li, L.; Lo, W.; Zhang, N.; Wu, Q.; Keller, B.; Eshun, A.; Abeyasinghe, N.; Banaszak-Holl, H.; Goodson, T. I.; Yu, L. Two Photon Absorption Study of Low-Bandgap, Fully Conjugated Perylene Diimide-Thienoacene-Perylene Diimide Ladder-Type Molecules. *Chem. Mater.* **2017**, *29* (16), 6726–6732. https://doi.org/10.1021/acs.chemmater.7b01512.

(64) Sandoval, J. S.; Haley, M. M.; Goodson, T. I. Nonlinear Optical Properties of Bis(Dehydrobenzoannuleno)Benzenes: An Experimental and Computational Approach. *J. Phys. Chem. A* **2025**, *129* (5), 1240–1251. https://doi.org/10.1021/acs.jpca.4c06285.

(65) Mandal, H.; Ogunyemi, O. J.; Nicholson, J. L.; Orr, M. E.; Lalisse, R. F.; Rentería-Gómez, Á.; Gogoi, A. R.; Gutierrez, O.; Michaudel, Q.; Goodson, T. I. Linear and Nonlinear Optical

Properties of All-Cis and All-Trans Poly(p-Phenylenevinylene). *J. Phys. Chem. C* **2024**, *128* (6), 2518–2528. https://doi.org/10.1021/acs.jpcc.3c07082.

(66) Zheng, T.; Cai, Z.; Ho-Wu, R.; Yau, S. H.; Shaparov, V.; Goodson, T. I.; Yu, L. Synthesis of Ladder-Type Thienoacenes and Their Electronic and Optical Properties. *J. Am. Chem. Soc.* **2016**, *138* (3), 868–875. https://doi.org/10.1021/jacs.5b10175.

(67) Schlawin, F.; Dorfman, K. E.; Fingerhut, B. P.; Mukamel, S. Suppression of Population Transport and Control of Exciton Distributions by Entangled Photons. *Nat. Commun.* **2013**, *4* (1), 1782. https://doi.org/10.1038/ncomms2802.

(68) Varnavski, O.; Giri, S. K.; Chiang, T.-M.; Zeman, C. J.; Schatz, G. C.; Goodson, T. Colors of Entangled Two-Photon Absorption. *Proc. Natl. Acad. Sci.* **2023**, *120* (35), e2307719120. https://doi.org/10.1073/pnas.2307719120.

(69) Schlawin, F.; Dorfman, K. E.; Mukamel, S. Entangled Two-Photon Absorption Spectroscopy. *Acc. Chem. Res.* **2018**, *51* (9), 2207–2214. https://doi.org/10.1021/acs.accounts.8b00173.

(70) Noda, H.; Nakanotani, H.; Adachi, C. Excited State Engineering for Efficient Reverse Intersystem Crossing. *Sci. Adv.* **2018**, *4* (6), eaao6910. https://doi.org/10.1126/sciadv.aao6910.

(71) Masui, K.; Nakanotani, H.; Adachi, C. Analysis of Exciton Annihilation in High-Efficiency Sky-Blue Organic Light-Emitting Diodes with Thermally Activated Delayed Fluorescence. *Org. Electron.* **2013**, *14* (11), 2721–2726. https://doi.org/10.1016/j.orgel.2013.07.010.

(72) Notsuka, N.; Nakanotani, H.; Noda, H.; Goushi, K.; Adachi, C. Observation of Nonradiative Deactivation Behavior from Singlet and Triplet States of Thermally Activated Delayed Fluorescence Emitters in Solution. *J. Phys. Chem. Lett.* **2020**, *11* (2), 562–566. https://doi.org/10.1021/acs.jpclett.9b03302.

(73) Vázquez, R. J.; Yun, J. H.; Muthike, A. K.; Howell, M.; Kim, H.; Madu, I. K.; Kim, T.; Zimmerman, P.; Lee, J. Y.; III, T. G. New Direct Approach for Determining the Reverse Intersystem Crossing Rate in Organic Thermally Activated Delayed Fluorescent (TADF) Emitters. *J. Am. Chem. Soc.* **2020**, *142* (18), 8074–8079. https://doi.org/10.1021/jacs.0c01225.

(74) Bhaskar, A.; Ramakrishna, G.; Lu, Z.; Twieg, R.; Hales, J. M.; Hagan, D. J.; Van Stryland, E.; Goodson, T. Investigation of Two-Photon Absorption Properties in Branched Alkene and Alkyne Chromophores. *J. Am. Chem. Soc.* **2006**, *128* (36), 11840–11849. https://doi.org/10.1021/ja060630m.

(75) Yildiz, E. A.; Sevinç, G.; Tekin, S.; Karatay, A.; Hayvalı, M.; Elmali, A. Great Enhancement of Two Photon Absorption Cross Section Value by Intramolecular Charge Transfer in Newly Synthesized Triphenylamine-BODIPY Derivative. *Dyes Pigments* **2021**, *193*, 109522. https://doi.org/10.1016/j.dyepig.2021.109522.

(76) P. Beerepoot, M. T.; H. Friese, D.; Ruud, K. Intermolecular Charge Transfer Enhances Two-Photon Absorption in Yellow Fluorescent Protein. *Phys. Chem. Chem. Phys.* **2014**, *16* (13), 5958–5964. https://doi.org/10.1039/C3CP55205E.

(77) Jia, J.; Wu, X.; Zhang, X.; Wang, Y.; Yang, J.; Fang, Y.; Song, Y. Effect of Intramolecular Charge Transfer on Nonlinear Optical Properties of Chalcone Derivatives: A Visual Description of the Charge Transfer Process. *Phys. Chem. Chem. Phys.* **2022**, *24* (2), 955–965. https://doi.org/10.1039/D1CP04567A.

(78) K. Samanta, P.; Mehboob Alam, M.; Misra, R.; K. Pati, S. Tuning of Hyperpolarizability, and One- and Two-Photon Absorption of Donor–Acceptor and Donor–Acceptor–Acceptor-Type

Intramolecular Charge Transfer-Based Sensors. *Phys. Chem. Chem. Phys.* **2019**, *21* (31), 17343–17355. https://doi.org/10.1039/C9CP03772A.

(79) Eshun, A.; Cai, Z.; Awies, M.; Yu, L.; Goodson, T. I. Investigations of Thienoacene Molecules for Classical and Entangled Two-Photon Absorption. *J. Phys. Chem. A* **2018**, *122* (41), 8167–8182. https://doi.org/10.1021/acs.jpca.8b06312.

(80) Kang, G.; Nasiri Avanaki, K.; Mosquera, M. A.; Burdick, R. K.; Villabona-Monsalve, J. P.; Goodson, T. I.; Schatz, G. C. Efficient Modeling of Organic Chromophores for Entangled Two-Photon Absorption. *J. Am. Chem. Soc.* **2020**, *142* (23), 10446–10458. https://doi.org/10.1021/jacs.0c02808.

(81) Sarma, M.; Wong, K.-T. Exciplex: An Intermolecular Charge-Transfer Approach for TADF. *ACS Appl. Mater. Interfaces* **2018**, *10* (23), 19279–19304. https://doi.org/10.1021/acsami.7b18318.

(82) Ryoo, C. H.; Han, J.; Yang, J.; Yang, K.; Cho, I.; Jung, S.; Kim, S.; Jeong, H.; Lee, C.; Kwon, J. E.; Serdiuk, I. E.; Park, S. Y. Systematic Substituent Control in Blue Thermally Activated Delayed Fluorescence (TADF) Emitters: Unraveling the Role of Direct Intersystem Crossing between the Same Charge-Transfer States. *Adv. Opt. Mater.* **2022**, *10* (24), 2201622. https://doi.org/10.1002/adom.202201622.

(83) Chen, J.-X.; Xiao, Y.-F.; Wang, K.; Sun, D.; Fan, X.-C.; Zhang, X.; Zhang, M.; Shi, Y.-Z.; Yu, J.; Geng, F.-X.; Lee, C.-S.; Zhang, X.-H. Managing Locally Excited and Charge-Transfer Triplet States to Facilitate Up-Conversion in Red TADF Emitters That Are Available for Both Vacuum- and Solution-Processes. *Angew. Chem.* **2021**, *133* (5), 2508–2514. https://doi.org/10.1002/ange.202012070.

(84) Chen, X.; Zhang, X.; Xiao, X.; Wang, Z.; Zhao, J. Recent Developments on Understanding Charge Transfer in Molecular Electron Donor-Acceptor Systems. *Angew. Chem. Int. Ed.* **2023**, *62* (16), e202216010. https://doi.org/10.1002/anie.202216010.

(85) Imahori, H.; Kobori, Y.; Kaji, H. Manipulation of Charge-Transfer States by Molecular Design: Perspective from "Dynamic Exciton." *Acc. Mater. Res.* **2021**, *2* (7), 501–514. https://doi.org/10.1021/accountsmr.1c00045.

(86) Tian, T.; Li, J.; Guo, D.; Zhang, H. Bridge-Tuned through-Space Charge Transfer for TADF and HLCT Emissions. *J. Mater. Chem. C* **2024**, *12* (37), 14987–14996. https://doi.org/10.1039/D4TC02682A.

(87) Varnavski, O.; Giri, S. K.; Chiang, T.-M.; Zeman, C. J.; Schatz, G. C.; Goodson, T. Colors of Entangled Two-Photon Absorption. *Proc. Natl. Acad. Sci.* **2023**, *120* (35), e2307719120. https://doi.org/10.1073/pnas.2307719120.

(88) Zhou, B.; Chiang, T.-M.; Varnavski, O.; Giri, S. K.; Rani, C.; Schatz, G. C.; Goodson, T. I. Enhanced Photochemical Reaction Rates with Entangled Photons. *J. Phys. Chem. Lett.* **2025**, *16* (18), 4372–4381. https://doi.org/10.1021/acs.jpclett.5c00836.

(89) Ogunyemi, O. J.; Rani, C.; Varnavski, O.; Wajahath, R.; Norscia, M.; Malaikal, B.; Qiu, Y.; Sun, S.; Gu, Y.; Mukamel, S.; Wasielewski, M. R.; Goodson, T. I. Understanding the Correlation of the Quantum Dephasing Time and Entangled Photon Interaction in Crystalline Tetracene Derivatives. *J. Phys. Chem. C* **2024**, *128* (47), 20287–20296. https://doi.org/10.1021/acs.jpcc.4c05907.

(90) Lee, D.-I.; Goodson, T. Entangled Photon Absorption in an Organic Porphyrin Dendrimer. *J. Phys. Chem. B* **2006**, *110* (51), 25582–25585. https://doi.org/10.1021/jp066767g.

(91) Samanta, P. K.; Kim, D.; Coropceanu, V.; Brédas, J.-L. Up-Conversion Intersystem Crossing Rates in Organic Emitters for Thermally Activated Delayed Fluorescence: Impact of the Nature of Singlet vs Triplet Excited States. *J. Am. Chem. Soc.* **2017**, *139* (11), 4042–4051. https://doi.org/10.1021/jacs.6b12124.

(92) Huang, R.; Avó, J.; Northey, T.; Chaning-Pearce, E.; Santos, P. L. dos; Ward, J. S.; Data, P.; Etherington, M. K.; Fox, M. A.; Penfold, T. J.; Berberan-Santos, M. N.; Lima, J. C.; Bryce, M. R.; Dias, F. B. The Contributions of Molecular Vibrations and Higher Triplet Levels to the Intersystem Crossing Mechanism in Metal-Free Organic Emitters. *J. Mater. Chem. C* **2017**, *5* (25), 6269–6280. https://doi.org/10.1039/C7TC01958K.

(93) Franca, L. G.; Long, Y.; Li, C.; Danos, A.; Monkman, A. The Critical Role of Nπ* States in the Photophysics and Thermally Activated Delayed Fluorescence of Spiro Acridine-Anthracenone. *J. Phys. Chem. Lett.* **2021**, *12* (5), 1490–1500. https://doi.org/10.1021/acs.jpclett.0c03314.

(94) Mageswari, G. V.; Chitose, Y.; Tsuchiya, Y.; Lin, J.-H.; Adachi, C. Rational Molecular Design for Balanced Locally Excited and Charge- Transfer Nature for Two-Photon Absorption Phenomenon and Highly Efficient TADF-Based OLEDs. *Angew. Chem.* **2025**, *137* (8), e202420417. https://doi.org/10.1002/ange.202420417.

Supplementary Information

Table of content

Experimental section: Synthesis route for the MI, D1 and T1.

Figure S6.1: NMR spectrum of M1-Br in CD_2Cl_2

Figure S6.2: NMR spectrum of D1 in $CDCl_3$

Figure S6.3: NMR spectrum of T1 in $CDCl_3$

Figure S6.4: Kinetic of the GSB for the M1, D1 and T1

Figure S6.5: NTO of the excited state of the M1

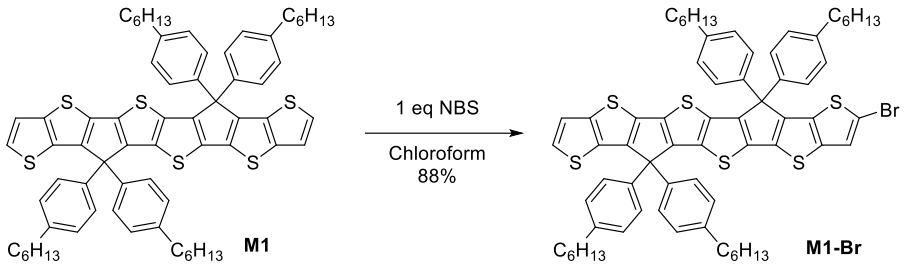
Figure S6.6: NTO of the excited state of the D1

Figure S6.7: NTO of the excited state of the T1

Table S6.1: Electronic calculation of the coupling between the singlet and triplet states

Table S6.2: Electronic calculation of the energy of the singlet and triplet states

Experimental section: Synthesis route for the MI, D1 and T1.

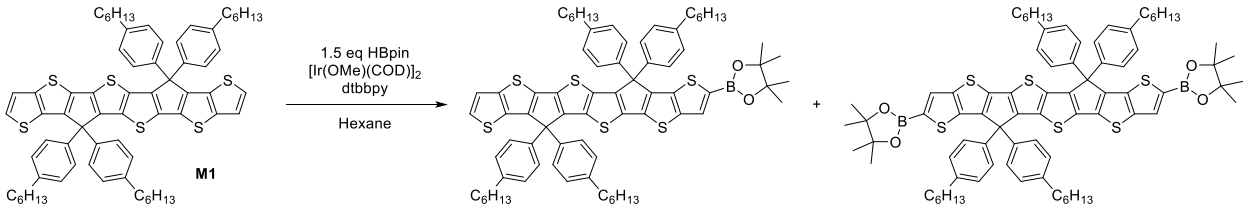


Synthesis of M1-Br

To a 250 mL flask, **M1** (540 mg) is dissolved in chloroform (250 mL). Under 0 C, N-bromosuccinimide (NBS, 89 mg) is added in portions. The reaction is stirring under dark overnight before 20 mL silica gel is added. The solvent is removed and the remaining product-silica gel mixture is subjected to coloum chloromatography using hexane as the eluent. The product M1-Br is obatiend as orange solid (462 mg, 88%).

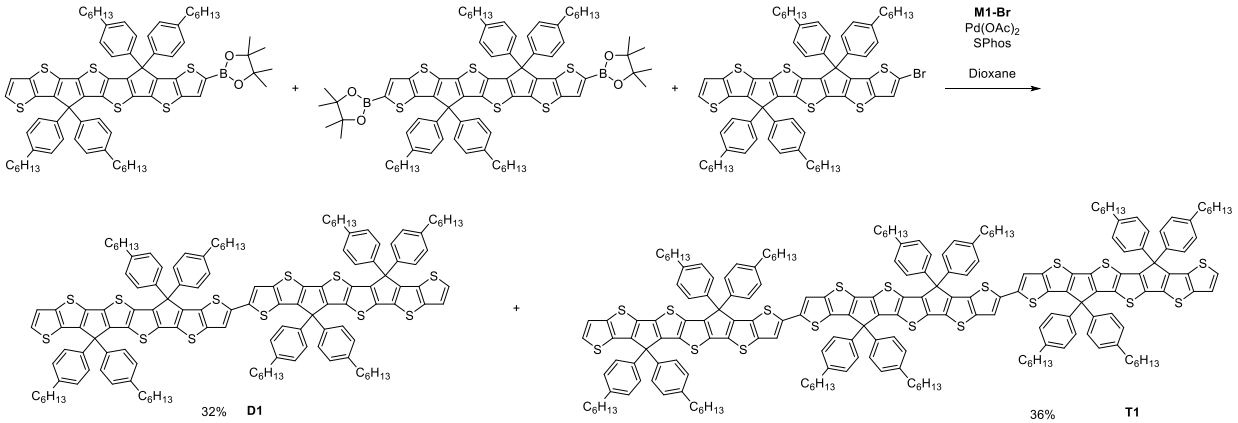
1H NMR (600 MHz, CD_2Cl_2) δ 7.292 (br, 3H), 7.096 (m, 16H), 2.534 (t, 8H), 1.557 (m, 32H), 0.88 (t, 12H).

HRMS([m]·) m/z calcd. for C68H71BrS6 1158.3063, found 1158.3031.



Synthesis of M1-Bpins

Under inert atmosphere, compound **M1** (1 eq.) was dissolved in dry THF and the reaction was cooled with a dry ice/acetone bath. Next, 2.5 M *n*-BuLi in hexanes (2 eq.) was added to the flask, still at -78 °C and under argon. The mixture was stirred at -78 °C for 1 h. A 1 M solution of trimeythltin chloride (1.5 eq.) was added dropwise, and the resulting solution was stirred at -78 °C for 1 hour. The reaction mixture was allowed to warm to room temperature for 45 minutes and was then quenched with water. After extraction with hexanes, the organic layer was washed with brine (x3), dried with magnesium sulfate, filtered, and concentrated under reduced pressure/rotovap to give the product as a brown solid without further purification.



Synthesis of D1 and T1

A mixture of M1-Br and M1-Bpins (1.5 eq), palladium tetrakis(triphenylphosphine) (5 mol%) were mixed in a RB flask, which was degassed via vacuum and refilled with argon three times. Subsequently, degassed toluene was added to the mixture. Then the mixture was stirred at 100 °C

overnight. The reaction was quenched by water and extracted by chloroform. The organic phase was dried over magnesium sulfate. Dry loading the mixture on silica gel and hexane was used for hex/CF(5:1) column chromatography to give the product 33 as orange solid and 34 as purple solid.

D1: 1H NMR (600 MHz, $CDCl_3$) δ 7.26 (m, 6H), 7.132 (m, 32H), 2.547 (m, 16H), 1.275 (m, 64H), 0.88 (m, 24H).

HRMS([m]·) m/z calcd. for C136H142S12 2158.7760, found 2158.7712.

T1: 1H NMR (600 MHz, $CDCl_3$) δ 7.26 (m, 8H), 7.122 (m, 48H), 2.551 (m, 24H), 1.277 (m, 96H), 0.88 (m, 36H).

HRMS([m]·) m/z calcd. for C204H212S18 3237.1562, found 3237.1589.

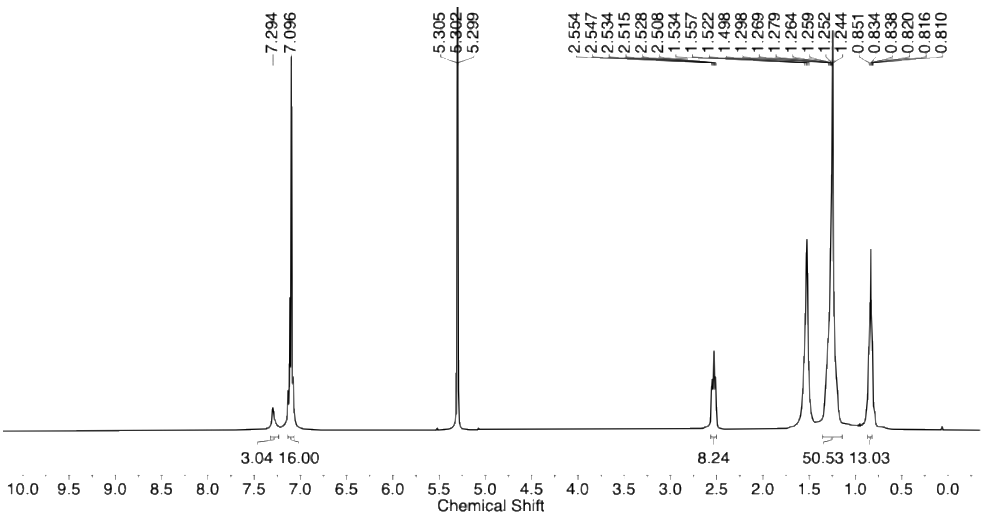


Figure S6.1: NMR spectrum of M1-Br in CD_2Cl_2

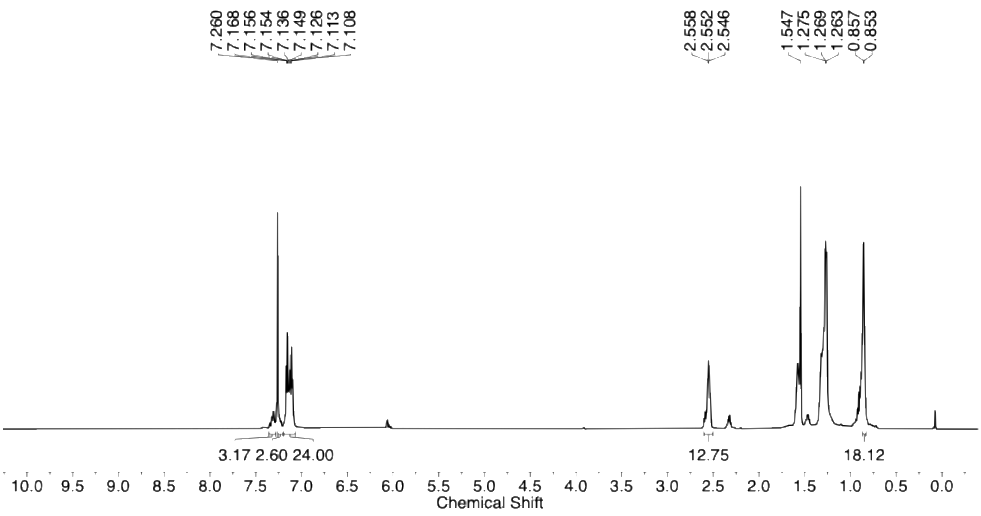


Figure S6.2: NMR spectrum of D1 in $CDCl_3$

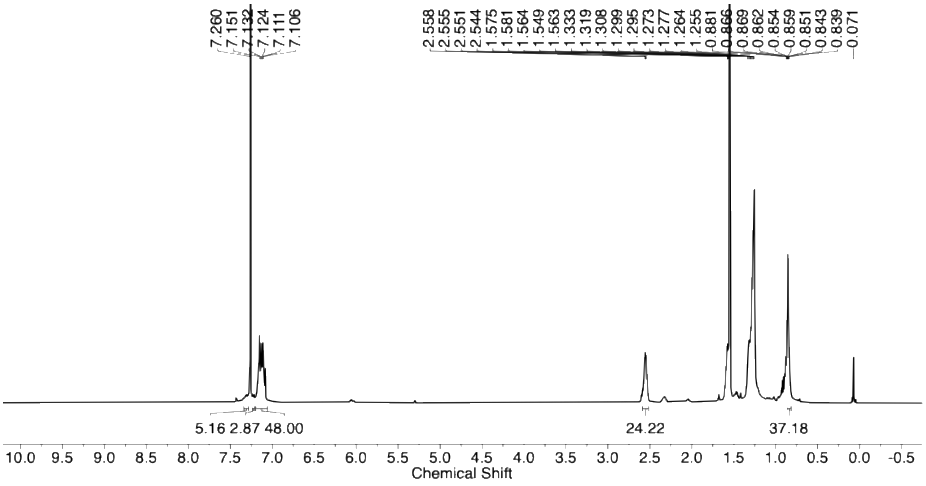


Figure S6.3: NMR spectrum of T1 in $CDCl_3$

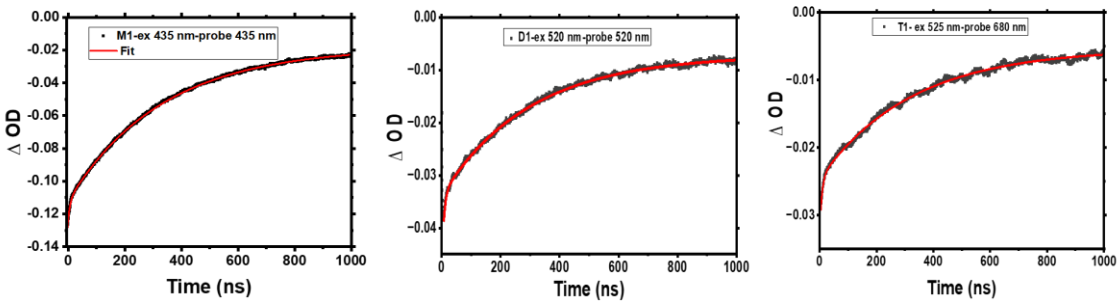


Figure S6.4: Kinetic of the GSB for the M1, D1 and T1

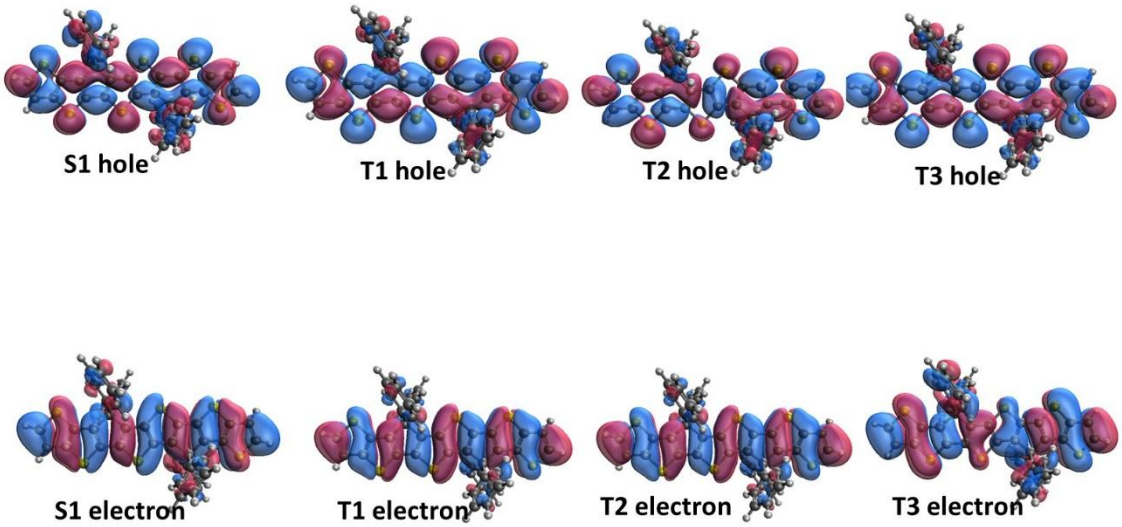


Figure S6.5: NTO of the excited state of the M1

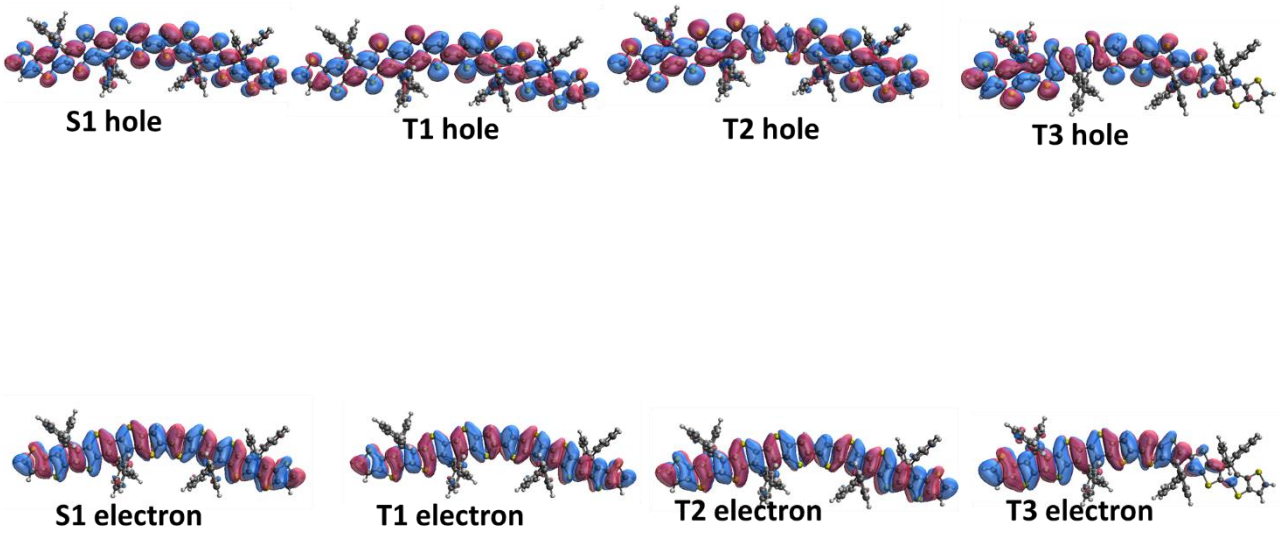


Figure S6.6: NTO of the excited state of the D1

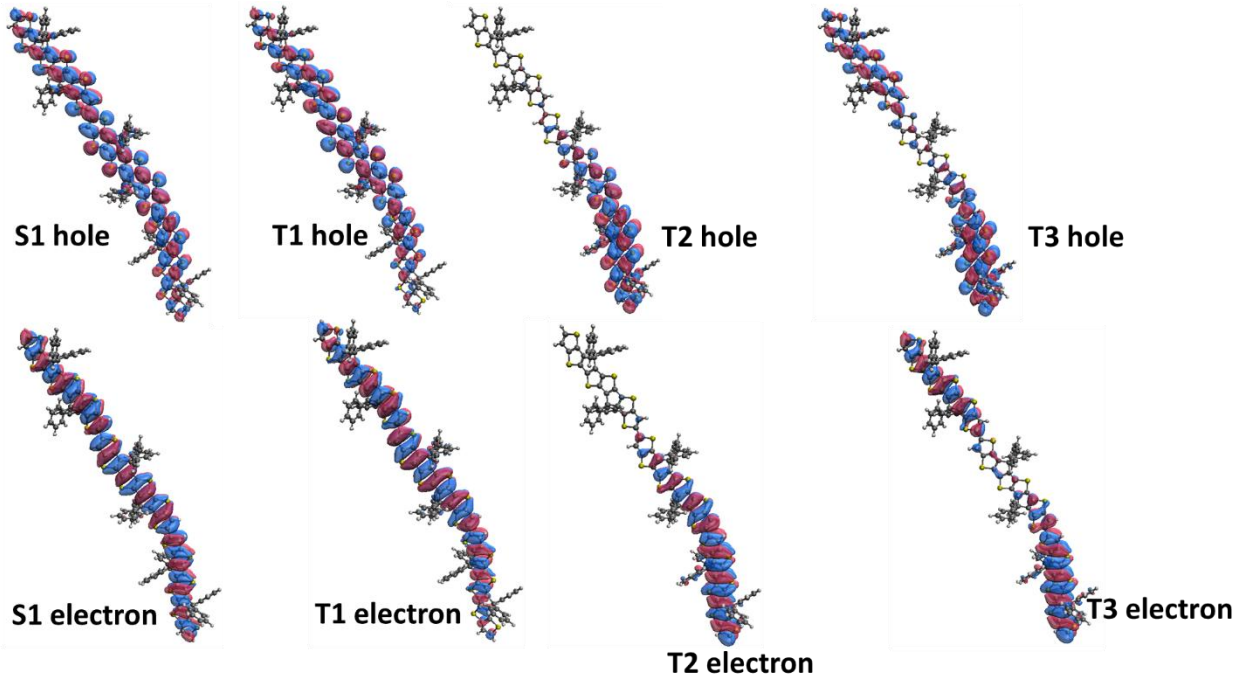


Figure S6.7: NTO of the excited state of the T1

Table S6.1: Electronic calculation of the coupling between the singlet and triplet states

		TDA TDDFT	Full TDDFT
Molecule	**States Involved**	**Coupling value between the states (cm^{-1})**	**Coupling value between the states (cm^{-1})**
Monomer	$S_1 \rightarrow T_1$	**0.80**	
	$S_1 \rightarrow T_2$	**0.001**	
	$T_1 \rightarrow T_2$	**0.005**	**0.006**
Dimer	$S_1 \rightarrow T_1$	**0.12**	
	$S_1 \rightarrow T_2$	**0.67**	
	$S_1 \rightarrow T_3$	**0.10**	
	$T_1 \rightarrow T_2$	**2.11**	**2.03**
	$T_1 \rightarrow T_3$	**0.29**	**0.27**
	$T_2 \rightarrow T_3$	**2.38**	**2.27**
Trimer	$S_1 \rightarrow T_1$	**0.06**	
	$S_1 \rightarrow T_2$	**0.23**	
	$S_1 \rightarrow T_3$	**0.77**	
	$T_1 \rightarrow T_2$	**0.70**	**0.68**
	$T_1 \rightarrow T_3$	**2.20**	**2.18**
	$T_2 \rightarrow T_3$	**1.15**	**1.12**

Table S6.2: Electronic calculation of the energy of the singlet and triplet states

		TDA TDDFT	Full TDDFT
Molecule	**States**	**Energy with respect to ground state (eV)**	**Energy with respect to ground state (eV)**
Monomer	S_1	**2.77**	**2.60**
	T_1	**1.74**	**1.55**
	T_2	**2.48**	**2.33**
Dimer	S_1	**2.09**	**2.01**
	T_1	**1.46**	**1.29**
	T_2	**1.71**	**1.55**
	T_3	**2.12**	**1.99**
Trimer	S_1	**1.88**	**1.83**
	T_1	**1.39**	**1.22**
	T_2	**1.55**	**1.39**
	T_3	**1.69**	**1.55**
	T_4	**1.99**	**1.87**

Chapter Seven
Photocatalytic Alkene Hydrofunctionalization Utilizing Acridine-Lewis Acid Complexes

7.1. Author Contribution Statement

This chapter describes the collaboration by Professor Melanie Sanford (Department of Chemistry, University of Michigan, Ann Arbor) and Professor Theodore Goodson III (Department of Macromolecular Science and Engineering, University of Michigan, Ann Arbor, and Department of Chemistry, University of Michigan, Ann Arbor). In this project, the synthesis and mechanistic investigation was done by Professor Melanie Sanford group; while I worked on the investigation of the back electron transfer and radical cation formation using the nanosecond transient absorption spectroscopy.

The manuscript based on this work is currently in preparation for submission to *ACS Catalysis*. As a result, certain details may be refined prior to submission, and the final published version may differ in emphasis from the content presented in this dissertation. The author information for this work is as follow: Daniel S. Brandes, Emily Jimenez Andrade, Matthew R. Lasky, Olusayo J. Ogunyemi, Siqi Dong, Theodore Goodson III, and Melanie S. Sanford. (To be submitted to *ACS Catalysis)*

7.2. Abstract

Acridinium photocatalysts are important tools for visible-light-promoted single-electron photoredox transformations, including the *anti*-Markovnikov hydrofunctionalization of alkenes. However, use of these systems is limited by the synthetic complexity of the photocatalysts, which require costly synthesis and/or purchase. We report a highly modular and cost-effective photocatalyst derived from the *in situ* 2:1 complexation of acridines with Lewis acids, leading to catalysts with very high excited state potentials of up to +2.65 V vs SCE. We demonstrate the utility of these photocatalysts via the *anti*-Markovnikov hydrofunctionalization of alkenes of potentials up to ~+2.50 V vs SCE. Different nucleophiles are demonstrated, including azoles, alcohols, water, and pyridines, the latter of which has not yet been reported in the literature. Finally, we highlight the modularity of this photocatalytic system. Using transient absorption spectroscopy, we show that the choice of Lewis acid has a significant effect on electron transfer kinetics, leading to different catalytic outcomes for different substrates. These studies highlight the inherent tunability of this catalytic system.

7.3. Introduction

Alkenes are a versatile feedstock for diverse chemical transformations. Photoredox catalysis has emerged as a powerful tool for the hydrofunctionalization of alkenes, allowing for the incorporation of valuable functionality.[1] [1] Nicewicz and co-workers have pioneered the development of a platform for anti-Markovnikov alkene hydrofunctionalization, through the use of acridinium photocatalysts (PC) (**Figure 7.1a**).[1a, 2] These catalysts typically operate by a mechanism involving: (i) excitation of the PC with visible light to afford PC*, (ii) single-electron transfer (SET) between PC* and the alkene to generate alkene radical cation **I**, (iii) reversible

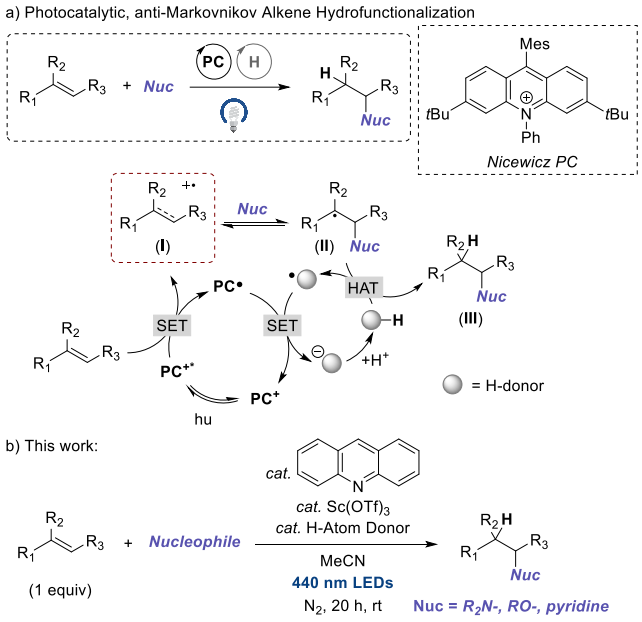
attack of **I** by a nucleophilic coupling partner, and (iv) hydrogen atom transfer (HAT) to provide the desired hydrofunctionalization product (**Figure 7.1a**).[1a, 3] While these methods are robust means to access useful products, they are limited by the requirement for preassembled photocatalysts, which are typically costly and/or require multiple synthetic steps to access. Accessing electronically diverse derivatives is time consuming and synthetically demanding. Furthermore, reported derivatives have a limited range of excited state reduction potentials (E^*_{red}), such that they are only effective with substrates that have oxidation potentials (E_{ox}) of ≤ +2.2 V vs. SCE.[1b, 4]

Recently, our lab has developed and deployed a series of inexpensive and highly modular *in situ* visible-light photocatalysts in C(sp^2)–H amination and cation-radical accelerated (CRA) S_NAr reactions. These catalysts are formed *in situ* from the combination of two readily available components: an acridine derivative and a Lewis acid.[5] These photocatalysts possess high E^*_{red} values (up to +2.65 V vs SCE) and thus promote transformations that are challenging for acridinium derivatives, including C(sp^2)–H amination of benzene (E_{ox} ~ 2.48 V vs SCE)[6] and CRA-S_NAr of chlorobenzene[7] (E_{ox} ~ 2.46 V vs SCE)[6] with arene as the limiting reagent.

Based on this precedent, we hypothesized that these modular *in situ* catalysts could similarly be leveraged for photoredox alkene hydrofunctionalization. Further, we anticipated that their modular nature and high E^*_{red} values could facilitate rapid optimization for different classes of substrate/nucleophile while opening up a wider scope of electronically diverse alkene substrates. Notably, while our work was in progress, Ritter demonstrated that related protonated acridines are effective photocatalysts for the anti-Markovnikov hydration of alkenes.[8] We report herein that acridine/Lewis acid derivatives catalyze a wide variety of alkene hydrofunctionalization reactions to form alkyl amine, ether, alcohol, and pyridinium products. Furthermore, we show that variation

of the Lewis acid leads to divergent reactivity for substrates of different electronics and electrochemical potentials. Transient absorption spectroscopy studies implicate the kinetics of substrate oxidation in this phenomenon.

Figure 7.1. (A) General, photocatalytic *anti*-Markovnikov alkene hydrofunctionalization with mechanism (B) Proposed transformations using in situ LA-Acr PC



7.4. Results and Discussion

Initial studies focused on the *anti*-Markovnikov hydroamination of styrene derivatives with azoles,[9] a transformation that was originally reported by Nicewicz using acridinium photocatalysts.[10] The reaction of cinnamyl alcohol (**1a,** E_{ox} = +1.85 V vs SCE) with 4-chloropyrazole (**2a**) was selected as a model reaction. Using the first-generation photocatalyst derived from acridine (10 mol %) and $Sc(OTf)_3$ (5 mol %) and diphenyl disulfide $(PhS)_2$ (20 mol %) as a co-catalyst for H-atom transfer,[10b] the reaction was conducted under N_2 in MeCN with irradiation from 440 nm Kessil LEDs (see Table S1 for reaction condition optimization studies).

Without Sc, the hydroamination product **3a** was not detected (Table 1, entry 1). However, upon the addition of 5 mol % of $Sc(OTf)_3$ under otherwise identical conditions **3a** was formed in 58% yield (entry 2). For comparison to Ritter's work, we also evaluated acridinium tetrafluoroborate as the PC and showed that it performed equivalently, providing **3a** in 51% yield (entry 3).[8] Employing Nicewicz's di-tBu-Mes-Acr-Ph PC, and Fukuzumi's Mes-Acr-Me PC, the reaction proceeded smoothly in 81% and 72% yield, respectively (entry 4,5).

Since numerous Lewis acids are commercially available, this component can be readily varied for reaction optimization. Evaluation of 15 Lewis acids led to several key observations (Table S2, Table 1). First, compared to $Sc(OTf)_3$ most of the Lewis acids afforded comparable or lower yield of **3a**. Even $Al(OTf)_3$ (which showed superior performance in $C(sp^2)$–H functionalization reactions)[5] gave just 50% yield of **3a** (entry 6), versus 58% with $Sc(OTf)_3$. Second, the stoichiometry of Lewis acid to acridine (1:1 versus 1:2) generally had minimal impact on the yield of **3a**. The sole outlier to these trends was $Cu(OTf)_2$, which afforded noticeably improved yield (73%) and overall mass balance at 1:1 stoichiometry (entry 14).

The latter result led us to consider whether a combination of $Cu(OTf)_2$ with another Lewis acid might lead to improved results. Intriguingly, when a combination of $Sc(OTf)_3$ and $Cu(OTf)_2$ was employed, the additive effect of both Lewis acids led to a greatly improved yield of 84% (entry 8), leading to comparable reactivity as Nicewicz and Fukuzumi's acridinium PCs. This catalyst system was chosen as the standard condition for the demonstration of scope. A similar result was found when $Al(OTf)_3$ was used with $Cu(OTf)_2$ (entry 9), but interestingly, the combination of $Sc(OTf)_3$ with $Al(OTf)_3$ did not provide any improvement in yield (entry 10). A panel of other Cu(I) and Cu(II) salts (including in combination with $Sc(OTf)_3$) was assessed as

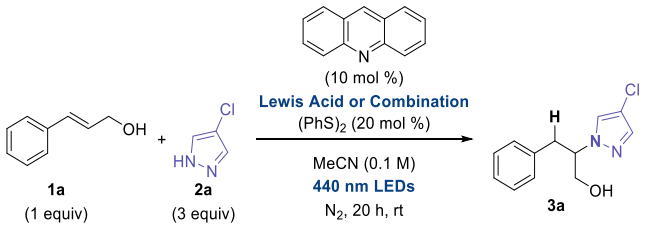
well (Table S3), and $Cu(OTf)_2$ was confirmed to be the most effective additive, increasing mass balance and yield relative to the no-additive condition.

The role of the copper additive was then probed by assessing the inclusion of $Sc(OTf)_3$ and $Cu(OTf)_2$ at lower loadings (2.5 mol % each) such that an overall population of 2:1 Acridine:Lewis acid could be maintained in solution (**Table 7.1**, entry 11). Here, the reaction outcome was not improved relative to just $Sc(OTf)_3$. We thus hypothesize that the copper may not be acting only as a Lewis acid when included in excess but instead may play a stabilizing role in the formation of radicals as well as in preventing deleterious decomposition pathways (*vide infra*). This role is supported in that the inclusion of copper, whether on its own or in combination with another Lewis acid, typically provides a higher overall mass balance in the crude reaction mixture. Finally, each Lewis acid was employed at 10 mol %; the $Sc(OTf)_3$ and $Al(OTf)_3$ catalyst systems showed no change relative to the corresponding 5 mol % conditions (entry 12-13). However, doubling the amount of copper additive in solution had a noticeable effect on reaction yield, indicating again that copper may be playing a role in preserving mass balance (entry 14).

Given the dramatic synergistic effect that the addition of a $Cu(OTf)_2$ additive caused in overall reactivity, we were motivated to perform additional mechanistic studies to probe its role in the reaction. We hypothesized that $Cu(OTf)_2$ may be acting on its own as a photooxidant, thereby increasing the rate of alkene oxidation. However, the use of $Cu(OTf)_2$ as the PC alone without acridine provided only 97% starting material, indicating that $Cu(OTf)_2$ does not act as a photooxidant under the optimal reaction conditions. We further wondered whether $Cu(OTf)_2$ might instead serve as a reservoir for triflic acid, causing the slow, catalytic formation of protonated acridinium species. In order to rule out the slow release of triflic acid from the $Cu(OTf)_2$ additive, we probed the standard reaction with triflic acid itself in place of the $Cu(OTf)_2$, and found a slight

decrease in yield relative to the Sc-only condition. When $Sc(OTf)_3$ is removed from the system, the presence of catalytic triflic acid enabled moderate conversion to product. Here, we hypothesize that the acridinium triflate formed *in situ* is sufficiently oxidizing to catalyze modest reactivity, but does not outcompete the complex formed with Lewis acids. Taken together, these results indicate that $Cu(OTf)_2$ is not enhancing reactivity due to slow release of triflic acid. Having ruled out these different mechanistic hypotheses, we presume that the most likely role for $Cu(OTf)_2$ involves the coordination and stabilization of radical intermediates, preventing side-reactivity and unwanted degradation products.[11,12]

Table 7.1. Photocatalytic Alkene Hydroamination Catalyst Optimization[a]



Entry	*Lewis Acid*	*Yield **3a***	*Recovered **1a***
1	No Lewis Acid	0%	80%
2	$Sc(OTf)_3$ (5 mol %)	58%	0%
3	Acridinium BF_4 (5 mol %)[b]	51%	6%
4	Nicewicz PC (5 mol %)[b]	81%	0%
5	Fukuzumi PC (5 mol %)[b]	72%	0%
6	$Al(OTf)_3$ (5 mol %)	50%	0%
7	$Cu(OTf)_2$ (5 mol %)	49%	51%
8	**Sc (5 mol %) + Cu (5 mol %)**	**84%**	**0%**
9	Al (5 mol %) + Cu (5 mol %)	85%	0%
10	Sc (5 mol %) + Al (5 mol %)	55%	0%
11	Sc (2.5 mol %) + Cu (2.5 mol %)	60%	23%
12	$Sc(OTf)_3$ (10 mol %)	58%	0%
13	$Al(OTf)_3$ (10 mol %)	49%	0%
14	$Cu(OTf)_2$ (10 mol %)	73%	0%

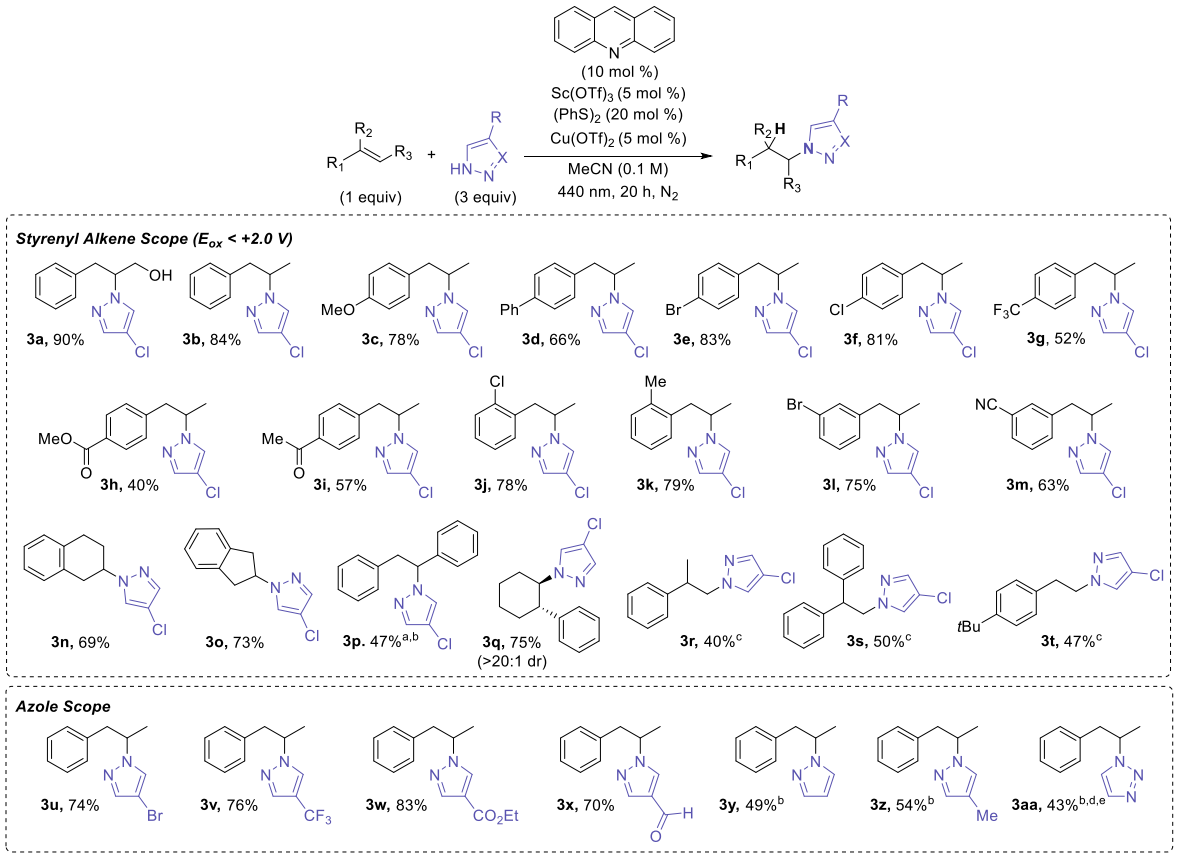
[a]Yields determined by ^{1}H-NMR using pentamethylbenzene as a standard. [b]No acridine.

We next evaluated the substrate scope with this Sc/Cu *in situ* photocatalyst (**Figure 7.2**). We employed a variety of internal styrenes bearing different electronic elements **3b-3m,** and found

that derivatives with both electron-donating (**3c, 3d, 3k**) and -withdrawing substituents (**3e-3j, 3l-3m**) are compatible with this transformation, as long as the alkene potential is in range of the catalyst. *Ortho*- and *meta*-substituents were compatible as well, providing products **3j-3m** in excellent yield. Next, we explored other fused bicyclic styrenyl systems, dihydronaphthalene, and indene, which provided desired product (**3n**, **3o**) in good yield. We were pleased to observe moderate yield using *trans*-stilbene, given its low potential (+1.50 V vs. SCE, in MeCN), providing **3p**. This reaction was performed in CH_2Cl_2, in which we hypothesize the excited state potential of our *in situ* catalyst to be lower relative to MeCN;[13] this reduces competing overoxidation of the substrate. 1-Phenylcyclohexene was an effective substrate, providing product **3q** in excellent yield and >20:1 dr. Terminal styrenes, including α-methylstyrene (**3r**), 1,1-diphenylethylene (**3s**), and 4-*tert*-butylstyrene (**3t**) provided product in moderate yields. For these terminal systems, the use of a somewhat higher loading of Cu(II) was beneficial. When copper was not employed, varying amounts of the sulfur-addition product were observed, indicating a role for Cu in stabilizing thiyl radicals during the course of the reaction.

Next, we went forward to investigate the nucleophile scope for this transformation. This reaction demonstrated good scope with respect to azole coupling partner. Different electronically deficient pyrazoles were compatible, including 4-Cl (**3b**), 4-Br (**3u**), 4-CF_3 (**3v**), 4-CO_2Et (**3w**), and 4-CHO (**3ax**). Electronically neutral and rich azoles could also be incorporated, including pyrazole (**3y**), 4-methylpyrazole (**3z**), and 1,2,3-triazole (**3aa**). However, the incorporation of Cu additive led to no conversion of starting material and it was therefore omitted for these substrates.

Figure 7.2. Hydroamination Scope of Styrenyl Alkenes.

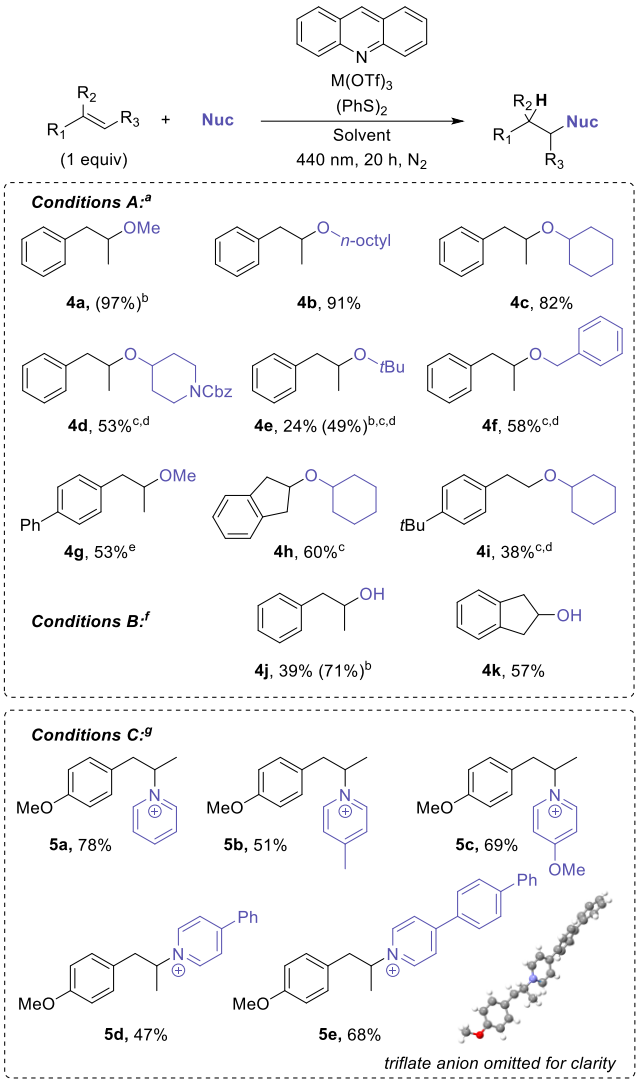


[a]Reaction performed in CH_2Cl_2 [b]no $Cu(OTf)_2$ [c]$Cu(OTf)_2$ (20 mol %) [d]$Al(OTf)_3$ as Lewis [e]40 h

After evaluating alkene hydroamination, we were interested in exploring different nucleophilic coupling partners. Oxygen nucleophiles have been employed as intermolecular coupling partners for hydroetherification[2a, 8] employing an acridinium PC. Alcohol addition, however, has been limited in the literature to intramolecular hydroetherification, with only a few intermolecular examples provided for the addition of simple alcohols.[2a, 8] Employing our *in situ* catalyst system, we were able to develop a new intermolecular hydroetherification reaction (**Figure 7.3**). With only minor changes from our optimized hydroamination conditions (employing a higher concentration of 0.5 M, and using $Al(OTf)_3$ as the Lewis acid), we were able to access

volatile methanol-adduct **4a** in 97% crude yield. Other alcohol substrates were compatible in excellent yield, including the primary aliphatic 1-octanol (**4b**) and branched 2° cyclohexanol (**4c**). More complex alcohols could also be included, such as a Cbz-protected piperidine alcohol (**4d**). This reaction was also compatible with the bulky *tert*-butanol, which could be employed in higher loading to achieve a synthetically useful yield (**4e**). Benzyl alcohol was also compatible with the transformation, providing **4f** in good yield. Additionally, we were able to demonstrate scope with different alkene substrates, including 4-phenyl β-methylstyrene (**4g**), indene (**4h**), and 4-*tert*-butyl styrene (**4i**). This primary styrene substrate was notably accessible in synthetically useful yield, though was limited by a competing thiol-ene reaction between the styrene and thiol derived from the disulfide.[2e] Finally, we demonstrated that water itself could be used as an oxygen-nucleophile, and could be added to different alkenes as well (**4j**, **4k**). Such photochemical hydrations were very recently reported in the literature using acridinium-based PCs that required pre-synthesis.[8]

Figure 7.3. Hydrofunctionalization of alkenes with varied nucleophiles.



Conditions A:[a] 5 equiv alcohol, 10 mol % acridine, 5 mol % $Al(OTf)_3$, 20 mol % $(PhS)_2$, MeCN (0.5 M). [b]Crude yield in parenthesis. [c]10 equiv alcohol [d]40 h. [e]In 1:1 CH_2Cl_2, MeOH (0.5 M). *Conditions B*:[f] 20 equiv H_2O, 10 mol % acridine, 5 mol % $Sc(OTf)_3$, 20 mol % $(PhS)_2$, MeCN (0.1 M). *Conditions C*:[g] 3 equiv pyridine, 10 mol % acridine, 105 mol % $Sc(OTf)_3$, 20 mol % $(PhS)_2$, DCE (0.1 M).

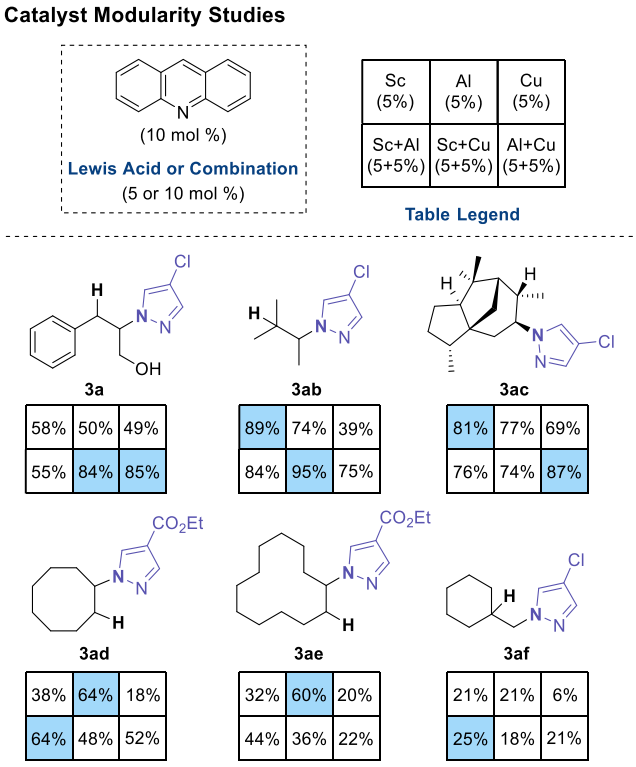
Our group previously showed that pyridines can act as nucleophiles for arene C–H pyridination employing the same *in situ* photocatalyst.[5] We therefore evaluated pyridine derivatives as nucleophilic coupling partners to afford alkyl pyridinium products. We hypothesized that alkenes could serve as effective new synthons for pyridinium salts of the type developed by Katritzky[14] and later popularized in the context of cross coupling by Watson and others.[15] Alkyl pyridinium salts are typically synthesized either through the nucleophilic displacement of alkyl halides by pyridines, the Zincke reaction, or by condensations of pyrylium salts and amines.[16] This new approach represents a mild procedure from more abundant alkene feedstocks.

Treatment of anethole (**1c**) with different pyridine nucleophiles under slightly modified conditions provided desired alkyl pyridinium products in excellent yields (**5a**-**5e**) (**Figure 7.3**). Both electron-neutral (**5a**) and -rich (**5b-5e**) pyridines were effective in this transformation. We validated the absolute structure of this new class of alkyl pyridinium salts by X-ray crystallographic analysis of **5e**,[17] which was the sole crystalline solid of the series (**Figure 7.3**). However, the scope of this reaction was limited to anethole – higher potential alkene substrates such as **1a** showed very low reactivity. This reaction represents a new research direction: with the development of more potent PCs, we may be able to access the hydropyridination of more photochemically challenging alkene substrates.

Having demonstrated the hydrofunctionalization of styrenyl systems, we were interested in assessing the reactivity of aliphatic alkenes possessing higher oxidation potentials of +1.9 V or higher. Upon beginning these investigations using cyclic aliphatic alkenes, we quickly found that the standard Lewis acid conditions (Sc/Cu) provided poor results for these substrates (*vide infra*). We thus considered the exploration of higher potential substrates as an opportunity to demonstrate catalyst modularity employing different Lewis acids.

We thus investigated the modularity of this system across a variety of high-potential alkene substrates, including 2-methylbutene **1ab** (E_{ox} = +1.98 V vs SCE), α-cedrene **1ac** (E_{ox} = +1.92 V vs SCE), (*Z*)-cyclooctene **1ad** (E_{ox} = +2.14 V vs SCE), *cis/trans*-cyclododecene **1ae** (E_{ox} = +2.20 V vs SCE), and methylenecyclohexane **1af** (E_{ox} ~ 2.50 V vs. SCE)[18] (Scheme 4; for full tables of conditions and isolated yields, see Tables S5-S10). Notably, each compound had a different reactivity profile. In Scheme 4 all catalyst combinations within 10% of the highest percentage are highlighted for clarity. Importantly, across these electronically dissimilar substrates, the most common trend showed that the addition of a $Cu(OTf)_2$ (5 mol %) additive to either $Sc(OTf)_3$ or $Al(OTf)_3$ (5 mol %) caused a dramatic increase in yield relative to either Lewis acid alone. Further, while $Cu(OTf)_2$ was typically the worst Lewis acid when employed on its own, when loaded in 10 mol %, often performed comparably to the other Lewis acid mixtures, with some exceptions (for example, (*Z*)-cyclooctene) (Tables S5-S10). Despite observing this general trend, we noticed outliers, particularly in the unactivated cycloalkene systems, where the addition of copper was in no case beneficial, but 5 mol % $Al(OTf)_3$, 10 mol % $Sc(OTf)_3$, or an Al/Sc mixture (5+5 mol %) all provided similarly high yields. For some systems, such as 2-methylbutene, α-cedrene and methylenecyclohexane, multiple conditions performed similarly. These results showcase the modularity of the *in situ* catalyst system. For any given substrate, a screen of catalysts derived from different Lewis acids can be rapidly performed, often leading to the demonstration of synergistic effects.

Figure 7.4. Lewis acid modularity screens for representative alkenes.



Yields determined by ^{1}H-NMR using pentamethylbenzene as a standard. Isolated yields reported in Supporting Information. Standard reaction conditions employed (see **Table 7.1**). All conditions within 10% of the highest yielding condition per grid are highlighted.

Having observed significant differences in catalytic outcomes when modulating the PC, we were interested in probing the mechanistic relationship between the choice of Lewis acid and catalytic outcomes. First, we studied the PCs in the context of fluorescence lifetime. Ultimately, we observed little difference in lifetime between the different Lewis acids: $(AcrN)_2$-$Sc(OTf)_3$, τ = 31.0 ns; $(AcrN)_2$-$Al(OTf)_3$, τ = 31.2 ns; $(AcrN)_2$-$Cu(OTf)_2$, τ = 30.4 ns (**Table 7.2**). We hypothesize that this negligible difference in fluorescence lifetime is consistent with catalytic

differences being caused by higher order singlet or triplet states, which cannot be detected using fluorescence spectroscopy.

We further probed our mechanistic hypothesis *via* Stern-Volmer fluorescence quenching studies to determine whether the change in Lewis acid might enhance the rate of alkene oxidation (**Table 7.2**). Employing the standard cinnamyl alcohol **1a** as a quencher, the fluorescence quenching of the Sc (5%), Al (5%), Cu (5%), and Sc+Cu (5+5%) systems were measured. Each of these catalysts displayed nearly identical quenching. The bimolecular quenching rate constant, k_q, was found to equal 1.3 x 10^{10} M^{-1} s^{-1} in MeCN for each system, except for the Al catalyst, for which k_q = 1.4 x 10^{10} M^{-1} s^{-1}. Similarly, Stern-Volmer studies were performed using cyclooctene as a quencher for the Sc and Al systems. Despite these catalysts providing significantly different catalytic outcomes, the bimolecular quenching rate constant was very similar for the two catalysts (Sc: k_q = 7.4 x 10^9 M^{-1} s^{-1}; Al: k_q = 7.6 x 10^9 M^{-1} s^{-1}). These studies indicate that modulation of the Lewis acid does not confer an appreciable change in the rate of fluorescence quenching of the PC excited state. Our catalyst series showed faster quenching than the Fukuzumi (Mes-Acr-Me BF_4) acridinium PC, which provided k_q = 9.8 x 10^9 M^{-1} s^{-1} for cinnamyl alcohol, and k_q = 5.0 x 10^9 M^{-1} s^{-1} for cyclooctene. Finally, Stern Volmer studies were performed for the Sc, Al, and Fukuzumi PC's using anethole as quencher. Consistent with anethole's low oxidation potential, these studies showed faster quenching, with the *in situ* PC's again quenching faster than Fukuzumi (**Table 7.2**).

In addition to our spectroscopic study, we wondered what effect modulating the Lewis acid might have on the E^*_{red} for given PCs (**Table 7.2**). One potential role that the $Cu(OTf)_2$ additive may be playing in our optimal condition would be to preferentially form new acridine/$Cu(OTf)_2$ 2:1 catalysts with higher excited state potentials, enhancing the overall oxidative power of the catalyst system. However, we measured E^*_{red} for this in situ catalyst (acridine/$Cu(OTf)_2$) to be

+2.43 V vs. SCE, while the E^*_{red} for the acridine/$Sc(OTf)_3$/$Cu(OTf)_2$ system was +2.42 V vs. SCE. These are both within error of the known acridine/$Sc(OTf)_3$ (+2.47 V) and acridine/$Al(OTf)_3$ (+2.44 V) systems,[5a] indicating that the differences we observed in reactivity were likely not related to photochemical potential as long as the substrate potential was within range of the PC.

Table 7.2. Summary of photophysical data comparing catalysts.

PC	E^*_{red} [a]	τ [b]	K_q (**1a**)[c]	K_q (**1c**)[c]	K_q (**1ad**)[c]
Fukuzumi	2.12	7.3	0.98	2.2	0.50
Sc-Acr_2	2.47	31.0	1.3	3.8	0.74
Al-Acr_2	2.44	31.2	1.4	4.0	0.76
Cu-Acr_2	2.43	30.4	1.3	--	--
Sc+Cu-Acr_2	2.42	31.4	1.3	--	--

1a = cinnamyl alcohol; **1c** = anethole; **1ad** = cyclooctene. [a]E^*_{red} = excited state reduction potential (V vs. SCE). [b]τ = fluorescence lifetime (ns). [c]K_q = Stern Volmer bimolecular quenching constant (10^{10} M^{-1} s^{-1}).

We wondered whether transient absorption spectroscopy might be an effective tool to measure kinetic differences between the different PCs, drawing from precedent by Nicewicz and co-workers.[3] The transient absorption spectra of the $(AcrN)_2$-$Sc(OTf)_3$, $(AcrN)_2$-$Al(OTf)_3$ and Mes-Acr-BF_4 (Fukuzumi) photocatalyst was done in MeCN. The excited state absorption (ESA) at 438 nm and 510 nm had been reported to be attributed to the triplet excited state of acridine (^{3}AcrN*) and the radical anion of the metal triflate-acridine complex formed respectively.[19] Upon addition of anethole, a known electron-rich donor, to each metal triflate-acridine system and the Fukuzumi photocatalyst followed by photoexcitation at 350 nm, a new ESA band appeared at 600

nm (Figure S20) which is attributed to the formation of the anethole radical cation, indicating successful photoinduced electron transfer from anethole to the photoexcited acridine complexes.[3]

We anticipated that the rate of decay of the anethole radical cation to the ground state or the growth in the different photocatalyst systems might play a unique role in contributing to the rate of reaction leading to the difference in the product yield observed in our experiments. The decay of the radical cation peak to the ground state had been ascribed to back electron transfer (BET) process. However, from our transient experiment, the decay of the ESA at 600 nm corresponding to the anethole radical cation was determined to be approximately 10^4 s^{-1} in both photocatalyst systems. This is consistent with the findings of Johnston and co-workers, who reported a decay rate of approximately 10^4 s^{-1} for the trans-anethole radical cation, measured during a Diels-Alder cycloaddition using a triarylaminium salt as the electron transfer catalyst. Furthermore, using the Fukuzumi catalyst as a control experiment, the rate of decay of the anethole radical cation peak at 600 nm was determined to be about 10^4 s^{-1}. The mechanism of BET and the role of acetonitrile as a charge mediator in driving the process had been previously described by Narra and co-workers.[23] In our experiment, we deduce that there is no significant difference in the BET process since the anethole radical cation decay to the ground state at the same rate irrespective of the photocatalyst. However, we observed a significant difference in the rise time at 600 nm which we attributed to growth of the anethole radical cation. Experimentally, we observed that the rate of the growth of the anethole radical cation generated by $(AcrN)_2$-$Al(OTf)_3$ complex is about 1.5 times faster compared to the growth in the $(AcrN)_2$-$Sc(OTf)_3$ process. From the control experiment, the rate of the growth of the anethole radical cation with the Fukuzumi catalyst was about an order of magnitude faster in comparison to the $(AcrN)_2$-$Sc(OTf)_3$ and the $(AcrN)_2$-$Al(OTf)_3$ as seen in (**Figure 7.5**).

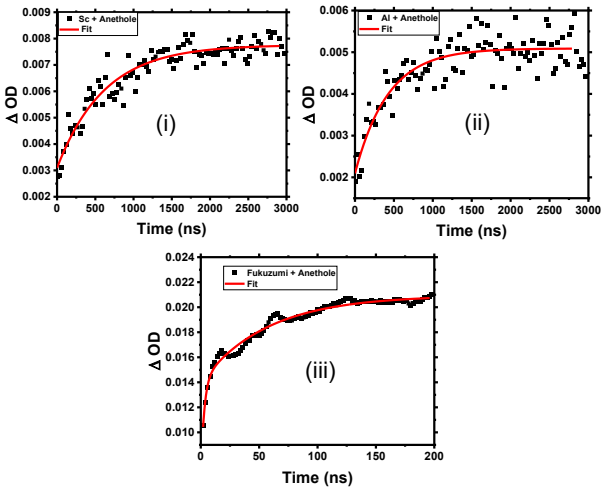


Figure 7.5: (a) Kinetic of the ESA growth time of the (i) Sc PC with anethole (ii) Al PC with anethole and (iii) Fukuzumi PC with anethole.

Table 7.3: Kinetic of the PC's with anethole, where τ_{Growth} = growth time at 600 nm, K_{growth} = rate of growth, τ_{ESA} = ESA lifetime at 600 nm and K_{ESA} = rate of decay of the ESA.

	τ_{Growth} (ns)	K_{Growth} ($x10^6$ s^{-1})	τ_{ESA} (μs)	K_{ESA} ($x10^4$ s^{-1})
Sc PC + *Anethole*	613	0.16	25.1	4.0
Al PC + *Anethole*	424	0.23	24.6	4.1
Fukuzumi PC + *Anethole*	57	1.7	17.3	5.8

Thus, we rationalized that the faster formation of the anethole radical cation might be responsible for the difference in the reaction yields in the $(AcrN)_2$-$Sc(OTf)_3$ and $(AcrN)_2$-$Al(OTf)_3$ complexes. The observed faster formation of the anethole radical cation in the presence of $Al(OTf)_3$ compared

to $Sc(OTf)_3$ is likely attributed to differences in coordination strength and complex dynamics. Although $Sc(OTf)_3$ exhibits stronger Lewis acidity and forms more stable complexes with electron-rich donors such as anethole, this tighter binding may overly stabilize the donor-Lewis acid complex, potentially hindering the optimal orbital alignment or slowing down the reorganization required for efficient photoinduced electron transfer (PET). In contrast, the comparatively weaker coordination of $Al(OTf)_3$ might enable more rapid complex dissociation and reorganization, thereby facilitating a faster electron transfer to the singlet excited state of acridine (AcrN*). The increased lability of the aluminum complex may also promote faster turnover and accumulation of the radical cation in solution.

These studies show definitively that PCs containing different Lewis acids are capable of performing electron transfers from alkene substrates at variable rates, and the magnitude of the rise times implicates electron transfer arising from a triplet state. We conclude that this effect must have an impact on the different alkene substrates, leading to our observed modularity. Future work will examine this relationship between catalyst identity and electron transfer kinetics with the aim of discovering a predictive model.

7.5. Conclusion

We herein demonstrate the hydrofunctionalization of alkenes with diverse nucleophiles, using the highly modular and tunable photocatalytic system employing an *in situ* PC derived from a 2:1 complex of acridines with Lewis acids. We showed that various nucleophiles, including azoles, alcohols, water, and pyridines are competent for anti-Markovnikov alkene hydrofunctionalization, and that alkenes of up to E_{ox} ~ +2.50 V vs SCE could be oxidized under these conditions. Critically, we discovered that this photocatalytic system is highly modular in that different Lewis acid/acridine combinations have significant and unpredictable effects on reactivity,

leading to disparate outcomes for different alkenes. Future work will aim to elucidate the physical bases for this observation, which cannot be explained by excited state potential or excited state lifetime. These results demonstrate a new, cost-effective photocatalytic approach to single electron chemistry and provide a basis for future studies of this catalyst platform in the creation of a tunable and predictive photocatalytic toolkit.

References

1. (a) Margrey, K. A.; Nicewicz, D. A. A General Approach to Catalytic Alkene Anti-Markovnikov Hydrofunctionalization Reactions via Acridinium Photoredox Catalysis. *Acc. Chem. Res.* **2016**, *49* (9), 1997-2006. DOI: 10.1021/acs.accounts.6b00304; (b) Romero, N. A.; Nicewicz, D. A. Organic Photoredox Catalysis. *Chem. Rev.* **2016**, *116* (17), 10075-10166. DOI: 10.1021/acs.chemrev.6b00057

2 (a) Hamilton, D. S.; Nicewicz, D. A. Direct Catalytic Anti-Markovnikov Hydroetherification of Alkenols. *J. Am. Chem. Soc.*, **2012**, *134* (45), 18577-18580. DOI: 10.1021/ja309635w; (b) Perkowski, A. J.; Nicewicz, D. A. Direct Catalytic Anti-Markovnikov Addition of Carboxylic Acids to Alkenes. *J. Am. Chem. Soc.* **2013**, *135* (28), 10334-10337. DOI: 10.1021/ja4057294; (c) Nicewicz, D. A.; Hamilton, D. S. Organic Photoredox Catalysis as a General Strategy for Anti-Markovnikov Alkene Hydrofunctionalization. *Synlett* **2014**, *25* (9), 1191-1196. DOI: 10.1055/s-0033-1340738; (d) Wilger, D. J.; Grandjean, M.-J., M.; Lammert, T. R.; Nicewicz, D. A. The direct anti-Markovnikov addition of mineral acids to styrenes. *Nat. Chem.* **2014**, *6*, 720-726. DOI: 10.1038/nchem.2000; (e) Onuska, N. P. R.; Schutzbach-Horton, M. E.; Rosario Collazo, J. L.; Nicewicz, D. A. Anti-Markovnikov Hydroazidation of Activated Olefins via Organic Photoredox Catalysis. *Synlett* **2020**, *31* (1), 55-59. DOI: 10.1055/s-0039-1690691; (f) Qian, S.; Lazarus, T. M.; Nicewicz, D. A. Enantioselective Amino- and Oxycyanation of Alkenes via Organic Photoredox and Copper Catalysis. *J. Am. Chem. Soc.* **2023**, *145* (33), 18247-18252. DOI: 10.1021/jacs.3c06936

3. Romero, N. A.; Nicewicz, D. A.; Mechanistic Insight into the Photoredox Catalysis of Anti-Markovnikov Alkene Hydrofunctionalization Reactions. *J. Am. Chem. Soc.* **2014**, *136* (49), 17024-17035. DOI: 10.1021/ja506228u

4. Roth, H. G.; Romero, N. A.; Nicewicz, D. A. Experimental and Calculated Electrochemical Potentials of Common Organic Molecules for Applications to Single-Electron Redox Chemistry. *Synlett* **2016**, *27* (5), 714-723. DOI: 10.1055/s-0035-1561297

5. (a) Lasky, M. R.; Liu, E.-C.; Remy, M. S.; Sanford, M. S. Visible-Light Photocatalytic C-H Amination of Arenes Utilizing Acridine-Lewis Acid Complexes. *J. Am. Chem. Soc.* **2024**, *146* (21), 14799-14806. DOI: 10.1021/jacs.4c02991; (b) For a related catalyst system, see: Rickertsen, D. R. L.; Crow, J. D.; Das, T.; Ghiviriga, I.; Hirschi, J. S.; Seidel, D. Acridine/Lewis Acid Complexes as Powerful Photocatalysts: A Combined Experimental and Mechanistic Study. *ACS Catal.* **2024**, *14* (19), 14574-14585. DOI: 10.1021/acscatal.4c04897

6. Merkel, P. B.; Luo, P.; Dinnocenzo, J. P.; Farid, S. Accurate Oxidation Potentials of Benzene and Biphenyl Derivatives via Electron Transfer Equilibria and Transient Kinetics. *J. Org. Chem.* **2009**, *74* (15), 5163-5173. DOI: 10.1021/jo9011267

7. Reich, S. M.; Lasky, M. R.; Sanford. M. S. Visible-Light S_NAr Pyridination of Aryl Halides and Triflates with Acridine-Lewis Acid Photocatalysts. *J. Org. Chem.* **2025**, *90* (290), 10332-10337. DOI: 10.1021/acs.joc.5c01003

8. van der Worp, B. A.; Ritter, T. N-Protonated Acridinium Catalyst Enables Anti-Markovnikov Hydration of Unconjugated Tri- and Disubstituted Olefins. *J. Am. Chem. Soc.* **2025**, *147* (6), 4736-4742. DOI: 10.1021/jacs.4c18185

9. Escorihuela, J.; Lledós, A.; Ujaque, G. Anti-Markovnikov Intermolecular Hydroamination of Alkenes and Alkynes: A Mechanistic View. *Chem. Rev.* **2023**, *123* (15), 9139-9203. DOI: 10.1021/acs.chemrev.2c00482

10. (a) Nguyen, T. M.; Nicewicz, D. A. Anti-Markovnikov Hydroamination of Alkenes Catalyzed by an Organic Photoredox System. *J. Am. Chem. Soc.* **2013**, *135* (26), 9588-9591. DOI: 10.1021/ja4031616; (b) Nguyen, T. M.; Manohar, N.; Nicewicz, D. A. *anti*-Markovnikov Hydroamination of Alkenes Catalyzed by a Two-Component Organic Photoredox System: Direct Access to Phenethylamine Derivatives. *Angew. Chem., Int. Ed.* **2014**, *53* (24), 6198-6201. DOI: 10.1002/anie.201402443

11. (a) Zhang, H.; Huang, C.; Yuan, X.-A.; Yu, S. Photoexcited Chiral Copper Complex-Mediated Alkene $E \rightarrow Z$ Isomerization Enables Kinetic Resolution. *J. Am. Chem. Soc.* **2022**, *144* (24), 10958-10967. DOI: 10.1021/jacs.2c04040; (b) Zhang, H.; He, X.; Yuan, X.-A.; Yu, S. Kinetic Resolution of 2-Cinnamylpyrrolines Enabled by Photoexcited Chiral Copper Complex-Mediated Alkene $E \rightarrow Z$ Isomerization. *ACS Catal.* **2023**, *13* (5), 2857-2866. DOI: 10.1021/acscatal.2c06183; (c) Liu, L.; Ren. S.; Yu, S. Kinetic Resolution of *N*-Allylic Pyrazoles via Photoexcited Chiral Copper Complex-Catalyzed Alkene $E \rightarrow Z$ Isomerization. *Org. Lett.* **2024**, *26* (25), 5232-5236. DOI: 10.1021/acs.orglett.4c01220

12. Katritzky, A. R.; Marson, C. M. Pyrylium Mediated Transformations of Primary Amino Groups into Other Functional Groups. New Synthetic Methods (41). *Angew. Chem., Int. Ed.* **1984**, *23* (6), 420-429. DOI: 10.1002/anie.198404201

13. (a) He, F.-S.; Ye, S.; Wu, J. Recent Advances in Pyridinium Salts as Radical Reservoirs in Organic Synthesis. *ACS Catal.* **2019**, *9* (10), 8943-8960. DOI: 10.1021/acscatal.9b03084; (b) Basch, C. H.; Liao, J.; Xu, J.; Piane, J. J.; Watson, M. P. Harnessing Alkyl Amines as Electrophiles for Nickel-Catalyzed Cross Couplings via C-H Bond Activation. *J. Am. Chem. Soc.* **2017**, *139* (15), 5313-5216. DOI: 10.1021/jacs.7b02389; (c) Plunkett, S.; Basch, C. H.; Santana, S. O.; Watson, M. P. Harnessing Alkylpyridinium Salts as Electrophiles in Deaminative Alkyl-Alkyl Cross-Couplings. *J. Am. Chem. Soc.* **2019**, *141* (6), 2257-2262. DOI: 10.1021/jacs.9b00111; (d) Correia, J. T. M.; Fernandes, V. A.; Matsuo, B. T.; Delgado, J. A. C.; de Souza, W. C.; Paixão, M. W. Photoinduced deaminative strategies: Katritzky salts as alkyl radical precursors. *Chem. Commun.* **2020**, *56*, 503-514. DOI: 10.1039/C9CC08348K

14. Sowmiah, S.; Esperança, J. M. S. S.; Rebelo, L. P. N.; Afonso, C. A. M. Pyridinium salts: from synthesis to reactivity and applications. *Org. Chem. Front.* **2018**, *5*, 453-493. DOI: 10.1039/C7QO00836H

15. Fukuzumi, S.; Yuasa, J.; Satoh, N.; Suenobu, T. Scandium Ion-Promoted Photoinduced Electron Transfer from Electron Donors to Acridine and Pyrene. Essential Role of Scandium Ion in Photocatalytic Oxygenation of Hexamethylbenzene. *J. Am. Chem. Soc.* **2004**, *126* (24), 7585-7594. DOI: 10.1021/ja031649h

16. Ohkubo, K.; Fujimoto, A.; Fukuzumi, S. Visible-Light-Induced Oxygenation of Benzene by the Triplet Excited State of 2,3-Dichloro-5,6-dicyano-*p*-benzoquinone. *J. Am. Chem. Soc.* **2013**, *135* (14), 5368-5371. DOI: 10.1021/ja402303k

17. Pratihar, S.; Prasad, E. Effect of positional isomerism on the excited state charge transfer dynamics of anthracene-based D-π-A systems. *Phys. Chem. Chem. Phys.* **2023**, *25*, 5226-5236. DOI: 10.1039/D2CP03958C

18. Schepp, N. P.; Shukla, D.; Sarker, H.; Bauld, N. L.; Johnston, L. J. Calibration of Intramolecular Radical Cation Probes Based on Arylalkene Cycloadditions. *J. Am. Chem. Soc.* **1997**, *119* (43), 10325-10334. DOI: 10.1021/ja971307+

19. Narra, S.; Nishimura, Y.; Witek, H. A.; Shigeto, S. Mechanism of Back Electron Transfer in an Intermolecular Photoinduced Electron Transfer Reaction: Solvent as a Charge Mediator. *ChemPhysChem* **2014**, *15* (14), 2945-2950. DOI: 10.1002/cphc.201402411

Chapter Eight
Summary of the Dissertation and Possible Future Direction

8.1. Summary of the Dissertation

The work presented in this dissertation provided fundamental photophysical and electronic properties that govern the behavior of emerging organic materials. Although each chapter focuses on distinct classes of molecules, this thesis provides a unified understanding of how molecular structure dictates the excited-state dynamics, charge-carrier properties, and nonlinear optical responses that determine material performance across optoelectronic, quantum photonic, and photocatalytic applications.

Chapter one provided a detailed introduction to the fundamental photophysical mechanisms that underpin the applications explored throughout this dissertation. It outlined how processes such as electronic delocalization, charge transfer, exciton formation, intersystem crossing, and nonlinear light-matter interactions dictates material performance. By connecting these mechanisms to targeted applications in OSCs, OFETs, OLEDs, TADF emitters, quantum sensing, and photocatalysis, Chapter 1 set the framework for the structure-function relationships investigated in the subsequent chapters.

In Chapter two, the different spectroscopic techniques employed throughout this thesis ranging from nonlinear optical measurements to time-resolved spectroscopic techniques were presented in detail. This chapter outlined the operational principles, experimental configurations, and analytical approaches of each method, emphasizing how they enable direct probing of charge dynamics, excited-state processes, and electron-transfer pathways in organic molecular systems.

Together, these spectroscopic tools form the foundation for the structure-property relationships and mechanistic insights developed in the later chapters.

Chapter three focused on a new class of organic ladder oligomers, the benzo[k]tetraphene (BTp) series, designed with varying conjugation lengths and an unsubstituted backbone to isolate the intrinsic relationship between molecular structure and electronic properties. These rigid, π-extended BTps allows for the determination of how conjugation length enhances electronic delocalization, excited-state dynamics, and charge mobility; properties central to advanced organic semiconductor performance. In this thesis, I demonstrated that charge-transport relevant properties improve systematically with increasing conjugation and reach an optimum around BTp 9, where delocalization becomes sufficiently extended to enhance excited-state dynamics and nonlinear optical response without further increase from additional chain elongation. This identification of BTp 9 as the structural optimum establishes a clear molecular design principle for developing next-generation materials for organic solar cells (OSC), organic field-effect transistors (OFET), and other optoelectronic technologies that rely on efficient charge mobility.

Chapter four examines how structural modifications to tetracene-based chromophores influence their interaction with both classical and quantum light and how these properties correlate with coherence behavior in the excited singlet state. Classical two-photon absorption and entangled two-photon absorption measurements reveal that TCHS-tetracene and TIPS-tetracene exhibit significantly larger nonlinear optical cross-sections compared to unsubstituted tetracene, indicating a stronger light-matter interaction pathway enabled by their substituent-induced electronic coupling. Near-field scanning optical microscopy (NSOM) measurements further show that TCHS-tetracene supports substantially longer singlet-state coherence lifetimes, and this

enhanced coherence correlates with its higher classical and entangled photon absorption response. These findings highlight a key structure-property relationship: molecular architectures that interact more efficiently with both classical and quantum light also sustain longer photonic coherence, a critical requirement for quantum sensing and quantum transduction schemes relying on weak-light sensitivity. When placed in the broader context of previously reported work demonstrating that TCHS-tetracene forms a long-lived quintet multiexciton ^{5}(TT) state through singlet fission, the extended coherence observed here further reinforces its potential as a molecular platform capable of supporting long-lived multiqubit states. Thus, this chapter establishes how substituent-controlled tuning of nonlinear optical response and coherence dynamics can guide the design of tetracene derivatives for quantum-light–driven technologies.

Chapter Five presents a coordinated study of the excited-state dynamics of all-trans and all-cis PPV using ultrafast time-resolved spectroscopy, nonlinear optical measurements, and electronic structure calculations. By examining both stereochemical variants under identical experimental conditions, this work clarifies how backbone geometry controls their photophysical behavior. The all-trans PPV, with its more planar and extended π-system, shows faster fluorescence dynamics, which supports its suitability for conventional optoelectronic applications such as OLEDs. Its larger classical two-photon absorption cross-section further reflects the stronger transition dipole moment enabled by its more delocalized electronic structure. In contrast, the all-cis PPV exhibits slower excited-state relaxation and a significantly enhanced entangled two-photon absorption response. Electronic structure calculations indicate that this arises from its lower-lying electronic states and more localized geometry, which couple more effectively with quantum-correlated photons. These properties make the all-cis variant a strong candidate for quantum sensing and low-photon-flux detection. Overall, this study provides clear insight into how

PPV stereochemistry determines its performance across classical and quantum optical regimes. In practical terms, the all-trans PPV is better aligned with high-brightness optoelectronic applications such as OLEDs, while the all-cis PPV is better suited for quantum-light-driven technologies.

In this thesis, chapter six demonstrates how systematically extending the fused IDTT backbone from monomer to dimer and trimer directly enhances the electronic pathways that govern thermally activated delayed fluorescence (TADF). As the number of IDTT units increases, the electronic coupling between the excited singlet state and the nearby triplet manifold becomes more effective, giving the larger systems more accessible pathways for reverse intersystem crossing (rISC). This progression is further reinforced by the increasing number of sulfur atoms in the extended structures. The presence of sulfur introduces a measurable heavy-atom contribution that enhances spin–orbit coupling, particularly between the lowest triplet states and the emissive singlet. These combined effects allow the trimer to support the most efficient singlet-triplet conversion, reflected in its fastest rISC rate and highest delayed-fluorescence yield. The improved electronic coupling in the trimer also leads to a markedly stronger optical response. Classical two-photon absorption increases by roughly a factor of twenty relative to the monomer, and the entangled two-photon absorption cross-section grows by nearly an order of magnitude. The parallel rise in nonlinear optical activity and rISC efficiency demonstrates that the same electronic factors responsible for enhanced spin conversion also promote stronger interaction with both classical and quantum light. Overall, chapter six establishes that extending the IDTT unit from monomer through trimer provides a direct and effective means of enhancing the electronic interactions and spin-orbit coupling required for increasing the rate of reverse intersystem crossing. These results offer clear guidance for designing OLED emitters and molecular systems intended

for advanced photonic applications where strong light-matter coupling and efficient excited-state interconversion are essential.

Chapter seven explores a modular and cost-effective approach for generating highly oxidizing acridinium-based photocatalysts through simple in situ complexation with Lewis acids. By forming 2:1 acridine-Lewis acid complexes, the system achieves exceptionally high excited-state oxidation potentials up to +2.65 V vs SCE allowing it to promote challenging single-electron transformations, including anti-Markovnikov hydrofunctionalization of alkenes with oxidation potentials near +2.5 V. A major outcome of this work is the demonstration that the catalytic activity and substrate scope can be tuned by selecting different Lewis acids. Using transient absorption spectroscopy, the chapter shows that the Lewis acid identity directly influences electron-transfer rates and radical formation kinetics, ultimately dictating reaction efficiency. This tunability enabled successful functionalization with a broad array of nucleophiles, including azoles, alcohols, water, and even pyridines a reactivity not previously reported for this class of systems. Overall, this chapter establishes that acridinium-Lewis acid complexes provide a versatile platform for high-potential photoredox catalysis. The ability to tailor electron-transfer dynamics through simple coordination chemistry offers a powerful design strategy for expanding the capabilities of visible-light photocatalysis while significantly reducing cost and synthetic complexity.

8.2. Future Direction

The emerging classes of molecular systems explored in this work point toward several strategic opportunities for advancing next-generation materials across organic electronics, quantum information science, and photocatalysis. A primary direction for future research is the development of rigid, π-extended organic materials engineered to maximize charge delocalization

while maintaining structural stability. Such systems will be essential for pushing intrinsic carrier mobility to levels required for high-efficiency organic solar cells (OSC) and organic field-effect transistors (OFETs). Further innovation in backbone design through controlled heteroatom incorporation, steric control, and modular π-bridge extension will be crucial for achieving materials capable of supporting long-range charge transport under operational conditions. These advances have the potential to significantly enhance power-conversion efficiencies in OSCs and improve switching speed and stability in OFET architectures.

In parallel, there is substantial opportunity to expand the role of organic chromophores in OLED technologies, particularly through materials that support rapid and efficient harvesting of triplet excitons. Future efforts should focus on molecular systems that simultaneously strengthen charge-transfer character and modulate spin-conversion pathways, enabling faster reverse intersystem crossing and brighter, more stable emission. Molecular systems that pair extended conjugation with rigid molecular frameworks may yield emitters with reduced nonradiative losses and improved delayed fluorescence performance. Such materials can directly influence device lifetime, color purity, and energy efficiency in state-of-the-art OLED platforms.

The broader field of quantum information science (QIS) stands to benefit greatly from organic systems specifically designed to interact with quantum-correlated light and support long-lived spin states. Future research should aim to design chromophores that combine strong entangled-photon absorption with robust stabilization of correlated triplet pairs and high-spin multiexcitons. Embedding these molecules into ordered or spin-protected environments could enable the development of molecular qubits, low-photon-flux quantum sensors, and photon-to-spin transduction interfaces capable of operating near room temperature. By tailoring electronic

coupling and vibronic structure, researchers can significantly expand the role of organic materials in scalable quantum architectures.

Another promising direction involves using conformational and stereochemical control to tune whether a material favors classical high-flux optical processes or quantum-light specific interactions. This approach opens opportunities for multifunctional materials capable of serving as both efficient absorbers/emitters for traditional optoelectronics and highly sensitive detectors for quantum-light applications. Such dual-function systems could impact waveguide-integrated detectors, entangled-photon imaging, and hybrid quantum photonic applications.

In the area of photocatalysis, future progress will rely on the design of molecular catalysts whose redox potentials, excited-state lifetimes, and electron-transfer kinetics can be tuned through modular coordination environments. Expanding the use of tunable Lewis-acid, multidentate ligands, or hybrid organicmetallic complexes could yield photocatalysts capable of activating substrates with exceptionally high oxidation potentials. Such systems may enable previously inaccessible synthetic transformations, support greener reaction pathways, and reduce energy barriers in industrial catalysis. Integrating ultrafast spectroscopic and computational tools into catalyst design will accelerate the development of reactive intermediates and mechanisms that can be precisely controlled.

Collectively, these directions prioritize the design of organic materials that unite high charge mobility, enhanced spin control, strong nonlinear optical response, and tunable electron-transfer reactivity. Advancing these capabilities will directly impact the performance, efficiency, and scalability of OSC, OFET, OLED, QIS, and photocatalytic technologies. As molecular engineering becomes increasingly precise, these emerging material classes will form the

foundation for a new generation of high-performance, low-cost, and versatile devices across energy, electronics, quantum science, and chemical synthesis.